University of Nottingham
UK | CHINA | MALAYSIA

Development of in-service monitoring based models for remaining life management of thermally loaded ageing structures

Bonetti Rossella, MEng.

Thesis submission to the University of Nottingham
for the degree of Doctor of Philosophy

September 2024

Abstract

The primary aim of this thesis is to propose and develop a novel and practical life assessment methodology for power plant applications that uses more proactively both periodic and routine inspection data in conjunction with online operational data. This methodology facilitates the computation of the remaining life of high temperature components and essentially links the plant data routinely collected during outage inspections, via online monitoring or by testing of material samples to the life prediction models. High temperature pipework will be used as an example of the proposed approach and deployable creep life prediction models are reviewed that could function with these plant datasets. Of critical importance is that the output from the life prediction is used to inform plant operations on any necessary changes in order to mitigate damage accumulation.

A holistic empirical lifing approach, which accommodates the on-site information of replica, hardness and strain, is established. The approach is based on an extensive review and analysis of a large amount of outage inspection data on ageing high temperature parent ½Cr½Mo¼V (CrMoV) material and has been used to illustrate how such routinely collected inspection data can be better utilised to provide the plant operator with predictions of residual creep life. The model differentiates between long term and persistent thermal softening behaviour revealed by change in hardness over time and short-term creep cavitation that accelerates material damage. Importantly, the models developed are designed to be used iteratively with surface replica and hardness data available from an outage inspection. The study shows that the availability of more data will enable further refinements, but more importantly, it emphasises the importance of systematically capturing these data and processing them at the time of inspection to forecast residual life and then updating and tuning the model periodically at future inspections. The capture of strain data from pipe diametral measurements is also a routine outage activity and this data is included in a case study to demonstrate the capabilities in the residual life forecast by the new methods.

An integrated life assessment procedure for structures operating under thermomechanical loading is also developed. The methodology uses a viscoplasticity based framework combined with the R5 life assessment code. The viscoplastic

constitutive model used for the stress-strain analysis is derived from the Chaboche-Lemaitre formulation from which can be directly obtained the required parameters for the R5 assessment as stress relaxation per cycle and the elastic follow-up factor. The R5 procedure is therefore significantly simplified. The proposed life assessment procedure is demonstrated on a martensitic steel (FV566) industrial gas turbine rotor under a typical start up – shut down operation. The effect of creep-fatigue interaction at different locations within the rotor structure is assessed and the remaining life at each location is calculated. A sensitivity study is performed at half load, which shows an increase in lifetime of the rotor compared to the full load condition.

The developed lifing model techniques are backed up with a physical explanation by investigating the softening behaviour of a P91 steel due to its microstructural changes under creep testing. The creep degradation behaviour of ex-service-exposed P91 steel is investigated during interrupted creep tests at 660°C and 80 MPa using a number of material characterization techniques including TEM, SEM, EBSD, EDS and optical microscopy to identify the microstructural evolution and the associated deformation mechanisms during creep at temperature. Microhardness has also been measured in order to evaluate the softening mechanism. Under the creep conditions examined, microstructural degradation is found to be governed by the disappearance of the lath sub-structure, lath widening and recrystallization, dislocation density reduction, coarsening of $M_{23}C_6$ and creep cavitation while MX and Laves phases are stable. Hardness evolution, extrapolated from hardness data obtained from uniaxial creep tests, is used to characterize the softening of the material. On this basis, hardness decrease is justified in term of the aforementioned microstructural changes. Implications of the findings for specific in-service life management in thermal plant piping systems are finally addressed.

Acknowledgements

I would like to take this opportunity to express my gratitude to my supervisors, Professor Wei Sun, Professor Philip Shipway and Andy Morris, for their guidance, patience and invaluable support throughout the course of my PhD studies. I would not have been able to complete this PhD without their continuous encouragement.

I would like to thank the technical staff, particularly Mr Shane Maskill and Dr Nigel Neate, who helped me throughout all the experimental work.

I would like to acknowledge the support of EDF Generation (UK) for its sponsorship.

This thesis was supported by the Engineering and Physical Sciences Research Council (Grant numbers: EP/G037345/1; EP/ L016206). The funding is provided through the EPSRC Centres for Doctoral Training in Carbon Capture and Storage and Cleaner Fossil Energy (www.ccscfe-cdt.ac.uk). The author would like to thank also RWE for their valuable contribution, support and for permission to publish their data.

I would like to acknowledge also the support from Ansaldo Nuclear that allowed me to join the company part-time gaining experience in the nuclear sector as I continue working towards the completion of my PhD.

Also, I would like to express my highest gratitude to my partner Massimo and to my twins baby boys, Giovanni and Francesco, to have made our life unforgettable in the small things and full of funny memories. This work is also for them, to teach them to aim high and to be resilient in the tough moments.

List of publications

1. R. Bonetti, A. Morris, P.H. Shipway, W. Sun., *"Requirements for developing high temperature creep life models for ageing pipework systems using power plant condition monitoring and inspection data"*, International Journal of Pressure Vessels and Piping 188 (2020) 104233.

   R. Bonetti: Conceptualization, Methodology, Writing – Original Draft, Writing - Review & Editing, Visualization, Project administration. **A. Morris:** Conceptualization, Writing – Original Draft, Writing - Review & Editing, Supervision, Funding acquisition. **P.H. Shipway:** Writing - Review & Editing, Supervision. **W. Sun:** Conceptualization, Methodology, Writing - Review & Editing, Funding acquisition, Project administration, Supervision.

2. R. Bonetti, P. Hadjipakkos, Y. Rae, J. Hughes, W. Sun, *"A lifing method based on R5 and viscoplasticity modelling and its application to turbine rotor under thermomechanical loading"*, Engineering Failure Analysis 110 (2020) 104416.

   R. Bonetti: Methodology, Writing – Original Draft, Writing - Review & Editing, Visualization, Project administration, Software, Investigation, Visualization. **P. Hadjipakkos:** Methodology, Writing – Original Draft, Writing - Review & Editing, Software, Investigation. **Y. Rae:** Software. **J. Hughes:** Writing - Review & Editing, Supervision. **W. Sun:** Conceptualization, Methodology, Writing - Review & Editing, Funding acquisition, Project administration, Supervision.

3. R. Bonetti, A. Morris, P.H. Shipway, W. Sun, *"Empirical relationships between hardness, replica and strain and their roles in health monitoring based life assessment for aged power plant materials"*, International Journal of Pressure Vessels and Piping 199 (2022) 104735.

   R. Bonetti: Conceptualization, Methodology, Writing – Original Draft, Writing - Review & Editing, Visualization, Project administration, Formal analysis, Investigation, Visualization. **A. Morris:** Conceptualization, Writing – Original

Draft, Writing - Review & Editing, Supervision, Funding acquisition, Resources. **P.H. Shipway:** Writing - Review & Editing, Supervision. **W. Sun:** Methodology, Writing - Review & Editing, Funding acquisition, Project administration, Supervision.

4. R. Bonetti, N.C. Neate, A. Morris, P.H. Shipway, W. Sun, *"Microstructure evolution and deformation mechanisms of service-exposed P91 steel via interrupted uniaxial creep tests at 660^{o}C"*, Journal of Materials Research and Technology 33(2024) 3529-3549.

   R. Bonetti: Conceptualization, Methodology, Writing – Original Draft, Writing - Review & Editing, Visualization, Validation, Project administration, Formal analysis, Investigation, Visualization. **N.C. Neate:** Investigation, Validation, Writing – Original Draft, Writing - Review & Editing. **A. Morris:** Conceptualization, Writing – Original Draft, Writing - Review & Editing, Supervision, Funding acquisition, Resources. **P.H. Shipway:** Writing - Review & Editing, Supervision. **W. Sun:** Methodology, Writing - Review & Editing, Funding acquisition, Project administration, Supervision.

Nomenclature

To aid the reader's understanding a nomenclature of commonly used symbols is presented here. Symbol definitions are given also in the text to avoid confusion and have been divided into subject areas to make context recognition easier. Note that, in general, symbols in a bold typeface are vectors or tensors.

General

D	Diffusion coefficient
D_0	Pre-exponential factor in diffusion equation
Q_D	Activation energy for diffusion
R	Universal gas constant (8.314 J mol^{-1} K^{-1})
T	Temperature
λ	Interparticle spacing
μ	Shear modulus
b_1	Burgers vector
α'	Particle/dislocation interaction parameter
σ	Applied uniaxial stress
σ_h	Hoop stress
σ_{UTS}	Ultimate tensile strength
σ_0	Orowan stress
E	Young's modulus
ρ	Density of mobile dislocations

v	Average dislocation velocity

Creep Material Models

a_i, b_i, c_i, d_i	θ projection method material constants
k_1, k_2, k_3, u, v, w	Wilshire model constants
m, M	Monkman-Grant constants
m_1	Time exponent in primary and secondary creep strain equation
t, t_r	Time (instant, rupture)
t_a, T_a, MHP	Manson-Haferd constants and parameter
t_ε	Time to reach a specified strain level, ε
C_{LM}, LMP	Larson-Miller constant and parameter
$C_{OSD}, OSDP$	Orr-Sherby-Dorn constant and parameter
Q_c	Activation energy for creep
Q_c^*	Apparent activation energy
$\varepsilon_c, \dot{\varepsilon}_c$	Creep strain at time *t* and creep strain rate
$\dot{\varepsilon}_{ss}$	Minimum (steady) creep rate
ε_o	Instantaneous strain
$\dot{\varepsilon_{t0}}$	Omega model initial (reference) tertiary creep rate
ε_r	Creep strain at rupture (failure)
ε_{tot}	Total strain
$\theta_1, \theta_2, \theta_3, \theta_4$	θ projection method parameters

Ω	Creep damage variable in the Omega model
A	Material parameter in Norton's law
n	Creep exponent in Norton's law
A_0	Constant in the Failure Forecast method
α	Exponential constant in the Failure Forecast method
A_1	Constant in the Masuyama hardness drop relationship
A_2	Parameter in the Shammas equation
a, b	Constants in the hardness-minimum creep rate relationship by Morris et al.
B	Constant in the creep rupture equation
HV	Hardness at time *t*
HV_0	Initial hardness
ΔH	Hardness drop
k_1, k_2, k_3	Constants in the ECCC hardness equation
k_A	Temperature exponential constant
K, q	Constants relating interparticle spacing to hardness
K_s	Fitting coefficient in the Masuyama hardness drop relationship
p	Correction constant in Allen-Fenton hardness model
S	Dimensionless stress parameter in the Allen-Fenton equation
u, w	Scaling and exponential factor in the hardness relationship for straight pipes

v, z	Scaling and exponential factor in the hardness relationship for bends
ω	Creep damage variable defined as cavity ratio
Λ	Secondary to tertiary creep strain ratio in Shammas equation

Chaboche Unified Visco Plasticity Model

$\dot{\boldsymbol{\varepsilon}}_{\mathbf{p}}$	Inelastic strain rate tensor
$\boldsymbol{\varepsilon}_{\mathbf{p}}$	Inelastic strain tensor
$\dot{p}$	Accumulated viscoplastic strain rate
Δp	Accumulated plastic strain
$\boldsymbol{\varepsilon}$	Total strain tensor
f	Yield function
Z_1, n	Viscous stress material constants
$\boldsymbol{\sigma}$	Stress tensor
$\boldsymbol{\chi}$	Kinematic hardening tensor
$\dot{\boldsymbol{\chi}}$	Kinematic hardening evolution
χ_i	i^{th} uniaxial kinematic hardening component
a_i, C_i	Temperature-dependent material coefficients in the kinematic hardening evolution law
R	Isotropic hardening parameter
$\dot{R}$	Isotropic hardening evolution
b, Q	Coefficients in the isotropic hardening evolution law

k	Initial yield surface size
σ_{v}	Viscous stress
Φ	Viscoplastic residue

Fatigue Material Models

S_a	Stress amplitude
S_m	Mean stress
ΔS	Cyclic stress range
R	Stress ratio
N_f	Cycles to failure
σ'_f , b_2	Coefficients in the Basquin equation
$\Delta\varepsilon_p$	Plastic strain amplitude
ε'_f , c	Coefficients in the Coffin-Manson equation
$\Delta\varepsilon$	Total strain amplitude

R5 Model Parameters

$\Delta\sigma'$	Stress relaxation
Z	Follow-up parameter
A_3, C, D	Material constants in the fatigue damage calculation
$\Delta\bar{\varepsilon}_{\mathrm{t\,max}}$	Maximum equivalent total strain range during the start-up and shut-down
ε_{ij}	Strain component

$\bar{\varepsilon}(t, t')$	Equivalent strain range between time t and t'
d_{f}	Fatigue damage for each cycle
d_{c}	Creep damage per cycle
t_{h}	Dwell period
ε_L	Lower shelf ductility
ε_U	Upper shelf ductility
D	Total damage
D_{f}	Total fatigue damage
D_{c}	Total creep damage
n_j	Number of cycles of type j
$N_{\mathrm{f}j}$	Value of N_{f} for cycles of type j
$d_{\mathrm{f}j}$	Value of d_{f} for cycles of type j
d_{cj}	Value of d_{c} for cycles of type j

Contents

1 Introduction

In the thermal power generation industry, heavy section components such as steam boilers, steam pipes, high temperature headers, turbine rotors etc., are subjected to operation at high temperatures and pressures. The typical operating conditions consist of steam temperatures up to 600 °C and steam pressure up to 25 MPa. At the same time, these components operate under variable and cyclic thermal and mechanical loadings depending on the market demand for power and due to a rise in intermittent renewable sources. In addition, the worldwide energy request is expected to increase in the next years but with lower greenhouse emissions. This will require the plants to run more efficiently, with this being achieved by operation at even higher temperatures (up to 700 °C) and pressures (up to 30 MPa). Under these conditions, the aging effects that most affect the damage (and thus remaining lifetime) of power plant components are creep, fatigue and their combination [1-3].

To answer to an increasingly demanding energy market, better performing materials under creep-fatigue are being selected to build new power stations or to replace existing components. Over the years, there has been a transition from low-alloy ferritic steels (CrMoV) to high-strength martensitic steels (9-12% Cr) that show superior characteristics under creep and fatigue under more demanding operating conditions. In particular, Grade 91 (9% Cr-molybdenum steel) amongst the 9-12% Cr steels has been widely used in the UK since the 1990s for retrofit superheater headers and drums in coal-fired plant thanks to its higher creep strength enabling a reduced section size and hence reduced risk of thermal fatigue compared with the low alloy steel headers which it has replaced [4-6].

It is always extremely important to understand the evolution of the in-service properties of component materials to guarantee safe and reliable operations while maintaining the profitable operations of the plant. In fact, premature in-service 9-12% Cr steel failures have happened in several UK coal-fired stations and worldwide before the end of the estimated design life especially in the weld heat-affected zones (Type IV cracking) [7]. In addition, CrMoV steel systems have been observed to be particularly susceptible to the initiation and growth of defects in welds, which could

lead to steam leakage, or even to a complete fracture of the pipework. Catastrophic and less catastrophic creep failures have been registered in boiler headers or hot reheat pipes in UK mainly due to operational temperatures being higher than the design temperature which caused an acceleration of creep life consumption rates resulting in huge commercial losses [8, 9].

Standard design practice, based on parent material strength data, has therefore failed to ensure adequate performance in practice. The risks may also be exacerbated by adverse factors related to design, compositional variations, heat treatment, and service conditions. There is also the hazard that material with an incorrect microstructure (and consequently substandard high temperature properties) due to out-of-specification heat treatments can enter in service causing the unexpected failure of the base material within the design life. The failure of the parent material after long time exposure before reaching the design life may also occur by violent rupture. Nevertheless, due to the conservatism in the design there may equally be a significant likelihood that components can be justified for operation beyond the design life, subject to suitable monitoring and surveillance to keep risks to a minimum [1, 10-12].

Plant condition monitoring in terms of in-service monitoring and inspection, repair and where necessary replacement is therefore the mainstay of plant life management, with these seeking to address the risks associated with cracking, potential steam leaking and/or violent failure of pressure part components during service. The current management strategy that aims to guarantee safe operations includes the characterisation of the material conditions by on-site inspection using non-destructive techniques (NDT) and surface replication, specification of the inspection periodicity based on priority and parallel in-service material monitoring behaviour models that utilise operational data such as steam temperature and pressure. Site investigation techniques are applied for the estimation of creep damage during a planned site outage and the most common include diametrical measurements on conventional locations using micrometers, hardness measurements, replica metallography, ultrasonic testing, acoustic emission and magnetic testing. Currently the most deployed inspection techniques are hardness measurement which is the most reliable mean for the identification of material conditions and replication [9, 10].

Inspection techniques (even if extremely important because allow the determination of the actual degradation characteristics of the material) alone are not perceived as enough for the purpose of life management since they are part of a reactive approach and normally are very expensive and invasive [8]. An inspection-based approach should always be used in conjunction with an in-service monitoring approach that studies the health and safety of a system. The in-service monitoring approach is based on the monitoring of temperature and pressure data that are captured from key points in the plant at regular intervals and are used in creep rupture life models for the estimation of creep life consumption [13]. However, there is often a discrepancy between the life consumption calculated by in-service monitoring models and the one indicated by site inspections and this makes the planning of an accurate maintenance schedule difficult to achieve [9, 13].

The purpose of the present thesis is therefore the development of a more informed and proactive condition monitoring strategy for the prediction of remaining life as opposed to a continued implementation of traditional, periodic and increasingly costly inspection-based assessment approaches, repairs and replacements.

The thesis is organised as follows:

Chapter 2 presents the Literature Review where the creep phenomenon and creep lifing models applied to power plant components are first described. This is followed by an introduction to fatigue fundamentals and a more in-depth explanation to creep-fatigue interaction failure mechanisms and the industrial approach to creep-fatigue. The Literature Review provides also details about the materials used in high temperature applications with an emphasis on CrMoV and P91 steels. The current approach to condition monitoring and its application to high temperature materials is also briefly illustrated. In addition, models for life assessment based on inspection techniques are reviewed to provide a foundation for the development of the new monitoring strategy. In view of the findings from the Literature Review, the aims of the present thesis are discussed and addressed in the following chapters.

Chapter 3 describes first the requirements for developing creep life models for components operating under ageing effects in order to overcome the actual industrial challenges. A new approach to condition monitoring is then proposed which considers

the peculiarities of different material behaviour by using ad-hoc creep models to predict the remaining life. The new approach combines a predictive model that uses online data coupled with site inspection data. The use of a life assessment transfer function (LATF) is investigated as deemed necessary in order to enable the material model to communicate efficiently with disparate sets of monitoring data.

Chapter 4 proposes an improvement to the current industrial lifing methodology for creep-fatigue interaction based on R5 by linking it with the Chaboche viscoplasticity theory. The use of this new lifing model is demonstrated on an industrial gas turbine rotor made from FV566 martensitic steel (12% Cr steel).

Chapter 5 assesses methodically large datasets from periodic outage inspection reports for ½Cr½Mo¼V (CrMoV) material in order to find possible correlations between inspection data. The purpose is to establish a holistic empirical lifing approach, which accommodates the on-site information of replica, hardness and strain and is used to illustrate how such routinely collected inspection data can be better utilized to provide the plant operator with predictions of residual creep life. A hardness and creep replica assessment relationship is presented, for the first time, for parent material straight and bend sections.

Chapter 6 studies the creep damage evolution of an ex-service exposed P91 material pipe through interrupted creep tests and metallurgical investigation. EBSD, SEM, optical microscopy and TEM techniques have been deployed to characterize the microstructural evolution and the softening behaviour of the material. Physical investigations have been conducted on P91 material in order to provide physical underpinning for the models proposed in the previous chapters by studying the effect of microstructural changes on the softening of the material.

Concluding remarks and suggestions for possible future work are made in Chapter 7.

2 Literature Review

As indicated in the introduction, there is now a need to be able to extend the service life of power plant components whilst avoiding mechanical failures. The key mechanisms of potential mechanical failure are creep and fatigue, and the risk of these increase with the time that a particular component has spent in service due to the fact that in both cases (creep and fatigue), damage accumulates over time. In this Literature Review, an overview of creep and fatigue mechanisms, fundamental laws and the industrial design approaches for components operating at high temperatures under fatigue and creep is presented. The review concentrates on the most common steels used in power plants for steam pipework and other major components, their mechanical behaviour and microstructural evolution under service. Within the expected operating life of the plant, a condition monitoring strategy is adopted by power plant operators to control the real status of systems and components. The outcomes of this strategy trigger repair/replacement actions aiming at avoiding huge financial losses and unexpected failures. The current most common employed monitoring technique to high temperature materials is the physical examinations during a plant outage with non-destructive techniques (NDT). For this reason, predictive life assessment methods based on data from NDT and developed over the years are explained and discussed at the end of the chapter.

The state of the knowledge of the aforementioned topics is outlined in this chapter.

2.1 Creep Fundamentals

Creep represents a major concern for engineers and metallurgists when components operate under high stresses and temperatures (typical conditions in the power generation industry) which cause mechanical degradation and may lead creep failure.

Creep is defined as time-dependant permanent (plastic) deformation that takes place under constant load at elevated temperature. Metals normally creep under stresses below the yield strength of the material at temperatures higher than 0.5 Tm where Tm is the absolute melting temperature in [K] of the material [14]. The main parameters

that define creep and creep rate are therefore exposure time, t, applied stress, σ, temperature, T and material properties (Equation 1).

$$\varepsilon_c = f(t, T, \sigma, microstructure) \quad (1)$$

At temperatures higher than 0.5 Tm various microstructural processes, that are negligible at lower temperature, are activated leading to creep and to the decrease of the mechanical strength of the material. These main processes are diffusion, which shows an exponential relation with temperature (Equation (2)), dislocation mobility, change of equilibrium vacancy concentration, activation of new slip systems and deformation at grain boundaries [15].

The diffusion coefficient as a function of temperature is defined as follows:

$$D = D_0 \exp\left(-\frac{Q_D}{RT}\right) \quad (2)$$

where D is the diffusion coefficient, D_0 is a pre-exponential factor, Q_D is the activation energy for diffusion [kJ mol^{-1}], R is the universal gas constant (8.314 J mol^{-1} K^{-1}), T is the temperature in [K] [16-18].

Operating stress and temperature govern the physical mechanism responsible for creep deformation. Various deformation mechanisms are illustrated through deformation mechanism maps developed first by Ashby and co-workers [15]. Figure 1 is a schematic illustration of the deformation mechanism map for a generic polycrystalline material. In the figure, the different regions of the map identify different creep mechanisms according to different stress and temperature combinations. The stress is normalized to the material's shear modulus (G) and the temperature to the material's melting temperature (Tm) [19]. The creep deformation mechanisms can be grouped as:

- Dislocation glide: for high stress, $\sigma/G > 10^{-2}$;
- Dislocation creep: for $10^{-4} < \sigma/G < 10^{-2}$;
- Diffusion creep: for $\sigma/G < 10^{-4}$. This category includes the Nabarro-Herring and Coble creep.

At high stress (above the theoretical strength of the material) plastic flow occurs instantaneously without dislocations. Dislocation glide involves the movement of dislocations along slip planes and the overcoming of barriers to their motion by thermal activation. Dislocation creep (also known as Power Law creep) involves the glide of dislocations helped by thermally assisted mechanisms such as vacancy or interstitial diffusion.. Diffusion creep involves the atomic diffusion of vacancies and interstitials under the applied stress and results in the elongation of grains in the material along the direction of the applied stress. In Nabarro-Herring creep, there is a flow of vacancies through the lattice inside the grains from grain boundaries subjected to tensile stresses to grain boundaries subjected to compressive stresses. In Coble creep, the diffusion involves the grain boundaries resulting in their sliding [15, 18]. Each deformation mechanism is described by a specific constitutive equation [15]. Although diffusional and dislocation creep processes are independent and both contribute to the overall creep rate, one of these processes is defined as the 'dominant' when the contribution made by the other process is negligible [20]. In real word applications, as in the power generation industry, the dominant creep mechanism depends on the service conditions. Advanced heat resistant steels may exhibit the transition from dislocation to diffusion creep at stress levels relevant for engineering applications [21] For high-temperature materials as 9-12%Cr steels the transition from dislocation creep to diffusional creep happens at around 100 MPa at 600 °C [22]. the normal applications of these materials are mainly in the lower stress regimes governed by diffusional processes [23].

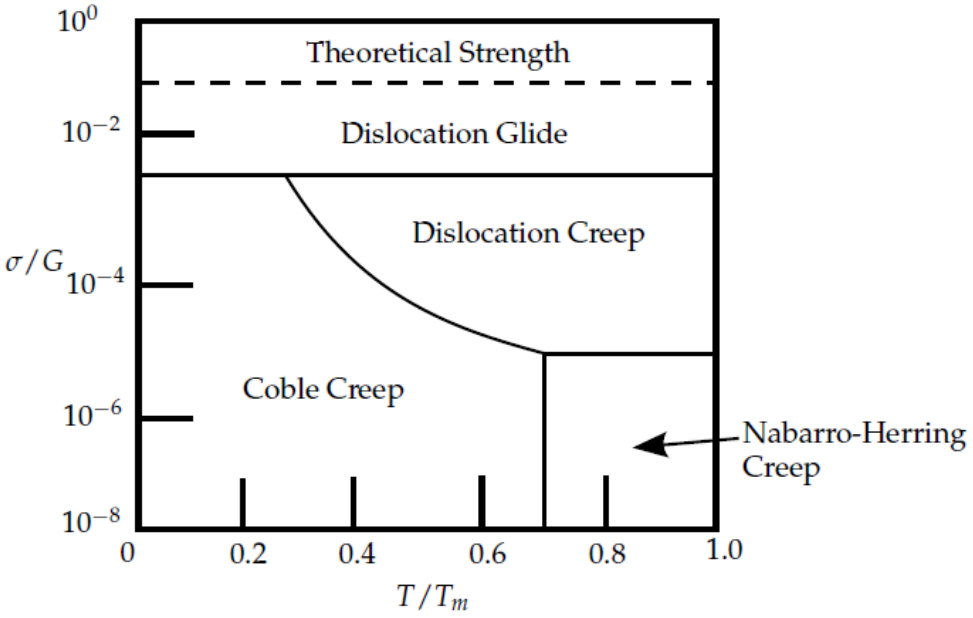

Figure 1: Schematic representation of creep deformation map [19]

The most common method employed to investigate the creep behaviour of a material is uniaxial creep testing of a specimen under constant stress and constant temperature until failure. The conditions for a laboratory creep test are typically more severe than the in-service operating conditions in order to accelerate the development of damage since creep deformation accumulates only slowly over time. The severity is increased by a combination of higher temperature and / or higher applied stress. In the creep test, the strain ε (extension) is recorded over time *t* and a typical curve is shown in Figure 2.

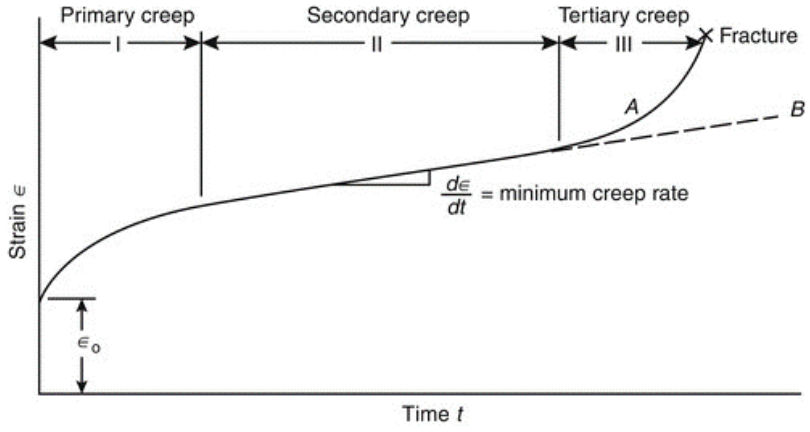

Figure 2: Typical creep curve under constant nominal stress and temperature showing three different stages [24]

After an initial instantaneous elastic or elasto-plastic strain $\varepsilon_o$generated by the application of the load, the creep curve is generally characterized by three distinctive stages: primary, secondary and tertiary creep. Each creep stage is governed by operation of a different physical mechanism. The primary or transient creep stage is governed by strain-hardening which causes a reduction of strain rate as a consequence of dislocation multiplication and entanglement. In the secondary or steady-state creep stage, the balance between strain-hardening (strengthening mechanism) and dynamic recovery (softening mechanism) leads to a constant (steady-state or minimum) creep rate. The tertiary creep stage is characterized by an effective reduction in cross-sectional area either because of necking or internal void formation [19]; at the onset of the tertiary creep stage the balance between strain-hardening and recovery is broken due to the acceleration of microstructural changes that lead to a rapid increase of creep strain rate until the final fracture. The degradation mechanisms responsible for the reduction of creep strength and for creep damage can be grouped as follows: dynamic recovery and recrystallization, coarsening of precipitates, nucleation and agglomeration of cavities and micro-crack formation [25].

The most important parameter in the ε-*t* curve is the steady-state (or minimum) creep rate $\dot{\varepsilon}_{ss}$ because it is used for the determination of creep rupture life [26]. It is important to remember that many engineering steels do not show a secondary creep stage in their creep curve but the primary stage leads directly to the tertiary stage (Figure 3). For this reason in many texts the steady state creep rate $\dot{\varepsilon}_{ss}$ is reported as minimum creep rate $\dot{\varepsilon}_{min}$ but in the following thesis for clarity just $\dot{\varepsilon}_{ss}$ will be used [6].

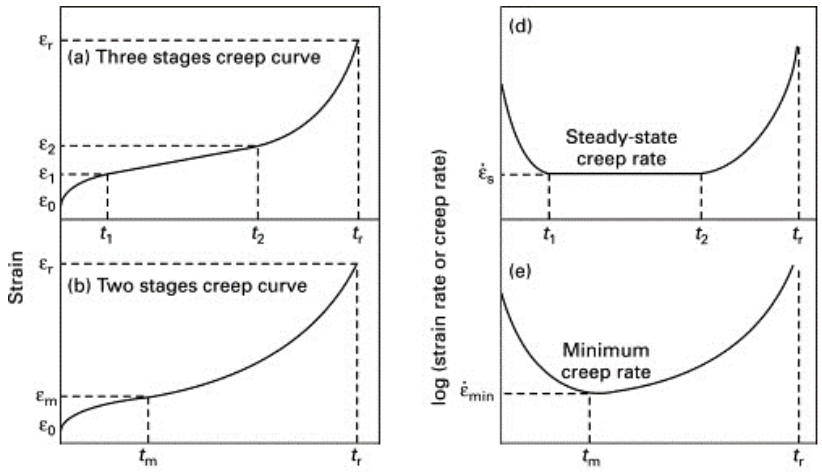

Figure 3: Creep curves for different engineering steels showing a steady-state or minimum creep strain rate. Adapted from [6]

In addition, different combinations of stress and temperature generate different shapes of creep curve with different extents of the various creep stages (Figure 4). An increase in stress and/or temperature will result in a reduction of time to rupture t_r and in an acceleration of $\dot{\varepsilon}_{ss}$ [6, 19, 25, 26].

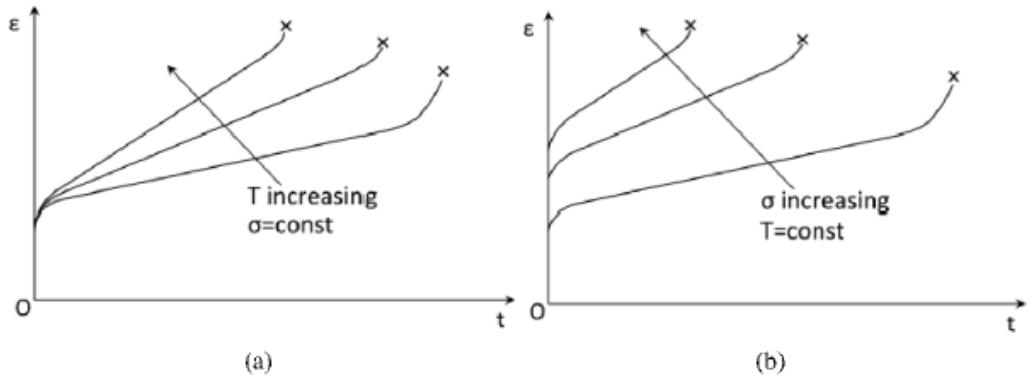

Figure 4: Creep curve variation as function of stress and temperature [27]

2.1.1 Creep constitutive equations

A constitutive equation describes the material behaviour via a basic equation which relates the creep strain and creep strain rate to readily measurable factors such as time, temperature and stress and variables such as damage which are not directly measurable in-situ in operational plant [28-30].

The total strain from Figure 2 is represented as the sum of the instantaneous strain ε_o and the creep strain (or time-dependent plasticity) ε_c (Equation 3).

$$\varepsilon_{tot}(t) = \varepsilon_o + \varepsilon_c \tag{3}$$

The primary creep strain is normally described by the time-hardening law (Equation 4) or the strain-hardening theory (Equation 6).

$$\varepsilon_c = A\sigma^n t^{m_1} \tag{4}$$

where A, n and m_1 are temperature dependent material parameters and are determined from uniaxial creep tests. $m_1 < 1$ in the primary creep to represent a decreasing creep rate.

The primary creep strain rate is obtained by differentiating Equation 4 respect to the time whilst keeping the stress σ constant (Equation 5).

$$\dot{\varepsilon_c} = m_1 A\sigma^n t^{m_1 - 1} \tag{5}$$

Substituting the time in Equation 5 with the time extracted from Equation 4, the strain-hardening law is obtained that relates the creep strain rate, $\dot{\varepsilon_c}$, directly to the creep strain, ε_c, and the stress, σ (Equation 6).

$$\dot{\varepsilon_c} = m_1 A^{1/m_1} \sigma^{n/m_1} \varepsilon_c{}^{(m_1 - 1)/m_1} \tag{6}$$

The secondary creep strain is defined using Equation 7.

$$\varepsilon_c = \dot{\varepsilon}_{ss} t^{m_1} \tag{7}$$

where $m_1 = 1$ represents a situation with a constant creep rate and $\dot{\varepsilon}_{ss}$ is the steady-state creep rate.

For its simplicity, the Norton-Bailey power law is commonly used to describe the relation between the steady-state creep rate and the applied stress at a given temperature in the uniaxial case (Equation 8). Other well-known stress dependence equations are the Prandtl, Dorn, Garofalo, Soderberg, Johnson et al. and friction stress theories [29, 31].

$$\dot{\varepsilon}_{ss} = A\sigma^n \tag{8}$$

The dependence of creep rate on temperature is represented by adding to Equation 8 an Arrhenius-type term (Equation 9)

$$\dot{\varepsilon}_{ss} = A\sigma^n \exp\left(\frac{-Q_c}{RT}\right) \tag{9}$$

where Q_c is the activation energy for creep that has been found to be often equal to the diffusion activation energy Q_D [14]. The creep stress exponent,n, is an important creep parameter because provides information on the dominant fundamental creep deformation mechanism which is operating (see Figure 1). It is obtained by recording different creep curves at the same temperature but different stresses and plotting the steady-state creep rate versus the stress on a logarithmic scale. It is found that *n* varies between 3 and 10 under the most common conditions used for creep tests under high stresses (due to dislocation creep) but at low stress (due to diffusional creep), $n \sim 1$ [32]. Lab creep tests are generally conducted at different temperatures and stresses in order to replicate the creep mechanism under service conditions. If this is not possible, the long-term creep properties are predicted with extrapolation techniques using accelerated tests obtained under increased stress and temperature to the in-service loading conditions [21]. It should be emphasized the importance to understand the actual creep mechanism in order to better predict the creep behaviour of the steel under different service conditions [23]. Any extrapolation from a different creep mechanism (generally from power-law creep to lower stresses) may lead to a serious underestimation of the creep rate predicted [22].

2.1.2 Creep cavitation and cavitation damage modelling

The concept of creep damage is introduced in order to describe the degradation processes that characterize the tertiary creep phase and the acceleration of creep rate. Creep damage is a broad term aiming to define the irreversible loss of the material capability to withstand an external load due to strain accumulation which finally leads to creep failure via the accumulation of internal defects. Creep damage is part of the Continuum Damage Mechanics (CDM) approach that is a global theory with the aim to understand and model component failure before the initiation of the macro-cracking

process and is based on the use of internal state variables which describe material deterioration [33].

Different physical mechanisms are involved in creep deterioration of a material, as listed above, but normally just a single parameter is chosen as a measure of damage and this is often referred to be intergranular cavitation. The nucleation of cavities followed by their growth and interlinkage leads to the creep failure of the material [34]. It is generally observed that creep cavities form along grain boundaries in proximity of second phase particles [34]. The cavities gradually agglomerate forming microcracks as creep progresses [34]. The size and density of the cavities increase from the secondary to the tertiary creep stage [34]. A first ranking to classify the creep damage was proposed by Neubauer. He introduced a schematic assessment of the microstructure by using a grade of evolution ranging from 0 equivalent to normal microstructure to 5 equivalent to macrocracks [35].

The nucleation and growth of voids along grain boundaries on a microscopic level is defined by the creep damage parameter ω. The introduction of a damage parameter used to describe a phenomenon associated with a mechanism, in this case creep, is typical of the phenomenological approach to avoid a physical description of the creep process even if it is more simplistic and less reliable than a physical approach since it only mimics what it is observable at macroscopic level [28]. In order to model the damage accumulation, the ω parameter is introduced in the strain rate equation to allow an increase in strain rate as damage increases (Equation 10).

$$\dot{\varepsilon_c} = f(\sigma, t, \omega) \tag{10}$$

Equation 10 is coupled necessarily with a damage rate equation $\dot{\omega}$ that describes how the damage parameter ω evolves with time (Equation 11).

$$\dot{\omega} = g(\sigma, t, \omega) \tag{11}$$

In the uniaxial case, Equations 10 and 11 take often the form of Equations 12 and 13.

$$\dot{\varepsilon_c} = A\left(\frac{\sigma}{1-\omega}\right)^n t^m \tag{12}$$

$$\dot{\omega} = B\frac{\sigma^{\chi}}{(1-\omega)^{\Phi}}t^{m} \tag{13}$$

where A, n and m are the material parameters that control the primary and secondary creep as defined above, while B, χ and Φ are material constants that control the tertiary creep and are determined by the basic uniaxial creep curves [29]. In the undamaged state ($\omega = 0$) and with $m = 1$, Equation 12 leads back to the Norton-Bailey power law (Equation 8). At rupture, ω approaches unity.

The most common and well-known phenomenological approach from which Equations 12 and 13 are extracted is the Kachanov-Rabotnov theory which was the first to represent damage as an effective loss of resisting material cross-sectional area due to the formation of internal voids [36, 37].

2.1.3 Creep lifing and deformation models

The different creep rupture theories that are most widely used for the calculation and modelling of remaining creep life of a component in service is presented in more detail in this section.

A wide variety of models [38-44] are available for the evaluation of remnant creep life and for the deformation behaviour of materials operating at high temperature and pressure. The various models can be categorized as follows:

a) Empirical models (e.g. Larson-Miller [45], Manson-Haferd [46], Orr-Sherby-Dorn [47], Monkman-Grant [48], θ projection method [49], Wilshire [50], Omega [51]), which are mostly used in industrial applications;
b) Phenomenological models (e.g. Kachanov-Robotnov [36, 37], Liu-Murakami [52], Dyson [43, 53]), which are based on continuum damage mechanics (CDM) approach;
c) Physically based models [54-59], which formulate creep constitutive equations from microstructural features (such as dislocation density and interparticle spacing) varying over time and temperature.

The aforementioned creep models could be classified based on the following criteria: complexity, accuracy and widespread use (Figure 5).

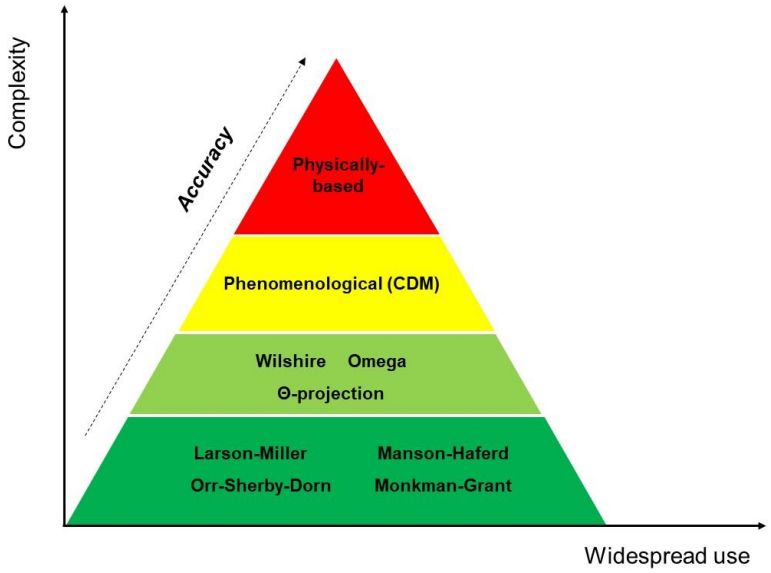

Figure 5: Perception of some common creep lifing models [60]

From Figure 5, it is evident that empirical models (indicated by the two shades of green) are the most widespread and commonly used for practical purposes. Despite their potential to provide an improved remaining life assessment, phenomenological (CDM) and physically-based models are less straightforward to use. Phenomenological (CDM) models employ a large number of material constants estimated after uniaxial creep tests and an optimization procedure [44]. In physically-based models, the accuracy of the measurements of certain features depends on the surface preparation and on the ability of operators to correctly evaluate and compute microstructural factors [56]. Therefore, the following section gives a review of empirical models illustrating their usefulness together with their limitations while phenomenologically-based and physically-based models will be treated more briefly.

2.1.3.1 Empirical Models

Empirical (or parametric) models such as Larson-Miller [45], Manson-Haferd [46] and Orr-Sherby-Dorn [47, 61], described by Equations from 14 to 16 respectively, predict the rupture life of materials from short-term creep tests by deriving a parameter which is function of the applied stress only. Experimental data from uniaxial accelerated short-term creep rupture tests performed at high stresses and high temperature are fitted with a master curve, which allows the prediction of longer-term creep rupture

properties by using a constant time-temperature parameter (LMP, MHP, OSDP) [62]. The advantage of these extrapolation methods is that they allow the estimation of rupture time for plant components that need to operate over 100,000 hours from just performing short-term creep tests.

$$LMP\ (\sigma) = T(C_{LM} + log\ t_r)\ /1000 \tag{14}$$

$$MHP(\sigma) = (log\ t_r - log t_a)/(T - T_a) \tag{15}$$

$$OSDP(\sigma) = lnt_r - C_{OSD}/T \tag{16}$$

where t_r is the rupture time in hours and *T* is the operating temperature in Kelvin. *LMP* and C_{LM} are the Larson-Miller parameter and material constant [40]. *MHP* is the Manson-Haferd parameter, *ta* and *Ta* are the respective constants [44]. *OSDP* and C_{OSD} are the Orr-Sherby-Dorn parameter and material constant respectively [62]. The relationship between the parameter and the stress is user-defined to best fit the experimental creep rupture data [44]. When these models were originally developed, C_{LM}, t_a, T_a and C_{OSD} were defined as standard material constants (C_{LM} is considered equal to 20 for most engineering materials), but in reality they vary under different stress-temperature conditions according to the creep mechanism, resulting in a variability in the prediction of creep rupture time and strength. In order to ensure operational safety, minimum values of the constants are selected leading to a conservative estimation of rupture time [20]. In addition, components in service are subjected to less severe operating conditions, which lead to different long-term microstructural evolution and degradation than the one observed in accelerated creep tests. Despite the variability in predictive capability, these models are relatively easy to deploy.

The Manson-Brown equation (Equation 17) is a 4th degree polynomial formula that represents the general form of parametric models, Equations 14 ÷ 16, and employs operational data (stress and temperature) and a reference stress for the component [13, 63].

$$\frac{\log t_r - p_5}{(T - p_6)^{p_7}} = p_0 + p_1 \log\sigma + p_2(\log\sigma)^2 + p_3(\log\sigma)^3 + p_4(\log\sigma)^4 \quad (17)$$

where t_r is the predicted creep rupture time in hours and *T* is the operating temperature in Kelvin. The stress is equivalent to a reference stress ($\sigma = 1.25\sigma_{ref}$) and $p_0, p_1, \ldots p_7$ are material constants.

The Monkman-Grant equation predicts the creep rupture time t_r through the minimum (steady-state) creep strain rate $\dot{\varepsilon}_{ss}$ [48]. Its simplest form is given in Equation 18 where t_r increases linearly with the decrease of $\dot{\varepsilon}_{ss}$. When secondary creep is dominant, this essentially predicts a constant creep ductility that is independent of stress and temperature. It is widely used in industrial practice because of its simplicity.

$$t_r \, \dot{\varepsilon}_{ss}{}^m = M \quad (18)$$

where *M* and *m* are material constants; *m* varies in the range 0.8–1 even if in most applications, it is set equal to 1 [38] while *M* has a broader range of variation (normally from 3 to 20) depending on the alloy considered and on temperature and is determined from short-term tests [64]. The Monkman-Grant equation (Equation 18) gives a first indication of time to fracture but does not consider creep damage that happens in the tertiary stage [65]. For example, materials with similar shape of creep curve and the same minimum creep rate can have different failure time and elongation due to microstructural evolution during prolonged exposure [66]. Also, there is still disagreement on the values to give to the variables and if they are stress- or/and temperature-dependent [62, 67].

The θ-projection method [43, 68] extracts the full creep curve and estimates creep rupture properties under different range of temperature and stress by extrapolation of short-term uniaxial creep data. Results from tests up to 1,000 hours are analysed to predict the creep behaviour at operating service up to 100,000 hours whereas time-temperature equivalence parameters (LMP, MHP, OSDP) are generally recommended for extrapolation only up to three times the longest reliable rupture life [20]. The original and general form of the θ-projection method is the 4-θ equation as presented in Equation 19, where θ_i are characterizing parameters derived by a linear relationship with stress and temperature given in Equation 20 [69].

$$\varepsilon_c = \theta_1 [1 - \exp(-\theta_2 t)] + \theta_3 [\exp(\theta_4 t) - 1] \quad (19)$$

in which θ_1 and θ_3 are strain scaling parameters for the primary and tertiary creep respectively, θ_2 and θ_4 define the rate of strain accumulation for the primary and tertiary creep respectively. The stress- and temperature-dependence of θ_i are described as follows:

$$ln\theta_i = a_i + b_i\sigma + c_i T + d_i \sigma T \qquad (i = 1,2,3,4) \quad (20)$$

where a_i, b_i, c_i, d_i are material constants determined by a least squares regression analysis on Equation 20 [46]. However, it has been noticed that the θ-method gives poor analysis of creep rupture performance at low stresses leading to deviations from experimental creep curves. An improved version is the 6-θ equation [70] but errors are still not well understood for predictions of long-term creep life [38].

Wilshire's creep life prediction model [71, 72] based on 5,000 hours data has been found to be consistent with experimental data at 100,000 hours reported in NIMS and ECCC [6] and lately the model has been used to reconstruct the full creep curve [65]. Through Equations from 21 to 23, the Wilshire model predicts rupture time t_r, minimum creep strain rate $\dot{\varepsilon}_{ss}$ and the time to reach a desired strain level t_ε.

$$\frac{\sigma}{\sigma_{UTS}} = exp\left\{-k_1\left[t_r\, exp\left(-\frac{Q_c^*}{RT}\right)\right]^u\right\} \quad (21)$$

$$\frac{\sigma}{\sigma_{UTS}} = exp\left\{-k_2\left[\dot{\varepsilon_{ss}}\, exp\left(\frac{Q_c^*}{RT}\right)\right]^v\right\} \quad (22)$$

$$\frac{\sigma}{\sigma_{UTS}} = exp\left\{-k_3\left[t_\varepsilon\, exp\left(-\frac{Q_c^*}{RT}\right)\right]^w\right\} \quad (23)$$

where R is the universal gas constant (8.314 J mol^{-1} K^{-1}), T is the operational temperature in [K], $Q_c^*$is the apparent activation energy in [kJ mol^{-1}]. The constants, k_1, u, k_2 v, k_3 and w are determined by plotting respectively $ln[t_r\, exp\ (-Q_c^*/RT)]$, $ln[\dot{\varepsilon_{ss}}\, exp\ (Q_c^*/RT)]$ and $ln[t_\varepsilon\, exp\ (-Q_c^*/RT)]$ against $ln[-ln(\sigma/\sigma_{UTS})]$ [48] once the value of Q_c^* is known [49]. Full creep curves are reconstructed from equation 23 expressing w and k_3 over a range of selected strains such that $w = f(\varepsilon)$ and $k3 = f(\varepsilon)$

[65]. In the Wilshire model, the dislocation processes are deemed to govern strain accumulation and thus the resulting creep behaviour of materials whereas the influence of ageing factors that is relevant especially at low stresses is neglected [50]. Using the Wilshire equations, a transition in material's behaviour (break point) is normally identified where the values of the parameters change. Further investigations are needed in order to clarify the reasons for this transition which can be due to a change in the creep mechanism [6].

The Omega method developed by Prager [51] is based on the concept that the strain rate is a direct measure of material damage allowing a direct estimation of rupture and remaining life through Equations 24 and 25. The model is at present included in API 579–1/ASME FFS-1 standard [73].

$$t_r = \frac{1}{\Omega \dot{\varepsilon_{t0}}} \tag{24}$$

$$t_r - t = \frac{1}{\Omega \dot{\varepsilon_c}} \tag{25}$$

where Ω is the stress-temperature dependent damage coefficient and $\dot{\varepsilon_{t0}}$ is the initial or reference creep rate and $\dot{\varepsilon_c}$ is the instantaneous creep strain rate at time *t*. The stress-temperature dependent damage coefficient, Ω, is experimentally calculated as $\Omega = d \ln \dot{\varepsilon}_c / d\varepsilon_c$ which expresses the rate at which strain rate accelerates due to creep strain [51]. In the Omega model, only tertiary creep is considered since the strain rate accelerates due to microstructural damage occurring in the last stage of creep and Equation 26 is the corresponding constitutive equation for the development of the tertiary creep rate.

$$\dot{\varepsilon_c} = \dot{\varepsilon_{t0}} \exp(\varepsilon_c \Omega) \tag{26}$$

The applicability of the Omega method is restricted to cases where a linear relationship is found between the creep strain and the logarithm of remaining life or between the logarithm of strain rate versus strain [74]. Improved estimations of Ω, and thus of creep life, are obtained at lower stresses where microstructure evolution takes place due to diffusional processes [66]. The assumption within the model to neglect primary and

secondary creep is not always valid; depending on the magnitude of the applied stress and temperature, creep cavities could also nucleate in the later stage of secondary creep [75].

2.1.3.2 Phenomenological models

Phenomenological models have as their object the description of the macroscopic behaviour of the material when subjected to a combination of effects such as a multiaxial state of stress and softening induced by damage during creep deformation. As opposed to this approach, the objective of physically-based models is to understand the physical mechanisms by which material degradation and failure under creep occur [42]. Constitutive equations such as the ones presented in paragraph Creep constitutive equations are developed following the phenomenological approach for predicting the rupture life and deformation behaviour of components and are focussed on representing the tertiary creep stage. The accuracy of these equations is verified by conducting both experimental uniaxial and notched bar / plates tests [42, 76].

As already mentioned, the continuum damage mechanics (CDM) theory is a broad framework in which these models are derived. Early work CDM work addressing creep was conducted by Kachanov and Rabotnov who developed the concept of a single damage variable ω and used this to formulate the power-law constitutive Equations 12 and 13 for uniaxial stress. Whilst a physical meaning of ω was not assigned by Kachanov and Rabotnov, later in CDM theory, it became common to define ω as the volume element area occupied by cavities over the overall area (Equation 27) [33].

$$\omega = \frac{S_D}{S} = 1 - \frac{\tilde{S}}{S} \tag{27}$$

where S_D is the element cross-sectional area occupied by voids, S and $\tilde{S}$ are respectively the overall and the effective resisting, un-damaged cross-sectional area of the volume element. In the un-damaged state $\omega = 0$ while at rupture $\omega = 1$. A graphical representation of ω is given in Figure 6.

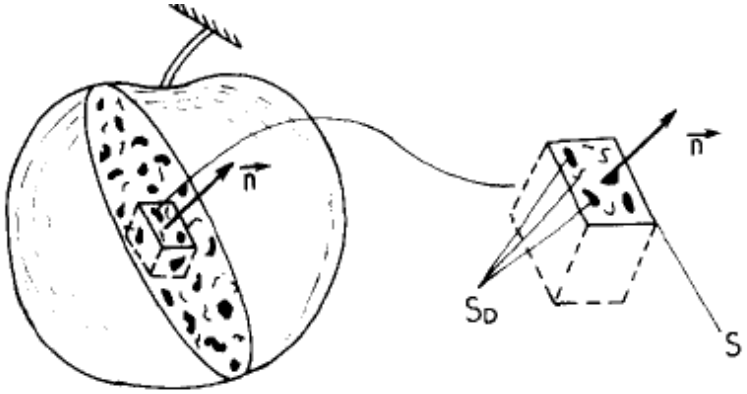

*Figure 6: Schematic representation of a damaged body on the left with view of cross-sectional area defined by the normal **n**. Volume element with defects on the right [76]*

The formulation for the rupture time is then obtained by integrating the damage evolution law (Equation 13) between $\omega = 0$ and $\omega = 1$ (Equation 28).

$$tr = \left\lfloor \frac{m+1}{B(\Phi+1)\sigma^{\chi}} \right\rfloor^{\frac{1}{m+1}} \tag{28}$$

where the material constants B, χ, Φ and m are derived from a procedure of estimates of initial values from fitting of the uniaxial creep tests and final optimisation [44, 77]. Since components in service operate under a multiaxial stress state, the Kachanov-Rabotnov equations have been generalized to a multiaxial form by Leckie and Hayhurst. In the multiaxial formulation of the creep strain rate, the stress is substituted with the equivalent von-Mises stress, the creep strain with the multiaxial creep strain components and the deviatoric stress component is introduced. In the multiaxial damage rate equation the stress is substituted with the rupture stress that is related to the von-Mises stress through a triaxial stress state material constant [78].

The inherent limitation of the Kachanov-Rabotnov is that, by not providing a critical level of damage, at rupture (when ω tends to unity), the damage rate and creep strain rate approach infinity. For this reason and despite its simplicity in calculating the rupture time, the Kachanov-Robotnov model is impractical when implemented in finite element analyses (FEA) because requires a huge computational effort [19]. In order to overcome this disadvantage, Liu and Murakami proposed and alternative

exponential phenomenological model. The uniaxial formulation of the Liu-Murakami model is represented by Equations 29 and 30 [77, 79, 80].

$$\dot{\varepsilon_c} = A\sigma^n exp\left[\frac{2(n+1)}{\pi\sqrt{1+\frac{3}{n}}}\,\omega^{3/2}\right] \tag{29}$$

$$\dot{\omega} = B\frac{1-\exp(-q_2)}{q_2}\,\sigma^p \exp(q_2\omega) \tag{30}$$

A, n, B, q_2 and p are material constants which are always determined through a fitting and optimisation process [77, 81]. The Liu-Murakami model, like the Kachanov-Rabotnov one, is based on the definition of a single state variable but in most applications the softening mechanism is due to a combination of different degradation effects and this can lead to a poor prediction of long-term failure times when extrapolation is performed from short-term tests results [44]. In order to provide a better estimate of the failure times and creep deformation, Dyson developed a three state variable damage model where each variable represents a main degradation mechanism. The Dyson model uses a hyperbolic sine (sinh) stress function that gives a better quantification of creep deformation for wider stress / temperature ranges. In the model, the three state variables represent: (i) the damage mechanisms of strain-hardening during primary creep; (ii) coarsening of lattice precipitates and (iii) grain boundary creep cavitation; an evolution law is associated with each variable [43]. A multiaxial formulation for the Liu-Murakami and Dyson models are available in literature [19]. The Dyson model equations are not reported here because they are not used in this thesis; however, a detailed description of the model is presented in the literature [43, 78, 82, 83].

Since phenomenological models are validated on the basis of experimental results from accelerated tests conducted in a higher stress / temperature regime than the conditions of service, it is important to pay attention when these models are used to extrapolate the material behaviour for longer times to ensure that the stress and temperature boundaries defined by Ashby maps (see Figure 1) are not crossed in order to not change the creep mechanism involved [15, 42, 84].

2.1.3.3 Physical-based models

The physical approach aims to describe the creep damage process through a physical understanding of the material and is more reliable since it is based on the evolution of internal microstructural state variables. Over the years, different damage parameters have been selected to best represent structural degradation and to formulate lifing models. A mechanistic model was developed by Cane [57] on the basis that most engineering materials lose their resistance to creep deformation by coarsening of precipitates (and the consequent changes in the way that dislocations interact with these precipitates in the creep process) and by intergranular creep cavitation. A flow stress equation was established as function of the evolution of interparticle spacing and of creep cavities and this was subsequently related to the creep strain rate via a modified Norton's law formulation which includes also temperature.

A similar approach was followed by Ellis [56] where metallographic methods for determining remaining creep life were developed and a distinction was proposed between creep in base metal and creep in the heat affected zone (HAZ) of a weld. In the base metal model, carbide coarsening is identified as the main creep damage mechanism and is correlated with time and temperature to represent microstructural degradation. The carbide coarsening is measured through transmission electron microscopy (TEM). In contrast, a constrained creep cavitation growth model was developed for the HAZ based on the fraction of life consumed during service via cavities or cracks measurable with surface replicas. The HAZ model takes inspiration from the Kachanov approach but assigns a physical meaning to the damage parameter. Both Cane [57] and Ellis [56] underlined the importance of hardness measurements to assess the microstructural degradation. In fact, interparticle spacing can be expressed as function of hardness so that a creep lifing model using hardness rather than interparticle spacing is proposed [57]. This provides an approach to overcome the difficulties and limitations in measuring accurately the microstructural features, such as interparticle spacing, via microscopy techniques.

Subsequently, the hardness-based approach for remaining life assessment was further improved by other authors such as Mukhopadhyay et al. [85] who related the hardness to a range of microstructural effects (i.e. solid-solution strengthening, precipitate

strengthening, dislocation strengthening and grain-boundary strengthening) and their evolution. Microstructural evolution kinetic equations as function of time and temperature were formulated in order to represent the changes in these parameters and thus to hardness degradation. The final formulation is quite complex and requires the arduous determination of a number of microstructural parameters.

Another interesting formulation was proposed by Estrin [58, 59] starting from the original work of Kocks-Mecking [86] which concerned modelling of material work-hardening behaviour to understand creep deformation [54]. Estrin based his approach on a unique damage parameter able to describe the plastic behaviour of the material. This unique parameter is defined as the strength required to move dislocations over obstacles and is related directly to dislocation density which was chosen originally by Kocks-Mecking. In these models, dislocation density represents therefore the key structure variable. The principle of the Estrin approach is to combine an evolution law of the dislocation glide strength (also named flow stress) with a kinetic equation where the stress is function of strain rate at a given temperature and at a given state of the parameter. The evolution law for the governing parameter is based on the dislocation density variation established by the competition between work-hardening (dislocation multiplication) and recovery (dislocation annihilation).

Even if a physical approach can give more confidence in the prediction of life, because of its inherent complexity in establishing with accuracy the microstructural state parameters, it has a limited application and up to now has been deemed inappropriate for industrial use [3].

2.2 Creep – fatigue interaction and lifing models

2.2.1 Fatigue fundamentals

Alongside to creep, fatigue represents the other major mode of failure high temperature power plant applications. Fatigue failure occurs by initiation of cracks generally at a free highly stressed surface followed by crack growth due to repeated cyclic loading and then to final fracture. Figure 7 is a schematic representation of a fatigue rupture surface showing the three characteristic regions: crack initiation at surface, crack propagation region with beachmarks and a region of fast fracture. Therefore, the understanding of mechanisms and rates of fatigue and the factors

influencing them such as service conditions (temperature, stress, frequency etc.) and material (microstructure, grain size, internal defects, heat treatment etc.) are of paramount importance for dealing with fatigue damage accumulation problems and for the prediction of fatigue life [87, 88].

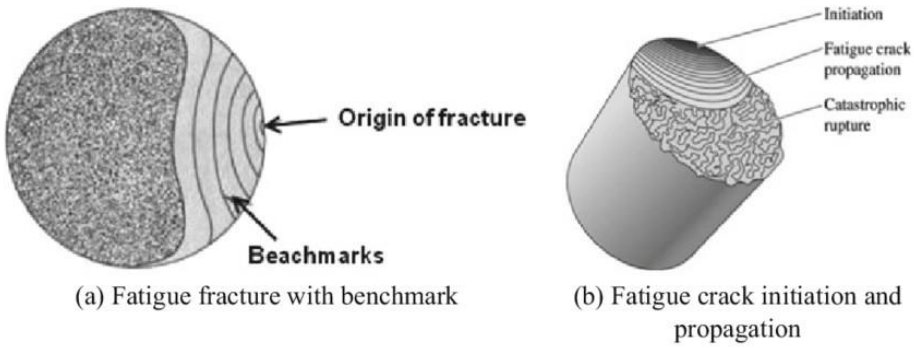

Figure 7: Schematic representation of fatigue failure surface [89]

Generally speaking, fatigue is defined as the progressive loss of material strength due to the accumulation of plastic strain during cyclic or fluctuating loads which can lead to component failure at a stress level much lower than the one required in static (i.e. creep) or monotonic (i.e. tensile test) conditions [90].

Complex service load histories (characterized by a variable amplitudes and mean loads) are substituted in laboratory fatigue tests by more simplified loadings with constant amplitude and mean load as represented in Figure 8 where a typical stress vs time curve used in fatigue design is shown.

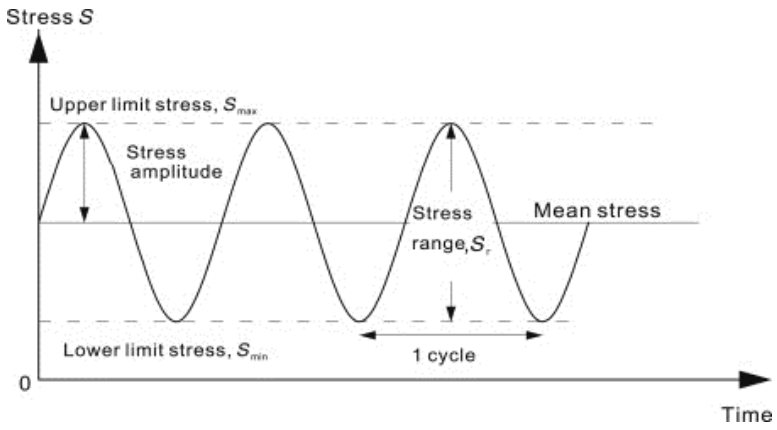

Figure 8: Schematic diagram showing key fatigue parameters [91]

Figure 8 underlines the nomenclature useful in the fatigue discussion: cyclic stress amplitude $S_a = \frac{S_{max}-S_{min}}{2}$, mean stress $S_m = \frac{S_{max}+S_{min}}{2}$, cyclic stress range $\Delta S = S_{max} - S_{min}$ and stress ratio $R = S_{min}/S_{max}$.

Different approaches are available for fatigue design and these can be summarized as follows [92]:

1) Total-life approaches
2) Defect- tolerant approaches
3) CDM approaches.

Total-life approaches represent the classical methods to fatigue design and include the cyclic stress range life approach (S-N curve) introduced first by Wohler and the strain-range life approach. These approaches aim to estimate the fatigue life (defined as the total number of stress or strain cycles to induce fatigue failure) in an initially uncracked and flawless specimen under constant amplitude of cyclic stress or strain. Fatigue failure occurs when a major crack is initiated and then propagates until the final catastrophic rupture.

The stress-life (S-N curve) approach has found a widespread use in the high-cycle fatigue (HCF) applications that involve a large number of cycles to failure (normally $> 10^3$) due to the application of a low-amplitude cyclic stresses which induce an elastic response in the material [3]. From tests on unnotched specimens (e.g. rotating bending tests or uniaxial tests), the S-N curve is obtained by plotting the applied cyclic stress amplitude $S_a$versus the number of fatigue cycles to failure N_f. Some materials (e.g. mild steels, strain-aged steels) show a plateau in their S-N curve where there are stresses where failure does not occur even at very large numbers of cycles ($N \gg 10^6$); this is termed the fatigue limit (Figure 9). Other materials such as copper, aluminium and other high strength steels do not exhibit a fatigue limit and the endurance limit in these cases is defined as the stress amplitude which the specimen can support for at least $N_f = 10^7$ [90].

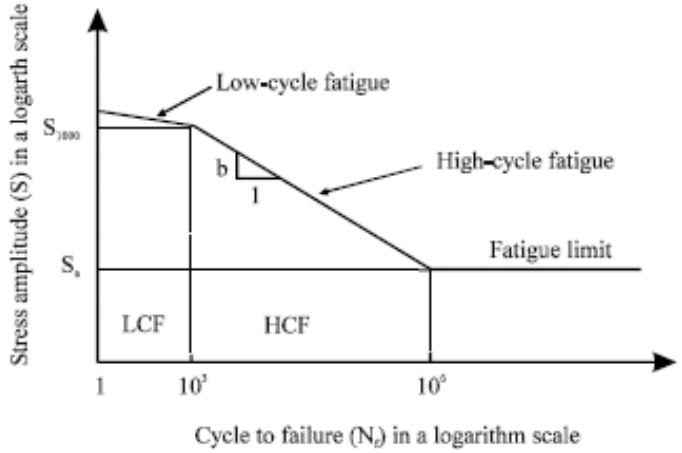

Figure 9: Typical S-N curve showing HCF and LCF limit [93]

The Basquin equation is used to describe the relationship between the stress amplitude and the number of load reversals to failure $2N_f$ (Equation 31).

$$S_a = \sigma'_f \, (2N_f)^{b_2} \tag{31}$$

where σ'_f is the fatigue strength coefficient and b_2 is the fatigue strength exponent.

Modifications to the Basquin equation have been proposed to consider the effect of the mean stress on fatigue life since in most applications, this is not zero. The most commonly employed models for estimating the effect of mean stress on fatigue life are represented by the Gerber, Goodman and Soderberg relationships.

In addition to mean stress, engineering components are usually subjected to cyclic stresses with varying amplitude. The fatigue damage caused by each set of cyclic stresses at the same amplitude, in a sequence of blocks of different stress amplitudes, is predicted by the Palmgren – Miner cumulative damage rule [94]. This relationship is a linear damage model where failure occurs when the linear sum of damage from each stress level equals unity. Experience shows that for different applications, the Palmgren – Miner rule is not sufficiently accurate leading to an unacceptable estimation of fatigue damage, with this shortcoming being attributed to the fact that it does not consider the multitude of mechanisms responsible for damage accumulation [92].

When plastic strain occurs under fatigue loadings, the fatigue life is significantly shortened. This is the case for the low-cycle fatigue (LCF) mechanism that is governed

by the plastic response of a material as a result of alternating stresses with magnitude between the yield and the ultimate tensile strength of the material. As a result of plastic strain, a hysteresis loop on the stress - strain cycle is observed during cyclic strain-controlled loading (Figure 10) [95].

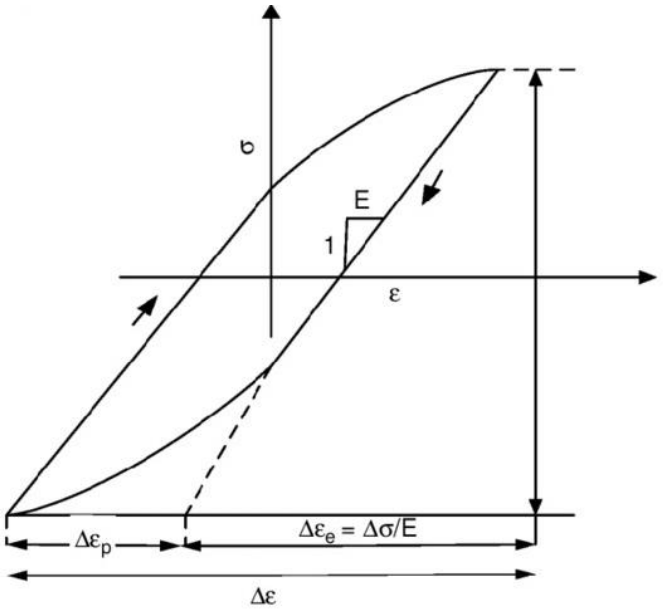

Figure 10: Schematic cyclic stress-strain hysteresis loop [96] as response of the material under cyclic loading

The area enclosed by the hysteresis loop represents the energy per unit volume exhausted per cycle by the material [97].

The strain-life approach was introduced to characterize the LCF and was first proposed by Coffin and Manson. The Coffin-Manson equation relating the total fatigue life to the plastic strain amplitude is shown in Equation 32:

$$\frac{\Delta\varepsilon_p}{2} = \varepsilon'_f\,(2N_f)^c \tag{32}$$

where $\frac{\Delta\varepsilon_p}{2}$ is the plastic strain amplitude, $2N_f$ is the number of strain reversals ε'_f is the fatigue ductility coefficient and *c* is the fatigue ductility exponent. Equation 32 is applicable to strain controlled problems with a constant strain range [98].

The total strain amplitude, $\Delta\varepsilon$, which is the sum of elastic and plastic strain components, is found by combining Equations 31 and 32 obtaining:

$$\frac{\Delta\varepsilon}{2} = \frac{\sigma'_f}{E}(2N_f)^b + \varepsilon'_f(2N_f)^c \quad (33)$$

where the first and second components on the right hand side of Equation 33 are respectivly the elastic and plastic strain terms. Equation 33 is the basis for estimating fatigue life in different industrial applications including aerospace, automotive, oil and gas, and power generation industries [99].

The defect – tolerant approach is applied to fatigue by using the linear elastic fracture mechanics that is based on the assumption of pre-existing cracks in engineering components. Fatigue life is here defined as the number of cycles needed to propagate the dominant crack to a critical size. The most widespread model for the analysis of the crack propagation is based on the definition of the stress intensity factor range and its relationship with the crack growth rate per cycle. This approach will not be further discussed as it is deemed out of scope of this thesis.

A CDM approach for fatigue was first proposed by Chaboche and Lesne to describe the damage caused by fatigue before crack initiation [100]. The model is known as the Non-Linear Continuous Fatigue Damage model and is supported by the CDM theory. In the model the damage rate per cycle (d*D*/d*N*), is defined as function of the main loading parameters, such as maximum stress and mean stress per cycle, and the current damage state *D*. The non-linear damage accumulation and sequence effects are taken into account by defining in the function the maximum stress and the current damage state as unseparable variables. This leads to the development of a specific damage constitutive equation that, when integrated between the damage variable $D = 0$ (initial undamaged state) and $D = 1$ (macro-crack initiation)), yields the failure life, N_F. The material parameters required in the model are easily determined from testing data such as the S-N curve. Measurements of the damage variable *D* can be performed with varying criteria [101] but the most applicable are based on measures of the stress-strain material response obtained in terms of Young's modulus (elastic strain), plastic strain range or stress range changes [102]. This type of damage measurements uses the concept of effective stress and leads to a different but equivalent form of damage rate [103] that is used to predict the fatigue life. Starting from the original work of Chaboche and Lesne, other accumulation damage models based on damage mechanics

were developed for the purpose of fatigue life prediction. Lemaitre and Plumtree [104] and later Cheng and Plumtree [94] used a cyclic plasticity criterion and a ductility exhaustion criterion respectively to express the cumulative damage evolution during strain and stress controlled fatigue. The resulting final damage formulation is very similar to the one from Chaboche and Lesne but with a different meaning of the material parameters involved [94]. A ductility dissipation model was also derived by Shang and Yao [88] and by Fan et al. [105].

2.2.2 Creep – fatigue interaction mechanism

Traditional power generation plants are required to operate at higher frequency of start-ups and shutdowns in order to match a fluctuating market demand. The shifting from conventional 'base-load' operation mode at constant high temperature and pressure in which creep is the main damage mechanism to an 'intermittent' mode with fluctuating conditions introduces new failure mechanisms such as thermomechanical fatigue (TMF) damage [106, 107]. Additionally, cyclic operations combined with hold periods lead to fatigue-creep interactions, which accelerate material degradation and ultimately result in premature component failure [108, 109]. Investigating the combined effects of fatigue-creep on the damage evolution of power plant critical components (such as superheater and reheater tubes, headers and main steam pipelines) is of primary importance in order to accurately assess their structural integrity and predict their remaining life. A schematic illustration of different damage mechanism cases is presented in Figure 11 for a polycrystalline metallic material. In the fatigue-dominated case (with no imposed dwells), the fatigue crack nucleates at the surface in an area of stress concentration and propagates in a transgranular manner inside the material. In the creep-dominated case, for long dwell times, increased cavitation occurs so that the predominant cause of failure is intergranular damage. In the first creep-fatigue interaction case with increasing dwell periods where the creep damage influences the fatigue damage ('additive' or 'interactive' mode), the initial nucleated transgranular crack becomes intergranular as creep damage develops. In the second creep-fatigue interaction case, where creep and fatigue occur simultaneously but separately ('competitive' mode), the damage interaction is less pronounced [110].

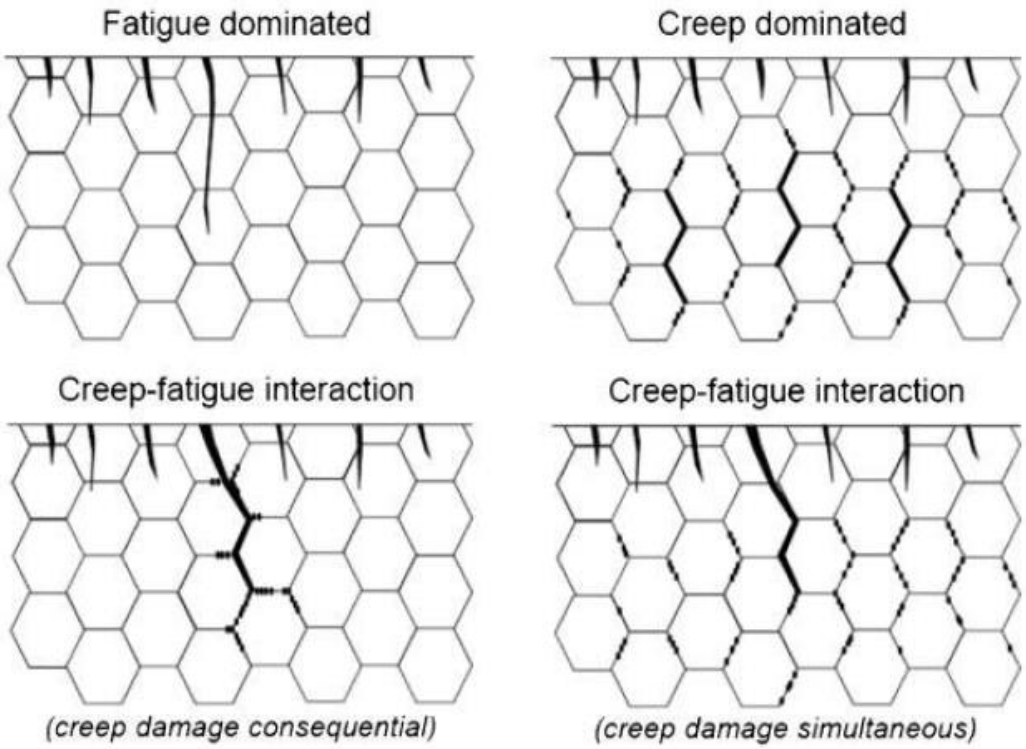

Figure 11: Damage cases for creep-fatigue interaction in high temperature components [111]

The most difficult situation for an accurate prediction of the design life of a component is when creep and fatigue are interactive and the primary concern is the understanding of how damage accumulates more rapidly than when considering each mechanism separately. Laboratory testing with metallographic study aims to identify creep-fatigue interaction by trying to replicate power plant operations, e.g. base load conditions (creep) followed by temperature cycles (fatigue) or fast/slow start-ups and shut-downs with full hold load [110].

The most common experimental tests performed to extract the features of creep-fatigue interaction are fully reversed uniaxial strain-controlled low cycle fatigue (LCF) and stress-controlled cycling with tensile and/or compressive strain/stress hold periods of different duration, different rates and temperatures according to the material under investigation and to the service conditions [112]. The material response under LCF and stress-controlled loadings is characterized by cyclic hardening or softening (defined respectively as the increase or decrease in stress/strain amplitude with cycle number) as consequence of changes in the microstructure. Austenitic stainless steels

show a cyclic hardening behaviour induced by the formation of dislocations networks that leads to a reduction in creep rate while high strength martensitic steels (9 to 12 % Cr steels) are characterised by cyclic softening as result of microstructural coarsening and a decrease in dislocation density [113]. Figure 12 illustrates the cyclic hardening and softening mechanism for strain-controlled cycling and how the hysteresis loops in the cyclic stress-strain curve change as the number of cycles increases. Under stress-controlled cycling, the behaviour will be inverted; the strain response for cyclic hardening will show a decreasing strain peak whilst that for cyclic softening will show an increasing strain range. The hysteresis loop, after an initial unstable period, will reach a saturation condition at around 100 cycles and the material thus arrives at an equilibrium condition [15, 92].

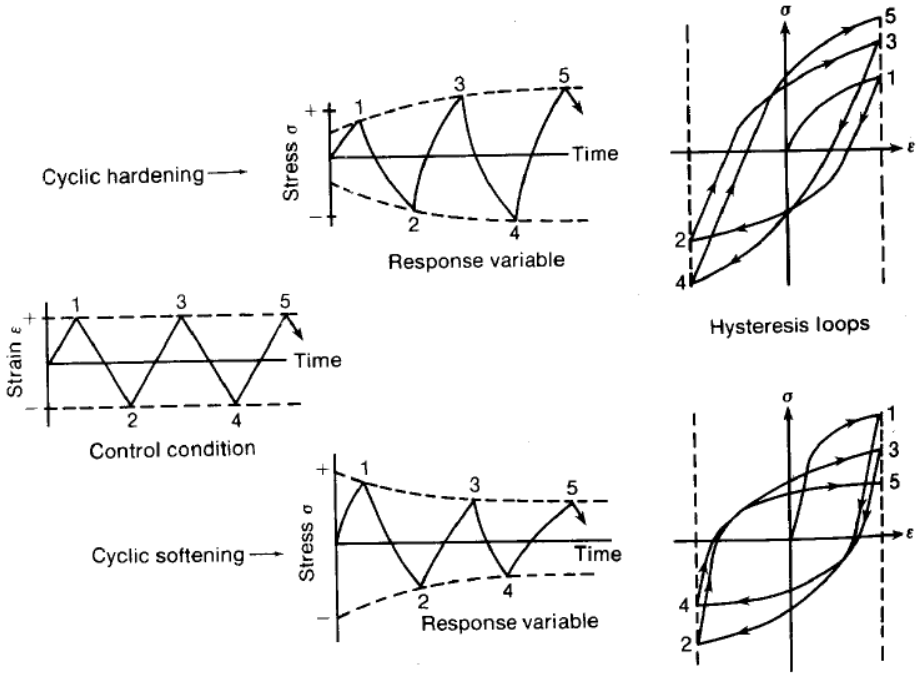

Figure 12: Material response under strain-controlled cycling

Under pure stress-controlled cycling, ratcheting deformation (cyclic creep) (defined as a progressive plastic strain accumulation as the number of cycles increases) may also take place in addition to cyclic hardening or softening. Ratcheting is caused by a non-zero mean stress S_m (asymmetric stress cycling) and leads to an open hysteresis loop shifted along the strain axis. Ratcheting is an important phenomenon that needs to be taken in consideration for the purpose of design and life estimation of the

components since it has a highly detrimental effect on fatigue life [114, 115]. Figure 13 shows schematically the phenomenon of ratcheting.

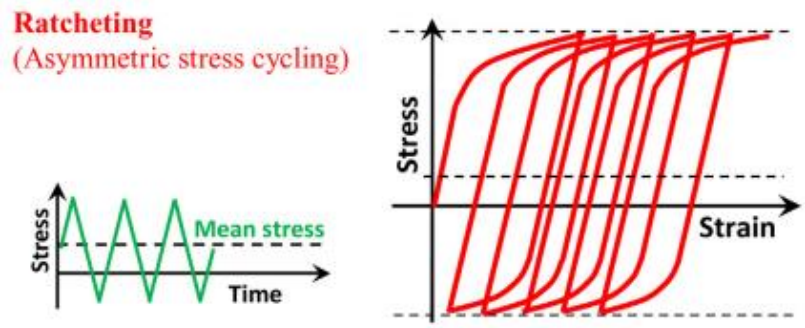

Figure 13: Schematic illustration of ratcheting behaviour [116]

As mentioned previously, the interaction between creep and fatigue is studied by introducing in the cyclic triangular stress-time or strain-time waveform a dwell period so that a trapezoidal waveform is obtained (see Figure 14 as example). Creep deformation is introduced using stress-hold periods at maximum stress in purely stress-controlled mode tests whilst stress-relaxation can be studied under strain-hold conditions at maximum strain in purely strain-controlled mode tests (relaxation-fatigue tests).

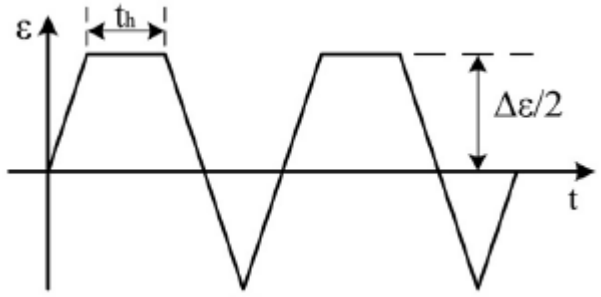

Figure 14: Schematic representation of relaxation-fatigue waveform [97]

Typical schematic representations of the hysteresis stress-strain curve for both creep and stress-relaxation mechanisms are given in Figure 15 [117]. σ_{relax} in Figure 15a is the stress-relaxation degree that occurs during a tensile strain hold period, whereas ε_{creep} in Figure 15b is the creep strain that occurs during a tensile stress hold and $\Delta\varepsilon_{fat}$ is the fatigue plastic strain range.

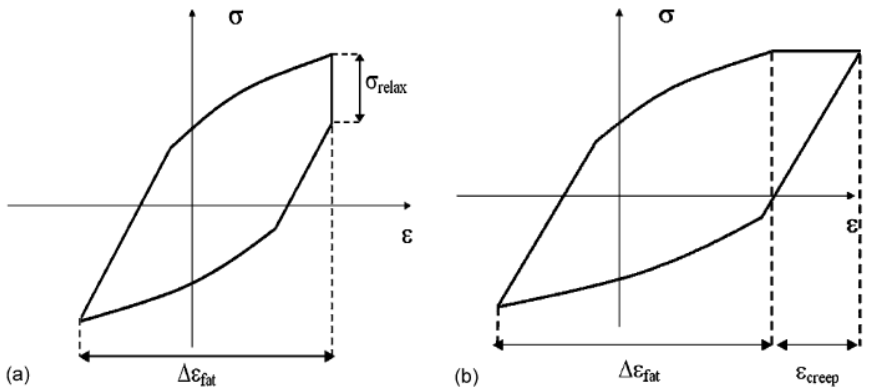

Figure 15: Hysteresis loops for (a) stress relaxation test and (b) creep fatigue test [117]

It is normal practice to represent the degree of stress-relaxation in a stress evolution graph by plotting the resulting stress versus test time. The hysteresis loop responses of LCF and relaxation-fatigue tests are compared in Figure 16 where also the stress-relaxation behaviour is shown. From this figure, it can be seen that the plastic strain range (here indicated as $\Delta\varepsilon_p$) is higher in the relaxation-fatigue test than in the LCF and that the stress-relaxation happens at the maximum stress (σ_{max}).

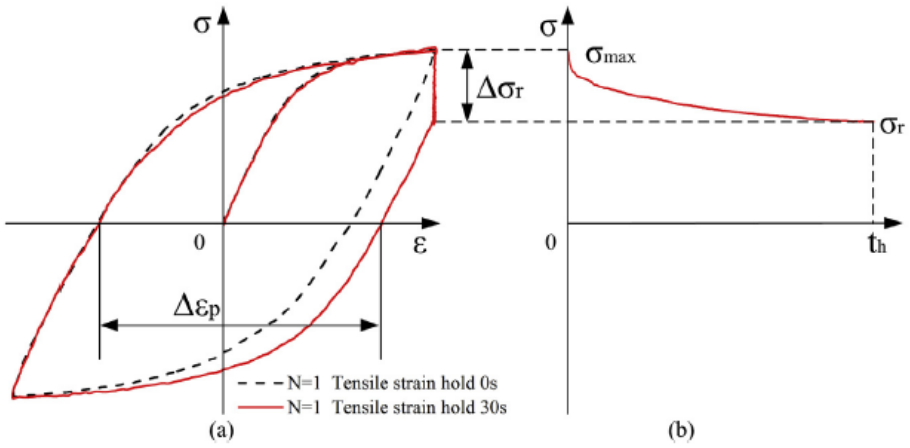

Figure 16: (a) Hysteresis loops comparison for LCF (black dashed line) and relaxation-fatigue (red solid line) tests and (b) stress-relaxation behaviour during the hold period [97]

Relaxation-fatigue and / or fatigue-creep as well as a combination of fatigue loadings contribute to an acceleration of the deterioration of material properties leading to a reduction in component lifetime [118-120]. The damage mechanisms during creep–fatigue conditions are mainly influenced by microstructural coarsening and cavity growth. For example, cavity growth has been identified in 1CrMoNiV steels during

stress relaxation [6]. Nickel-base superalloys (commonly used for turbine discs) exhibit a combined trangranular (fatigue) and intergranular (creep) mode of failure under creep-fatigue testing. For these alloys, increasing dwell time leads to a transition from fatigue-dominated failure to creep-dominated failure causing a reduction in lifetime [121].

2.2.3 Unified viscoplasticity model

Many advanced viscoplasticity constitutive models have been presented in the literature which aim to simulate the creep-fatigue response of metallic materials such as 9-12%Cr steels. These models are ascribable to two frameworks: (i) the unified viscoplasticity theory and (ii) the non-unified viscoplasticity theory [109]. In the unified viscoplasticity framework, the inelastic strain includes both plastic (rate-independent) and viscous (rate-dependent) effects. In contrast, in the non-unified theory plastic and viscous effects are decoupled [122-125] and described with two strain components that have different governing rules and hardening equations [126]. The unified theory, despite being characterized by more complex determination of material parameters, is the most widely employed thanks to its ease of implementation in finite element codes and its improved ability in simulating the cyclic fatigue-creep interaction. Among all unified viscoplasticity constitutive models developed in the past decades (e.g. Bodner [127], Miller [128], Robinson [129], Walker [130], Krempl [131], Watanabe and Atluri [132], Delobelle [133], Barrett et al [134]), the most widely used is the one initially proposed by Chaboche [135-139] where the viscosity function is expressed as a power law function (in the same fashion as Norton's law for creep). A comprehensive summary of the available literature for viscoplasticity modelling has been published by Chaboche [140].

The Chaboche unified constitutive viscoplastic model relates the non-linear kinematic (the back stress) hardening and isotropic (the drag stress) hardening together with the yield stress σ_y for the definition of the yield function f.

The yield function aims to represent the change of the yield surface after the material hardens or softens under a multiaxial state of stress. One widely used criterion to describe yielding is the von Mises yield criterion where the concept of yield function is introduced. The yield function is written such that the elastic behaviour occurs for f

<0, perfectly plastic yielding for *f =0* and viscoplastic behaviour for *f >0*. The von Mises yield criterion can be graphically represented by an infinitely long cylinder with the coordinate axes represented by the principal stresses (σ_1 , σ_2 , σ_3). The axis of the cylinder represents the hydrostatic stress and stress points inside the cylinder are associated with elastic stress states whereas stress points on the surface of the cylinder represent plastic stress states. The yield surface is graphically represented by the π-plane which passes through the origin ($\sigma_1 + \sigma_2 + \sigma_3 = 0$) and its intersection with the von Mises yield surface appears as a circle called the yield locus (Figure 17) [19, 141].

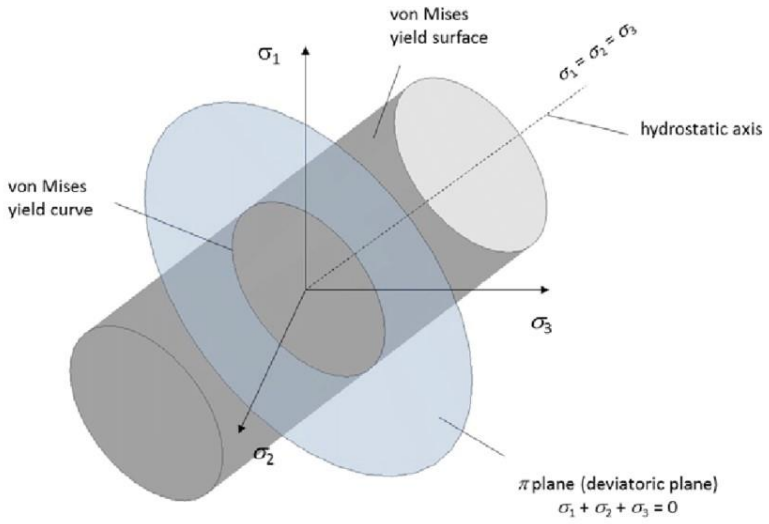

Figure 17: von Mises yield criterion in principal stress space [142]

After the initial yield, subsequent loadings produce plastic deformation which may be accompanied by a modification of the shape and/or position of the yield surface. The representation of these changes depends on the material model selected and is defined by the yield function. For a kinematic hardening material, the original yield surface is translated to a new position in the stress space as the plastic strain is increased with no change in size or shape. For an isotropic hardening material, the yield surface increases in size with increasing plastic strain but maintains its original shape (Figure 18) [19, 143].

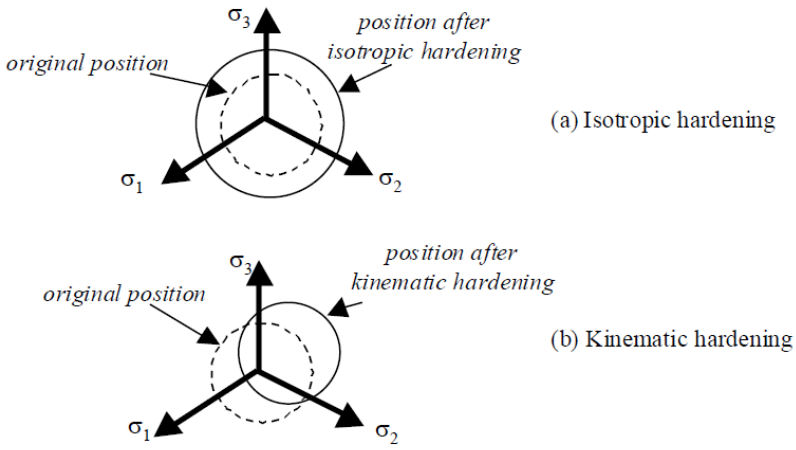

Figure 18: von Mises yield criterion with hardening

The kinematic hardening law (shifting in the yield surface) was developed from the initial works of Prager (linear kinematic model) [144] and further modified by Armstrong-Frederick (non-linear kinematic model) [145]. Several non-linear dynamic recovery terms, proportional to the inelastic strain rate, are introduced in the kinematic hardening formulation to better predict the viscoplastic material response including behaviours such as ratchetting and cyclic deformation [146, 147]. A static recovery term, which represents time / rate dependent and thermally-activated mechanisms, is also added in the non-linear kinematic hardening model to simulate creep deformation and stress-relaxation phenomena. The original power law function used by Chaboche to define the static recovery term [148] was later improved by Yaguchi et al [149] to account for the mean stress evolution during cyclic deformation. More recently, significant contributions were presented in the work of Guo et al to include thermal recovery effects [150] and the work of Zhang-Xuan to model the interaction between cyclic softening and stress relaxation for 9-12%Cr steels [109].

The isotropic hardening rule, referred as the change in the yield surface size respect to the plastic flow, is used to model the cyclic evolution (hardening / softening) of the material. The original isotropic hardening rule proposed by Chaboche [151] and Ohno [152] with the strain memory variable to describe the plastic strain range history effects, was modified later by Lemaitre-Chaboche [153] to include the linear term for cyclic evolution. The modified isotropic hardening rule was used extensively for

example by Bernhart et al for 55NiCrMoV8 martensitic steel [154] and by Saad [155] and Wu [156] for 9-12%Cr steels to simulate their linear softening stage.

2.2.4 Industrial approach to creep and fatigue damage (R5 assessment procedure)

In the power generation industry, the interaction of complex types of loadings makes the material response and its remaining life hard to predict. Many power plant components, for example steam generators, steam pipes, super-heater and re-heater headers and turbine rotors operating at elevated and cycling temperatures and / or pressure (stress) and are subjected to fatigue, creep, fatigue-creep interaction damage. This loading complexity and the need to guarantee safe and reliable operations result in a conservative approach for the estimation of the design life [1].

In design codes (ASME III Boiler and Pressure Vessel Code Subsection NH, R5, RCC-MR etc.) the linear damage accumulation rule, where the fatigue damage and the creep damage are calculated separately and then summed up linearly, is the most popular used to predict life when creep and fatigue are present at the same time in a component [6].

Following this rule, the fatigue damage D_f is estimated from the Miner's rule (Equation 34) [110]:

$$D_f = \sum_{i}^{P} \frac{n_i}{N_{i,f}} \tag{34}$$

where n_i is the number of cycles at stress level σ_i, $N_{i,f}$ is the number of cycles to failure at σ_i and P is the total number of the different loading types.

The creep damage D_c (Equation 35) is commonly estimated from a time-fraction rule proposed first by Robinson [110]:

$$D_c = \sum_{j}^{Q} \frac{t_j}{t_{j,r}} \tag{35}$$

where t_j is the time spent at load condition j, $t_{j,r}$ is the creep rupture time at the same condition and Q is the total number of the different loading conditions.

The total cumulative damage D is finally given by the linear summation as [1] :

$$D_f + D_c = \sum_{i}^{P} \frac{n_i}{N_{i,f}} + \sum_{j}^{Q} \frac{t_j}{t_{j,r}} \leq D \tag{36}$$

D is the total allowable damage before crack initiation occurs which prompts component inspection or replacement activities. In ASME and RCC-MR, the value of D depends on the material while in R5 code, D is always set to unity [110].

The fatigue damage and creep damage are plotted on the axes of a damage interactive diagram. Figure 19 represents the creep-fatigue damage curve adopted in ASME for different materials; fatigue damage is assigned to the horizontal axis and creep damage to the vertical axis. The component design is deemed to be safe if the point representing the total damage lies inside the curve for the desired material.

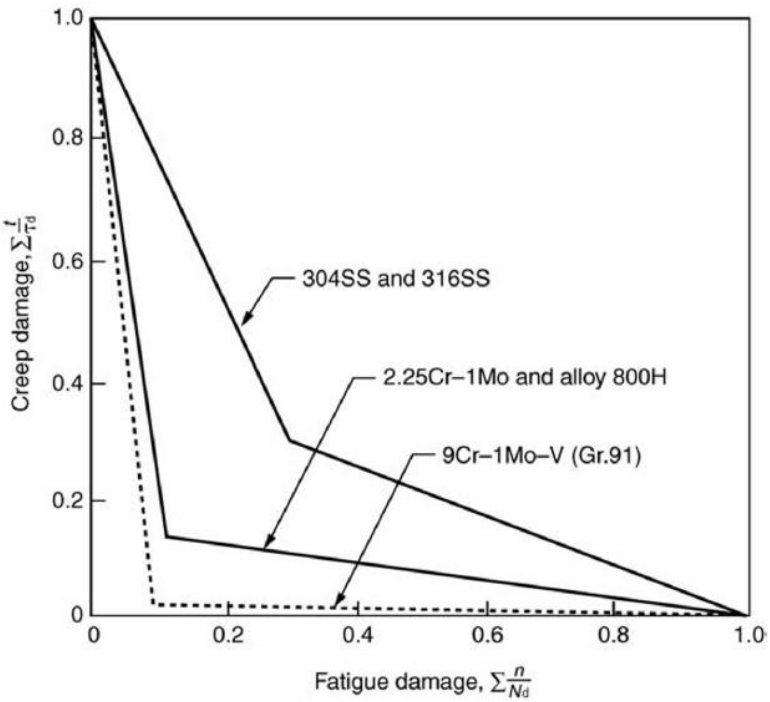

Figure 19: Creep-fatigue interaction damage diagram in ASME [2]

The use of the time-fraction concept for the calculation of creep damage results in a conservatism in predicting the life of a factor of 2 to 3. This limitation is due to the lack of the ability to include satisfactorily important phenomena such as stress relaxation, strain softening / hardening effects and microstructural evolution [6, 111,

113]. In addition, the resulting factor of conservatism changes depending on the code considered. Different codes give different results according to the safety factors applied, different test conditions and different material properties [110, 157].

Another alternative method, already used in R5 code, which attempts to overcome the limitations of the time-fraction rule is the strain-based ductility exhaustion rule. In this approach, inelastic strain is the controlling parameter rather than stress for the calculation of creep damage [157]. The creep damage per cycle d_c is given by Equation 37 [158]:

$$d_c = \int_0^{t_h} \frac{\dot{\varepsilon_c}}{\varepsilon_{r(\dot{\varepsilon_c})}} \, dt \tag{37}$$

where $\dot{\varepsilon_c}$ is the creep strain rate during the holding period t_h and ε_r is the creep ductility (strain limit) that include stress state and strain rate effects [8, 158]. After the estimation of fatigue damage as in Equation (34), the total damage is always calculated as a linear sum between fatigue damage and creep damage. The number of cycles to failure is finally estimated as the inverse of the total damage [157].

It is important to note also that the ductility exhaustion rule, being an empirical model, is subjected to scatter according to uncertainties related to the estimation of material parameter values.

Both of the described models can be used successfully for damage monitoring and remaining life prediction when employed in conjunction with physical monitoring techniques that measure the actual plant damage [8].

2.3 Low-alloy ferritic steels and high-strength martensitic steels behaviour under creep and fatigue

Low allow ferritic steels have been historically employed in the power generation industry for components operating at high temperature in the range of 500-550 °C (for example, in steam piping and boiler superheater outlet headers) thanks to their good creep resistance. The most common types of low alloy ferritic steels are 2Cr1Mo, 2.25Cr1Mo, 1Cr0.5Mo and 0.5CrMoV [8].

In the last decades, due to the demand to operate the plants more efficiently at increasing temperature and pressure and with higher flexibility, high-strength martensitic steels (9-12% Cr) have been introduced. These steels can operate at steam temperatures of 600-650 °C and supercritical pressure up to 350 bar [6]. They have superior creep properties and allow a reduction in the pipe wall thickness with the consequence that there are smaller temperature gradients in these components which is beneficial in the mitigation of the damage from creep-fatigue interaction [2]. The development along the years of power plants steels in presented in Figure 20.

.

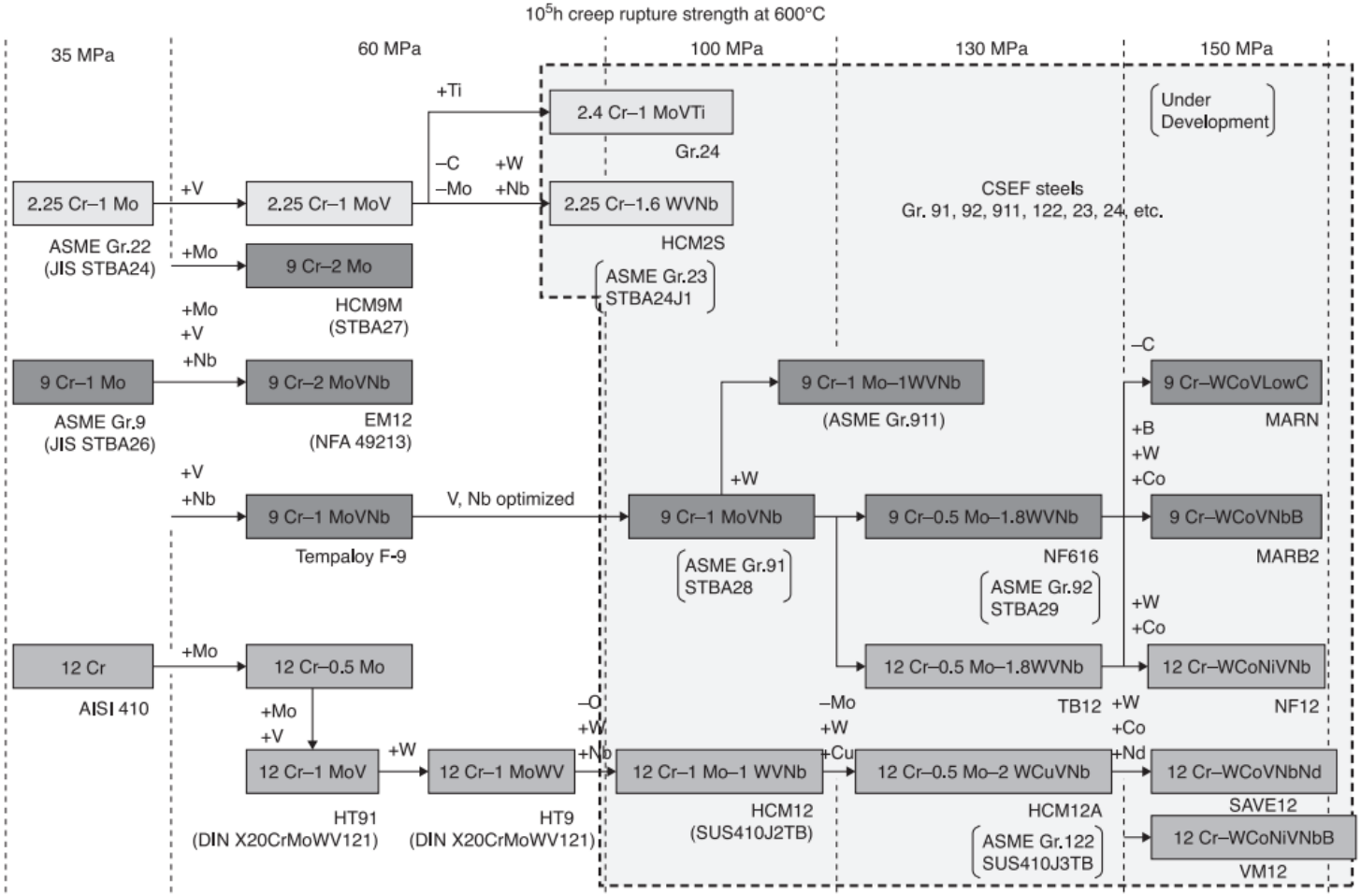

Figure 20: Development in steels for power generation applications [159]

2.3.1 Low alloy ferritic steels

Low alloy ferritic steels have been traditionally used in tubes and pipes of steam boilers and heat exchangers and structural components in power generation industry before the development of high-strength martensitic steels. Their alloying consists of Cr and Mo as main elements with the addition of elements such as V, Nb, Ti and others. The final properties of the steel depend on its microstructure. Low alloy ferritic steels (hereafter referred as Cr-Mo steels for brevity) are characterized by a good creep and corrosion resistance, good oxidation resistance, good mechanical properties (tensile strength and toughness) and good weldability [2, 160]. The most common Cr-Mo steels are listed in Table 1. T11 and T22 are the conventional Cr-Mo steels that form chromium carbides which are stable above 500°C [159]. The next generation of Cr-Mo steels is represented by T23 and T24 developed with a higher amount of alloying elements (V, Nb, Ti and boron) that give and improved creep strength in order to meet the industrial needs of higher superheater temperatures (up to 600°C) [159].

Cr-Mo steels assume different microstructures according to the cooling rate from the austenitizing temperature from which they transform to a body-centred cubic (BCC) lattice [160]. The typical final microstructure is ferritic - pearlitic after annealing, ferritic - bainitic after normalization and tempering or martensitic after quenching and tempering. Generally, it is accepted that the best microstructure for creep resistance is bainite even if under long-term exposure this depends mainly on precipitation hardening behaviour during both the heat treatment and service aging at high-temperatures [161]. Figure 21 shows the optical microstructures of the same steel (T22) after being subjected to two different heat treatments.

Table 1: Chemical composition (%wt) of commonly employed low-alloy ferritic steels [161]

General type	%	C	Si	Mn	Cr	Mo	Ni	V	Al	Spec	Name
0.5%Mo	Min.	0.10	0.10	0.30		0.44				ASTM A209	T1
	Max.	0.20	0.50	0.80		0.65					
0.3%Mo	Min.	0.12		0.40		0.25				EN 10216-2	16Mo3
	Max.	0.20	0.35	0.90	0.30	0.35	0.30		0.040		
1.25%Cr0.5%Mo	Min.	0.05	0.50	0.30	1.00	0.44				ASTM A213	T11
	Max.	0.15	1.00	0.60	1.50	0.65					
2.25%Cr1%Mo	Min.	0.05		0.30	1.90	0.87				ASTM A213	T22
	Max.	0.15	0.50	0.60	2.60	1.13					
0.5%CrMoV	Min.	0.10	0.15	0.40	0.30	0.50		0.22		EN 10216-2	14MoV6-3
	Max.	0.15	0.35	0.70	0.60	0.70	0.30	0.28	0.040		

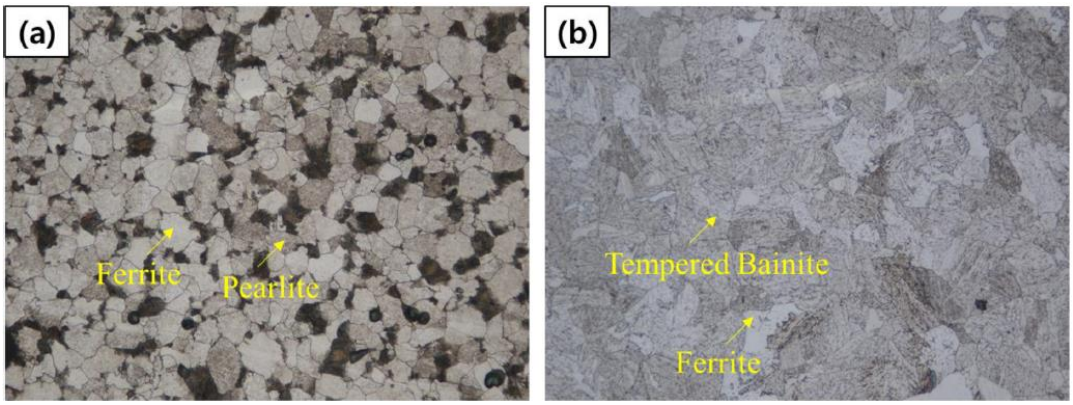

Figure 21:Microstructure of two different 2.25%Cr-1%Mo steels which had been subjected to different heat treatments to produce microstructures as follows; (a) a ferrite-pearlite microstructure; (b) a ferrite-bainite microstructure [162]

Carbides precipitate during tempering and evolve during service exposure. In fact, after tempering the steel is in a meta-stable condition and service exposure at high temperatures for prolonged time will result in metallurgical changes that lead to a more stable condition. These metallurgical changes depends on many factors but the most important are time, temperature, stress and environment [2, 161].

The most important classes of carbides that are found in Cr-Mo steels are presented in the table below:

Table 2: Main classes of carbides for low alloy creep resistant steels [159]

Carbides	Description
M_3C	Essentially cementite, Fe_3C, but often including, other metallic elements (in particular Mn)
M_7C_3	A family of chromium-rich carbides that can also include Mn, Mo and V
$M_{23}C_6$	Cr carbide with Cr, Fe, and small amount of Mo
M_6C	Ternary carbide of Fe and Mo or Fe and W with appreciable solubility for other elements
MC	Carbides formed by V, Nb and Ti
M_2C	Usually a Mo-rich carbide

The presence of different carbides in the steel depends on the original chemical composition and heat treatment applied [35]. The most stable carbide forming during tempering in low alloy steels without vanadium is Mo2C. It forms needle-shaped particles finely distributed in the matrix and along grain boundaries that grow very slowly during service thanks to its coherency with the surrounding ferrite lattice matrix

[159, 161]. In steels containing vanadium, another stable carbide that contributes to creep strength is V4C3 (MC class in Table 2) [161].

During creep, the most important microstructural degradation processes that cause a reduction in creep strength are the tendency to pearlite / bainite spheroidisation, coarsening and coalescence of precipitates in the matrix and at grain boundaries and zones without precipitates being formed along the grain boundaries [35, 160, 163]. $M_{23}C_6$ precipitation during service is seen as a deleterious for creep resistance since this phase removes alloying elements from the matrix decreasing their effect on creep strength via solid-solution hardening [160]. Nucleation of cavities at grain boundaries, especially at the junctions with precipitates occurs with the progress of creep at elevated temperatures [164]. Cavity formation accelerates during the secondary creep stage and their size and density increase at the onset of tertiary creep stage. Cavity interlinkage causes the formation of microcracks that lead to final rupture [35]. A common schematic representation used to describe damage in low alloy ferritic steels is shown in Figure 22.

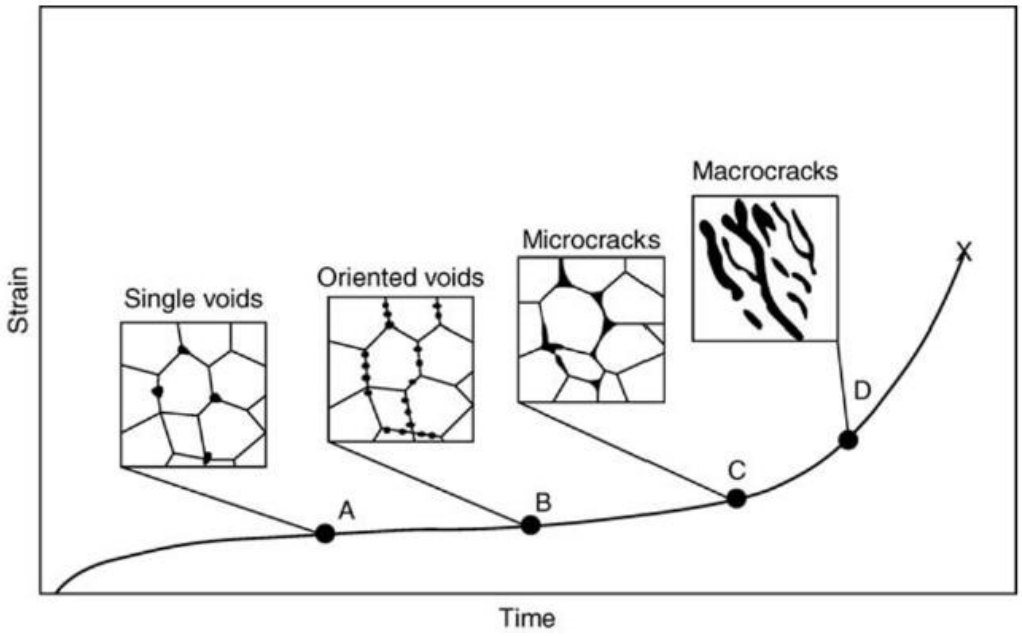

Figure 22: Defect evolution for low alloy steels during long-term operation (adapted from [165])

Under LCF conditions, Cr-Mo steels exhibit a cyclic softening behaviour mainly caused by the rearrangement of dislocations that leads to local areas of stress concentration. These areas promote local plastic deformation and propagation of

microcracks. The cyclic softening curve is divided into three stages: (i) a rapid softening stage up to 20% of life; (ii) a steady-state phase up to 80% of life and (iii) a final rapid failure stage due to crack initiation and propagation. Cyclic softening is accelerated at higher temperatures and at higher strain amplitude. The introduction of hold time to represent the fatigue-creep interaction further accelerates the cyclic softening process with this being attributed to the generated creep strain that affects the microstructural stability. Thus, the creep-fatigue interaction leads to a reduction in the material life and this is exacerbated by increasing hold times. Furthermore, stress relaxation is observed for low alloy steels during hold time which influence negatively the fatigue life by introducing more crack sources [166, 167].

2.3.2 High-strength martensitic steel

The most common material used for boiler critical components (i.e. superheater and reheater tubes, headers and main steam pipelines) in fossil power plants are high chromium martensitic steels (containing from 9 to 12%Cr) thanks to their superior microstructure compared to more traditional materials such as CrMoV steels [168]. High chromium martensitic steels are also candidate material for nuclear reactor applications being originally developed for the application in the steam generator of fast-breeder reactors thanks to their lower thermal expansion coefficient [5, 157, 169]. Compared to CrMoV steels, 9-12%Cr steels show higher creep and thermal-fatigue strength, improved steam oxidation and corrosion resistance, better hardenability, fracture toughness and weldability. Under cyclic operations, an additional benefit of 9-12%Cr steels is that reduced wall thicknesses can be used, thus promoting more uniform thermal and stress gradients along component section [170]. Grade 91, within the 9-12%Cr steels family, has 9%Cr-1%Mo and mainly iron to balance and is used commonly for superheater tubes and main steam pipes in power plants subjected to high temperature and pressure. The high creep strength of these steels results from a combination of grain structure, solid solution and precipitation strengthening mechanisms. The chemical composition of the main industrially significant high chromium martensitic steels is shown in

Table 3 together with the country of development, commercial name and the creep properties at 600 °C.

The effect of the main alloying elements is hereafter briefly described. Carbon (C) stabilizes the austenitic and ferrite phases by occupying interstitial sites and causes the precipitation of carbides. Carbon has also the effect to increase the hardness and tensile strength of the material while decreasing its ductility and weldability. Chromium, molybdenum and tungsten (Cr, Mo and W respectively) have the principal effect of enhancing the creep rupture strength by solid solution hardening and precipitation hardening with the formation of carbides of $M_{23}C_6$ type. Vanadium and niobium (V and Nb) have a similar contribution; they stabilize the ferritic phase in the metal matrix and promote the precipitation of fine dispersed carbide and carbonitride particles of MX type. Nitrogen (N) increases the creep rupture strength by occupying interstitial sites in the ferritic matrix. Nickel (Ni) improves the toughness and strength of the steel while improving its oxidation and corrosion resistance. Boron (B) is added in small amounts to reduce the coarsening of thermally stable $M_{23}C_6$ type precipitates [2, 112].

Table 3: Chemical composition and creep rupture strength for 9-12% Cr steels [6]

Country		Steel	Chemical composition (weight%)									Rupture strength at 600°C (MPa)	
		Basic steels	C	Cr	Mo	Ni	W	V	Nb	N	B	10^4 h	10^5 h
Germany	1.	X22CrMoV 12 1	0.22	12.0	1.0	0.50	–	0.30	–	–	–	103	59
UK	2.	H46	0.16	11.5	0.65	0.70	–	0.30	0.30	0.05	–	118	62
		FV448	0.13	10.5	0.75	0.70	–	0.15	0.45	0.05	–	139	64
France	3.	56T5	0.19	11.0	0.80	0.40	–	0.20	0.45	0.05	–	144	64
Japan	4.	TAF	0.18	10.5	1.5	0.05	–	0.20	0.15	0.01	0.035	216	(150)
USA	5.	11%CrMoVNbN	0.18	10.5	1.0	0.70	–	0.20	0.08	0.06	–	165	(85)
		Advanced steels											
USA	6.	P 91	0.10	9.0	1.0	<0.40	–	0.22	0.08	0.05		124	94
Japan	7.	HCM 12	0.10	12.0	1.0		1.0	0.25	0.05	0.03			75
Japan	8.	TMK 1	0.14	10.3	1.5	0.60	–	0.17	0.05	0.04		170	90
		TMK 2	0.14	10.5	0.5	0.50	1.8	0.17	0.05	0.04		185	90
Europe	9.	X18CrMoVNbB 91	0.18	9.5	1.5	0.05	–	0.25	0.05	0.01	0.01	170	122
Europe	10.	X12CrMoWVNbN	0.12	10.3	1.0	0.80	0.80	0.18	0.05	0.06	–	165	90
		E911	0.11	9.0	0.95	0.20	1.0	0.20	0.08	0.06	–	139	98
Japan	11.	P92	0.07	9.0	0.50	0.06	1.8	0.20	0.05	0.06	0.003	153	113
Japan	12.	P122	0.10	11.0	0.40 1.Cu	<0.40	2.0	0.22	0.06	0.06	0.003	156	101
Japan	13.	HCM 2S	0.06	2.25	0.20	–	1.6	0.25	0.05	0.02	0.003		80
Germany	14.	7CrMoTiB	0.07	2.40	1.0	–	–	0.25	–	0.01	0.004 0.07Ti		60

Although the chemical compositions of these 9-12%Cr steels can vary slightly in terms of alloying elements, their microstructure and their degradation behaviour under creep and fatigue are very similar [171].

The unique microstructure of these steels is obtained after quenching from the high temperature austenite phase into martensite, and subsequent tempering. Sun et al. in [172] argued that the final metallic structure is tempered martensitic body-centered cubic (BCC) structure consisting of large prior austenitic grains (PAG) formed from the retained austenite. PAGs (15-60 μm) contain packets that are divided into blocks (2-10 μm in size) which in turn are composed of laths (0.2 to 1 μm in size) with high dislocation density [173-177]. Following the transformation model of Kurdjumov–Sachs (K-S), PAGs, packets and blocks are characterized by high-angle boundaries (HAB) with misorientation greater than 20°, while laths are classified as low-angle boundaries (LAB, below 20°) with a minimum angle between two blocks of laths of around 5° [177, 178]. The larger $M_{23}C_6$ (M stands for Cr, Fe) precipitates with size in the range of 100-300 nm are distributed along lath, block, packet and PAG boundaries, while the finer MX carbonitrides (M stands for V, Nb, Ta and X for C, N) of size 30-50 nm are mainly distributed within laths and at the grain boundaries. The lath structure and its microstructural evolution into subgrains during service together with the dispersion of fine precipitates are hardening mechanisms that retard plastic deformation by the inhibition of dislocation motion and therefore give the superior characteristics of 9-12%Cr steels [179, 180]. Figure 23 shows a pictorial representation of the typical microstructure for 9-12% Cr steels.

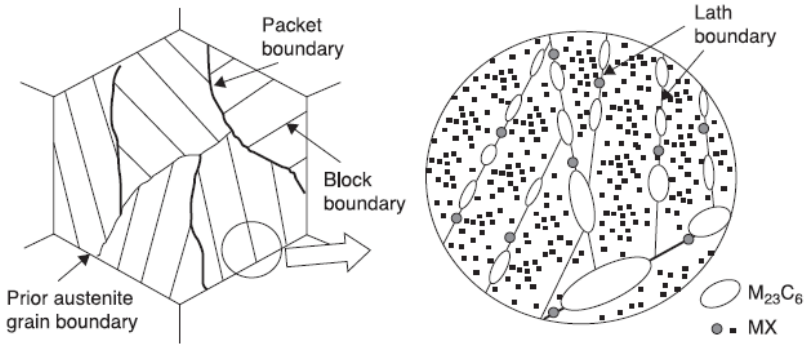

Figure 23: Schematic representation of tempered martensitic microstructure [5]

The viscoplastic response of 9-12%Cr steels to fatigue-creep has been investigated by performing various experimental tests under loading-unloading cycles with and without hold periods at constant strain or stress. Under pure fatigue loading, 9-12%Cr steels exhibit a cyclic softening behaviour under strain-controlled conditions while ratcheting occurs under stress-controlled cycling. Other degradation mechanisms are introduced by adding dwell periods (such as creep deformation at stress-hold conditions and stress relaxation under strain-hold conditions) [109].

In 9-12%Cr steels, the degradation process of cyclic softening (decrease of stress amplitude with number of cycles) is attributed to a recovery phenomenon that consists of the coarsening of the original lath structure with consequent disappearance of LABs (laths and sub-grains boundaries) and a decrease in dislocation density [170, 181]. The primary driver for the microstructural changes responsible for the softening of the material has been ascribed to the applied plastic strain per cycle [182]. A typical cyclic softening response to strain-controlled fatigue for martensitic steels is divided in three stages: (i) primary softening characterized by a decreasing softening rate; (ii) a steady-state phase with constant softening rate and (iii) a third softening stage with an accelerated rate until failure [180]. The first stage occupies around 20% of fatigue life and is associated with the initiation of cracks. The second stage then dominates until around 80% of fatigue life and is characterized by a linear decrease of stress amplitude accompanied by steady crack propagation. In the third stage, from 80% of fatigue life to failure, cracks reach a critical size with the consequent acceleration in the decrease of stress amplitude [183]. A schematic representation of the cyclic softening with the division in three stages is provided in Figure 24.

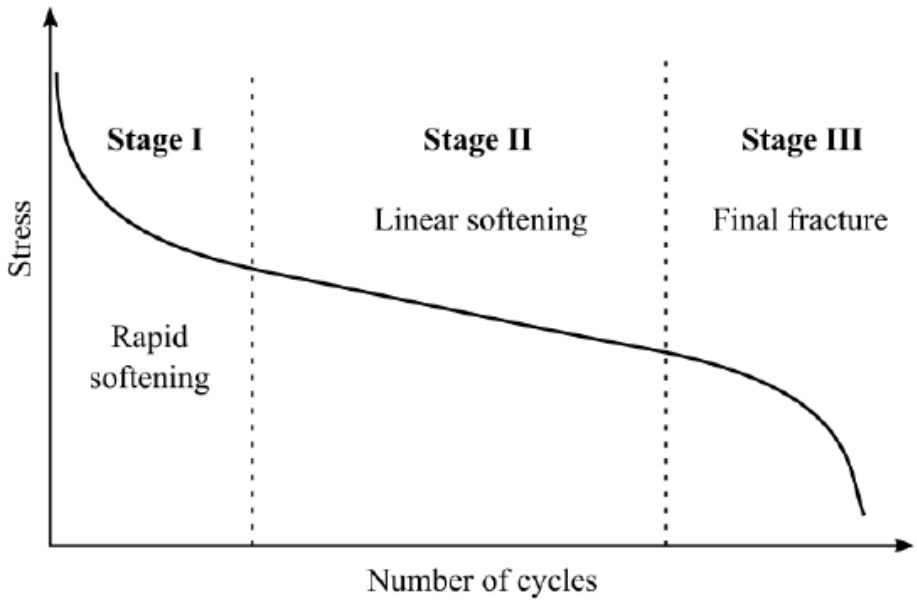

Figure 24: Typical softening curve for 9-12%Cr steels [3]

In addition, sub-grain coarsening and the decrease in dislocation density is accelerated under creep-fatigue loading leading to a more rapid material deterioration [182]. The final sub-grain size and the final dislocation rearrangement are directly related and proportional to the viscoplastic strain range and the hold time applied. In contrast, precipitate coarsening is the typical degradation mechanism observed under creep exposure and under creep-fatigue interaction rather than under short-term pure fatigue tests. Precipitates ($M_{23}C_6$, MX and Laves phase) are nucleation sites for cavities under creep and creep-fatigue leading to intergranular fracture [184]. The accelerated recovery of the microstructure under fatigue and creep-fatigue compared to creep is attributed to the higher mobility of dislocations under the plastic strain applied that promote annihilation of the grain boundary dislocations [170, 182]. Moreover, the stress-relaxation behaviour of 9-12%Cr steels under tensile strain-hold periods [134] is decelerated with repeated cycles as a consequence of the continuous cyclic softening in which the peak stress at the start of the hold period is reduced [109].

Under cyclic stress-controlled loading, 9-12% Cr steels always exhibit a cyclic softening behaviour related to the increase of the strain amplitude with progressive cycles but with no obvious division into three distinct stages as was observed under strain-controlled conditions. In addition, the tension-compression asymmetrical

behaviour of 9-12%Cr steels (i.e. the different deformation resistance under compression and tension) induces a progressive accumulation of inelastic strain (ratcheting) which reduces the fatigue lifetime [183]. Ratcheting is a time-independent phenomenon linked to plasticity effects and is related to the stress amplitude as well as to the applied stress ratio [185]. A ratcheting strain-rate acceleration is observed when creep deformation is generated by the introduction of stress-hold periods. Higher ratcheting-strain rates are produced by longer holding times that finally cause a faster damage evolution and premature failure [114]. The ratcheting response is also influenced by the cyclic softening of the material. As has been shown by Yaguchi and Takahashi, the ratcheting strain rate of modified 9Cr-1Mo steel increases when a prior cyclic strain range is applied [115].

2.4 Condition monitoring in industrial application: the current approach

2.4.1 Condition monitoring in industry

Condition monitoring can be described as the 'process of monitoring relevant parameter(s) to evaluate the developing condition of the component or system being monitored', typically to advise on avoiding losses due to unplanned system breakdowns. Failure of power plant components can be catastrophic in terms of human causalities and financial cost associated with prolonged outages. Condition monitoring evaluates the real status of the components in service and if deviation from what are termed "healthy conditions" are noticed, corrective actions are taken [186]. As with all condition monitoring approaches, the challenge is to determine an optimum inspection and maintenance interval. For materials and components operating at high temperature, condition monitoring is made more complex by the non-linearity of the damage mechanisms and their sensitivity to operating conditions. Condition monitoring techniques currently routinely used on high temperature power plant are traditional, inherently conservative and have stood the test of time, albeit for operational conditions that were far more predictable and financially lucrative than those currently faced or expected in the future. Current condition monitoring involves data collected from every component during an outage, analysis of the data and prediction of remaining life with empirical models [187].

Hence, as alluded to in the introduction, there is a need to evolve the current approach into one that is more closely aligned with the broader industrial application of condition monitoring as a routine plant activity to continuously optimise plant operation and therefore extend useful life whilst ensuring safe operation.

2.4.2 Application to high temperature materials

Commonly employed monitoring techniques currently applied to high temperature materials are as follows:

a) Physical examinations and assessments during a plant outage with non-destructive techniques (NDT);
b) Trend monitoring, based on the data obtained during the outage inspections and from other similar plant;
c) Limited online monitoring taking advantage of available operational parameters.

Condition examination occurring during the outage is typically associated with diametral strain measurements as illustrated in Figure 25 [13], surface metallurgy (hardness and replication) and macro-crack detection using non-destructive techniques such as magnetic particle and ultrasonic inspections.

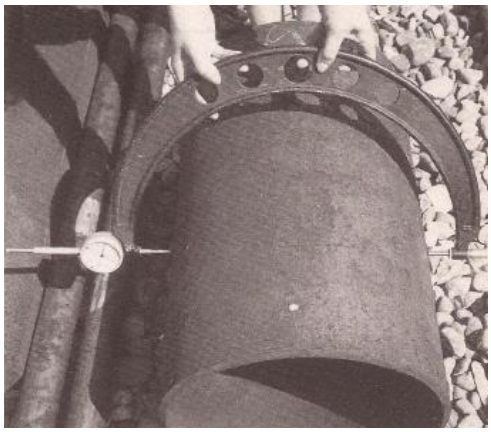

Figure 25: Bow gauge micrometer with dial gauge for diametral strain measurements

Hence, if sufficient repeat examinations are available, then a trend over time can be obtained, which is usually bounded by specified permissible limits before repair or replacement. This periodic and backward-looking sampling inspection approach becomes more problematical as materials age in service or as the operational conditions are modified, possibly beyond the original design intent, as a result of

commercial imperatives. Examples of some recent significant and unexpected problems identified during an outage are:

a) Extensive creep damage on stub and branch welds on steam header systems, leading to temporary repairs to enable return to service with a 12-month lead time to procure and plan the installation of a replacement header system, costing £1–2 M [188, 189].

b) Adverse findings from the original creep replica and hardness inspection scope on weld and parent material on main steam line systems, leading to significant escalation of work across multiple units during the outage, costing > £1 M, with lost generation costs an order of magnitude more [190].

Engineering critical assessments [191] are undertaken for cracked structures if repairs cannot be completed during an inspection and in some more critical cases supplemented by online condition monitoring of temperature and strain, supplemented by frequent shutdowns for further ultrasonic inspections [60]. Hence, practical creep life prediction models that use online operational data which can be supplemented by periodic datasets obtained during outage overhauls, are required, with an emphasis on the direct feedback to plant operators. The key challenge is which creep models can be practically and appropriately implemented, either as they currently exist or after modification.

2.5 Applications of hardness, replica and strain monitoring for life assessment

2.5.1 Strain life models

In 1982, Cane introduced a lifing model for low alloy ferritic steels based on strain measurements rather than the application of traditional life fraction rules with the aim to overcome the conservativeness of creep design codes and allow for a more accurate life estimation [41]. Cane's model is developed from the original work of Kachanov and Rabotnov on creep damage in order to relate the strain accumulated with the remaining fraction life neglecting the primary creep strain [192]. In the uniaxial case, the model takes the form of Equation 38:

$$\varepsilon_c = \varepsilon_r \left[1 - \left(1 - {}^{t}/_{t_r}\right)^{{}^{M}/_{\varepsilon_r}}\right] \tag{38}$$

The life fraction consumed (Equation 39) is obtained by rearranging Equation 38:

$${}^{t}/_{t_r} = 1 - \left(1 - {}^{\varepsilon_c}/_{\varepsilon_r}\right)^{{}^{\varepsilon_r}/_{M}} \tag{39}$$

where ε_c is accumulated total creep strain at any time, ε_r is the creep rupture strain, M is the Monkman-Grant constant that represents the secondary creep strain, t is the creep time, t_r is the creep rupture time. The model is relatively insensitive to ε_r so that M represents the only material parameter needed to assess residual life. Under low stress conditions, m remains approximately constant in many materials [41]. Equation 39 is of limited practical use for operational plant because the measure of accumulated creep strain can be inaccurate and is often unavailable. For this reason, the strain rate $\dot{\varepsilon}_c$ is used rather than the absolute strain for remnant creep life calculation according to Equation 40 [193]:

$$\dot{\varepsilon}_c t = m\left({}^{t}/_{t_r}\right)\left(1 - {}^{t}/_{t_r}\right)^{{}^{M}/_{\varepsilon_r}-1} \tag{40}$$

Cane's model was adopted within the former UK Central Electricity Generating Board (CEGB) [193] with modifications to allow non-uniform states of stress and temperature to be considered.

The concept of strain rate as a direct measure of material damage is also the underlying principle in the Omega method developed by Prager [51] whose constitutive equation that describes the post-primary creep rate is presented by Equation 26 and whose formulation for rupture life is given by Equation 24. It is also noted that there is a striking similarity between Equation 24 and the Monkman-Grant relationship given in Equation 18 and the approximation between $\dot{\varepsilon_{t0}}$ and the minimum creep strain $\dot{\varepsilon}_{ss}$ rate is often made [51].

The Cane, Omega and Monkman-Grant models can be essentially harmonised by the Failure Forecast method. This is a more recent empirical approach that predicts the remnant creep life based on the rate of change of a damage quantity and can be applied

without any prior knowledge of stress state, temperature or material properties. The approach suggests that the increase in the rate of change happens as a consequence of a change in the material's creep behaviour identified as a point of criticality. The application of the Failure Forecast framework to creep life assessment is a consequence of creep being a positive feedback damage mechanism where an increase in strain leads to an increase in strain rate after the minimum strain rate has been reached [194]. The remnant creep life is predicted with the Failure Forecast method by using Equation 41.

$$t_r - t = \frac{1}{A_0(\alpha - 1)}\left(\frac{1}{\dot{\varepsilon}_c}\right)^{\alpha-1} \tag{41}$$

where A_0 and α are best-fitting parameters that define the shape of the inverse rate-time curve and the gradient respectively. The projection of the best-fitting line through the inverse rate values allows an estimation of the failure time to be made and is specific to a set of operating conditions. When $\alpha = 2$ and the strain rate is substituted with the minimum strain rate, Equation 41 becomes the Monkman-Grant relationship. Also, the Omega method collapses to the Failure Forecast method assuming $\alpha = 2$ and $A_0 = \Omega$ even if A_0 is not defined as a function of stress and temperature.

Application of a validated Failure Forecast approach is attractive to the plant operator because it utilises the rate of change of a monitored parameter, which is usually the focus of a plant operator when scrutinising inspection or health monitoring data. Materials in high temperature applications invariably show a change in the rate of deterioration as they approach failure.

2.5.2 Hardness models

Methods to evaluate the remaining life based on hardness measurements have been available for many years. The first significant contribution was given by Cane in 1985 [57] that formulated a hardness evolution law for low alloy ferritic steels by using the correlation between hardness and interparticle spacing. Cane's model has no practical plant application due to its complexity and difficulties in determining some key parameters such as the hardness of the component due to solid solution strength and in the overaged condition [13].

Since hardness is a function of temperature and stress, relationships based upon the Larson-Miller parameter (LMP) to find the remaining life through Equation 14 have been proposed. From the initial work of Gooch et al. on 1CrMoV rotor steel, the European Creep Collaborative Community (ECCC) developed a more general equation for hardness changes in low alloy ferritic steels shown in Equation 42 [35]:

$$\frac{HV(t,T)}{HV_0} = k_1 LMP + k_2 LMP^2 + k_3 \tag{42}$$

where HV is the hardness measured at the time of inspection and HV_0 is the initial hardness before service that, if unavailable, could be found from a cold and unstressed region of the same cast in the plant. k_1, k_2 and k_3 are nondimensional material dependent fitting constants [35].

Cardoso, referring to the original work by Goto, introduced a modified function of hardness vs LMP to incorporate the effect of the applied stress in addition to thermal ageing. Under an applied stress, the softening of the material is accelerated and consequently the hardness reduction is more evident [195].

In more recent years, Masuyama introduced Equation 43 to express the hardness drop as function of LMP for creep strength enhanced ferritic steels (P91, P92 and beyond) [196].

$$\ln(\Delta H) = K_s LMP \tag{43}$$

where K_s is a fitting coefficient related to the degree of applied stress [9]. Furthermore, Masuyama related the increase in creep strain ε_c with the increase in hardness drop ΔH using Equation 44 [196, 197].

$$\ln(\Delta H) = A_1 \, ln\varepsilon_c \tag{44}$$

where A_1 is a fitting constant. Equation 44 shows that the change in hardness can be used to estimate the creep strain and consequently this can be used to estimate the remaining life from the Omega method, the Monkman-Grant relationship or the Failure Forecast method [198]. Similarly, a novel empirical correlation between

minimum (steady-state) creep strain rate and hardness was proposed by Morris et al. in [77] with the equation in the form:

$$\dot{\varepsilon}_{ss} = a\left(\frac{1}{HV}\right)^{b} \tag{45}$$

where a and b are fitting constants. $\dot{\varepsilon}_{ss}$ is then used in Monkman-Grant relationship (Equation 18) for the estimation of rupture time.

By using a multivariate analysis approach on Ni-based alloys, Saito et al. found a regression equation for hardness as a function of service temperature T and stress σ (Equation 46) [198].

$$HV = 0.11252T + 0.075789\sigma + 36.86338\,{}^{t}/_{t_r} + 95.33299 \tag{46}$$

Knowing the service temperature, the stress and the measured hardness, the creep life fraction ${}^{t}/_{t_r}$ can be calculated from Equation 46 with an accuracy of ±18.5% between the predicted and the measured hardness creep life fractions. The validation of the model requires the collection of much creep data under different test conditions and a process of parameter optimization to improve the prediction accuracy.

A similar approach based on multiple regression was followed by Allen and Fenton [199] to derive a creep rupture model for P91. The model is presented in Equation 47 and correlates the creep performances with the high temperature tensile properties in the same manner as in the Wilshire formulation [200]. Starting from an Arrhenius type function, Allen-Fenton use a normalised stress parameter, S/HV, where S = applied stress/flow stress, that characterises the high temperature properties of the material.

$$\ln t_r - {}^{Q}/_{RT} = \ln B - n\ln S + pn\ln HV \tag{47}$$

where Q is the activation energy, R is the universal gas constant, B is a constant, T is the absolute temperature, n is the Norton's law constant and p is a model correction constant [77]. The activation energy is assumed constant in the model while n and p are changing according to the applied stress. The limitation of the model is that the

flow stress is not assumed to be temperature dependent resulting in an overprediction of creep life [77, 199].

2.5.3 Models based on replica data

There are many guides available describing how to take surface replicas and complete the creep cavity count assessment; it is worth noting that a high degree of expertise and experience is required to become competent in replica assessment on a particular material being examined.

More quantitative assessment methods have been proposed; those based on measuring the volume or area fraction occupied by cavities tend to be heavily influenced by the control of metallographic preparation, which makes these approaches difficult to use in a predictive life assessment model. Hence, researchers have tried to define mechanistic life models that use information from the metallurgical examination but are much less sensitive to the sample preparation procedures. Examples of these models include those by Shammas [201] that define an 'A_2' parameter that is based on a fraction of the grain boundaries damaged by cavitation or cracking (Equation 48); however, this method still requires accurate detection of grain boundaries and damage.

$$\left(1 - {}^{t}/_{t_r}\right) = (1 - A_2)^{n\Lambda/(\Lambda-1)} \tag{48}$$

where Λ is the ratio of secondary to tertiary creep strain. The relationship between the 'A_2' parameter and life fraction has been assessed for a range of 1CrMo and 2CrMo steels [202]; however, the model appears to be too conservative compared to experimental data. Riedel [203] proposed a modification to the 'A_2' parameter model to reduce the excessive over conservatism which was based on a more refined assessment of the damage occurring at the grain boundaries.

These quantitative models are not sufficiently refined to use in a practical plant assessment; however, the approaches where the metallurgical damage is ascribed to a life assessment model is interesting when considering more recent developments for assessing the level of creep damage using ultrasonic, electromagnetic [204] or alternating current potential drop (ACPD) [205] techniques. These are at various stages of development and (if successful in field applications) may provide the opportunity to develop more reliable quantitative life prediction models. The

electromagnetic and ACPD techniques provide an assessment of the condition of the surface, or near surface region, whereas the use of ultrasonic techniques has the potential to provide a volumetric assessment. The publication by Sposito et al [206] provides a useful overview of a wide range of non-destructive techniques used for the detection of creep damage in power plant steels.

Hence currently, the best quantitative surface replica life assessment model is based on a correlation of the Neubauer damage classification against life fraction, which has been reported by Shammas [201]. However, the correlations required by this approach are material specific and require calibration.

2.6 Summary and thesis aims

This chapter has sought to give a summary of the pertinent knowledge available and the work conducted so far in different fields relevant to the aims of this thesis that encompass engineering, mechanics, power plant industrial applications and material modelling.

High-temperature alloys such as CrMoV and 9-12%Cr steels are largely employed in power plant applications to resist against the main damage mechanisms that are creep and fatigue. An overview of creep in terms of its constitutive equations and lifing models has been provided, followed by a brief description of fatigue. A review of creep-fatigue interaction mechanisms and the unified viscoplasticity theory used to model this interaction is also given. The current industrial practice with the main design codes (R5, ASME Boiler and Pressure Vessel Code, RCC and BS EN for pressure vessels) that are employed to determine the design life, to assess the condition and estimating residual life under creep and fatigue has been reported and discussed.

Low-alloy ferritic steels (CrMoV) and high-strength martensitic steels (9-12%Cr steels) are widely used for boiler components operating at high temperatures and pressures. Their mechanical behaviour and microstructural evolution under service conditions are extremely complex mainly due to variability in loading (mechanical and thermal), initial material microstructure and geometry effects. During service, low-alloy ferritic steels experience a reduction in creep strength caused by the coarsening and agglomeration of precipitates and the nucleation of cavities along grain boundaries and cyclic softening due to the rearrangement of dislocations. High-

strength martensitic steels exhibit also a cyclic softening behaviour and ratcheting as response to creep and fatigue. These phenomena are attributed to the recovery of microstructure, decrease in dislocation density and precipitate coarsening.

It is therefore of paramount importance to have (and develop) accurate material models able to predict the remnant life of components when their initially-estimated end of life is approaching. The accuracy of such models has significant implications for both safety and economics of continued plant operation. In addition, having a better understanding of condition at any point in material life is beneficial since it allows the generator to modify operations to suit market conditions and regulations that invariably will change during the operational life of the station.

A considerable problem in lifing theory is that the design life is often underestimated with the consequence of expensive and unnecessary replacements. This is the result of inaccuracies and over-conservative assumptions and simplifications in the current life predicting approach based on empirical models (see paragraphs 2.1.3.1 and 2.2.4) in which a large number of material variables and safety factors are involved and from which extrapolation from uniaxial rupture data is performed.

The current industrial condition monitoring strategy tries to eliminate this imprecision in predicting the component lifetime by a combination of non-destructive damage monitoring with NDT, limited trend monitoring and online monitoring. This combination allows scheduling of a programme of repair and replacement and a better estimation of service life in order to maximize the plant revenues while keeping the operations safe. Online monitoring is based on data regularly taken from the plant (typically pressure and temperature) that are then used in predictive models such as the Manson-Brown formula to determine the component rapture life. These models use a reference stress that is introduced to approximate the complex multiaxial state of stress under which the component is subjected in real situations. The equivalent stress is often made equivalent to the mean diameter hoop stress and depends on the operating pressure, the pipe outside diameter and wall thickness. Key NDT techniques are strain measurements and surface hardness measurements which are employed in conjunction with metallographic replica assessment to evaluate the life consumption through hardness-based models and strain life models. However, both the inspection-

based and online monitoring models are still not used proactively in a predictive life assessment framework. Instead, trends from inspection data collected over different outages are analysed to trigger repair/replacement activities and to tune the life estimated from online monitoring data. There is therefore a requirement to develop life prediction models to support forward planning for plant inspections, repairs or replacements based on hardness and/or strain.

2.6.1 Aims and objectives

The aims of this dissertation work can thus be summarized as follows:

- To develop more informed condition monitoring strategy as opposed to continued implementation of traditional, periodic and increasingly costly inspection-based assessment approaches, repairs and replacements;

- To develop 'point of application' material models with a holistic approach that can seamlessly use site metallurgical/inspection and operational data from the station to provide the operator with a timely and predictive life assessment capability;

- To seek correlation between data from well-established inspection techniques such as hardness and replica measurements and to establish inspection-based models;

- To characterize the microstructural evolution of 9% Cr steel and to develop the fundamental ideas for creep prediction based on factors responsible of the material softening.

The aforementioned aims will be achieved with the following actions:

- Study of in-service site metallurgical/inspection and operational data;
- Analysis of hardness and replica data collected in a database from inspection reports of different outages;
- Use of site operational data to support the development and demonstration of predictive computational models;
- Investigation of the 'rate of change' of inspection parameters and development of a methodology based on the concept of a life assessment transfer function (LATF)

that exploits readily available operational, component and periodic inspection data of various types;

- Carry out a programme of interrupted creep tests and analyse the microstructural evolution through microscope techniques such as SEM, TEM, EBSD and optical microscope and micro hardness measurements.

2.6.2 Summary of the selected constitutive equations for modelling

In the previous Sections 2.1 and 2.2, a review of the most common constitutive equations and lifing models used for creep, fatigue, and creep-fatigue together has been presented. As mentioned in Section 2.6.1, one of the main aims of this thesis is to develop a more proactive and accurate approach for the prediction of component remaining life and this will be achieved by use of appropriately selected equations from the aforementioned modelling equations.

In Chapter 3, the new approach to condition monitoring considers the peculiarities of the creep behaviour of different materials by use of material-specific creep models to predict the remaining life. Specifically, to enable the prediction of the steady-state creep strain rate and the time to reach it, the Wilshire formulations (Equations 22 and 23) will be employed thanks to its capability in extrapolating long-term creep information from short-term creep tests. In addition, in order to predict the failure time, the Monkman-Grant relationship (Equation 18), the Omega model (Equation 24) and the Failure Forecast model will be employed according to the material selected and their creep behaviour.

In Chapter 4, to improve the current industrial lifing methodology for creep-fatigue, the Chaboche viscoplasticity equations (Equation 55 to Equation 62) are linked with the R5 procedure. The Chaboche model is used to model the mechanical response in terms of stress distribution and deformation of a turbine rotor under a thermomechanical cyclic loading.

In Chapter 5, to enable the steady-state creep rate to be expressed as function of the applied stress and temperature, the Norton-Bailey power law (Equation 8) will be employed in combination with an Arrhenius type law (Equation 9). This formulation is then refined by adding the hardness in order to integrate for the first time in a predictive model the stress and temperature data with the field measurements. In

addition, in order to allow the effect of creep cavitation on strain rate to be included, the Kachanov-Robotnov model with the inclusion of the temperature dependence by an Arrhenius type law will be deployed. The creep cavitation is expressed by the damage parameter ω where the number of cavities is counted from creep replication. Finally, the rupture time t_r will be estimated by using the Monkman-Grant relationship (Equation 18).

2.6.3 Summary of the existing experimental work/data and justification for the new experimental work and data collection

In Chapter 5, large datasets from periodic outage inspection reports for ½Cr½Mo¼V (CrMoV) are collected methodically in a database in Excel. The current practice for the assessment of the condition of high temperature materials in-service is based on the acquisition of data in inspection reports captured on outage for surface replica, hardness and strain which are, in general, utilized *individually* in various empirical models. Such data have not been used in a predictive modelling approach for residual creep life assessment, with significant run-repair-replace decisions invariably being based on very conservative assessments, advised by expert elicitation and intelligence gained from other similar assets in service. The justification for the creation of the database in this thesis is to propose a new and different method to use these data more efficiently and more integrated to inform subsequent actions on plant.

In Chapter 6, the microstructural evolution of an ex-service exposed P91 material will be investigated through interrupted creep tests and metallurgical investigation to include SEM, TEM, EBSD and optical microscope and micro-hardness measurements. Interrupted creep tests have been extensively performed both under short-term and long-term creep conditions at different temperatures and stresses to study the microstructural mechanisms responsible for material degradation. Short-term and long-term creep tests are generally in accord in the identification of primary processes that govern the microstructural evolution for 9-12% Cr steels, the key ones being the transformation of the original martensitic lath structure, reduction in dislocation density and coarsening of precipitates [207]. Processes such as the precipitation of Z-phase and Laves phases are also observed under long-term creep exposure, but despite this, it has been argued that short-term creep tests are broadly

sufficient in providing key information related to material degradation as a result of microstructural changes [179, 207-210]. The justification for the conduction of the experimental creep tests on P91in this thesis a clarification of the major microstructural factors that are most influential for each creep stage is sought. This is deemed important because of the practical reliance on periodic physical inspections through life.

3 Requirements for developing high temperature creep life models for ageing pipework system

3.1 Introduction

The influence of legislation and the commercial market is critically important for the viability of a generating plant. In the UK for example many of the older conventional coal-fired stations are running to closure with limited remaining operating hours, whereas the gas-fired stations are under increasing pressure to extract more revenue from operation. These challenges arise due to various directives mandating reductions in emission levels and the increasing influx of renewable technologies onto the electricity grid [211]. This results in conventional fossil-fired plants operating very flexibly and potentially with extended periods of lay-up. Hence, over the typical 25–40 year life of a power plant there are significant commercial benefits if a more informed condition monitoring strategy can be adopted as opposed to continued implementation of traditional, periodic and increasingly costly inspection based (sampling) assessment approaches, repairs and replacements. As long as the condition-monitored data is interpreted correctly, the new strategy will enable power plants to remain competitive by optimising and ultimately reducing through-life costs associated with statutory periodic inspections and potential premature repairs and replacements [212, 213]. Figure 26 [13] shows an outline of the current practice used to evaluate the condition of the generation assets and hence advise the forward inspection and remediation plan. In this outline, the ‘off-load’ activities are undertaken during the main statutory outage and as indicated in Figure 26, there are a number of practical examination techniques deployed, including on-load condition assessment. The ‘off-load’ inspections account for the majority of the time and cost incurred to assure safe operation during the operational period up to the next statutory outage (typically 4 years).

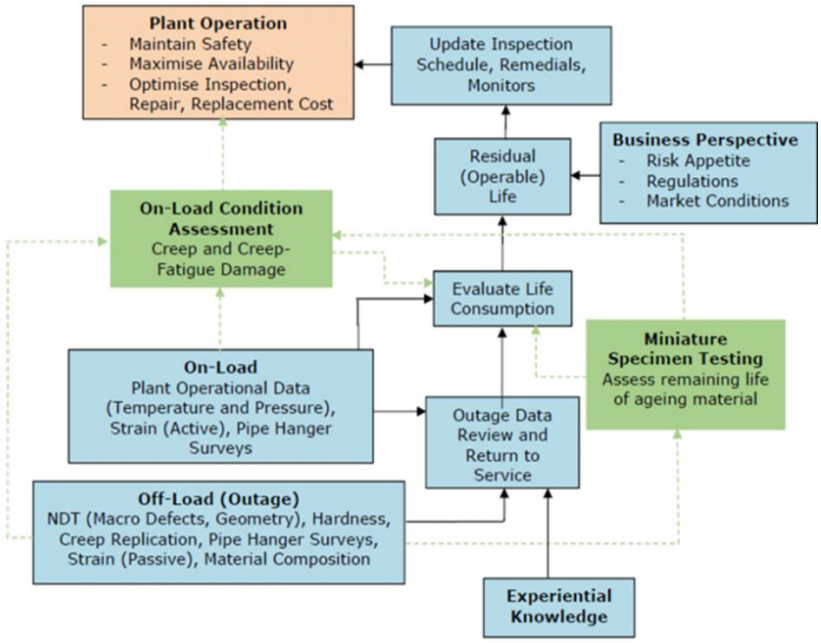

Figure 26: High temperature plant condition assessment approach [13]

Figure 27 [77] is based on surveys of outage inspection activity on main steam CrMoV pipework systems and illustrates the increase in the volume of inspection activity, normalised at time 't', where 't' represents the last outage before wholesale pipework replacement. The preceding 4-yearly statutory outages are indicated at intervals 't-1' …. 't-n' etc.

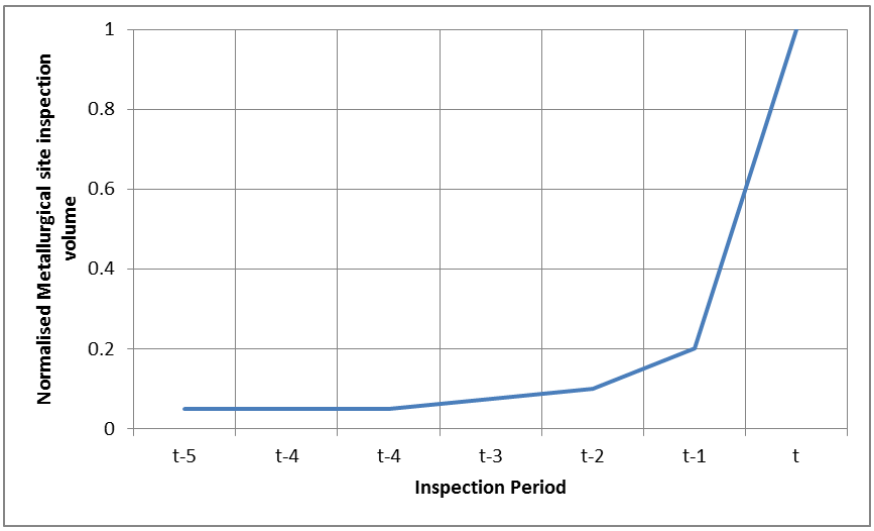

Figure 27: Normalised CrMoV metallurgical inspection volume against outage time period [77]

Examinations of 'life-expired' CrMoV pipework using through thickness small specimen creep tests and supplemented by metallurgical studies [214] illustrate how parent pipework material can be retired from service prematurely based on traditional examination techniques. Other studies [215] of the in-service performance of high temperature main steam line welds have emphasised the conservatism in the current approaches applied to assess the residual creep life, not least the use of simplistic stress values in creep rupture calculations that are used to supplement the physical inspections. As an illustration, a previous computational study of the residual creep life of main steam and hot reheat bends [216] used actual wall thickness measurements obtained from a population of 289 bends taken at various cross-section positions around the arc of the bend, which illustrated very significant differences of ~48% in the peak steady-state creep rupture stress. Significant differences in wall thickness arise due to induction bending during manufacture at the intrados (68–70 mm) compared to the bend extrados (58–60 mm) as shown in Figure 28 for a subset of 14 CrMoV main steam line bends. Other surveys of wall thickness variations in straight pipe sections show variability, albeit not as pronounced as those found in the bend population.

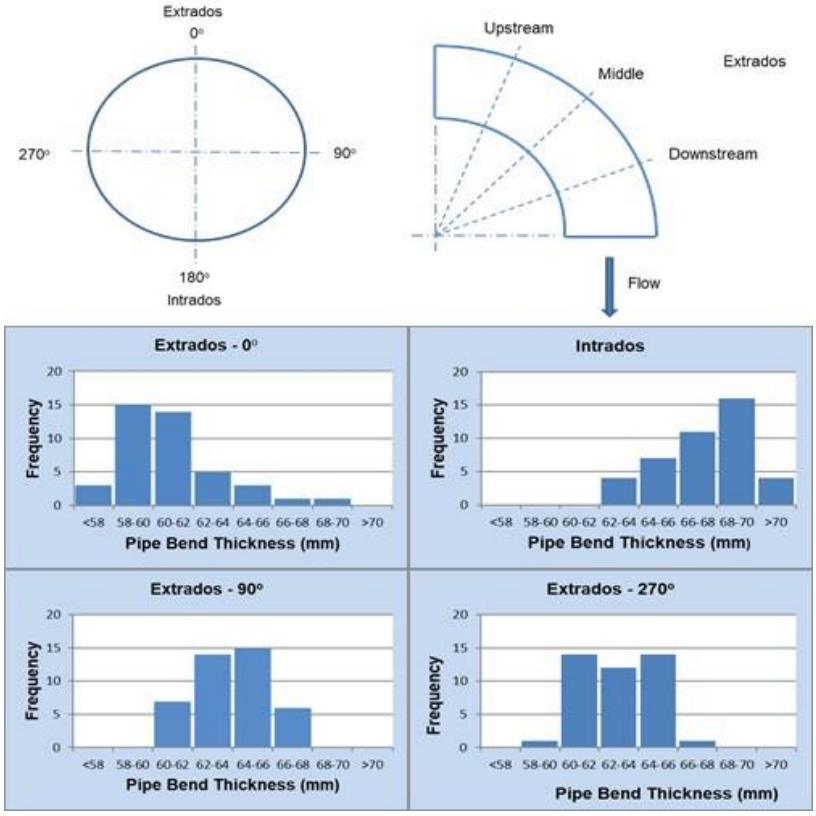

Figure 28: Example of the wall thickness variability in CrMoV main steam line bends [216]

Much useful data are routinely collected during a periodic plant outage and also from online measurements of operating steam pressure and temperature conditions [13]. From practical experience, these data are considered to be relatively unstructured and currently not ideally configured for use in a practical residual life assessment. This chapter focusses on the requirements for condition monitoring of materials (CrMoV, 9–12%Cr) operating at temperatures in the creep range where the complexity and sensitivity of the creep damage mechanisms to operational conditions is challenging. The possibility of more informed and longer-term creep life predictions, which support improved forward planning for plant inspections, repairs or replacements, is explored. A methodology is proposed based on the concept of a life assessment transfer function (LATF) that exploits readily available operational, component and periodic inspection data of various types and the potential to use available creep parametric methods (see section 2.1.3) in the LATF approach is discussed. An example is developed to illustrate how the proposed methodology will address and overcome some of the

current limitations for life assessment, exploiting real inspection data to improve estimates of residual life.

3.2 Industry requirements

The challenge for the operating stations, which are required to be more flexible, is to define the optimal inspection periodicity, the rate of change of key parameters and hence prompt the correct run-repair-replace actions. Residual life predictions on ageing plant are typically made with relatively pessimistic assumptions, which usually results in over-inspection during outages and eventual early retirement from service [213, 217]. Recent examinations of ex-service CrMoV pipe components [214] reveals a significant difference between the perceived residual life based on standard surface examinations undertaken during plant outages and the residual life obtained from laboratory examination and testing of the material extracted at different positions through the pipe wall thickness. There is great difficulty in establishing the absolute condition of any material operating at high temperature due to variability associated with: (i) inconsistent information on prior operational history, inspection records and original fabrication; (ii) the current operation (loading) that is invariably significantly different to original design intent due to requirements of the commercial market. However, one factor that can be established (or measured) in-service is associated with the rate of change in condition, using measurements from surface replicas, hardness measurements, metallurgical characteristics, propagation of macro-defects, deformation or extension etc. Invariably, the identification of a significant 'change' in the condition of the component is the trigger for invasive repairs of replacements; however, this is usually a very reactive process due to the absence of more sophisticated condition monitoring based predictive models [189, 190]. Hence, the industrial requirements are described by the following:

1. **Improved life prediction models**: the ability to practically account for the in-service operating conditions (temperature, pressure), state of stress, thermal ageing of the material and parameters based on inspection data, such as surface hardness and surface replicas;

2. **Deployment of an LATF tool**: the ability to process and integrate both periodic (outage) data and online data prior to use in the life prediction model;

3. **Flexibility:** the ability to update the life prediction model based on subsequent inspection findings and findings from opportunities to extract and examine ex-service material,

4. **Operator feedback:** the ability to effectively 'nudge' the plant to improve operating point(s) and reduce the rate of subsequent damage accumulation.

The construction of the life prediction models and LATF should allow the user to examine the effects of the main factors contributing to the change in material condition and performance in-service observed via statutory inspections. These contributing factors are typically associated with:

a) Material properties (composition, heat treatment, ageing in-service);

b) Operation (temperatures, pressures and transients);

c) Design (geometry, installation anomalies).

Being able to de-couple and hence improve understanding of the relative impact of these main contributors to in-service behaviour will permit the plant owner to implement the right course of action when faced with adverse inspection findings during an outage.

3.2.1 Evidence from site inspections

Hardness and surface creep replicas are taken periodically between plant outages often because of custom and practice in detecting microstructural degradation as the material ages. Importantly, it is not unusual to find small changes in the repeat replica and hardness data, dependent on the operating conditions, age and component design [190]. As an example, Figure 29 shows a range of parent CrMoV hardness data captured between two successive outages at 20 khr difference on aging plant, for one of the four operating units and from a limited number of high temperature pipe systems. In this example the mean diameter hoop stress of the main steam pipe (342 mm outside diameter and 60 mm wall thickness) was 40.8 MPa, and 37.9 MPa for the hot reheat pipework (482 mm outside diameter and 26 mm wall thickness). Operating conditions were nominally 173.8 bar and 568 °C for main steam and 43.2 bar and 368 °C for hot reheat.

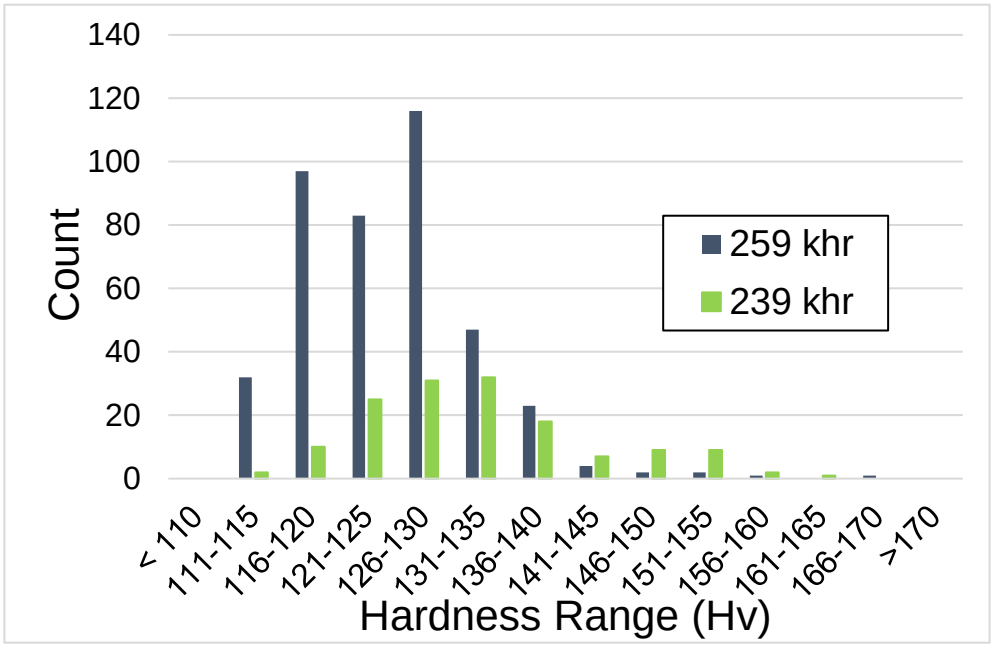

(a)

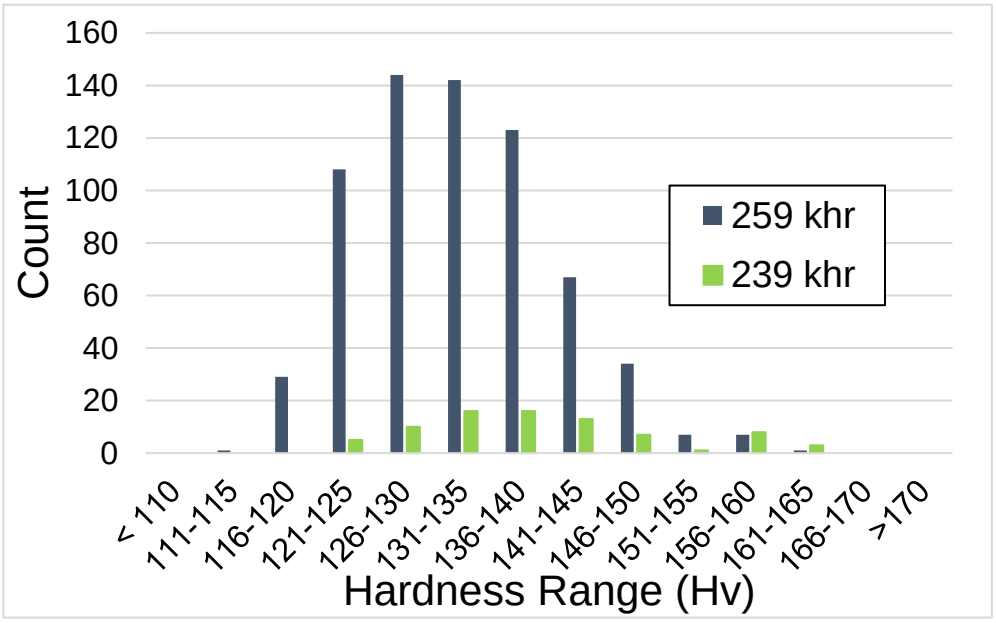

(b)

Figure 29: Outage hardness data captured from parent CrMoV pipe material on (a) main steam and (b) hot reheat pipelines over two successive outages. The legend indicates the total service time at each of the outages [77].

The general reduction in hardness over the 20 khr operating period is evident from the data sample (extracted from one 500 MW conventional fossil-fired unit). Figure 30 shows similar plots for creep replica assessments from the same unit and over the same

outage periods. The terminology used to describe the creep damage level is listed in Table 4.

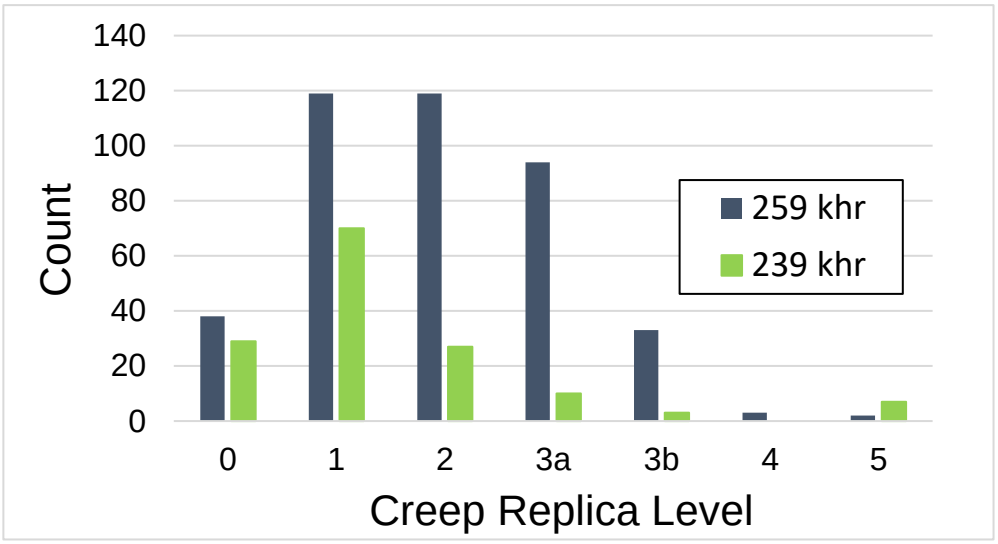

(a)

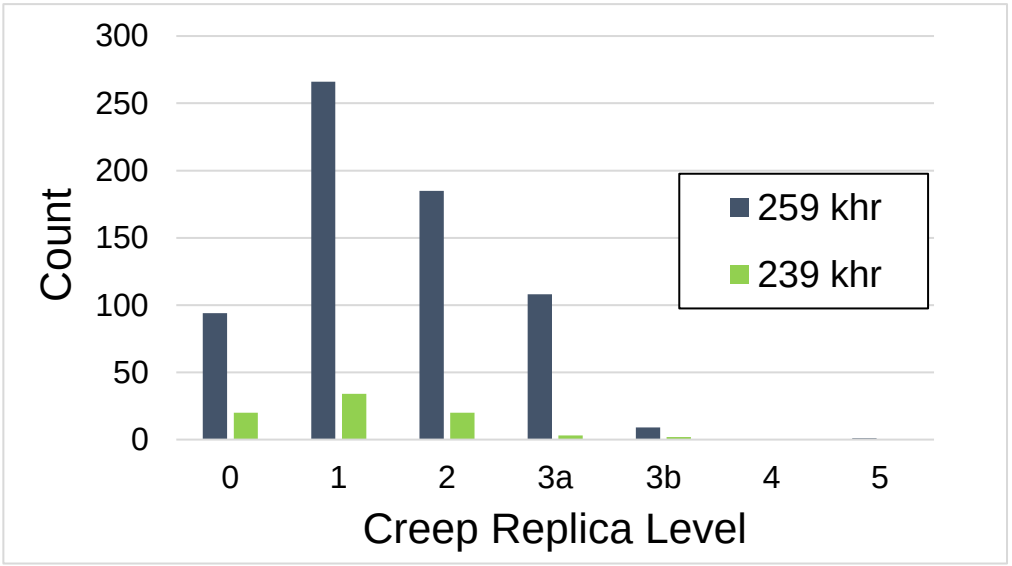

(b)

Figure 30: Outage creep replica assessment level data captured from parent CrMoV pipe material on (a) main steam and (b) hot reheat pipelines, over two successive outages. The legend indicates the total service time at each of the outages [77].

Table 4: Summary of descriptions of creep damage levels [12]

Creep Cavity Damage Level	Microstructure	Cavity density [cavities/mm^2]	Abbreviation
0	Clear	0	C
1	Very isolated	1-10	VI
2	Isolated	10-50	I
3a	Low orientated	50-250	LO
3b	Mid/High orientated	250-500	MO/HO
4	Grouped	500-1000	G
5	Aligned	1000-1500	A

In isolation, the change in creep replica damage level is somewhat less obvious to discern over the 20 khr interval in the operating period. However, there may well be a correlation, when comparing the change in hardness with change in creep replica assessment level, especially where both sets of data are acquired at the same position on the component, which has over time become the usual approach on site. Figure 31 and Figure 32 illustrate the correlation found between change in hardness and creep replica level (based on the data from the 259 khr outage illustrated in Figure 29 and Figure 30), with a general reduction of the upper values of hardness evident with increasing creep cavity count. Hardness testing is relatively easy and cost-effective to implement across a large number of locations whereas replica metallography is more time consuming and the interpretation of results is variable according to the experience of replicators [218]. Identifying a potential correlation between hardness and creep damage level would be extremely advantageous.

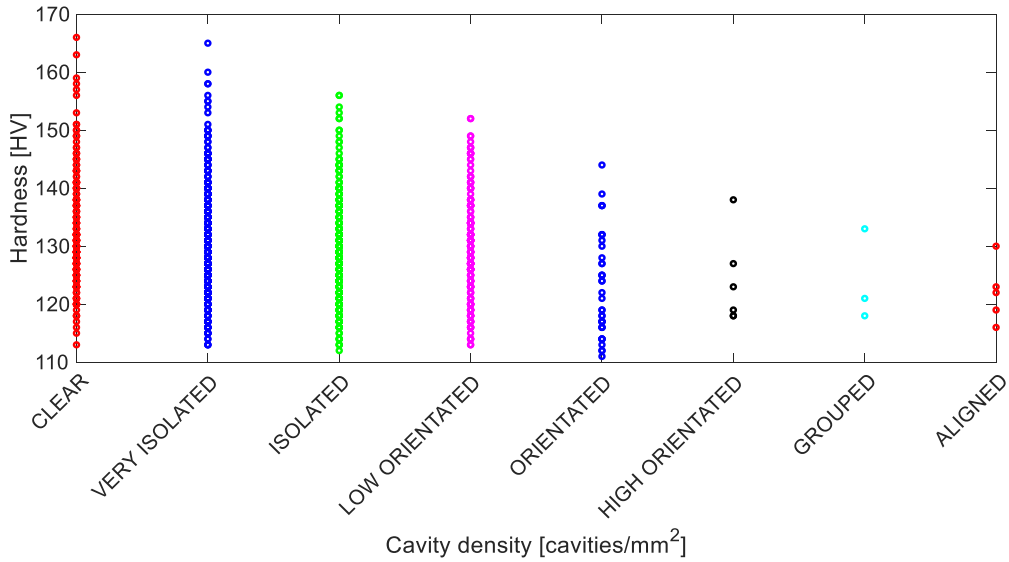

Figure 31: Hardness variation versus creep cavitation levels (see Table 4) for CrMoV parent material at 259 khr outage [190]

These site measurements have provided sufficient data for conducting meaningful statistical analysis: the reduced centered variable (Equation 49) and the amplitude (Equation 50) have been calculated. x is the test value, μ is the population mean and σ is the population standard deviation (Figure 32).

$$Z - score = (x - \mu)/\sigma \tag{49}$$

$$\Delta Z - score = (\max(Z - score) - \min(Z - score))/2 \tag{50}$$

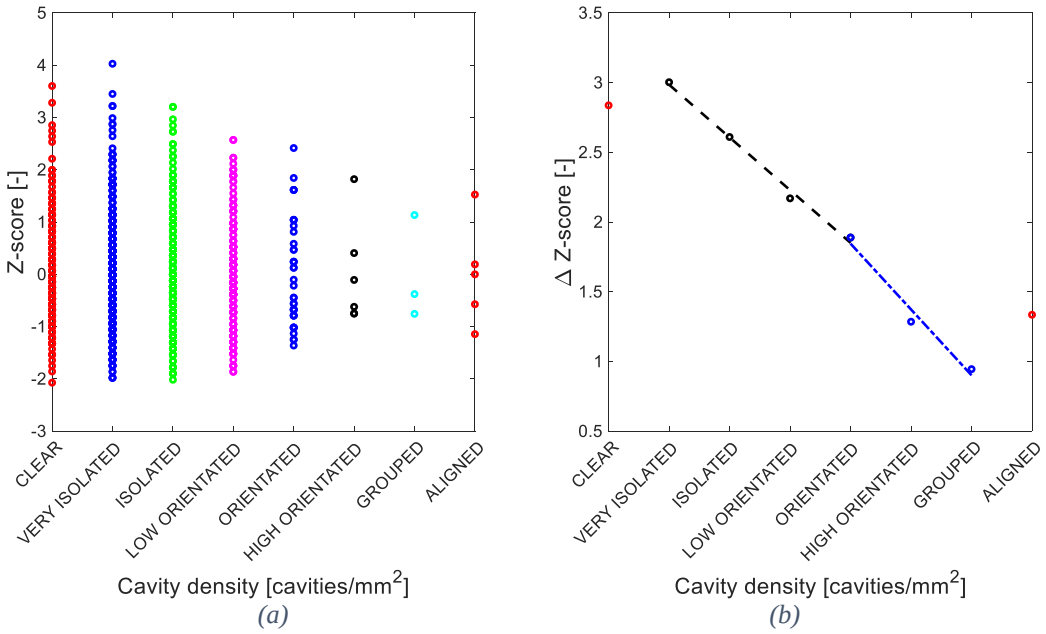

Figure 32: Statistical analysis on CrMoV parent material (a) $Z-score$ (b) $\Delta Z-score$

From Figure 32b, the fitting curve shows a slightly higher slope in correspondence of 'orientated' cavities level that is considered to mark the transition from secondary to tertiary creep stage [218]. Both the 'clear' and 'aligned' cavity density levels do not lie on the same curve (they are marked with red points in Figure 32b) because of the difficulty in being able clearly differentiate them from 'very isolated' and 'grouped' cavity density levels respectively during replica assessment. The results are promising because they show that the change in creep strength, associated with component damage, could be correlated with the change in hardness. The rate of change in hardness increases when approaching the critical (tertiary) creep stage. This is in accordance with the studies of Eggeler [219] and Masuyama [197] on 9-12%Cr steels where the cavity density development over time is represented by an exponential function with acceleration in the rate of change of damage close to failure.

3.2.2 Material behaviour considerations

During long-term service, commonly used power plants materials (CrMoV and 9–12%Cr steels) have different creep and mechanical behaviours due to distinct changes in their microstructure. Under service exposure, CrMoV steels are affected by the coarsening of M_2C and M_7C_3, which are precipitate phases rich in Cr and Mo depleted from the metal matrix. The consequence of this is an appreciable decrease in yield

strength, in creep resistance and in the hardness of CrMoV steels [163]. Instead, 9–12%Cr martensitic steels have a more complex microstructure where the precipitation of chromium-rich carbides ($M_{23}C_6$) and V–Nb carbonitrides (MX) enhances the creep resistance at high temperature. During high temperature service, $M_{23}C_6$ particles coarsen while MX carbonitrides remain essentially unchanged and intermetallic Laves phase $(Fe,Cr)_2(Mo,W)$ nucleates and grows with a fast rate in particular at temperatures between 600–650 °C. The effect of Laves phase, unstable at high temperature and responsible for the depletion of Mo and W in the metal matrix, is particularly detrimental on long-term creep properties since triggers cavity formation due to its irregular shape and large size [220]. In addition, the appearance of Z-phase, a nitride rich in Cr–V–Nb, which forms at the expense of MX carbonitrides, contributes also to a dramatic drop in creep resistance especially in 12%Cr steels [221]. All these factors contribute to the risk of premature failure in 9–12% Cr steels suggesting a faster deterioration rate than CrMoV steels as end of life is approached. Different rates of change in metallurgical properties in these common materials can initiate ad-hoc inspection planning with a variable periodicity. Figure 33 provides a schematic comparison between aging of CrMoV material and of P91 based on the results of hardness and replica assessments. For CrMoV steels, recent new pipework installations show an initial installed hardness of at least ~140-170 HV, contrasting with examples of ex-service specimens at ~250 khr showing ~135 HV [222], and similar aged pipework from site surveys showing values < 125 HV. There is clearly a wide range of initial surface hardness on any new plant installation and a measurable reduction in surface hardness occurring due to extended service. This trend is underpinned by site survey data from eight 500 MW coal units with several thousand data points on CrMoV parent pipework and welds acquired over three outages, which accounts for ~40 khr of service during this inspection period (data for two outages shown in Figure 29) [190, 223].

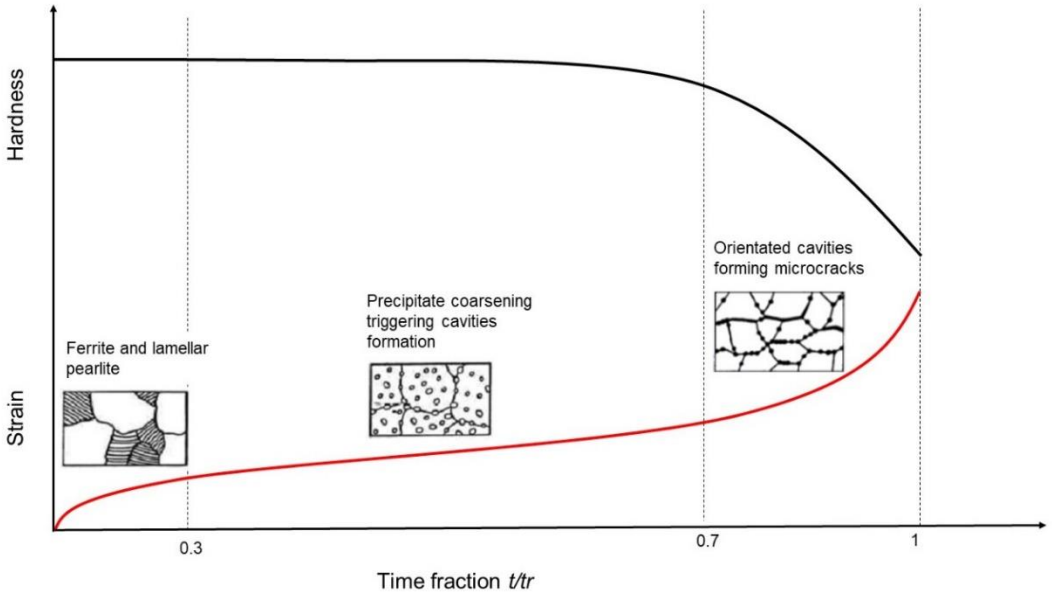

(a)

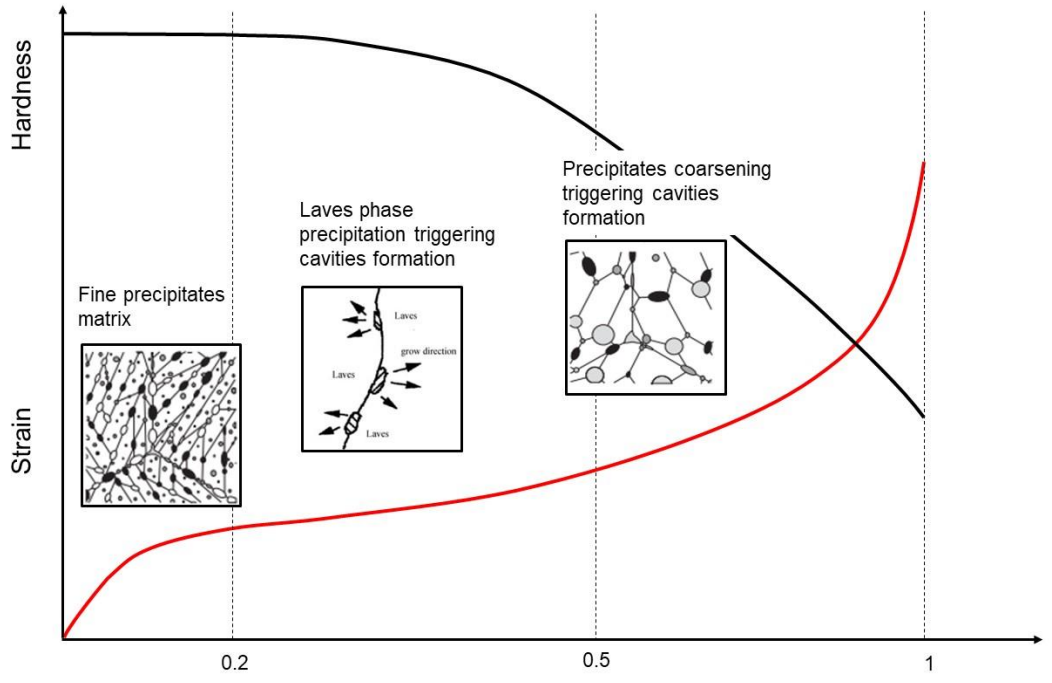

(b)

Figure 33: Schematic ageing characteristics represented by strain, hardness and microstructure, based on standard outage inspection techniques for (a) CrMoV, and (b) P91 pipework

Reviews of these techniques for contrasting materials [13, 77] show the care required on the physical inspection task and the current difficulty in using the information in a predictive assessment of residual life. It is clear from the above discussion that a

number of factors affect the aging behaviour of material in-service; however, it is certain that unexpected incidents and failures will continue to prevail unless there is a direct, timely and regular feedback to the operator on the effects of operation on the integrity of the assets. From inspection of the plant data in Figure 29 and Figure 30, along with consideration of the schematic trends depicted in Figure 33, it is evident that the rate of change in a measured parameter is also key for monitoring purposes when assessing the absolute condition [224] of the material and residual life.

3.3 Predictive model implementation for practical applications: a proposal

Currently, the most frequently used approach to determine creep rupture life is the Manson-Brown model (Equation 17). This approach is helpful in that it can be deployed relatively quickly and provides a means of ranking components and hence supports inspection scheduling. However, the sensitivity of the model to modest change in operational conditions make the information it provides only useful in conjunction with data acquired during outage inspections, where costs can rise significantly as the material ages [13]. In the following section, the objective is to propose an innovative approach in which a predictive model utilising online data (steam temperature, pressure, etc.) and component reference stress, is used in combination with data obtained from outage inspections, such as hardness and surface creep replicas. The rate of change of inspection-derived data is recognized as a key parameter in such a model, as indicated in Figure 31 and in Figure 32.

For practical purposes it is considered that a range of useable models of varying complexity are required by the plant engineer, which reflects the data available on material condition. The approach using the proposed LATF (described in section 3.3.3) is intended to pre-process what could be disparate sets of data for subsequent use in the predictive material life model. Implicit in this approach is the need to be able to assess the sensitivity associated with material properties, operational conditions and manufacturing/geometry factors, as defined in Section 3.2.

3.3.1 Assessing the significance of rate of change of inspection data

As previously mentioned, creep damage accumulation is linked with the formation and aggregation of cavities leading finally to a drop in creep strength. A decrease in

component hardness is also observed from outage inspections. The relationship between hardness and interparticle spacing λ is helpful in explaining hardness and creep strength variation. The rate of increase of λ is the major contributor responsible for a rapid deterioration in creep strength and consequently in the material hardness; an acceleration in the rate of change of hardness is thus expected in the proximity of failure [57].

The 'Failure Forecast Method' postulated first by Voight aims to predict the failure time based on the rate of change of an observable damage quantity, Ω [194] (see Section 2.5.1). This method describes the behaviour of a wide range of systems which shows an increase in the rate of change of the damage Ω to the proximity of the criticality (failure), e.g. the creep strain rate increase close to failure is indicative of damage [225]. Voight's postulation is expressed by Equation 51 and from the perspective of the current discussion it can potentially be developed to reflect change in hardness, assuming the form of Equation 52.

$$\frac{d^2\Omega}{dt^2} = A\left(\frac{d\Omega}{dt}\right)^{\alpha} \tag{51}$$

$$\frac{d^2HV}{dt^2} = A\left(\frac{dHV}{dt}\right)^{\alpha} \tag{52}$$

The 'Failure Forecast Method' allows the estimation of the remnant life by integrating Equation 51; thereby the point of criticality (failure time) is predicted earlier in the component life by projecting the best fitting-line of the points of the inverse damage rate over time (Figure 34). The remnant life prediction is given by Equation 53, where A and α are constants obtained by plotting the inverse rate of damage against time.

$$t_r - t = \frac{1}{A\,(\alpha - 1)}\left(\frac{1}{d\Omega/dt}\right)^{\alpha-1} \tag{53}$$

Similarly, the extension of Equation 53 for hardness variation gives the inverse hardness rate-time relationship represented by Equation 54:

$$t_r - t = \frac{1}{A\,(\alpha - 1)} \left(\frac{1}{dH/dt}\right)^{\alpha - 1} \tag{54}$$

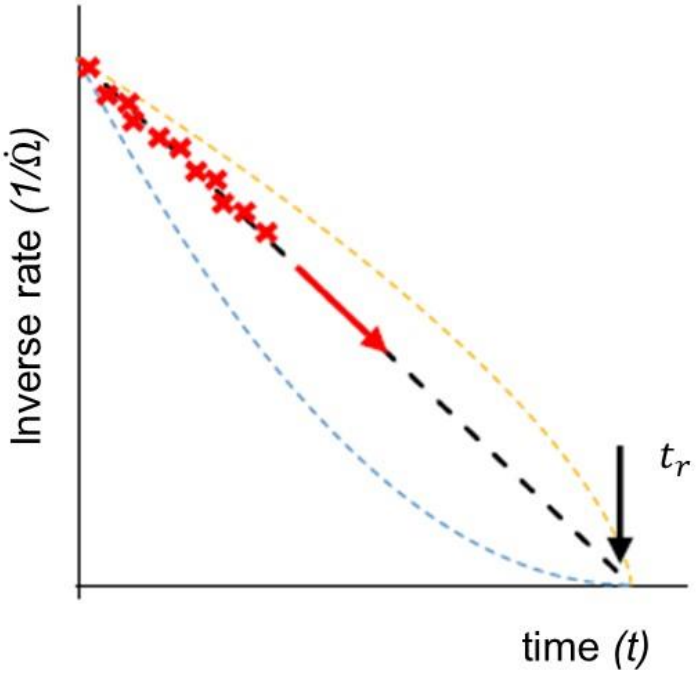

Figure 34: Schematic illustration of the inverse damage rate against time [194]

Some considerations are observed from Equations 52 and 54:

1. Routinely collected inspection data are implemented in a model in which the rate of change gives information on the real status of the material as the hardness variation is related to creep damage;
2. The rate of change becomes the most important factor for the prediction of the point of criticality (time to failure), whereas traditionally the focus has been on the absolute measure of damage [13].

Equations 52 and 54 are significant as they constitute the basis of a new life predictive model in which hardness data, currently taken during routine field inspections, is used more proactively for a projection of the failure time. For practical purposes this new predictive model would be used in parallel with other predictive methods currently used, such as online monitoring using steam pressure and temperature data, and it may be possible to further integrate these models. It is recognized that physical inspections

will still be required initially and to some extent thereafter to validate the approach and to identify further improvements.

3.3.2 A new approach to condition monitoring of engineering materials operating at high temperatures

At nominal plant operating conditions, relatively low stresses and high temperatures prevail, with the most widely used materials in power stations (CrMoV and 9–12% Cr) showing a different microstructural evolution that requires varied assessment techniques to correctly monitor their accumulated damage. Low alloy ferritic steels (CrMoV) exhibit a prolonged secondary creep with a steady-state strain rate and a limited tertiary creep phase [69], whereas enriched alloy steels (9–12% Cr) display a minimum strain rate followed by a prolonged tertiary creep [226] (Figure 33). In broader terms, CrMoV and 9–12% Cr belong to different classes of materials: one characterized by primary creep followed by a defined secondary stage where the acceleration of strain rate is only visible late once entering in the final stage, the other by a tertiary creep stage that offsets the primary step [35, 227]. Different creep models are therefore needed in order to properly monitor distinctive creep behaviours.

Strain-hardening is the primary cause of material strengthening in the primary creep stage, and thus it seems reasonable to describe the primary creep with the Wilshire model based on the assumption that dislocation creep plays the major role in creep material behaviour [228]. The minimum (steady-state) strain rate (and the time to reach it) can be accurately estimated by Equations 22 and 23 (Wilshire model) with the values of constants determined by the available literature or by short-term creep tests (miniaturised) on a small sample of material. Given the extrapolation capability of Wilshire model (Section 2.1.2.1), the prediction is expected to be accurate. A possible alternative to the Wilshire model is the θ projection method but in this case, more effort is needed to extrapolate the θ_i terms [229]. At this juncture, it is considered that materials showing different microstructural evolution behaviour must be modelled with quite distinctive methods. Low alloy ferritic steels (CrMoV), characterized by a prolonged secondary creep, can be modelled with the Monkman-Grant (Equation 18). This because the creep deformation mechanism remains the same (cavity nucleation and growth) and the tertiary creep appears late in life when creep cavities link [229]. The time to failure is predicted by using the minimum strain rate

obtained with the Wilshire model; *M* and *m* are derived from literature or short-term (miniature) creep tests for low alloy ferritic steels [66]. In contrast, the behaviour of creep strength enhanced ferritic (CSEF) 9–12%Cr steels could potentially not be easily modelled via the Monkman-Grant equation as the tertiary creep appears early in life after about 10% of consumed life when microscopic voids start to emerge [227]. One candidate method to represent the complex behaviour of 9–12% Cr steels after the primary creep could be the Omega model that has already successfully been applied for the estimation of remaining life [6]. In Equation 24, $\dot{\varepsilon_{t0}}$ is replaceable with the minimum strain rate [66] and Ω may be obtained as a single test of service-exposed material by performing strain measurements [51]. The approaches presented so far for CrMoV and 9–12% Cr provide options for improved models that use online data for the prediction of creep life consumption and aim to overcome the current limitations of the Manson-Brown methodology. Their output can be reviewed and correlated with the output from the Failure Forecast Model presented in section 3.3.1 by interrogation of periodic or intermittent site inspection data. Ideally, permanently installed strain sensors would facilitate frequent measurements of component creep strain and strain rate which could be compared with the response from predictive online models allowing a periodic and more objective feedback on the real components conditions [225]. However, experience has shown that the cost-benefit of installing strain gauges at multiple locations in operational plant is hard to justify [9]. Hence, the use of measured strain may at this juncture only realistically be achieved by improving passive strain measurements captured during an outage, typically with the component strain captured at the same location as other data such as hardness and surface replicas.

3.3.3 Life assessment transfer function

Figure 35 illustrates the intended arrangement of the LATF with respect to monitored data and the advice required by the end user. The LATF filters, harmonises and arranges the continuous online data and periodic data obtained from an outage inspection into a suitable format for assessment in the material model. The monitor data identified in Figure 35 is comprised of on-load, off-load and miniature specimen test data, illustrated in Figure 26.

The LATF and material model are necessarily closely aligned, and in this respect the ‘material model’ may by necessity comprise more than one model working either

independently or in conjunction and being activated once sufficient monitor data of the right type has been accumulated.

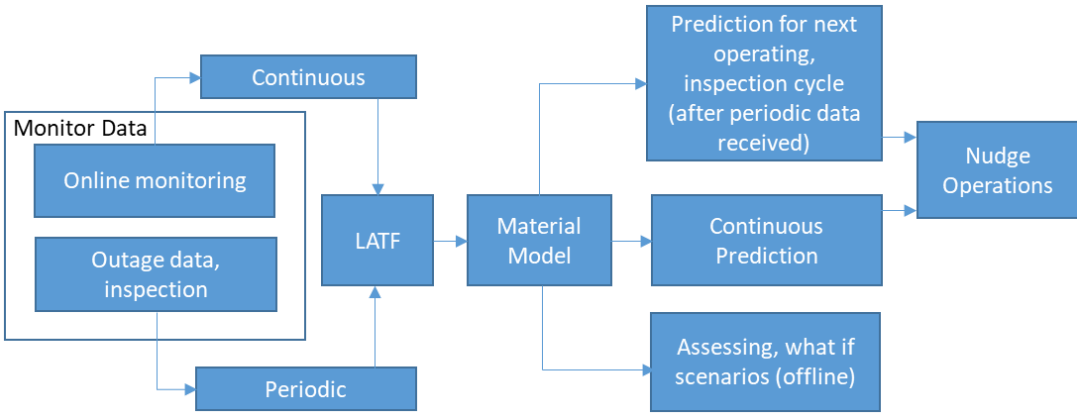

Figure 35: Arrangement of the LATF with respect to monitor data and plant operations

Recent examples of LATF's, to assess fatigue damage on high temperature material, have been developed by re-constructing the stress-time history from steam pressure and temperature sensors installed on complex steam headers [230]. However, the structure of these latest LATF's has not yet been developed sufficiently to accommodate the use of periodic outage data. The challenge in the model proposed in this chapter is to include some of the other routine monitor data, such as surface hardness, creep replicas and strain measurements, accounting for important characteristics such as rate of change, in a predictive life model, which is subsequently coupled to the LATF.

In this regard, the flowchart in Figure 36 has been developed to clarify the process of the proposed lifing approach. Three estimated lives *L1*, *L2* and *L3* are highlighted. *L1* refers to the predicted component life using the current industrial procedure; however, it is recognised that due to its conservatism, a new approach that combines more material specific creep models together with inspection data is required. *L2* will be the new calculated remaining life with the prediction based on an improved material model. However, the *L*2 life prediction can be further refined using collected site inspection data; hence allowing the estimation of *L3*. Figure 36 shows that refined life estimates using site inspection data could require the use of a range of parameters, with strain, hardness and replicas being strong candidates.

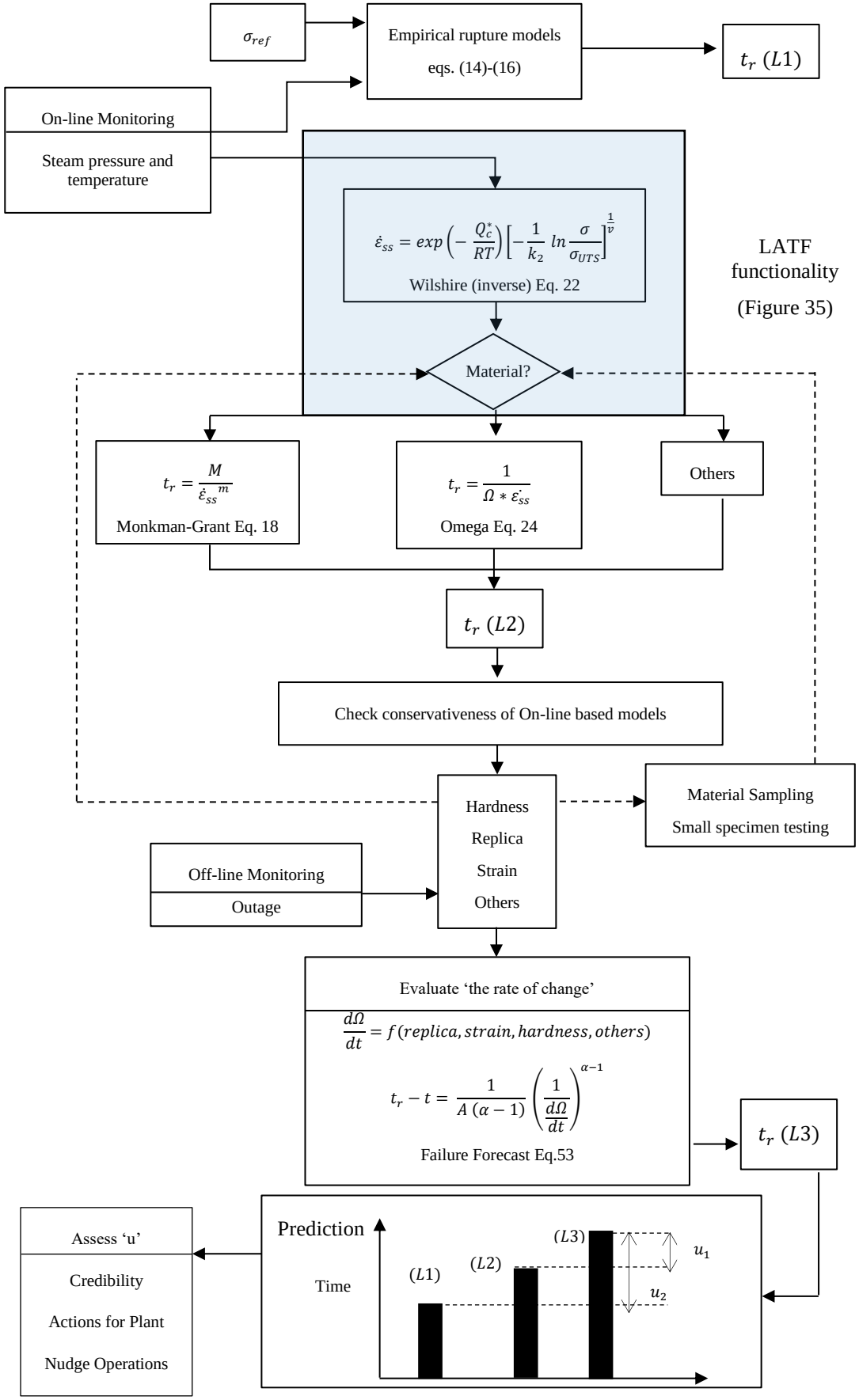

Figure 36: Flowchart of the proposed lifing approach

3.3.4 Case demonstration

To demonstrate the application of the proposed approach, an example is provided for 0.5CrMoV (CrMoV) main steam pipework based on in-service operational and inspection data obtained from an EDF Energy conventional fossil-fired power plant.

The example follows the flowchart in Figure 36 and estimated values for *L1, L2* and *L3* remaining life are provided. This example is explained using the current approach for condition assessment, exploiting real inspection data and with comments on the uncertainties and hence the requirements to adopt the new approach. Section 3.2.1 describes complimentary information regarding outage inspection trends obtained from larger samples of inspection data on operating plants.

A statutory outage was conducted in 2009 on one of the Units, having operated for 242,536 h and 3,552 starts. In accordance with industrial practice for plant of this age [231], both on-line (temperature, pressure) and off-line (surface hardness, metallurgical replication and strain measurements) monitoring was performed.

The pipework in this example was originally installed in 1968 and removed from service in 2009 due to moderate levels of creep damage on the surface, identified with replicas. The main steam line creep effective temperature (CET) calculated from operating temperatures is 563 °C, at an operating pressure of 173.8 bar, and this is consistent with similar periodic assessments dating back a further 15 years. The main steam line dimensions are 342 mm outer diameter with a wall thickness of 60 mm. Two straight pipe sections removed from the same main steam pipe, 'MS_Straight_A' and 'MS_Straight_B', were additionally subjected to extensive through-wall creep damage mapping. Interestingly, the results showed a general trend of the creep damage level decaying with increasing distance from the outer surface towards the pipe bore (Figure 37 for MS_Straight_B) [12].

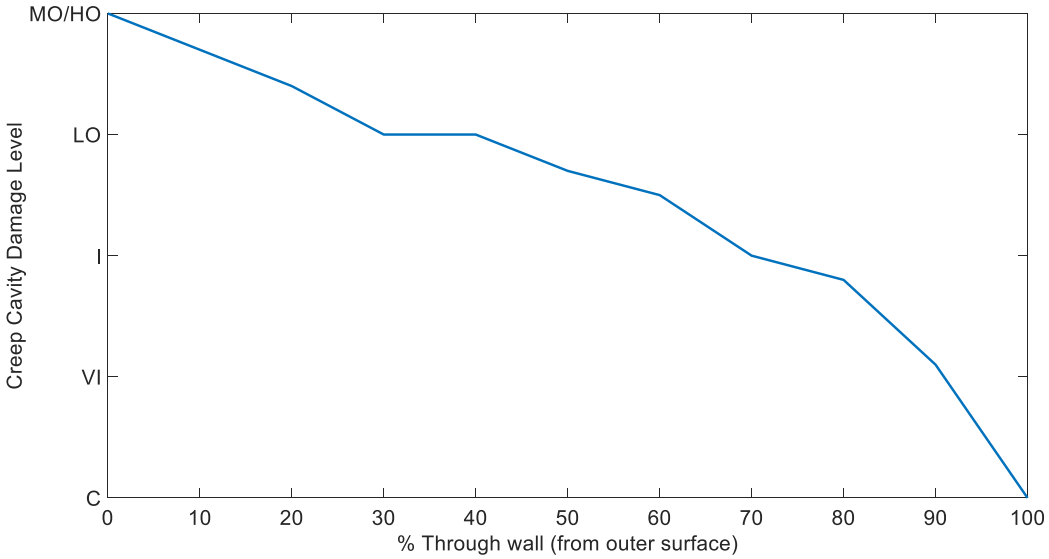

Figure 37: Through-wall Creep Cavity Damage Distribution for MS_Straight_B [12]

The results in Figure 37 are from one through-section examination and show only modest creep cavitation through the bulk of the pipe section at the time of removal, suggesting some useful remaining residual life in the main steam pipe. This pipe section was 2 m long and in addition to more general surface mapping, other through section examinations were undertaken, showing similar or reduced levels of creep cavitation. These observations are supported by separate ex-service assessments of similar pedigree CrMoV pipework [214]. These findings illustrate the conservative nature of current lifing procedures based on separate assessments of surface inspection data and on-line monitoring (Manson-Brown equation). The creep rupture life calculated with the traditional Manson-Brown Equation 17 is 158 khrs (Table 7), which is a lower bound estimate of residual life, and corresponds to *L1* in the flowchart of Figure 36.

The fitting constants $p_0 \ldots p_7$ for the Manson-Brown Equation 17 are taken from Ref. [13] and $\sigma = 1.25\sigma_{ref}$ providing the lower bound estimate of residual life, where σ_{ref} is the mean diameter hoop stress equal to 40.8 MPa at operating pressure. It is worth emphasising that 158 khrs is a minimum value used in the plant units for inspection scheduling but the mean estimate is 223 khrs. These figures are significantly lower than actual operation (242,536 hrs) at the time when the pipe was retired from service. Predictions using the Manson-Brown equation are one of the practical measures used

to help schedule physical plant inspections for creep damage. The new framework aims to use more advanced creep life models, integrated with off-line condition monitoring data, to give an improved estimate of remaining life. Surface hardness, replication, strain measurement and temperature monitoring will be used in conjunction to improve ranking of the susceptibility of components to creep damage and improve estimates of residual life.

As explained in Section 3.3.2, an estimate of the minimum creep strain rate $\dot{\varepsilon}_{ss}$ is obtained with the Wilshire Equation 22 and the corresponding value is 4.96×10^{-8} h^{-1}. The time to failure is then predicted with the Monkman-Grant Equation 18 because of the prolonged secondary creep stage shown by CrMoV steels. The estimated rupture life is 262 khrs (Table 7) (*L2* in flowchart Figure 36). The values of σ_{UTS}, k_2 and v for Wilshire equation are taken from the available literature [232, 233], m and M for Monkman-Grant from CEGB report [234] and reported in Table 5.

Table 5: Wilshire and Monkman-Grant constants

σ_{UTS} [MPa]	k_2	v	m	M
305	16.239	-0.132	1	0.013

Sufficient strain measurements were collected from the main steam pipe from the 2009 outage and preceding outage periods to allow a strain rate based assessment [233]. The average creep strain rate value calculated from diametral strain measurements across pipe creep pips on steam leg B1 and reported in Table 6. This strain rate is typical for straight pipe sections of this service age and plant design. In practice, strain rates are evaluated by comparing strain measurements over different sample operating periods, hence allowing trends to be established and enabling use of the Failure Forecast Method based on strain rate as the leading parameter in this case.

Table 6: Main steam pipe B1, leg creep strain rate measurements over the period 2005-2009 (21,737 hrs)

Steam Leg	**Boiler Level**	**Creep Strain Rate ($\times 10^{-8}\ h^{-1}$)**
B1	100’	3.173

The total creep life projection using the inspection creep strain rate from Table 6 has been calculated by the plant operator as 371 khrs (Table 7) [235] and corresponds to *L3* in the flowchart (Figure 36) where α was set equal to 2 and $1/A$ is a constant based on experience equal to 0.012. Interestingly, both *L2* and *L3* predict a failure life higher than the calculated Manson-Brown lower bound (and mean) life estimate, emphasising once again its conservatism. To put this into context; the difference in life prediction between *L2* and *L3* in Table 7 is equivalent to around 16 years of heavy base load operation.

Table 7: Rupture life estimation

***L1* [khrs]**	***L2* [khrs]**	***L3* [khrs]**
158	262	371

Another practical way to apply the Failure Forecast Method would be to use the collected surface hardness data, which has now become part of standard inspection practice, and estimate the failure life based on the rate of change in hardness from successive outage inspections. The variation of hardness is seen as an indirect indication of damage, which is easier and more convenient to measure during inspections than surface replicas. The bulk hardness trend data illustrated in Figure 29 from successive outages is encouraging.

At present, however, there is a lack of extensive repeated hardness and replica data from the same location on plant. For example, Table 8 shows a sample of typical site outage data collected from main steam legs B1 and B2 from one unit. This illustrates reality, where initial site practice resulted in data being captured on the basis of a broad sampling approach. Hence at this juncture, a robust demonstration for the estimation of rupture life with the Failure Forecast Method based on captured plant data and

applied to change in hardness at specific locations is limited. It should be noted that the bulk outage sample data presented in Figure 29 and Figure 30 illustrate the general change in surface replica and hardness data and this full dataset, which also include where available additional reference to operating conditions, stress and configuration (parent or weld, manufacture), has been developed and interrogated for the first time in the work reported in Chapter 5.

Table 8: Site survey data sample from the 2009 inspection, showing instances of repeat surface inspections at the same location on the component

Location	Reference	Year Tested	Hardness [HV]	Replica
Main Steam LEG B1	SM54 Straight	2005	133	Clear
		2009	Not Available	Low Orientated
	SM57 Bend Extrados	1997	Not Available	Very Isolated
		2009	138	Orientated
Main Steam LEG B2	SM8 Straight	2005	144	Orientated
		2009	134	High Orientated
	SM38 Straight	2005	Not Available	Very Isolated
		2009	133	Low Orientated
	SM41 Straight	2005	137	Isolated
		2009	136	Isolated

3.4 Concluding remarks

This chapter has focused on defining the requirements for adopting a new condition monitoring based approach to help to address the severe challenges imposed by the economic transition to a low carbon future. As the plant ages the current inspection-

based assessment approach becomes increasingly uneconomic and examination of components retired from service on this basis has concluded they have been retired too early [214, 221].

The current inspection-based assessment approach should be supplemented with advanced condition monitoring and improved use of predictive techniques to influence future plant operation and inspection scope. Importantly, this requires the use and integration of both online and offline (outage) inspection data, which typically plants have in abundance, but have insufficient time or tools at their disposal to exploit.

The new proposed condition monitoring approach combines a predictive model that uses online information coupled with site inspection data, typically associated with surface metallurgy (hardness and replication) and strain measurements. The use of a LATF is necessary to enable the material model to communicate efficiently with quite disparate sets of monitor data. Examples of the LATF approach have recently been developed and demonstrated [230] and there is sufficient in-service data available to support the development of what the authors describe as 'hybrid' creep life models, incorporating parameters based on in-service monitor data. Larger samples of outage inspection data and trends are shown in Figure 29 and Figure 30.

A case study example has been provided that illustrates the current assessment approach, its limitations and potential improvements based on the proposed new approach outlined in Figure 36. At this juncture, an estimation of rupture life from change in surface hardness and replicas over time is limited due to the lack of extensive repeated hardness and replica data from the same location on plant. The bulk change in surface hardness and replica categorisation illustrated in Figure 29 and Figure 30 indicates that this location specific change should be detectable. Current inspection practice has become more prescriptive over time and with more control ensuring consistent locations for both surface hardness and replica measurements, which will support the use of this approach. The structure of the LATF and material models outlined in Figure 35 and Figure 36 would also facilitate the application of appropriate multiaxial creep lifing models based on modification of existing methods [230].

In the new life assessment approach, the output from online (continuous) models is reviewed against the prediction from an outage inspection data based (periodic) model

to arrive at a more balanced view of the condition of the asset and hence define a more practical strategy that supports the plant operator. It may be possible for example to incorporate this periodic inspection data [77] into the online life assessment model.

The use of periodic inspection data acquired during an outage inspection will most likely utilize the concept of 'rate of change' (e.g. of hardness or other suitable parameters) to give an alternative prediction of the failure time. For example, the 'rate of change' in surface hardness reflects microstructural evolution and will inevitably prompt more consideration of run-repair-replace options. An effective model will permit the user to proactively assess the sensitivity to a) material properties, b) operational conditions and c) construction/geometry, thereby nudging the plant operator to action the most effective mitigations.

The key objective is to use the improved predictive capabilities to 'nudge' the plant to a better operating state, e.g. by a change in operation, undertaking a range of specific and targeted inspections, repairs or changing a component of concern at the right time to accommodate logistical issues.

4 Development of a new lifing method based on R5 and viscoplasticity modelling and its application to turbine rotor under thermomechanical loading

4.1 Introduction

The drive towards sustainability has led modern industrial plants, typically in the petrochemical and in the energy industries, to operate under extreme temperatures and pressures as well as to experience more frequent start-up and shut-down operations. Future designs of ultra-supercritical power plants aim to operate at temperatures up to 760 °C and pressures of 350 bar [236]. Furthermore, the changing nature of the electricity market, along with the significant addition of renewables in the grid, has forced power plants to become more 'flexible' in their operations, with a transition from base-load to intermittent modes of operation. These extreme operating conditions subject plant to time-dependent creep deformation due to elevated temperatures and pressures, as well as Low Cycle Fatigue (LCF) due to more frequent mechanical and temperature cyclic loadings. The combination of these two modes of failure (known as creep-fatigue interaction) can significantly reduce the safe, in-service life of components. The occurrence of LCF behaviour, especially on structures operating inside the creep regime can significantly accelerate their long-term deterioration and encourage crack nucleation and propagation, resulting in an early failure. Dundas also suggested that over 62% of the total damage costs of gas turbines involve cycle cooling, fatigue, creep and surge related failures [237]. Therefore, the failure of components due to the combined effects of creep and fatigue becomes a critical issue and of considerable interest to investigators for both design and in-service life assessment [238, 239]. Knowledge concerning the long-term behaviour of materials under such extreme conditions is required for the appropriate fail-safe design decisions. Accurate deformation, damage evolution and rupture life prediction

information could also result in economic and effective maintenance by appropriately scheduling inspection, maintenance and repair time periods, mitigating the risk of unexpected shut downs.

Great efforts have been made to investigate the response of materials subjected to cyclic loading conditions. As reported in the literature, most of the early material models were based on the Coffin-Manson and Basquin laws which describe the fatigue (elastic-plastic) behaviour of materials [240]. These models have been commonly used in industry due to their simplicity and accuracy in describing the material deformation at low temperature [241, 242]. Subsequently, many damage models were developed to predict the life of structures under variable temperature and loading conditions [243-245]. At high temperatures, the materials exhibit also creep (viscous) behaviour in the plastic region [246]. Thus, using a simple elastic-plastic model to reproduce the non-linear viscoplastic response of materials can result in poor predictions, especially during high temperature, cyclic loading. Instead, viscoplasticity models are needed for analysing creep and fatigue behaviour.

The Chaboche constitutive viscoplastic model is commonly employed for this purpose (section 2.2.3). Chaboche proposed a phenomenologically-based unified model which combined isotropic and kinematic hardening variables in a viscoplasticity-flow rule, taking into account cyclic hardening/softening and the Bauschinger effect [137]. The model has been used extensively by many authors to study the responses of materials under creep-fatigue conditions and shows a good agreement with the experimental results [126, 168, 247]. For the purpose of life assessment, creep-fatigue life prediction approaches generally involve the calculation of creep damage and fatigue damage separately. The rupture time or the number of cycles to failure can be then evaluated by combining both damage values using a linear interaction rule. A common approach to calculate creep damage is by using a time-fraction rule. This approach was also adopted in the life assessment procedure of the American Society of Mechanical Engineers (ASME) as well as in the French RCC-MR Codes [248, 249]. However, it was observed that the predicted results when the time-fraction rule was used differed in each code [157, 250]. The variation in the results is due to several detailed differences between the codes regarding the safety factors on creep rupture curves and the interaction rules used to combine the creep and the fatigue damage. Instead of

using a time-fraction rule, an alternative approach is to consider the ductility exhaustion method to be more capable of accurately predicting the material life. The ductility exhaustion approach has been adopted and further developed in the British R5 assessment procedure [250, 251]. The R5 life assessment procedure is currently used to assess plant integrity within the UK power generation industry and it involves numerous steps for the determination of required parameters, such as the stress relaxation per cycle and the elastic follow-up factor. The main objective of the present investigation is to develop a clear guideline and a framework to be used for the life assessment of structures subjected to thermomechanical loadings. This involves the possibility of linking the Chaboche constitutive viscoplasticity model with the R5 assessment procedure with the aim to allow more accurate life estimations and to simply the lifing assessment procedure. This integrated lifing model is applied to an industrial gas turbine rotor made from FV566 martensitic steel (12% Cr steel, see section 2.3.2), a common material used in high temperature applications [252] and the effectiveness of the new lifing procedure is demonstrated.

4.2 Methodology

The constitutive Chaboche viscoplasticity model is implemented in the ABAQUS FE software using the user-defined material sub-routine UMAT to perform the stress analysis of the turbine rotor, the details of which are given in Section 4.4. The UMAT is a Fortran-coded sub-routine and is an alternative for the user to code the material constitutive behaviour when those in the ABAQUS material libraries are not judged to be sufficient. The UMAT code was already developed by former colleagues at the University of Nottingham and is publicly available [141]. The UMAT subroutine was developed to allow the cyclic plasticity behaviour to be predicted in the ABAQUS FE software using the Newton-Raphson method to solve the nonlinear problems (see Section 4.2.1.2).

The model has the ability to describe the plastic deformation as well as the viscous behaviour of the material, so that accurate stress-strain predictions can be obtained. Additionally, important parameters required for the R5 life assessment procedure such as the stress relaxation per cycle and the elastic-follow up factor can be obtained

directly from the model, avoiding several complicated steps of the R5 procedure. A flowchart of the integrated life assessment procedure developed is shown in Figure 38.

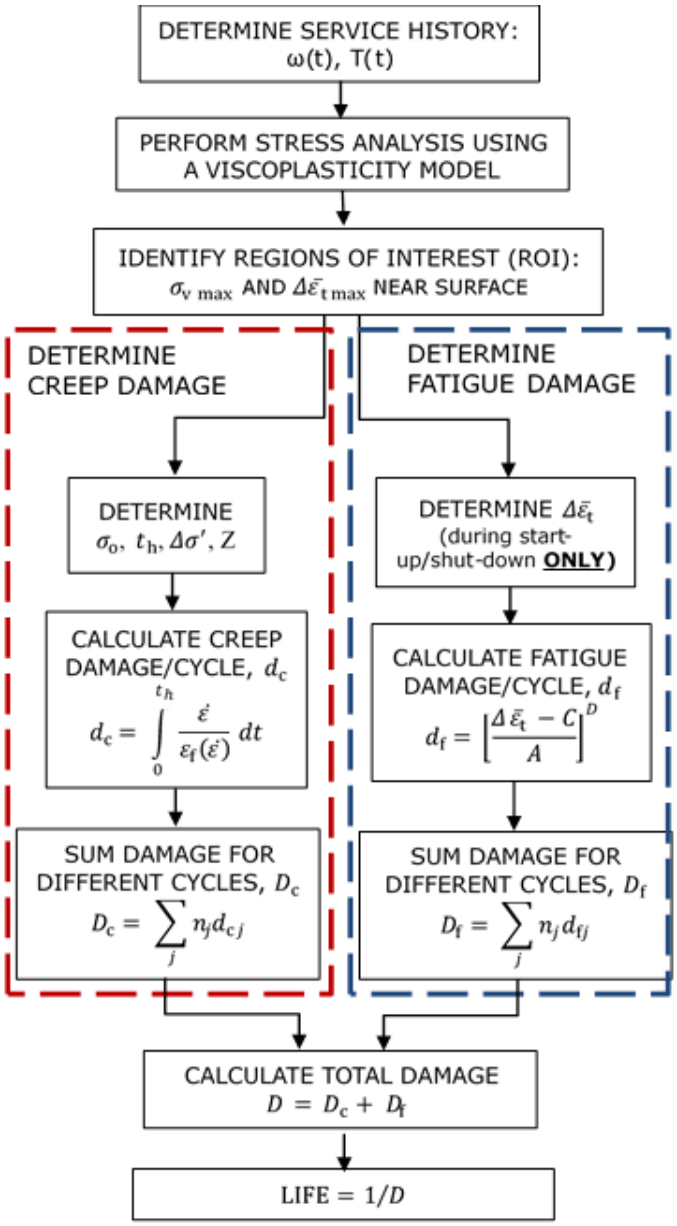

Figure 38: The process flowchart of the integrated lifing model developed

4.2.1 Unified viscoplasticity modelling

4.2.1.1 Constitutive equations

In the Chaboche unified constitutive model, the rate-dependent inelastic strain is used to represent both creep (viscous) and plastic strains [137]. This inelastic strain rate tensor $\dot{\boldsymbol{\varepsilon}}_{\mathbf{p}}$ is defined by the following equation:

$$\dot{\boldsymbol{\varepsilon}}_{\mathbf{p}} = \langle \frac{f}{Z_1} \rangle^n \; sgn(\boldsymbol{\sigma} - \boldsymbol{\chi}) \tag{55}$$

where f is a yield function which determines the elastic limit, n and Z_1 are material parameters which describe the evolution of viscous stress, $\boldsymbol{\sigma}$ is the total stress tensor and $\boldsymbol{\chi}$, the kinematic hardening tensor, also known as back stress, responsible for the cyclic loading and changes due to inelastic loading. The accumulated viscoplastic strain rate is defined by:

$$\dot{p} = |\dot{\boldsymbol{\varepsilon}}_{\mathbf{p}}| \tag{56}$$

The yield function for the model can be expressed as:

$$f = \; |\boldsymbol{\sigma} - \boldsymbol{\chi}| - R - k \tag{57}$$

where R is the isotropic hardening parameter, also known as drag stress. The elastic domain is defined by $f \leq 0$ and the inelastic domain is defined by $f > 0$. The evolution of R and χ_i values are controlled by the following equations. The isotropic hardening (drag stress) evolution $\dot{R}$ is represented by:

$$\dot{R} = b(Q - R)\dot{p} \tag{58}$$

where b determines how quickly the drag stress is stabilised, Q is a stabilised value of drag stress after a specific accumulation of plastic strain and $\dot{p}$ is the accumulated plastic strain rate. The kinematic hardening (back stress) evolution, $\dot{\boldsymbol{\chi}}$ is represented by:

$$\dot{\chi}_\iota = \; C_i(a_i \dot{\varepsilon}_{\mathrm{p}} \; - \; \chi_\iota \dot{p}) \tag{59}$$

$$\chi = \sum_{\iota}^{M} \chi_i \tag{60}$$

where a_i and C_i $(i = 1, 2)$ are temperature-dependent material constants, similar to Q and b. χ_i is part of the total back stress. The viscous stress can be expressed as:

$$\sigma_{\mathrm{v}} = Z_1 \dot{p}^{1/n} \tag{61}$$

and finally the total stress can be aggregated as:

$$\boldsymbol{\sigma} = \boldsymbol{\chi} + (R + k + \sigma_{\mathrm{v}})\, sgn(\boldsymbol{\sigma} - \boldsymbol{\chi}) = E(\boldsymbol{\varepsilon} - \boldsymbol{\varepsilon}_{\mathbf{p}}) \tag{62}$$

The constants of the viscoplasticity model are calibrated from isothermal fatigue and stress relaxation experiments on FV566 martensitic steel [253].

4.2.1.2 UMAT implementation

A UMAT subroutine has been developed to numerically implement the unified viscoplasticity model through the returning mapping algorithm [126]. The purpose of the subroutine is to update the stress tensor and the other relevant quantities (inelastic strain and both hardenings) at the end of a time increment by updating the accumulated plastic strain increment Δp upon which all model variables are dependent. The algorithm is composed of the elastic prediction and the inelastic correction steps.

In the elastic prediction step, there is no change of the internal variables (inelastic strain, isotropic and kinematic hardening) with only the total strain evolving. The material behaviour is thus considered fully elastic and the initial guess of the stress is determined directly by the elastic deformation. In the inelastic correction step, the stress value is corrected by allowing the internal variables to evolve while the total strain is fixed. The Newton-Raphson iteration method is used in this step to solve for the accumulated plastic strain Δp over the specified time increment (i.e. t_2-t_1) by minimising the viscoplastic residue Φ [253].

$$\Phi = \Delta p - \left(\frac{f}{Z}\right)^n \tag{63}$$

The viscoplastic residue is derived from the Hooke's law and the viscoplasticity model.

Equation 64 is solved with the Newton-Raphson iteration method resulting in [134]:

$$\Phi + \frac{\partial \Phi}{\partial \Delta p}\delta \Delta p + \frac{\partial \Phi}{\partial R}\delta R + \frac{\partial \Phi}{\partial \chi_i}\delta \chi_i = 0 \tag{64}$$

In this context, the symbol Δ identifies the change over the specified time increment with δ being the Newton-Raphson increment.

After the evaluation of the partial derivatives in Equation 64 and rearrangement, the Newton-Raphson increment of the accumulated plastic strain time increment $\delta\Delta p$ is obtained.

The accumulated plastic strain time increment Δp is finally updated by:

$$\Delta p = \Delta p + \delta\Delta p \tag{65}$$

The iterative scheme ends when convergence is achieved ($|\Phi|$ less than a tolerance). The inelastic strain time increment $\Delta\varepsilon_{\mathrm{p}}$ is determined from Equations 55 and 56. The stress increment is finally given as:

$$\boldsymbol{\Delta\sigma} = E(\Delta\boldsymbol{\varepsilon} - \boldsymbol{\Delta\varepsilon_{\mathrm{p}}}) \tag{66}$$

Extensive validation of the model has been performed and its capability to simulate hysteresis loops from experimental data has been checked. Isothermal hold-time low cycle fatigue tests have been conducted in the temperature range from 400 to 600°C for FV566 [126, 253] and on P91-P92 steels [254-256]. The stress-strain material response from the model and the experiments have been compared and a good agreement has been found [253]. Particularly, an example with stress relaxation is shown in Figure 39 for P92 tested at 600°C with a ±0.5% strain amplitude. The capability of the unified viscoplasticity model has shown to give a sufficiently accurate prediction for the stress-time curve [256] (see Figure 39) .

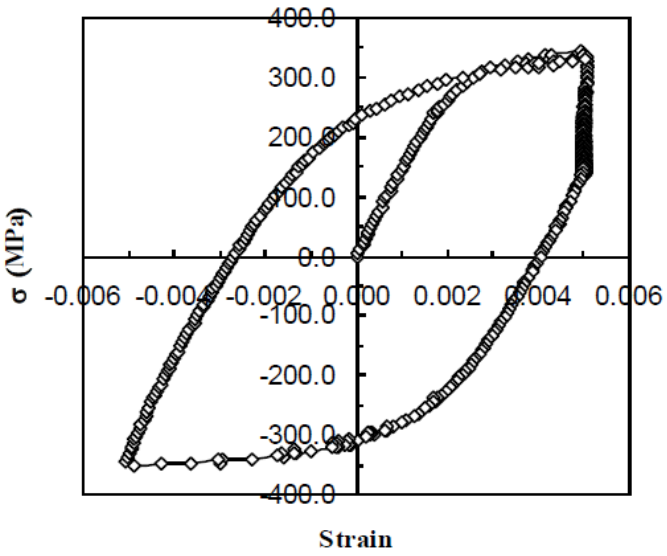

(a)

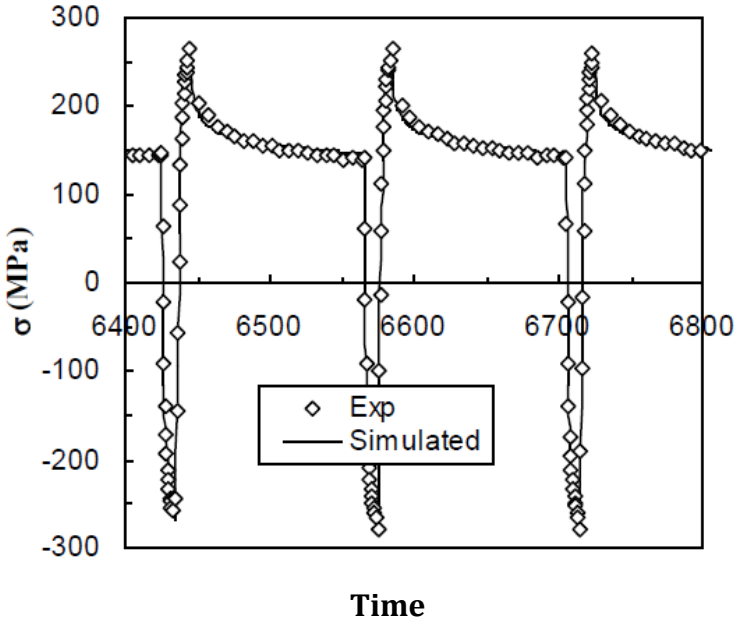

(b)

Figure 39: Results for P92 at 600°C and ±0.5% strain amplitude (a) experimental stress-strain hysteresis loop (b) experimental and model stress-time curves comparison [256]

4.3 Development of a new integrated life assessment procedure

Linking the viscoplasticity model with the R5 code, a novel integrated life assessment procedure is developed. The procedure consists of 6 steps which are described in the following sub-sections.

4.3.1 Resolution of the load history into different service cycles

The complete cyclic load history experienced by the component needs to be determined. A service cycle is defined as a repeated sequence of operation, where the initial and final loading and temperature states are the same. In most cases, raw data includes fluctuations which lead to the formation of small cycles inside a larger cycle. In this case, for simplicity, the small cycles can be superposed and form a unique cycle with a dwell. In cases where the cycles are of different loading magnitudes and also involve an associated dwell period, they are grouped accordingly to different cycle types. The actual load history can be then simplified and divided into distinct cyclic events or service cycles, each involving an associated cyclic load, a constant load during the dwell period and the associated temperature of the dwell. This resolves the actual load history into a well-defined number of different service cycles. A graphical representation of the procedure is presented in Figure 40.

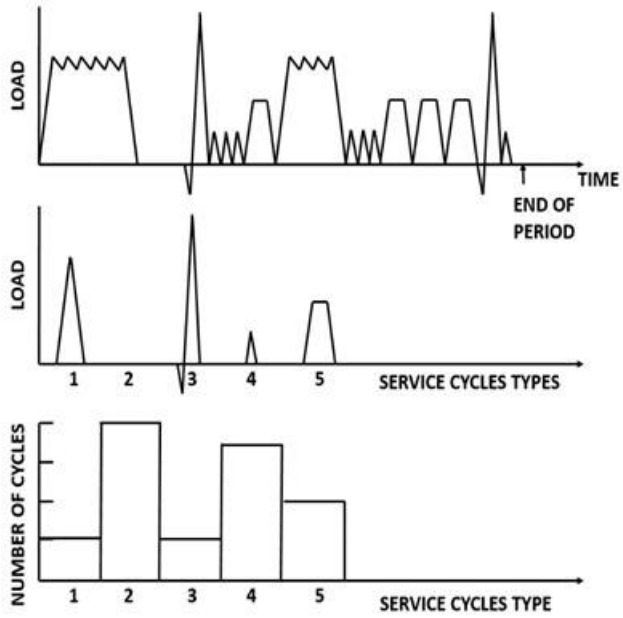

Figure 40: Resolution of loading history into different service cycles types

4.3.2 Stress analysis using a viscoplasticity material model

This step requires stress analysis to be performed on each different service cycle. The stress analysis should model the overall mechanical responses of the component. During the stress analysis, the main regions of interest have to be identified. These include:

(i) locations where the maximum von Mises stresses exist, usually near the surface of the geometry;

(ii) locations where the maximum total equivalent strain range occurs during the cycle, again usually near the surface and

(iii) the hottest locations where creep is significant.

These locations are considered to be the most damaging positions in the rotor, which are most likely to experience crack initiation eventually leading to failure. The accuracy of any stress analysis is always dependent on the ability of the material model and the associated material properties used to reproduce the cyclic responses of the material.

4.3.3 Construction of cyclic deformation loops

Results from the stress analysis can provide the necessary data to construct the cyclic deformation stress-strain loops for each of the different locations selected from the previous step and also for each of the different service cycles. The expected loop should not be closed but should include an increment of strain which is accumulated at each cycle. This accumulation of strain can be an effect of forward creep deformation due to the primary load or elastic follow-up. A typical cyclic deformation loop can be seen in Figure 41. From each of the stress-stain loops constructed, important information can be extracted that will be used in later steps of the life assessment. These include: i) the total cyclic strain range, $\Delta\varepsilon_t$, ii) the position of the dwell which can be characterized from the stress at the start of the dwell σ_o and the duration of the dwell t_h allowing the user to determine the stress relaxation $\Delta\sigma'$ due to the dwell for the cycle and iii) the elastic follow-up parameter, Z.

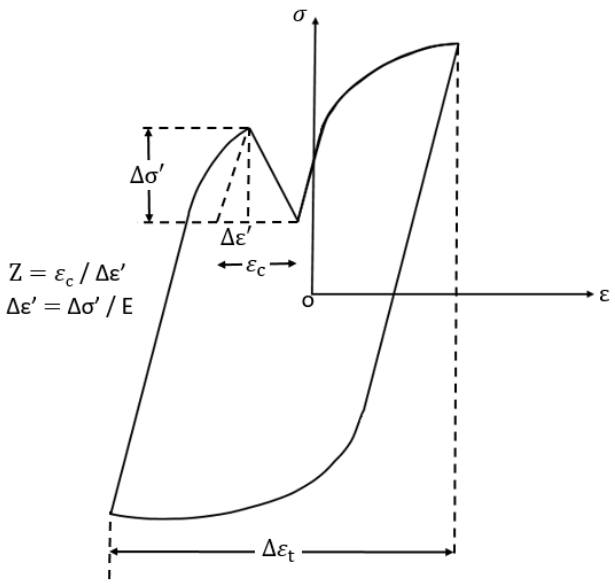

Figure 41: Schematic of the cyclic deformation loop

4.3.4 Fatigue damage calculation

The fatigue damage associated with each service cycle can be evaluated using the endurance curve approach. This approach requires a complete cyclic endurance data set of the material tested. These data can be usually obtained from simple specimen testing under uniaxial tensile control. The endurance curve can be expressed as:

$$N_{\mathrm{f}} = \left[\frac{A_3}{\Delta\bar{\varepsilon}_{\mathrm{t\,max}} - C}\right]^{D} \tag{67}$$

where A_3, C and D are material constants obtained by fitting, N_{f} is the number of cycles to failure and $\Delta\bar{\varepsilon}_{\mathrm{t\,max}}$ is the maximum equivalent total strain range during the start-up and shut-down operations of the cycle, excluding the dwell region as it is assumed that dwell contributes to creep damage only.

First, it is necessary to calculate the change of each strain component ε_{ij} between time t and t' inside the service cycle. For example, the strain range in the 11-direction is given by:

$$\varepsilon_{11}(t,t') = \varepsilon_{11}(t) - \varepsilon_{11}(t') \tag{68}$$

and more generally,

$$\varepsilon_{ij}(t,t') = \varepsilon_{ij}(t) - \varepsilon_{ij}(t') \qquad \forall \text{ i, j} \tag{69}$$

The equivalent strain range, $\bar{\varepsilon}(t,t')$ can be obtained from the components $\varepsilon_{ij}(t,t')$ by the following formula:

$$\begin{aligned}\bar{\varepsilon}(t,t') = \frac{\sqrt{2}}{3}\{&[\varepsilon_{11}(t,t') - \varepsilon_{22}(t,t')]^2 + [\varepsilon_{22}(t,t') - \varepsilon_{33}(t,t')]^2 \\ &+ [\varepsilon_{33}(t,t') - \varepsilon_{11}(t,t')]^2 \\ &+ 6[\varepsilon_{12}^2(t,t') + \varepsilon_{23}^2(t,t') + \varepsilon_{31}^2(t,t')]\}^{1/2}\end{aligned} \tag{70}$$

The strain range obtained with the highest value is considered to be the maximum equivalent total strain range value, $\Delta\bar{\varepsilon}_{\mathrm{t\,max}}$, in the cycle. This should be then converted into a percentage and used in the endurance equation to calculate the number of cycles to failure, N_{f}. The fatigue damage for each cycle d_{f} is defined as $1/N_{\mathrm{f}}$, the inverse of the number of cycles to failure.

4.3.5 Creep damage calculation

The creep damage associated with each service cycle can be evaluated using the ductility exhaustion approach. The creep damage per cycle, d_{c}, can be obtained by dividing the inelastic creep strain rate during the dwell period, t_{h}, by an appropriate

ductility value estimated with empirical expressions [158]. The ductility exhaustion approach involves the inelastic strain rate, the elastic follow-up as well as the dwell period and can be evaluated by:

$$d_c = \int_0^{t_h} \frac{\dot{\varepsilon}_c}{\varepsilon_{\mathrm{r}}(\dot{\varepsilon}_c)}\, dt \tag{71}$$

where $\dot{\varepsilon}_c$ is the instantaneous inelastic strain rate during the dwell period and $\varepsilon_{\mathrm{r}}(\dot{\varepsilon}_c)$ is the corresponding creep ductility that corresponds to the inelastic strain at failure [158]. During the steady-state period of operation, an inelastic strain is formed by the conversion of the elastic strain when the stress relaxation occurs in conjunction with the forward creep deformation from the primary load. The effect of the combination of the two processes can be defined as the elastic follow-up parameter, Z, and the increment of the inelastic strain for the cycle can be obtained by:

$$\varepsilon_c = -\frac{Z}{E}\, \Delta\sigma' \tag{72}$$

where E is the Young's modulus of the material and $\Delta\sigma'$ is the stress relaxation during the dwell period, t_{h}. Hence, the instantaneous deformation can be expressed as:

$$\dot{\varepsilon}_c = -\frac{Z}{E}\, \frac{\Delta\sigma'}{dt} \tag{73}$$

The creep damage can be then determined by two methods. The first method should be used when the dwell is in the tensile part of the cycle. By assuming that the engineering strain, ε_{R}, is independent of the strain rate and equal to the lower shelf ductility ε_L of the material, Equation 71 may be simplified to:

$$d_c = \frac{Z}{E}\, \frac{\Delta\sigma'}{\varepsilon_L} \tag{74}$$

Similarly, if the dwell is in the compressive part of the cycle, the upper shelf ductility of the material, ε_U, should be used and the creep damage of the cycle can be determined by:

$$d_c = \frac{Z}{E}\frac{\Delta\sigma'}{\varepsilon_U} \tag{75}$$

4.3.6 Total damage calculation

The total damage, D, is predicted to accumulate during the lifetime of the component and can be calculated from the fatigue and creep damage of each service cycle as outlined in the previous steps. The total damage, D, is defined as the linear sum of a fatigue component D_f, and a creep component, D_c. It is assumed that failure occurs when D reaches 1 as shown in Figure 42.

$$D = D_\mathrm{f} + D_\mathrm{c} \tag{76}$$

where,

$$D_\mathrm{f} = \sum_j n_j/N_{\mathrm{f}j} = \sum_j n_j d_{\mathrm{f}j} \tag{77}$$

and,

$$D_\mathrm{c} = \sum_j n_j d_{cj} \tag{78}$$

where n_j is the number of cycles of type j and $N_{\mathrm{f}j}$, $d_{\mathrm{f}j}$ and d_{cj} is the value of N_f, d_f and d_c corresponding to that cycle type.

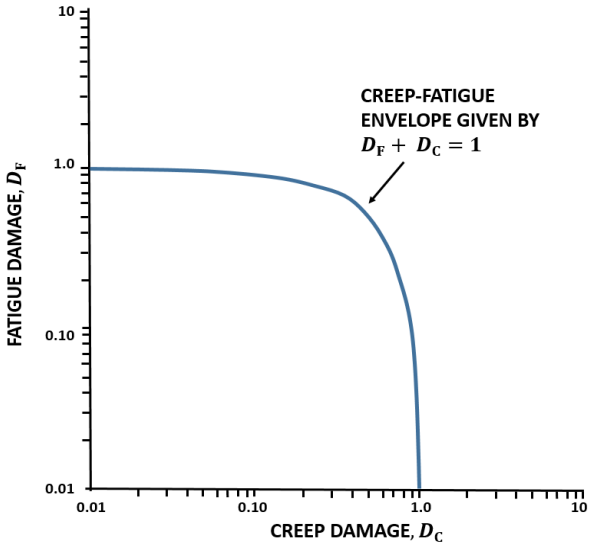

Figure 42: The total damage diagram [158]

4.3.7 Advantages of the new lifing methodology

There is a requirement to speed up the process of stress analysis and the calculations for assessing creep-fatigue damage before crack initiation and it is proposed that the suggested model will achieve that aim. The steps related to the cycling load histories resolution, the stress-strain curves construction and the total damage calculation are the same as in the R5 procedure.

In the R5 procedure, the recourse to simplified elastic stress analysis methods is often necessary to eliminate the impracticability of inelastic computation and repeated analysis for a number of different cycles. In contrast, the viscoplastic constitutive model is considered to be more accurate in modelling the real mechanical response of the component under thermomechanical cyclic loadings.

For the fatigue damage calculation in the R5 procedure, the continuous cycling endurance data are presented in terms of total strain range in order to determine the number of cycles to failure. The total strain range is evaluated with a two steps procedure. Firstly, an equivalent elastic stress and strain range are calculated from the stress history for each type of cycle. Secondly, the strain range calculated elastically from the first step needs to be increased to include any enhancement due to creep and plasticity. In the proposed methodology, the strain components are a direct outputs of

the FE simulation that allow the calculation of the maximum total strain range through Equation 70 in the start and shut-down (as dwell contributes to creep only).

The R5 procedure for creep damage follows a complex approach that requires a description of the stress relaxation behaviour of the material. According to the material under consideration, suitable creep laws are used to define the stress relaxation behaviour. The inelastic strain and strain rate are then obtained from stress relaxation data using the stress at the start of the dwell and the degree of the elastic follow-up parameter during the dwell period. It is usually assumed that Z is constant whereas in practice, Z changes with the stress relaxation. In contrast, in the new methodology, the creep strain as well as the stress relaxation are estimated from the FE analysis. The creep strain is the strain accumulated only over the dwell period and the start-end-of-dwell stresses are used for the calculation of stress relaxation.

4.4 Application of the new lifing model to an industrial gas turbine

The newly-developed life assessment procedure is demonstrated in the analysis of an industrial gas turbine rotor operating under realistic load conditions. The rotor assessed is taken from a 300 MW gas turbine used in a combined-cycle power plant. The rotor itself is made from FV566 martensitic steel and comprises 3 major sections: a 4-stage low pressure turbine (LPT), a single-stage high pressure turbine (HPT) and a 23-stage compressor. The full-geometry of the turbine rotor can be seen in Figure 43.

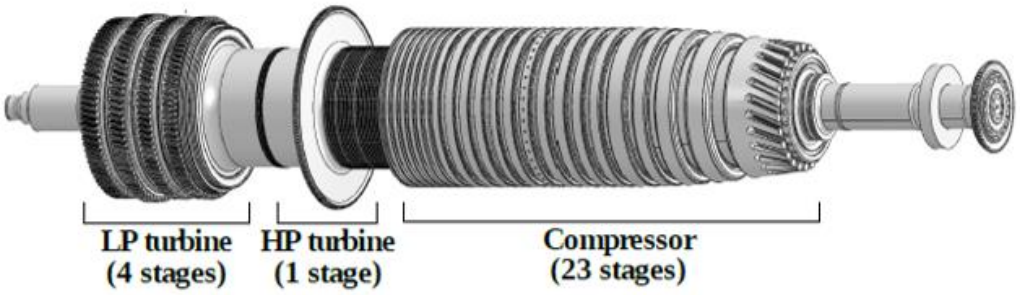

Figure 43: Full geometry of gas turbine rotor [253]

Atmospheric air enters at the compressor side and as it is compressed, it is brought to higher pressure and temperature. Energy is then added using combustion and a very

high-temperature flow is generated. When this gas enters turbine sections, it produces a shaft work output as it expands down to the exhaust pressure [3].

The rotor material behaviour is simulated in ABAQUS FE software using the constitutive Chaboche elasto-viscoplasticity model implemented using the UMAT sub-routine previously described [141]. Taking advantage of the radial symmetry in the geometry of the rotor, the model is built as a 2D axisymmetric problem. The geometry of the rotor used in ABAQUS was originally developed by Rae et al [253]. The material properties used including all material constants required for the UMAT subroutine were obtained from Rae et al [253] (Table 10).

FV566 (X12CrNiMo12-3) is a type of tempered martensitic steel often used in high temperature industrial applications for its high creep and thermal-fatigue strength. The specific chemical composition of FV566 is given in Table 9 [253]. The base FV566 microstructure shows prior austenitic grains (PAGs) that contain one or more packets. Inside the packets, blocks of laths and subgrain regions are identified. An EBSD image of FV566 base material is shown in Figure 44 [173].

Table 9: FV566 martensitic steel chemical composition [253]

Element	**C**	**Si**	**Mn**	**Cr**	**Mo**	**Ni**	**V**	**S**	**Fe**
Weight (%)	0.16	0.038	0.668	11.9	1.68	2.52	0.298	0.0006	Remainder

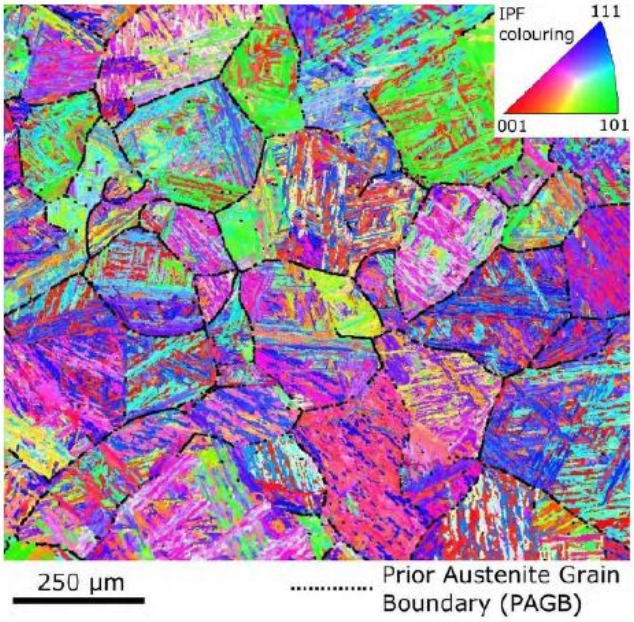

Figure 44: EBSD map of FV566 base material microstructure [173]

The viscoplastic model material properties are determined through a 2 steps process. Initial guess of material parameters are extracted from isothermal uniaxial strain-controlled saw-tooth (SWT) and dwell-type (DWT) tests. Following this, an optimisation procedure is performed with Matlab routine for model validation. The SWT and DWT waveforms together with the specimen geometry used for material parameters identification are depicted in Figure 45 [253].

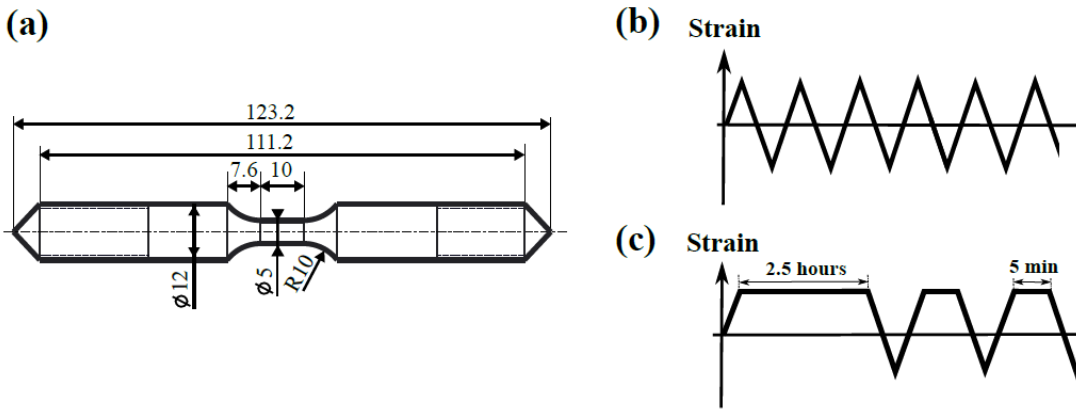

Figure 45: (a) dimensions and geometry of the specimen (measures in mm). Waveforms used for (b) fatigue saw-tooth and (c) creep-fatigue dwell type tests [253]

From experimental tests and the optimisation procedure, the Chaboche material model parameters are found to evolve linearly with the temperature. Their relationship is shown in Table 10 [253].

Table 10: Material parameters evolution with temperature [253]

Mechanical feature	Symbol	Unit	Fitting equation
Elasticity	E	GPa	-0.3726T+322.36
	k	MPa	-1.07T+806.98
Non-linear viscosity	Z	MPa	235.48T-93419
	n	-	-0.02375T+15.322
Kinematic hardening	C_1	-	-0.06525T+52.352
	a_1	MPa	-6.1245T+3989.3
Isotropic hardening	b	-	-0.00505T+4.945
	Q	MPa	-0.1678T-9.0067

4.4.1 Finite Element Model

The rotor FE model geometry and mesh are shown in Figure 46. Finer mesh is used near the surface of the rotor to accurately reproduce heat transfer effects on temperature and stress/strains. An uncoupled thermal-stress FE analysis was conducted to investigate the behaviour of the rotor following these steps:

1. Heat transfer step to determine the temperature distribution during the loading;
2. Thermo-mechanical stress analysis step performed using temperature data from step 1 together with mechanical loads.

The heat transfer step was performed using 8-node quadratic axisymmetric heat transfer quadrilateral elements DCAX8. The stress analysis was performed using 8-

node biquadratic axisymmetric quadrilateral elements. The rotor was simulated as an axisymmetric model exploiting the radial symmetry about its central axis [126, 253].

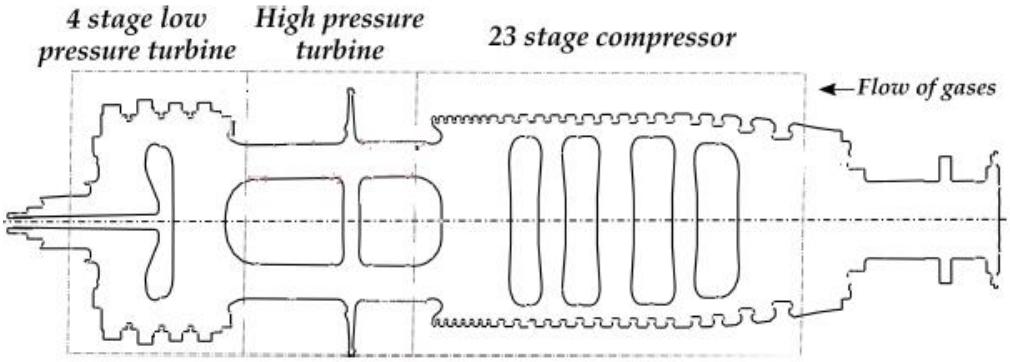

(a)

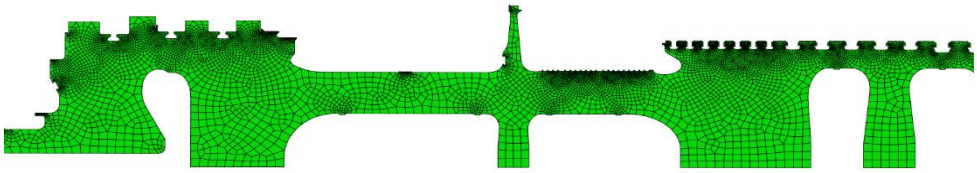

(b)

Figure 46: (a) Cross section of the axisymmetric gas turbine rotor model used in FEA showing major parts and direction of flow of gases, (b) Finite element mesh from a section of the gas turbine rotor [3, 126]

The simulation is taken through 10-cycles of operation. Each cycle represents a typical day (24 hours) for a peaking power plant. This includes a start-up, a dwell period at full load (3,000rpm), a shut-down and finally a dwell period at rest. A load sensitivity study is performed to estimate the variation on the final lifetime prediction with a second simulation at half load. The loading pattern showing the variation of the rotational speed and temperature during the cycles for the base case simulation is shown Figure 47.

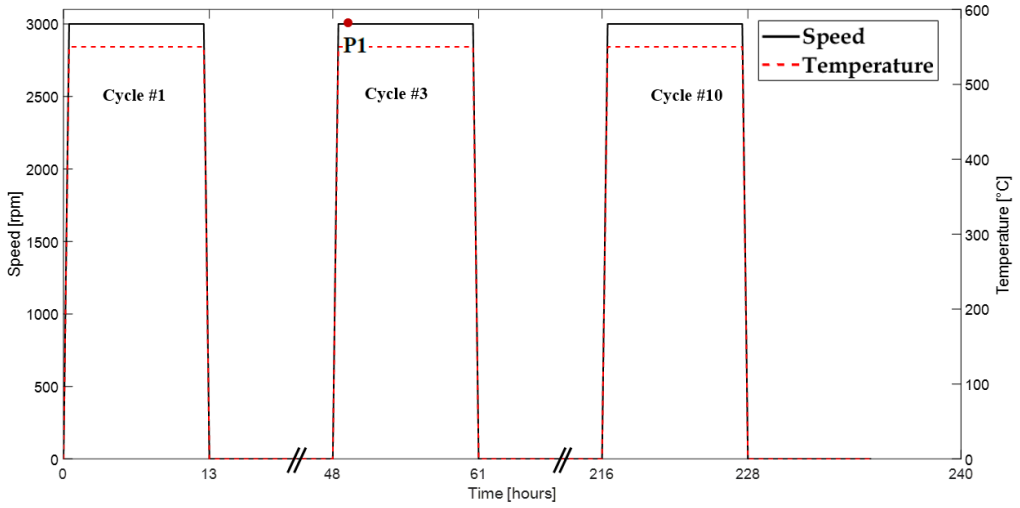

Figure 47: A typical loading patter experienced in a peaking power plant

4.4.2 Thermo-mechanical loading

The temperature distribution along the turbine rotor is non-uniform. This temperature profile has been estimated by the thermal assessment conducted at step 1 of the FE analysis. Gas temperatures along the turbine have been assumed to be equal to the metal surface temperatures. Metal surface temperatures were applied as thermal boundary conditions at each stage within the thermo-mechanical step in the finite element model, together with the corresponding heat transfer coefficients.

During operation, outside ambient air is drawn into the compressor inlet which keeps the rotor temperature relatively low in this region. For a cold start, the inlet air temperature is conservatively assumed to be at 11°C. As the air is compressed, its temperature increases, increasing the rotor temperature, as the surface of the rotor is exposed to the hot air. At the compressor outlet, the air is at its most compressed state which results in high temperatures in the region. The surface of the rotor at the compressor outlet reaches a maximum temperature of about 550°C. The rotor temperature in the HPT region continues to be kept high, as it is exposed to hot gases from the combustion chamber. The temperature variation along the rotor is due to the combination of hot gases from the combustion chamber and the forced cooling from the cooling holes. At the inlet of the HPT, the temperature of the gases is reduced to about 400 °C due to the addition of cooling air to the gas stream. In the LPT, the gas temperature is further reduced to about 200 °C by blade and rotor surface cooling.

The spatial temperature distribution along the outer surface of the turbine rotor during the dwell period at full load can be seen in Figure 48. Similar thermal profiles for different periods of the rotor operation (start-up and shut-down) are applied to the surface of the rotor in order to set the thermal boundary conditions of the model.

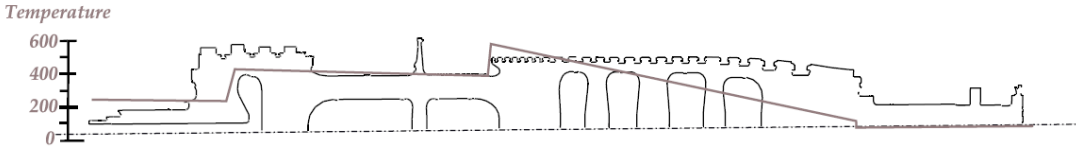

Figure 48: Surface temperature distribution along the length of the rotor at full load

The mechanical load on the turbine rotor is composed of the centrifugal forces generated due to the mass of the rotor and the contact pressure at the blade root locations. Both parameters vary with time as they both depend on the rotational speed. The rotational speed is applied directly within ABAQUS using a material density of 7,750 kg/m3. Additional pressure loads are also applied to the blade root locations. These are calculated using the mass and the centre of gravity of each blade.

4.5 Results and discussion

4.5.1 Temperature and stress analysis

The results of the simulation described in the previous section are analysed to identify the regions of interest within the rotor structure.

One important time point in the loading cycle (P1, Figure 47) is considered for the analysis in which the contribution of thermal stresses is expected to be high after the start-up. P1 is located at the start of the dwell (Figure 47) at the 3rd cycle. Figure 49 shows the temperature and von Mises stress response of the rotor at P1 after 3 cycles.

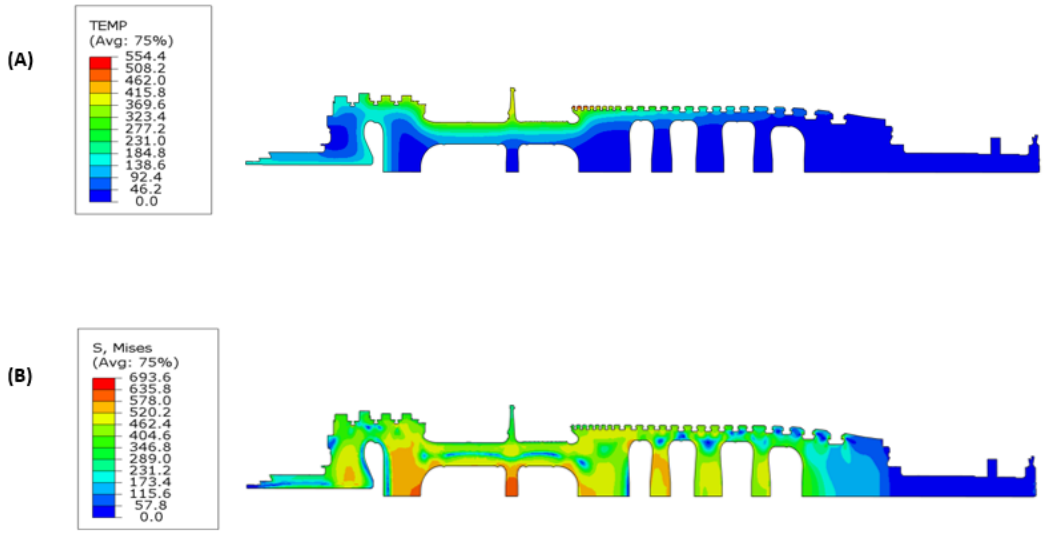

Figure 49: Contour plots for the 3rd cycle at P1 : (A) Temperature in °C and (B) von Mises stress in MPa

At the start of the dwell at point P1, a non-uniform temperature distribution is observed (A). The inside of the rotor still remains relatively cool although the temperature is already at the peak value of the dwell. More time is required for the heat transfer due to conduction to occur and which gradually moves the heat to the core of the rotor. The highest temperatures are observed in the final stage of the compressor as well as in the HPT region. The first stages of the compressor do not show any significant rise in temperature as they are continuously cooled from the cold air drawn inside. The corresponding von Mises contour plot at time point P1 shows a significant variation in the stress distribution, particularly in the central areas of the rotor (B). The maximum von Mises stress is located at the blade insertion groove of the second compressor stage mainly because of the large blade mass and the rotational speed. The geometric discontinuities in these regions act as stress concentrators. The main area where high stress variation occur is at the transition between HPT and LPT.

The second simulation at half load shows similar stress distributions as the full load model with identical temperature predictions.

4.5.2 Regions of interest

In Figure 50, two surface locations are presented for the purpose of life assessment. These include: i) a point of high stress in a hot region of the turbine rotor (Loc1) and

ii) a point of high stress in a cold region of the rotor (Loc2). (Loc1) is located at the first stage of the LPT whereas (Loc2) is located at the first stage of the compressor.

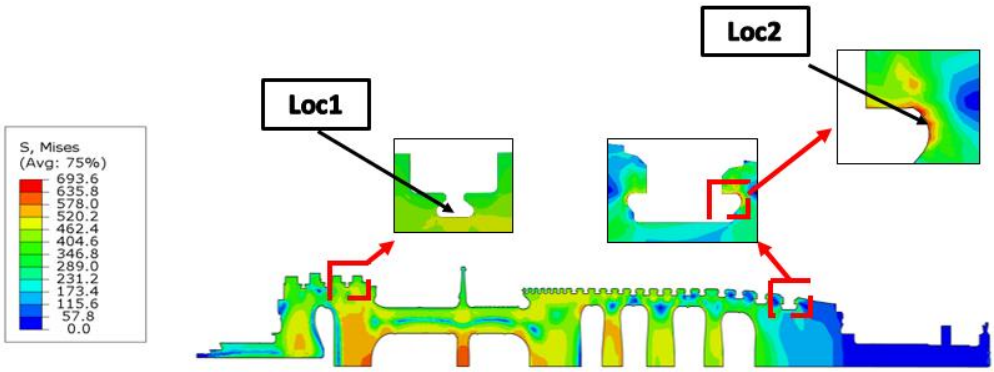

Figure 50: Life assessment locations based on von Mises stress

The highest stresses at both locations are observed during the end of the start-up operation, just when the dwell period starts. These high stresses are induced mainly because of the high pressures generated when the rotor reaches its maximum rotational speed (3,000 rpm) and also due to the addition of thermal stresses which are induced from the large temperature gradients during the start-up operation.

The highest von Mises stresses observed at (Loc1) and (Loc2) are 355 MPa and 440 MPa respectively. During the dwell period, the magnitude of the stresses at the entire surface of the rotor shows a decreasing trend with time due to stress relaxation behaviour. The dwell period during the 3rd cycle causes the stress at (Loc1) to relax by 115 MPa whereas at (Loc2) by only 21 MPa. These results would have a significant impact on the final life prediction, as can be observed from Equations 74 and 75. The stress relaxation behaviour for (Loc1) and (Loc2) can be seen in Figure 51.

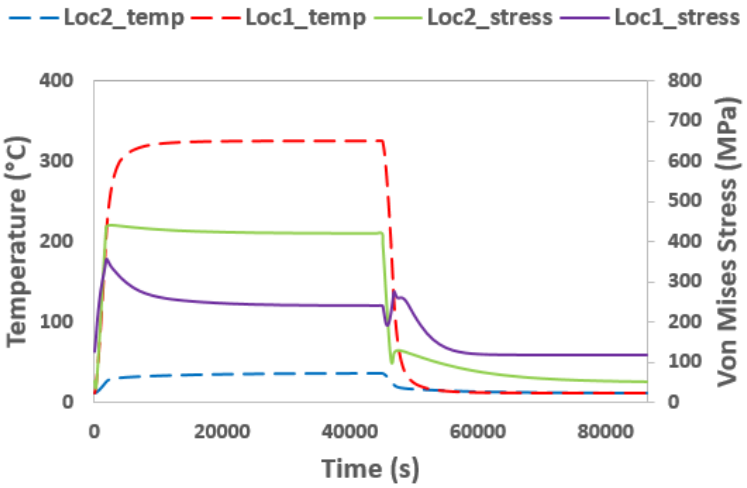

Figure 51: Evolution of von Mises stress and temperature for Loc1-2

4.5.3 Damage and life assessment

The life assessment procedure described in Section 4.3 is conducted for both locations identified within the rotor structure (Loc1, Loc2) under the base case scenario and half load operating conditions. The basic calculation steps of the procedure with the corresponding parameters values for Loc1 at full load simulation are shown in Table 11.

Table 11: Loc1 full load simulation calculation steps

	Symbol	Unit	Value	Comment
Fatigue Damage	A_3	-	81.94	From FV566 LCF tests
	C	-	0.3288	For FV566 LCF tests
	D	-	1.64	For FV566 LCF tests
	$\Delta\bar{\varepsilon}_{t\,max}$ max value of $\bar{\varepsilon}(t,t')$	-	0.0066	From FE analysis
Creep Damage	E	MPa	210580	Calculated at the temperature of the considered location

	$\Delta\sigma'$	MPa	115	From FE analysis
	ε_c	-	0.0000075	From FE analysis
	Z	-	0.0137	From equation in Figure 41
	ε_L	-	0.10	From [253]

The calculated damage values and the total lives of each location operating under each different loading condition are summarised in Table 12.

Table 12: Summary of the calculated damage values and total life estimations

Location	**Fatigue damage/cycle D_f**	**Creep damage/cycle D_c**	**Total damage D**	**Cycles to failure**	**Failure (hr)**
Original Load (3,000rpm)					
Loc1 (Hot region)	0.00012	0.000075	0.000195	5,128	123,077
Loc2 (Cold region)	0.000093	0.000012	0.000105	9,524	228,571
Half Load (1,500rpm)					
Loc1 (Hot region)	0.000035	0.000073	0.000108	9,259	222,222
Loc2 (Cold region)	0.000027	0.000011	0.000038	26,316	631,579

The failure in hours is calculated from the cycles to failure considering that the duration of one cycle is 24 hours as stated in section 4.4.1.

Under the typical (full load, i.e. 3,000rpm) loading condition, the predicted time of failure at the high temperature location (Loc1) is estimated at 123,077 hours while for the cold location (Loc2) the time of failure is estimated at 228,571 hours. The result shows a good agreement with the typical lifetime of an industrial gas turbine rotor which lies between 100,000 – 200,000 hours of operation. From the damage values of Table 3, it is clearly observed that fatigue damage dominates the cold region whereas the effect of creep-fatigue interaction becomes present in the high temperature region. A considerable increase in the life prediction for both locations is observed when the operating load is reduced to 1,500rpm. Although, the predicted lifetime shows a significant increase, as expected, it is believed that the results are still under-estimated. This is due to the identical temperature profile used in the half load simulation. In general, the calculated life of the gas turbine rotor operating under the selected typical loading condition shows a good agreement with the expected lifetime of a typical gas turbine. The average design life of a gas turbine is between 100,000 - 200,000 hours depending on the lifing criterion used and the class of the turbine [257]. This generally is equivalent to 30 years design life with a stable running time in between 150-300 days [257, 258]. The agreement between the calculated and the expected life is attributed to the ability of the procedure to generate appropriately accurate results.

4.6 Concluding remarks

This chapter presented a novel integrated lifing approach using a viscoplasticity based framework due to its ability to reproduce the material behaviour under cyclic loading conditions. Using the viscoplasticity model allows the user to extract important information directly, such as stress relaxation per cycle and the elastic follow-up factor which are required to conduct a R5 life assessment procedure. As a result, this significantly simplifies the R5 procedure, subsequently making the approach more attractive to be used at industrial level. The damage values obtained, show that fatigue dominates the damage process in cold regions whereas the effect of creep-fatigue interaction becomes more significant in high temperature regions. This indicates that temperature dominates the magnitude of creep damage. The results are compared with

those obtained when the load condition applied is halved. This loading configuration extends the predicted lifetime in all locations.

In general, the calculated life of the gas turbine rotor operating under the typical loading condition shows a good agreement with the expected lifetime of a typical gas turbine which is attributed to the ability of the procedure to capture accurate results.

Future research in this field should focus on three main areas: validating the model on real-world data, comparing the damage values of the present study with those obtained when an identical simulation is modelled in 3D, and performing a complete sensitivity analysis on the influence that each parameter has on the calculated damage. The eventual and ultimate goal of this study is to demonstrate the possibility of linking a viscoplasticity modelling approach with the R5 life assessment procedure in a way that would benefit both design engineers and industrial plant operators as a result of the simplicity and accuracy of the approach.

5 Empirical relationships between hardness, replica and strain and their roles in health monitoring based life assessment for aged power plant materials

5.1 Introduction

In this chapter, a holistic empirical lifing approach, which accommodates the routinely collected inspection data of replica, hardness and strain, is established based on a large amount of outage inspection data on ageing high temperature parent ½Cr½Mo¼V (CrMoV) material and has been used to illustrate how such routinely collected inspection data can be better utilized to provide the plant operator with predictions of residual creep life. The model differentiates between long term and persistent thermal softening behaviour revealed by change in hardness over time and short-term creep cavitation that accelerates material damage. Importantly the models developed are designed to be used iteratively with surface replica and hardness data available from an outage inspection. The study shows that the availability of more data will enable further refinements, but more importantly, it emphasises the importance of systematically capturing these data and processing them at the time of inspection to forecast residual life and then updating and tuning the model periodically at future inspections. The capture of strain data from pipe diametral measurements is also a routine outage activity and these data are included in the case study to demonstrate the capabilities in the residual life forecast by the new methods.

Normal practice for the assessment of the condition of high temperature materials in-service is based on the acquisition and interpretation of data captured on outage for surface replica, hardness and strain which are, in general, utilized *individually* in various empirical models. These data are not easily, nor routinely, used in a predictive model for residual creep life assessment, with significant run-repair-replace decisions

invariably based on very conservative assessments, advised by expert elicitation and intelligence gained from other similar assets in service.

There is great comfort in acquiring extensive field data during successive inspection campaigns, but the challenge is how to use these data efficiently to inform subsequent actions on plant [77]. Currently the overriding focus for health monitoring and assessment is placed on the data obtained from invasive inspections during an outage. Experimental studies on high temperature ½Cr½Mo¼V (CrMoV) materials retired from service has shown how this approach [214, 222] is very conservative. The currently-employed approach results in rapidly increasing inspection volume [77] as the plant ages and is only cost effective when the economics associated with plant operation are lucrative, which currently is not the case. During plant operation, limited assessments of creep rupture life are also made using operational steam temperature and pressure data, with well-established parametric relationships [259-261]. The challenge is how to better utilise and integrate this wide range of health monitoring data to reach more informed plant decisions.

In practical high temperature power plant health monitoring and life assessment, the role of hardness testing, surface replicas and strain measurement each play a part in the decision-making process that predicts the current condition of the assets and influences subsequent outage scope. Moreover, the effectiveness of how and when to deploy these health monitoring and assessment techniques is influenced by the material type, age, operating history and to some extent the original fabrication process [13]. Hardness measurement is a standard non-destructive technique that, in combination with other methods, typically surface replication, is used to support life assessment decisions for high temperature creep. Hardness is defined as the material resistance to plastic deformation under an applied load on a given indenter type and is a function of material, temperature, ageing and stress. Precipitate coarsening and coalescence, decrease in dislocation density and recovery processes are among the main causes for a reduction in hardness in service, which eventually leads to creep cavity and crack formation and finally to an eventual failure of materials at high temperature [195]. For this reason, hardness is considered a practical measure that can be used to quantify material degradation in service [196]. The occurrence of creep cavitation is a precursor to creep crack initiation that leads to creep failure in ferritic

steels. Hence, a systematic approach for surface replica assessments on power plant materials is one of the key approaches used for practical life management. Surface creep replicas are typically targeted at locations that are assessed to be more likely to accumulate creep damage. The first parent material inspection would typically occur after ~50% of the assessed creep rupture life, with pipe bends being the highest priority location. The relevant inspection body will apply a set of assessment criteria to the results of the surface replication, based on the cavitation count per mm^2 and on the degree of alignment or orientation of the observed creep damage at the grain boundaries [13]. These assessment criteria are invariably based on some version of the semi-quantitative Neubauer damage scale [262]. This practical metallurgical assessment approach is used to support run-repair-replace decisions during an outage inspection and influences the scope of subsequent outage campaigns. It is important to note that current practice encourages taking surface hardness measurements at adjacent locations to creep replicas and is also complemented by material composition checks where necessary to confirm that design intent has been adhered to. Strain assessment by measuring change in dimensions of targeted plant components is conducted periodically to predict the remnant creep life. Strain and strain rate are representative of material degradation [193], with high strain rates being exhibited as failure is approached.

This chapter explores trends obtained from an analysis of large datasets associated with plant inspection of parent CrMoV material. The capability, strength, and weakness of inspection methods (surface replicas, hardness and strain) currently deployed are explored and, on this basis, new empirical relationships are proposed that are informed from analysis of these plant datasets and reference to experimental testing. Models are developed based on data acquired from main steam straight and bend sections operating at ~173.8 bar and 568 °C and a case study illustrates how the methods would be applied in a practical context for straight pipe sections. Assessing the condition of the parent material on ageing plant is an additional challenge to that presented by the assessment of weld integrity. Inspecting, repairing, or replacing welds as they age can be reasonably managed and quantified, whereas decisions on the integrity of the extensive volume of parent material typically results in part or wholesale system renewal. Hence, more effective health monitoring and assessment

of residual life has significant benefits as plant ages and decisions are required regarding whether to pursue major refurbishments.

5.2 Methodology

5.2.1 Service exposure observations for CrMoV

The service history of CrMoV main steam pipework parent material, originally installed in 1968 is investigated using hardness, replica and strain data collected during consecutive outages on three 500 MW coalfired units identified with the acronyms Station A U1, U3 and Station B U3. Table 13 lists service hours and starts for which there is sufficient inspection data available on all three units, with the main steam system's parent material operating at 173.8 bar and 568 °C conditions since first generation in 1968.

Table 13: Dates for available outages inspection records

	Outage Year	Service Hours	Total Starts
Station A U1	2005	221,799	2,740
	2009	242,536	3,552
Station A U3	2008	239,649	3,425
	2012	259,733	3,971
Station B U3	2008	239,335	2,178
	2012	262,348	2,492

For Station A U1, during the 2009 outage a diametral measurement survey was carried out on the main steam straight pipe sections at 100 feet level for two of the four main steam legs indicating negligible creep strain compared with historic data. High level of creep damage (high orientated/grouped creep cavities) were identified in several main steam pipe bends and straight pipes during the 2005 outage. Therefore, a strategic replacement of the highest risk areas was conducted during the 2009 outage. More precisely, 9 straight sections and 16 bends were proactively replaced, of which 6 straights and 4 bends had previously been reported to contain moderate-to-high levels

of creep damage. Hardness measurements were recorded in 2009 for a total of 77 individual straight positions and 44 bend positions on the parent CrMoV main steam pipework.

For Station A U3, high levels of creep damage (high orientated/ grouped creep cavities) were identified in several main steam bends and straights during the 2008 outage. Consequently, a strategic replacement programme of the highest risk area was carried out during the 2012 outage. In addition to the planned replacement, representative bends and straights were inspected in 2012. Aligned creep damage was recorded for some main steam pipework sections resulting in further unplanned replacements. A limited diametral survey was conducted in 2012 on main steam straight sections at the 100 feet level for one main steam leg and the results indicated minimal creep strain rates in accordance with historic data. Hardness measurements were also recorded in 2012 for a total of 204 straights positions against 72 in 2008 and 107 bends positions against 53 taken in 2008 on the parent CrMoV main steam pipework.

For Station B U3, planned strategic replacement was undertaken and additional replacements were required on the main steam pipework due to creep damage or defects during the 2012 outage. The microstructures of all bend and straight sections examined were typical of those expected for low alloy steel after long exposure at high temperatures, with some coarsening of both the inter and intra-granular carbides being evident. During the 2012 outage, hardness measurements were recorded on a total of 486 individual pipe positions, including 73 bends (against 46 bends inspected in 2008), providing sufficient data for meaningful statistical analysis. Across the tested CrMoV systems, hardness values varied between 111 HV and 225 HV. The mean value for bends was 134 HV and the mean value for straights was 138 HV, which is similar to the other units and representative of CrMoV on other similar stations. These overall mean hardness values show a significant reduction in hardness when compared with an average start-of-life value of ~170 HV.

5.2.2 The development of a new database

A common problem in industry is the lack of a system to store huge amounts of raw data or if a warehousing system is present, there is a struggle to understand how to use

meaningfully these data to increase the profitability and the efficiency of companies [263].

In order to try to solve this problem with a familiar and readily-deployable solution, a database was constructed using an Excel spreadsheet with the purpose of systematically exploring possible relationships between hardness, surface replica and strain measurements from parent material pipes of power units described in the previous section. The required data were collected from integrity review reports prepared over the years following scheduled plant outages. These data were then imported and organized in an Excel worksheet to perform data analysis.

Although Excel is not a software developed primarily for database management system, its use for this reason is normal and well accepted in academy and industry thanks to the ease of data manipulation. In fact, Excel has several built in tools such as sorting, auto and custom filtering, statistics, regression models, graphs etc. that allow data to be analysed in order to make observations of possible trends [263].

The following steps contained in Ref. [264] were followed to create the database in Excel:

1. Planning the data to manage from which information need to be extrapolated before the construction of the database.
2. Open an Excel spreadsheet and add column headers with the names of the selected variables. The variables represent a classification of the data to enter and each gives a distinct piece of information. In this case the variables are: record number, station, unit, system, component, position/type, plant reference tag, report ref, reference stress, reference pressure, CET (Creep effective temperature), replica, hardness, strain rate measured at different positions and at different timeframes, year tested, year installed, time points, comments.
3. Insert the records (i.e. the data from step 1) into rows from left to right horizontally based on the reference variable.
4. Conversion of the records into a table using the Excel tool **Insert tab > Table > OK**. All the rows and columns are selected. Drop-down menus are created that allow the sorting and the aggregation of data to extract meaningful information.

Figure 52 shows a screenshot of the final electronic database built in Excel. The trends extracted from the analysis of the data are explained and discussed in the next sections of this chapter.

	A	B	C	D	E	F	G	H	I	J	K	L	M	N	O	P	Q	R	S	T	U	V
3	Record	Station	Unit	System	Component	Position/Type	Plant Reference Tag	Report Ref	Reference Stress Mpa	Reference Pressure bar	CET Creep effective temperature	Replica	Hardness	Strain rate (/hr, x 10-8) '04-'08 (21,401 h) 100 ft	Strain rate (/hr, x 10-8) '04-'08 (21,401 h) 160 ft	Strain rate (/hr, x 10-8) '94-'08 (75,110 h) 160 ft	Strain rate (/hr, x 10-8) '05-'09 (21,737 h) 100 ft	Strain rate (/hr, x 10-8) '05-'09 (21,737 h) 160 ft2	Year Tested	Year Installed	Time Points (hrs)	Comments
4	1	WBA	U3	HP Loop Parent	Bend	Extrados	HPA1/2 - HPA1/3	NT/13/TSP/WE/356/I	40.8	173.8	568.6	Clear		3.019	Neg	Neg			2000	1968		
5	2	WBA	U3	HP Loop Parent	Bend	Extrados	HPA1/2 - HPA1/3	NT/13/TSP/WE/356/I	40.8	173.8	568.6	Very isolated	134	3.019	Neg	Neg			2012	1968	259,733	
6	3	WBA	U3	HP Loop Parent	Straight	Parent-400mm	HPA1/3 - HPA1/4	NT/13/TSP/WE/356/I	40.8	173.8	568.6	Very isolated	139	3.019	Neg	Neg			2012	1968	259,733	
7	4	WBA	U3	HP Loop Parent	Bend	Extrados	HPA1/4 - HPA1/5	NT/13/TSP/WE/356/I	40.8	173.8	568.6	Very isolated		3.019	Neg	Neg			1996	1968		
8	5	WBA	U3	HP Loop Parent	Bend	Extrados	HPA1/4 - HPA1/5	NT/13/TSP/WE/356/I	40.8	173.8	568.6	Clear	144	3.019	Neg	Neg			2004	1968	218,248	
9	6	WBA	U3	HP Loop Parent	Bend	Extrados	HPA1/4 - HPA1/5	NT/13/TSP/WE/356/I	40.8	173.8	568.6	Very isolated	125	3.019	Neg	Neg			2012	1968	259,733	
10	7	WBA	U3	HP Loop Parent	Bend	D/S Tangent	HPA1/4 - HPA1/5	NT/13/TSP/WE/356/I	40.8	173.8	568.6	Very isolated	126	3.019	Neg	Neg			2012	1968	259,733	
11	8	WBA	U3	HP Loop Parent	Straight	ent-100mm D/S HP/	HPA1/5 - HPA1/6	NT/13/TSP/WE/356/I	40.8	173.8	568.6	Isolated	125	3.019	Neg	Neg			2012	1968	259,733	
12	9	WBA	U3	HP Loop Parent	Straight	ent-100mm U/S HP/	HPA1/5 - HPA1/6	NT/13/TSP/WE/356/I	40.8	173.8	568.6	Very isolated	122	3.019	Neg	Neg			2012	1968	259,733	
13	10	WBA	U3	HP Loop Parent	Cast bend	Extrados	FL - THP4/2	NT/13/TSP/WE/356/I	40.8	173.8	568.6	Clear	130	3.019	Neg	Neg			2004	1968	218,248	
14	11	WBA	U3	HP Loop Parent	Cast straight	Adjacent to THP4/4	THP/3 - THP/4	NT/13/TSP/WE/356/I	40.8	173.8	568.6	Clear		3.019	Neg	Neg			2008	1968	239,649	
15	12	WBA	U3	HP Loop Parent	Straight	500mm D/S HPA2/1	HPA2/1 - HPA2/3	NT/13/TSP/WE/356/I	40.8	173.8	568.6	Very isolated	128	3.019	Neg	Neg			2012	1968	259,733	
16	13	WBA	U3	HP Loop Parent	Straight	100mm U/S HPA2/3	HPA2/1 - HPA2/3	NT/13/TSP/WE/356/I	40.8	173.8	568.6	Very isolated	127	3.019	Neg	Neg			2012	1968	259,733	
17	14	WBA	U3	HP Loop Parent	Bend (<90°)	Extrados	HPA2/3 – HPA2/4	ENT/11/TSP/IA/1765/R	40.8	173.8	568.6	Clear		3.019	Neg	Neg			1998	1968	187,986	
18	15	WBA	U3	HP Loop Parent	Straight		HPA2/4 - HPA2/5	ENT/11/TSP/IA/1765/	40.8	173.8	568.6	Clear	149	3.019	Neg	Neg			2004	1968	218,248	
19	16	WBA	U3	HP Loop Parent	Straight	100mm D/S HPA2/4	HPA2/4 - HPA2/5	NT/13/TSP/WE/356/I	40.8	173.8	568.6	Very isolated	130	3.019	Neg	Neg			2012	1968	259,733	
20	17	WBA	U3	HP Loop Parent	Bend	Extrados	HPA2/5 - HPA2/6	NT/13/TSP/WE/356/I	40.8	173.8	568.6	Micro cracks		3.019	Neg	Neg			1996	1968		
21	18	WBA	U3	HP Loop Parent	Bend	Extrados	HPA2/5 - HPA2/7	NT/13/TSP/WE/356/I	40.8	173.8	568.6	Clear		3.019	Neg	Neg			2010	1968		
22	19	WBA	U3	HP Loop Parent	Bend	Extrados	HPA2/7 - HPA2/8	NT/13/TSP/WE/356/I	40.8	173.8	568.6	Very isolated		3.019	Neg	Neg			1994	1968	164,539	
23	20	WBA	U3	HP Loop Parent	Bend	Extrados	HPA2/7 - HPA2/8	NT/13/TSP/WE/356/I	40.8	173.8	568.6	Clear		3.019	Neg	Neg			1998	1968	187,986	
24	21	WBA	U3	HP Loop Parent	Bend	Extrados	HPA2/7 - HPA2/8	NT/13/TSP/WE/356/I	40.8	173.8	568.6	Very isolated	150	3.019	Neg	Neg			2008	1968	239,649	
25	22	WBA	U3	HP Loop Parent	Bend	Extrados	HPA2/7 - HPA2/8	NT/13/TSP/WE/356/I	40.8	173.8	568.6	Isolated	144	3.019	Neg	Neg			2012	1968	259,733	
26	23	WBA	U3	HP Loop Parent	Bend	D/S Tangent	HPA2/7 - HPA2/8	NT/13/TSP/WE/356/I	40.8	173.8	568.6	Very isolated	132	3.019	Neg	Neg			2012	1968	259,733	
27	24	WBA	U3	HP Loop Parent	Cast T	Adjacent to HPA2/8	HPA2/8 - BHP/2	NT/13/TSP/WE/356/I	40.8	173.8	568.6		139	3.019	Neg	Neg			2008	1968	239,649	
28	25	WBA	U3	HP Loop Parent	Bend	U/S Tangent	HPB1/2 - HPB1/3	NT/13/TSP/WE/356/I	40.8	173.8	568.6	Isolated	144	3.019	Neg	Neg			2012	1968	259,733	
29	26	WBA	U3	HP Loop Parent	Bend	Extrados	HPB1/2 - HPB1/3	NT/13/TSP/WE/356/I	40.8	173.8	568.6	Isolated		3.019	Neg	Neg			2000	1968		
30	27	WBA	U3	HP Loop Parent	Bend	Extrados	HPB1/2 - HPB1/3	NT/13/TSP/WE/356/I	40.8	173.8	568.6	Very isolated	147	3.019	Neg	Neg			2008	1968	239,649	
31	28	WBA	U3	HP Loop Parent	Bend	D/S Tangent	HPB1/2 - HPB1/3	NT/13/TSP/WE/356/I	40.8	173.8	568.6	Isolated	125	3.019	Neg	Neg			2012	1968	259,733	0mm U/S HPB1
32	29	WBA	U3	HP Loop Parent	Bend	D/S Tangent	HPB1/2 - HPB1/3	NT/13/TSP/WE/356/I	40.8	173.8	568.6	Low orientated	149	3.019	Neg	Neg			2012	1968	259,733	0mm U/S HPB1
33	30	WBA	U3	HP Loop Parent	Bend	D/S Tangent	HPB1/2 - HPB1/3	NT/13/TSP/WE/356/I	40.8	173.8	568.6	Very isolated		3.019	Neg	Neg			2014	1968	273,856	0mm U/S HPB1
34	31	WBA	U3	HP Loop Parent	Straight	100mm D/S HPB1/3	HPB1/3 - HPB1/4	NT/13/TSP/WE/356/I	40.8	173.8	568.6	Very isolated	146	3.019	Neg	Neg			2012	1968	259,733	
35	32	WBA	U3	HP Loop Parent	Straight	100mm U/S HPB1/4	HPB1/3 - HPB1/4	NT/13/TSP/WE/356/I	40.8	173.8	568.6	Very isolated	141	3.019	Neg	Neg			2012	1968	259,733	
36	33	WBA	U3	HP Loop Parent	Bend	U/S Tangent	HPB1/4 - HPB1/5	NT/13/TSP/WE/356/I	40.8	173.8	568.6	Isolated	137	3.019	Neg	Neg			2012	1968	259,733	0mm D/S HPB1
37	34	WBA	U3	HP Loop Parent	Bend	Extrados	HPB1/4 - HPB1/5	NT/13/TSP/WE/356/I	40.8	173.8	568.6	Clear		3.019	Neg	Neg			1996	1968		
38	35	WBA	U3	HP Loop Parent	Bend	Extrados	HPB1/4 - HPB1/5	NT/13/TSP/WE/356/I	40.8	173.8	568.6	Isolated	129	3.019	Neg	Neg			2012	1968	259,733	

Figure 52: Excel worksheet showing column headers with variables and records in rows

5.3 The relationships between hardness, replica and strain

The focus of this investigation is on both pipe bend and pipe straight parent material with the worst condition expected for the bends since they represent a more critical location in the pipe system due to the effect of system loading and the local thinning along the bend extrados and thickening along the bend intrados that occurs during fabrication [265, 266]. Two representative time-sets have been defined for the data assessment, with a time interval between these two time-sets of ~20 khrs, which represents a typical 4-year operating period.

- Time-set 1: based on outages occurring at 239,335, 239,649 and 242,536 h. This comprises 209 hardness and surface replica data points.
- Time-set 2: based on outages occurring at 259,733 and 262,348 h. This comprises 363 hardness and surface replica data points.

5.3.1 Investigation on field hardness and replica data

The hardness frequency distribution and the respective normal distribution for pipe straights and bends in time-set 1 and time-set 2 is plotted in Figure 53 and in Figure 54 respectively.

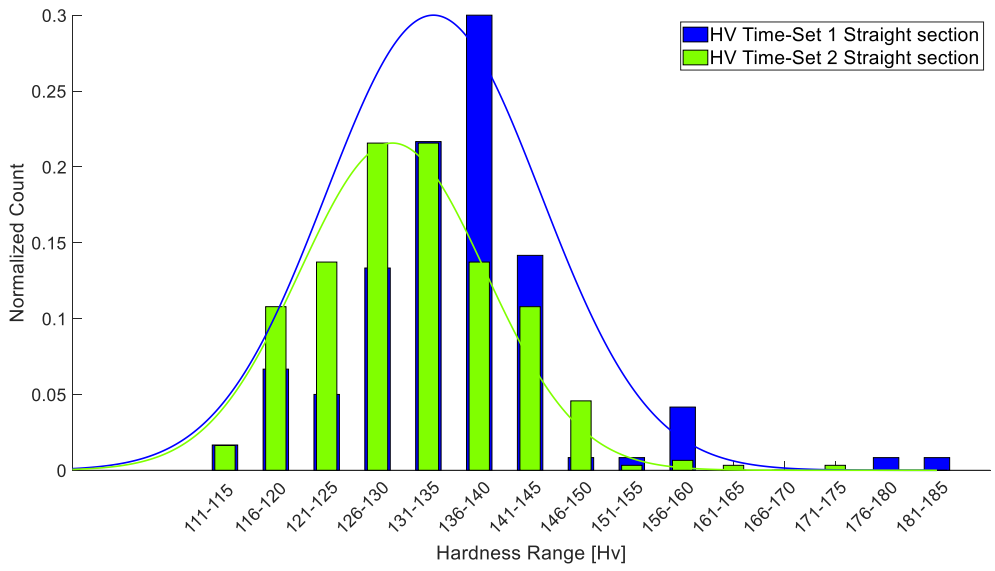

Figure 53: Hardness variation over two time-sets for CrMoV main steam straight pipes

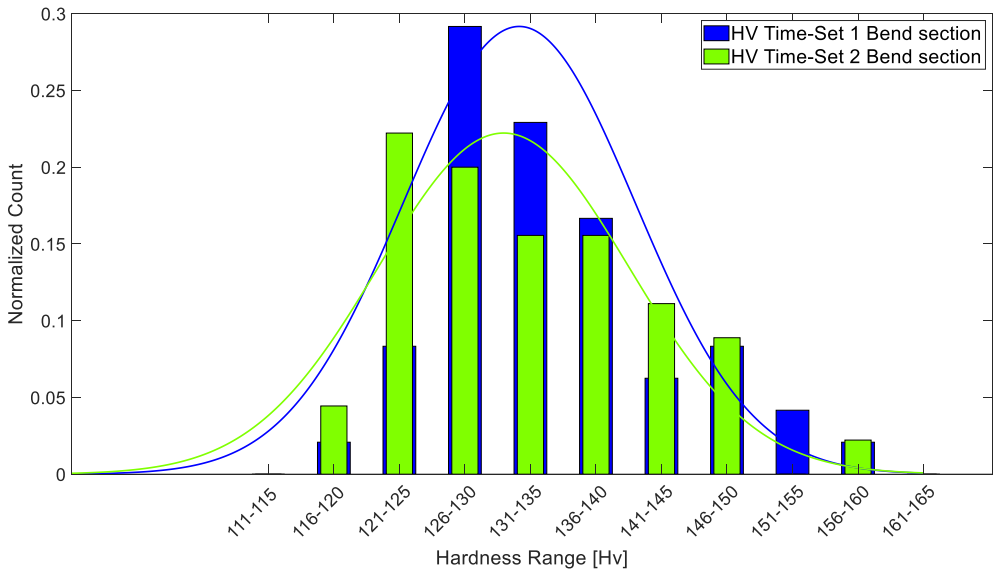

Figure 54: Hardness variation over two time-sets for CrMoV main steam pipe bends

Figure 53 shows a change in the straight pipe section population hardness, with the average value of 135.5 HV in time-set 1, reducing to 131.5 HV in time-set 2. Figure 54 shows a shift of the normalized curve as well indicating a decrease of hardness for the pipe bend sections. The average value is 134 HV in time-set 1, reducing to 132.9 HV in time-set 2.

Similarly, the creep replica level measurements associated with the two time-sets have been collected for the main steam pipe bends and straight pipes and are shown in Figure 55 and Figure 56. The creep replica level is assigned following the counting of the cavities found in 1 mm^2 of the material microstructure according to the classification in Table 14. This table is very similar to Table 4 with the addition to provide more details for the classification of creep cavities.

Table 14: Terminology used to describe creep cavitation levels [12]

Creep Cavity Damage Level	Microstructure	Cavity Density [cavities/mm^2]	Representative Cavity Density [cavities/mm^2]
1	Clear	0	0
2	Very Isolated	1 - 10	5
3	Isolated	10 - 50	50
4	Low Orientated	50 - 250	150
5	Mid Orientated	250	250
6	High Orientated	250 - 500	350
7	Grouped	500 - 1000	750
8	Aligned	1000 - 1500	1500
9	Microcracking	> 1500	> 1500

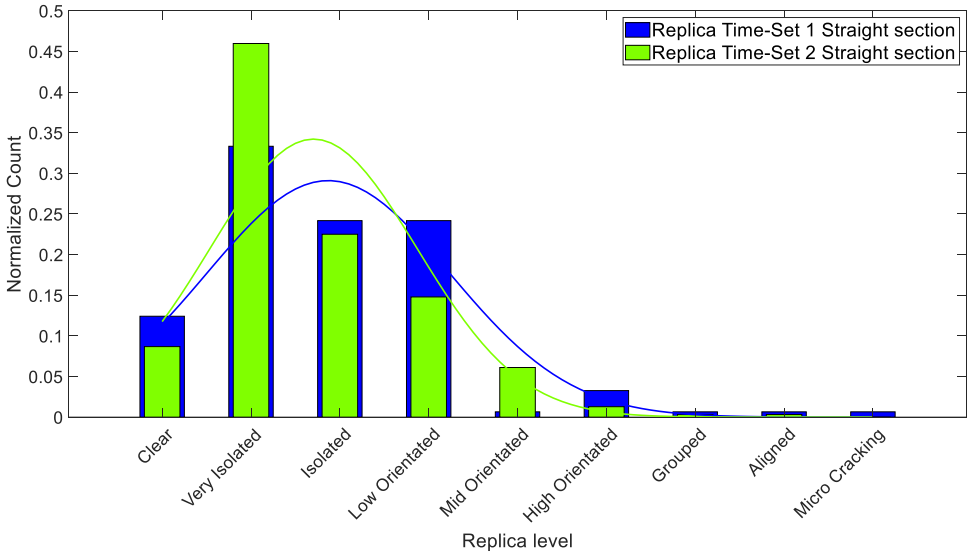

Figure 55: Replica variation over two time-sets for CrMoV main steam straight pipes

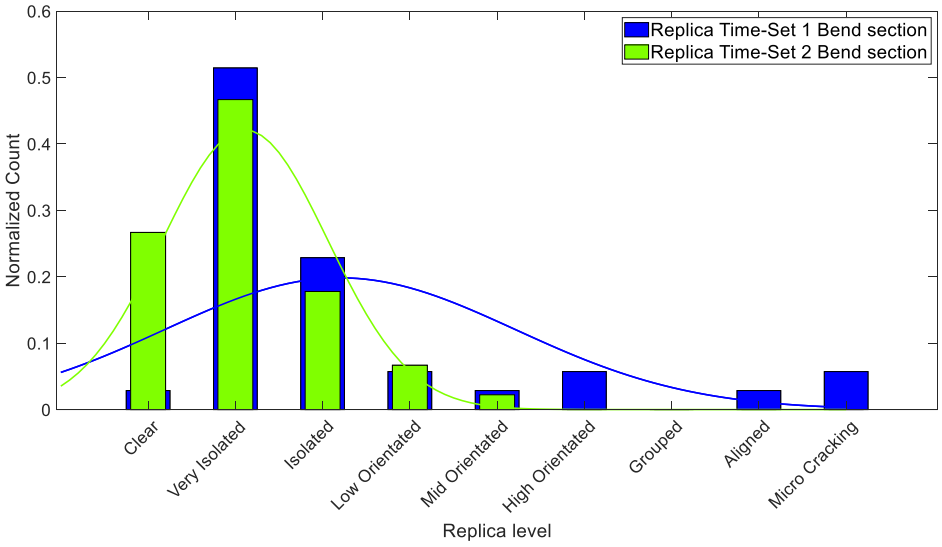

Figure 56: Replica variation over two time-sets for CrMoV main steam pipe bends

Figure 55 and Figure 56 do not seem to show a clear deterioration of the material microstructure between the two time periods. In Figure 55 the Gaussian curve for time-set 2 (green) does not shown a shift on the right towards higher creep replica levels. Anyway, it is interesting to note that for time-set 2 the very isolated count increases and the clear count decreases compared to time-set 1. Also, the mid orientated level increases for time-set 2 suggesting a shift from isolated and low orientated levels.

The replica level for time-set 2 is not clearly shifted in the right direction towards higher cavitation levels according to the replica classification (Table 14). This is possibly because as reported in the inspection reports, the pipe straights and bends found with ‘high orientated’, ‘grouped’, ‘aligned’ and ‘microcracking’ cavities in time-set 1 have been replaced directly during the same outage, thereby removing occurrences of the more damaged pipe sections from the population. In Figure 55, the inspection for time-set 2 shows materials with high orientated, grouped and aligned creep levels indicating a deterioration of the material compared to time-set 1 where the materials identified with high orientated or higher creep replica levels have been removed.

In addition, the increase in the number of inspections (frequency) identifying ‘clear’ and ‘very isolated’ replica classifications in time-set 2 is attributed to plant ageing that has prompted an increase in the volume of inspections. All time-set 1 and time-set 2

data was taken from originally installed pipework, so that the material is all from the same batch/stock as per original installation. Considering the CrMoV material, service experience shows that once cavitation is detected in parent material at the 'very isolated' level 2 it takes ~2 operating cycles (40 khr) before damage levels 5–7 is reached, hence prompting removal from service.

This illustrates the difficulty in interpretation of surface replication results with respect to residual life attributed to material in-service. The key indicator showing a change in the material microstructure and condition is observed in the shift in the population statistics highlighted in the hardness graphs, Figure 53 and Figure 54.

Another pipe specimen from the same original population was removed after ~272 khr of service, a slightly longer time in service than time-set 2 [222]. Four tensile specimens were extracted from different positions through the 60 mm pipe wall and tested at a service temperature of 570 °C, with an average 0.2% yield strength of 170 MPa and tensile strength of 207 MPa. These compared to original cast values of 220 MPa and 340 MPa respectively at 570 °C. This 23% reduction in yield strength and a 40% reduction in tensile strength is a significant reduction in strength. There was little difference recorded in the specimen yield and tensile strength values through the pipe thickness. In addition, the through section hardness range was 130–136.5 HV, taken in the radial direction, with a similar hardness range taken from the four specimens in the hoop direction. These values are consistent with data in the two time-sets. This highlights the potential for hardness data acquisition to be used in life assessment since the time span available to detect a change is much greater than for surface replicas.

5.3.2 Proposal for empirical relationships

For each time-set population the hardness data associated with a specific replica assessment level has been collated into population samples for straights and bends.

5.3.2.1 Hardness and replica for pipe straights

The hardness mean and the standard deviation for each replica-hardness sample have been computed for time-set 1 and time-set 2 as shown in Figure 57.

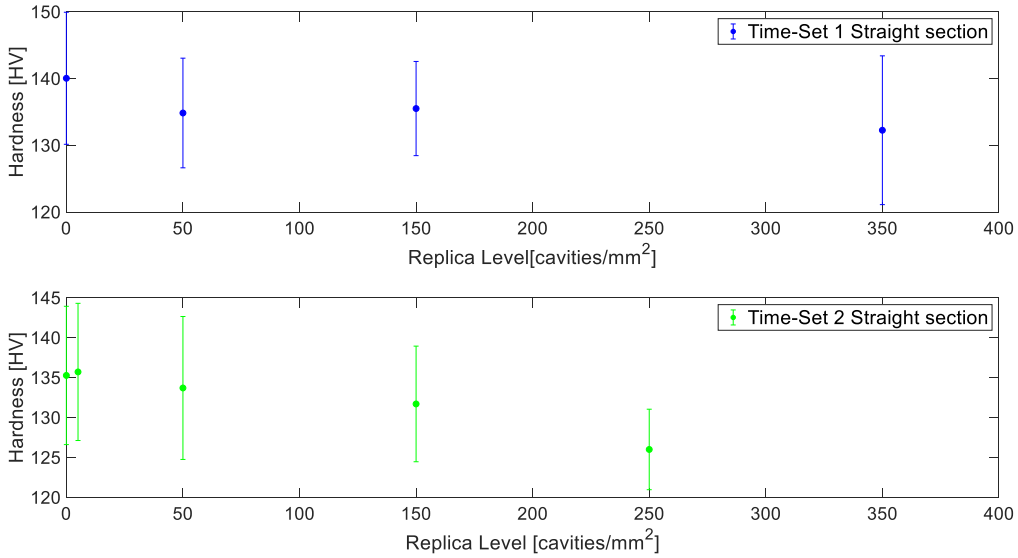

Figure 57: Hardness mean with standard deviation over two time-sets as function of cavities count (see Table 15) for CrMoV straight pipes

The highest standard deviation value for time-set 1 is for the 'high orientated' replica level (350 cavities/mm^2), equal to 11.4 HV, while for time-set 2 is equal to 9 HV for the 'isolated' replica level and similar to the 'clear' and 'very isolated' replica classes. A maximum sample variation of 11.4 HV can be expected from a field survey; however, this is too small to show appreciable changes in the microstructure. The standard error of the population has a maximum value of 5.5 HV.

The relationship between hardness and replica level has been determined using bespoke MATLAB coding based on hardness mean values from Figure 57 to give the lowest sum of squares error (SSE) value and the highest R^2. The optimal relationship found for straight sections for time-set 1 and time-set 2 is shown in Figure 58.

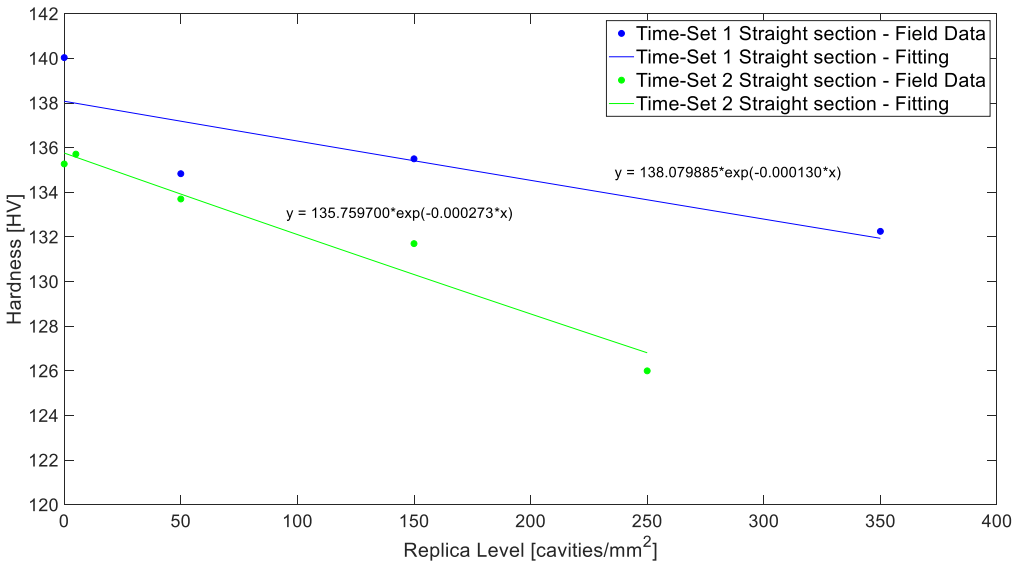

Figure 58: Hardness and creep damage (replica cavities count) relationship over two time-sets for CrMoV straight pipes

The best fit for main steam pipe straights hardness-replica field data is represented for the two time-sets by an exponential function with one term. The exponential functions are reported for clarity in Figure 58. The goodness of fit improves from time-set 1 to time-set 2 (SSE = 2.8 and R^2 = 0.95) where more field data is available to perform fitting considerations.

The general form of the function is given in Equation 79 :

$$HV = u(t)exp^{w(t)\,RL} \tag{79}$$

where *HV* is the hardness measured in [HV], *RL* refers to the creep damage in [cavities/mm^2] measured with the replica technique, u and w are two fitting parameters and a function of time t in [hours].

- w is a coefficient with unit of measure [cavities/mm^2]$^{-1}$ that describes the decay rate of the function, has negative values and is greater with increasing service time.
- u is a scaling factor that multiplies the whole function and is related to the hardness with the same unit of measure [HV]. When there are no cavities, u assumes the value of hardness for a specific time meaning it is indicative of the hardness decay of the material due to thermal ageing effects on the microstructure. When

cavitation is present, the real value of hardness at time t is acquired when u is multiplied with the contribution given by cavities through the replica measure.

The values of u and w at time-set 1 and time-set 2 are reported in Table 16.

Table 16: Fitting parameters values for equation 79 for straight pipe sections

		Time-Set 1	**Time-Set 2**
Straight Pipes	u	138.08	135.76
	w	-0.000130	-0.000273

The time dependency of u and w is extracted using the linear functions in Equation 80 and Equation 81 which have been obtained fitting the known values of u and w for the considered time-sets.

$$u(t) = -1.2315 \times 10^{-04} t + 167.85 \quad (80)$$

$$w(t) = -7.58 \times 10^{-09} t + 0.0017 \quad (81)$$

From Equation 80 and Equation 81 some observations can be made. At service time 0, which is the year of installation 1968, the value of coefficient u is 167.85, which corresponds to the received material Vickers hardness through Equation 79 when no cavitation is present. According to BS EN 10222-2 Table 1 [267], the room temperature tensile strength range for CrMoV (14MoV6-3) is 460-610 MPa depending on the manufactured supply. Using the relationship between hardness and tensile strength given in [268], the corresponding hardness range is 149-190 HV. The initial hardness value calculated with Equation 79 and Equation 80 for CrMoV straight sections can be therefore considered a good approximation of the start of life hardness for CrMoV.

Coefficient w assumes positive values until 224,590 service hours which, following Equation 79, implies an increase of hardness. These values are neglected because they give an incorrect interpretation of the processes involved in the change of the microstructure. Up to 224,590 service hours, the hardness change in straight sections is not influenced by creep cavitation but by thermal ageing effects that cause the

softening of the material. After 224,590 hours, creep damage caused by cavities causes an acceleration in the reduction of hardness for straight sections of CrMoV operating at 173.8 bar and 568 °C conditions.

Combining Equation 79 with Equations 80 and 81, Equation 82 is obtained:

$$HV = (-1.2315 \times 10^{-04} t + 167.85) exp^{(-7.58 \times 10^{-09} t + 0.0017) RL} \quad (82)$$

Equation 82 is a more general equation that combines 3 main variables, i.e. time, hardness, and replica count and can therefore be considered a master equation for CrMoV parent material straight pipe sections. Inserting the time in [hours] and the replica level in [cavities/mm^2], the hardness value is evaluated or vice versa, knowing the hardness from field inspection the corresponding value of replica is obtained. Therefore, Equation 82 allows projections over time of hardness or replica and has been extrapolated in Figure 59 for hardness.

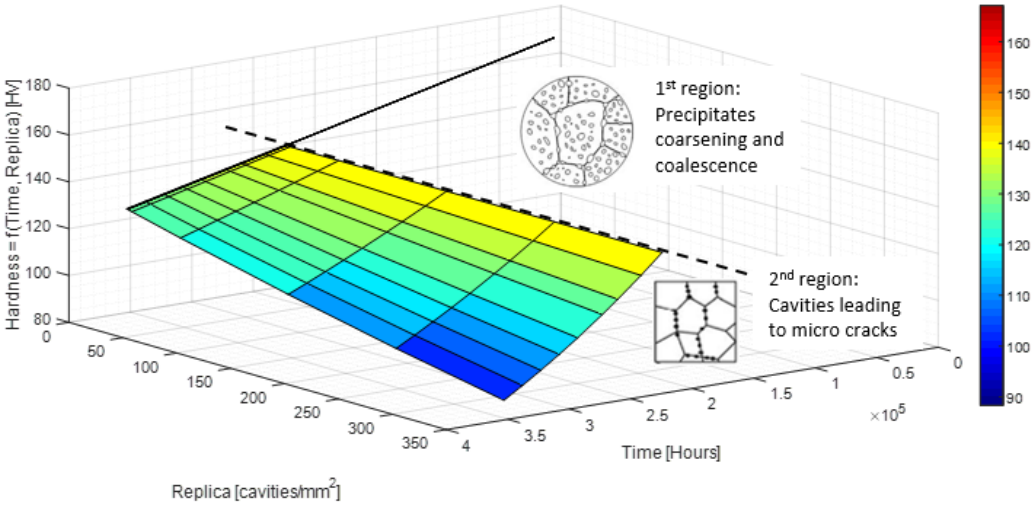

Figure 59: Hardness projection over replica for a selected time range for CrMoV straight pipes

Two regions can be distinguished in Figure 59. The first, associated on the graph with 'Clear Replica Level', from the installation year to 224,590 h, in which the hardness variation is not dependent upon creep cavities. As mentioned before, the hardness variation in this region is attributed to softening processes that happen over the time due to temperature exposure. The second region, from 224,590 h, where the effect of creep cavities on hardness reduction is more significant and combines with thermal softening.

5.3.2.2 *Hardness and replica for pipe bends*

The same approach used for straights has been followed for the analysis of pipe bends. Figure 60 shows the average value of hardness and its standard deviation for corresponding replica levels.

In the data selection process, replica levels associated with three or less hardness counts have been discarded because of insufficient data to give a reliable average hardness value.

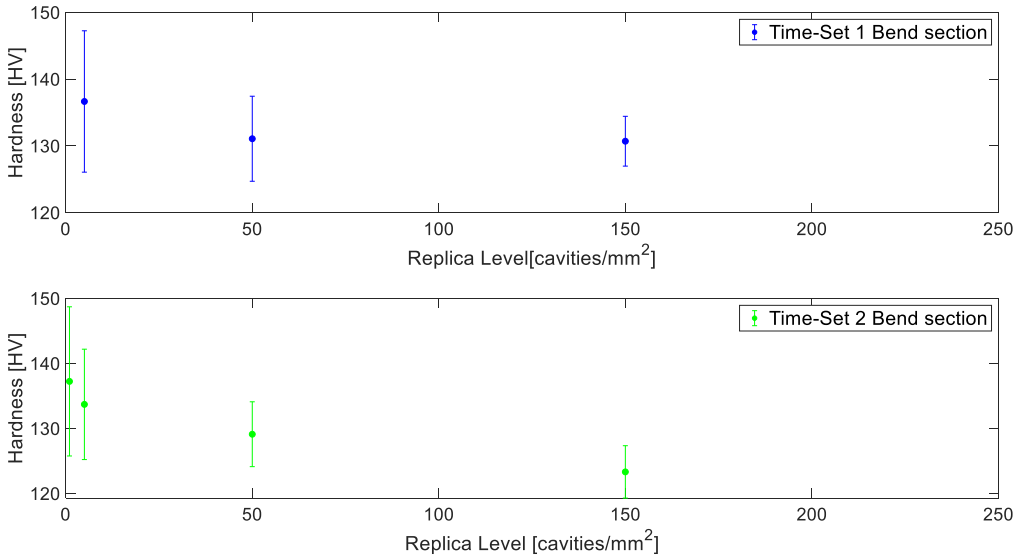

Figure 60: Hardness mean with standard deviation over two time-sets as function of cavities count (see Table 14) for CrMoV pipe bends

In Figure 60, the maximum standard deviation for time-set 1 is found for 'very isolated' creep replica and is equal to 10.6 HV while for time-set 2 is found for 'clear' creep replica and equal to 11.5 HV. These results are in accordance with the findings for time-set 2 in Figure 57 where the maximum standard deviation is associated with 'very isolated' or 'isolated' replica levels but close to the value for 'clear' replica level. The higher variability of hardness data seen for lower replica classes suggest a greater difficulty in distinguishing between 'clear', 'very isolated' and 'isolated' classes during the cavity count process.

The fitted relationships for CrMoV parent bend sections for time-set 1 and time-set 2 are shown in Figure 61.

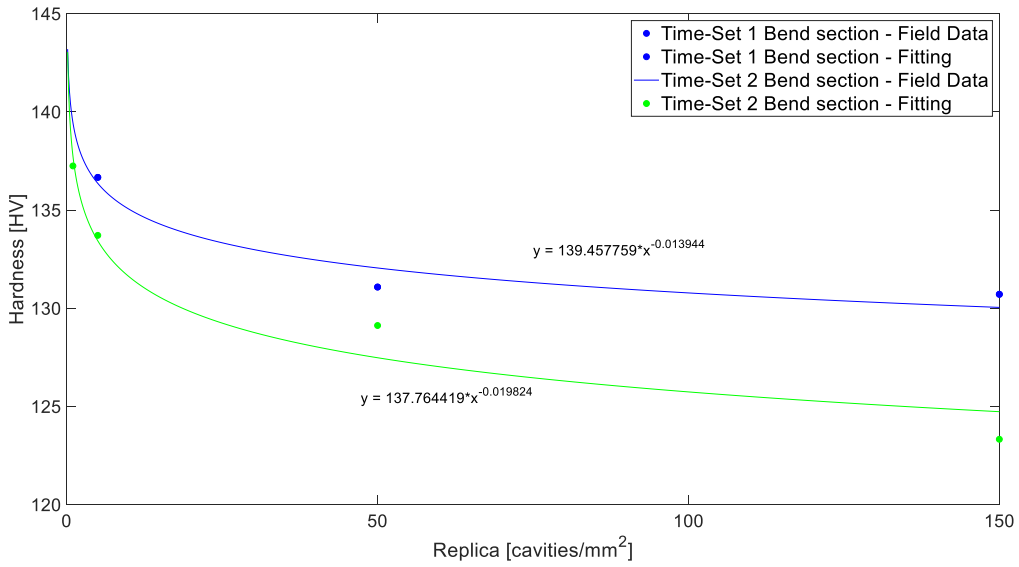

Figure 61: Hardness and creep damage (replica) relationship over two time-sets for CrMoV pipe bend

As shown in Figure 61, the best fitting for pipe bends is represented by a power function with a goodness of fit for time-set 1 of SSE = 1.48 and R^2 = 0.933 and for time-set 2 of SSE = 5 and R^2 = 0.95.

The general form of the power equation is:

$$HV = v(t)(RL)^{z(t)} \tag{83}$$

where HV is the hardness measured in [HV], RL refers to the creep damage measured in [cavities/mm^2], v and z are two fitting parameters function of time t. v and z have the same meaning as u and w for pipe straights. z defines the decay of the power function and has units of [cavities/mm^2]$^{-1}$ while v is the scaling factor that assumes the unit of measure of hardness [HV] to relate creep damage and hardness. The variation of v and z over time are reported in Table 17.

Table 17: Fitting parameters values for Equation (83) for pipe bend sections

		Time-Set 1	**Time-Set 2**
Pipe Bends	v	139.46	137.76
	z	-0.0139	-0.0198

The linear functions that describe the variation of v and z over time are presented in Equation (84) and Equation (85):

$$v(t) = -8.98 \times 10^{-05} t + 161.2 \quad (84)$$

$$z(t) = -3.12 \times 10^{-07} t + 0.0615 \quad (85)$$

From Equation (84) at service time 0 (year of installation 1968), v = 161.2 that gives an initial value of hardness for bends of 161.2 HV using Equation (83) when no cavities are detected. The value of 161.2 HV is within the hardness range of 149–190 HV calculated from Ref. [268]. The difference with the initial hardness for straights can be due to a different manufactured supply, hence the importance of tracking the change in hardness through life and when replicas start to show cavities. Another reason can be attributed to the manufacturing process that causes the bend to be a weak point in the pipe system [269]. Coefficient $z(t)$ is positive up to 197,060 h that implies an incorrect increase in hardness from Equation (83). These values are therefore discarded and only negative $z(t)$ values are considered for the correct estimation of hardness-replica relationship. Before 197,060 h, Equation (83) is not valid in describing creep cavitation because the hardness change is mostly influenced by microstructural softening processes as has been discussed in section 5.3.2.1 for the straights and later in section 5.3.2.3.

It is important to underline that the effect of creep cavity damage on bends starts after 197,060 h while for straights the hardness change due to creep cavities starts later from 224,590 h. This is mainly attributed to higher stresses acting on the bends. The main steam system design pressure is 173.8 bar with an outer diameter of 342 mm and 60 mm thickness for straight sections. The calculated mean diameter hoop stress for straights is 40.8 MPa. The pipe bends are characterized by a variation in thickness with a minimum in the bend extrados due to the manufacturing processes. Among different analysed bends measured in different positions, it has been reported an average thickness of 57.8 mm in the extrados. Discounting the effects of pipe system stress, the pressure induced hoop stress in bend is equal to 42.4 MPa, based on the extrados wall thickness, compared to the lower hoop stress in the straights. This enhanced stress will contribute to a faster deterioration rate in bends.

The general function for pipe bends obtained from combining Equations from (83) to (85) is expressed in Equation (86).

$$HV = (-8.98 \times 10^{-05} t + 161.2)(RL)^{(-3.12 \times 10^{-07} t + 0.0615)} \quad (86)$$

Equation (86) is the master equation for CrMoV pipe bend parent material that relates time in [hours], hardness in [HV] and replica count in [cavities/mm2]. Figure 62 shows the hardness projection over time and creep replica level calculated from Equation (86).

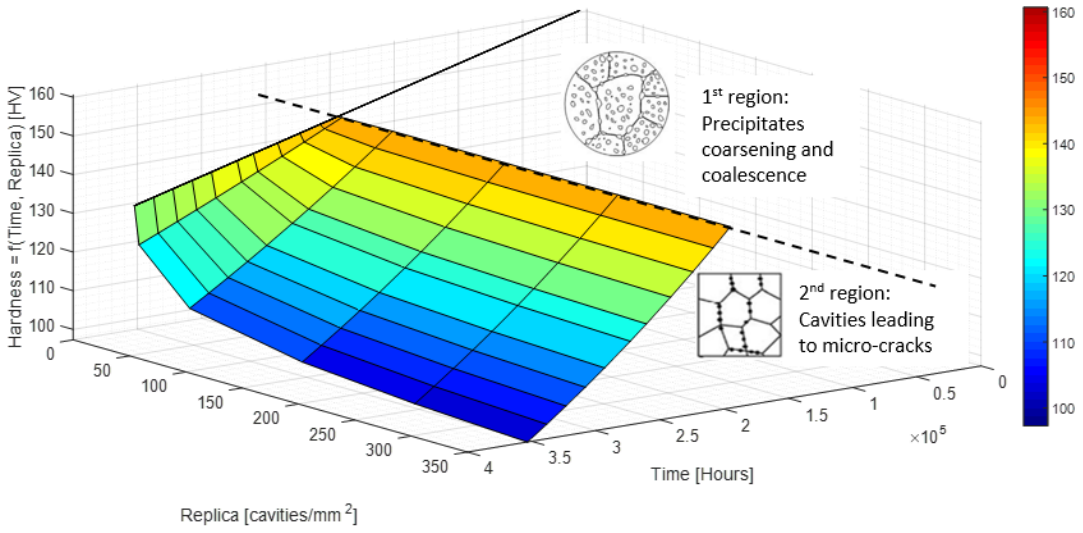

Figure 62: Hardness projection over replica for a selected time range for CrMoV pipe bends

As for the straight sections in Figure 59, also in Figure 62 two distinguished regions in the creep behaviour of pipe bends are identified. In the first region until 197,060 service hours the creep behaviour is dominated by the effect of precipitates coarsening and their coalescence that lead to the second region where cavities nucleate up to the formation of microcracks.

5.3.2.3 *Creep strain and damage assessment as function of hardness and replica*

The correct prediction of creep strain, and consequently of remaining creep life, is determined by the combination of different microstructural processes. Precipitate coarsening and creep cavitation have been identified as the two main conditions leading to creep damage in low alloy steels such as CrMoV [270].

During service exposure, thermal ageing is responsible for the evolution, coarsening and agglomeration of carbides and in combination with the primary stress arising from system operating pressure and other sources such as pipe system loading, for the subsequent nucleation of creep cavities. New secondary carbides species, mostly $M_{23}C_6$, M_6C, M_2C and M_7C_3 in CrMoV steels depending on process conditions and chemical composition [2, 165, 271], precipitate mainly along the material grain boundaries due to the transfer of Cr and Mo from the metal matrix to the carbides (Figure 63a). The depletion of strengthening elements in the metal matrix and the change of carbide structure cause a reduction in the mechanical resistance of the material in terms of yield strength, creep rupture strength and in the material hardness [60]. The subsequent agglomeration of carbides, due to the extended exposure to operation conditions, reduces the quantity of finely distributed carbides in the metal matrix and by facilitating the movement of dislocations, triggers cavity formation (Figure 63b) causing a further softening of the material mechanical properties [271]. The nucleation of cavities from carbides at grain boundaries is recognized to be the most probable nucleation mechanism [34, 164].

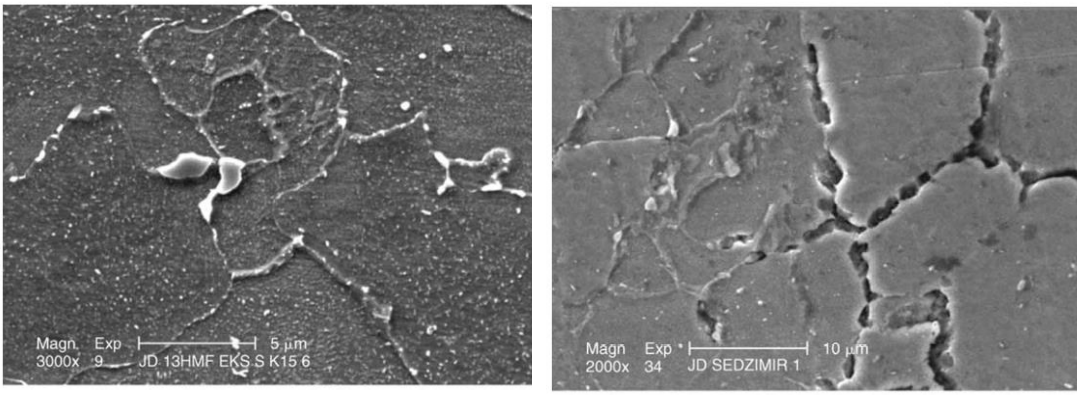

(a) *(b)*

Figure 63: (a) SEM micrograph showing carbides coalescence visible along CrMoV grain boundaries [165], and (b) SEM micrograph showing orientated cavities along CrMoV grain boundaries [165]

These two dominant mechanisms, namely carbide precipitation and creep cavitation, have been also identified in Figure 59 and in Figure 62, where the two regions of hardness change are related respectively to precipitate coarsening and coalescence and creep cavitation. While in the first region, softening caused by precipitate coarsening is considered the predominant damage condition, whilst in the second region, the two processes occur simultaneously but cavitation has the more significant role in leading to failure. Therefore, in the following paragraph, two methods, which reflect this change in material behaviour, are developed to model creep strain as function of surface hardness and replica condition.

The first method aims to describe the impact of hardness decrease due to particle coarsening on the material creep strain rate when no or limited cavities are detected from a surface replica. By expressing the dependence of stress and temperature to the minimum (steady-state) creep rate with the Norton's power law and an Arrhenius type law, Equation (87) is formulated:

$$\dot{\varepsilon}_{ss} = A\, exp(k_A\, T) \left(\frac{\sigma}{\sigma_o}\right)^n \tag{87}$$

where A and n are respectively the creep coefficient and the creep exponent according to Norton's law that vary according to the stress/temperature regime [50]. k_A is an exponential constant with unit $[1/\,\mathrm{K}]$ expressing the dependence with temperature and

T is the absolute temperature in Kelvin [43]. σ_o is the Orowan stress and as described by Cane [270] and by Dyson [43] and is the critical stress value required to move the dislocations past the particles obstacles characterizing in this way the tendency for plastic flow of the metal [272]. In the Allen-Fenton (Equation 47) [199], σ_o is the flow stress taken as the average between the yield and the ultimate tensile strength but both are an expression of the plastic deformation of the material. σ_o is inversely proportional to the interparticle spacing λ (Equation (88)) that has been demonstrated to be correlated with the hardness (Equation (89)) [270].

$$\sigma_o = \frac{\alpha' \mu b_1}{\lambda} \tag{88}$$

$$\lambda = K/HV^q \tag{89}$$

where α' is the particle/dislocation interaction parameter, μ is the shear modulus in [GPa] and b_1 is the Burgers vector in [nm] [270]. Substituting Equations (88) and (89) in Equation (87), Equation (90) is obtained:

$$\dot{\varepsilon}_{ss} = A\, exp(k_A\, T) \left(\frac{K}{\alpha' \mu b_1}\right)^n \left(\frac{\sigma}{HV^q}\right)^n \tag{90}$$

Finally, the rupture time t_r is estimated recalling the Monkman-Grant relationship (Equation 18) with the minimum creep strain rate:

$$t_r = B\, exp(-k_A\, T) \left(\frac{\alpha' \mu b_1}{K}\right)^n \left(\frac{HV^q}{\sigma}\right)^n \tag{91}$$

Equation (91) is very similar to the final expression given by Allen-Fenton in Equation 47 [199] and by Morris et al. in Equation 45 [77] with the addition of stress dependence and the characteristic parameter $(\alpha' \mu b_1)/K$ that is typical of the microstructure.

Creep cavitation is considered the dominant mechanism in the second region contributing more than just precipitation coarsening to the material loss of strength and consequently to the increase of creep strain rate as underlined in Figure 59 and in Figure 62. Therefore, in the second method, the effect of creep cavitation on strain rate is investigated by considering the continuum creep damage mechanics (CDM) model

introduced first by Kachanov-Robotnov. As explained in section 2.1.3.2, the Kachanov-Robotnov model is a phenomenological-based CDM model that herein is used for its simplicity in describing the relationship between the creep rate and the damage parameter with a power-law expression. Its inherent limitation occurs when the damage parameter approaches unity, which can be overcome by using more complex models such as the Liu-Murakami and the Dyson formulations [43, 44, 52, 199] but the basic concepts will remain unchanged (see section 2.1.3.2).

The Kachanov–Rabotnov model [33, 273, 274] with the inclusion of the temperature dependence by an Arrhenius type law is as follows:

$$\dot{\varepsilon}_c = A\, exp(k_A\, T) \left(\frac{\sigma}{1-\omega}\, \frac{1}{\sigma_o}\right)^n \tag{92}$$

where ω is the damage parameter, which effectively represents the area covered by microcracks and cavities and varies from 0, the undamaged state, to 1 at failure [275]. To account for the inspection data and the ability to represent material degradation, the damage parameter ω in a real industrial application can be thought to be defined in accordance with Equation(93):

$$\omega = \frac{cavities\ at\ time\ i}{\max acceptable\ cavities} = \frac{RL}{cavities_{max}} \tag{93}$$

The advantage of using Equation (93) to define the damage is its practicality. Cavities are counted directly from creep replication [cavities/mm^2] allowing for the assignment of a creep damage level to the inspected component according to the criteria in Table 14. The maximum number of cavities $cavities_{max}$ is represented by the highest acceptable damage level that triggers replacement actions, with RL representing the cavity density measured at time *t*. Observations show that this reference level typically corresponds to the 'high orientated cavities' level that according to Table 14 is 250 cavities/mm^2. The new defined damage parameter ω in Equation (93) always varies from 0, the undamaged state without cavities, to 1, the full damaged state.

Rearranging Equation (93) to include the relationship between creep replica and hardness for straight pipes and pipe bends according to Equations 79 and (83) respectively, Equations (94) and (95) are obtained:

$$\omega_{straight} = \frac{\frac{1}{w_i} ln \frac{u_i}{HV_i}}{cavities_{max}} \tag{94}$$

$$\omega_{bend} = \frac{\left(\frac{v_i}{HV_i}\right)^{1/z_i}}{cavities_{max}} \tag{95}$$

where w_i, u_i, v_i, z_i are the coefficients in the hardness equations calculated at time *i*.

The advantage of Equation (92) combined with Equations (94) and (95) and previously of Equation (87) is to allow a direct formulation of the creep rate as function of the main creep characteristic parameters, i.e. stress and temperature operating parameters and routinely collected hardness and replica data that give an insight on the microstructural condition of the material.

Recalling the strong dependence of the rupture time upon the secondary creep strain through the Monkman-Grant relationship and its insensitivity to the rupture strain as stated in [276], the rupture time in the second region is estimated as:

$$t_r = B \frac{(1-\omega)^n {\sigma_o}^n}{exp(k_A T)\sigma^n} \tag{96}$$

Equation (96) can be reconnected to the rupture time expression given by the Omega method in Equation 24 where the creep damage Ω has been expressed by the ω parameter defined through inspection data.

Equations (87) and (92) could be used as a proactive condition monitoring technique combined with on-site strain measurements for the estimation of the material remaining life by substituting the strain rate in the general expression for creep life in Equation 41.

5.3.3 The role in health monitoring based life assessment

The new approach for health monitoring using routine monitoring data such as hardness, replica metallography and strain measurements is summarized in the flowchart in Figure 64.

A first estimate of rupture time can be obtained through the Failure Forecast Method in Equation 41 when sufficient strain measurements are available to allow the calculation of the strain rate. Another possible use of the Failure Forecast Method would be with the measure of hardness change through successive outages with sufficient data.

The hardness and replica cavities count relationship is applied according to the pipe component (bend or straight). This relationship is used to develop creep strain rate models and consequently it allows a prediction of rupture time. In this chapter, Equations (91) and (96) have been developed for CrMoV pipes to define the rupture time in the softening and in the cavitation regions, respectively, according to the material condition. Strain measurements could also be correlated with hardness and replica count data. The prediction of rupture time obtained from the different methodologies is then compared to check for convergence and thus confirm a value for rupture time or further review [60].

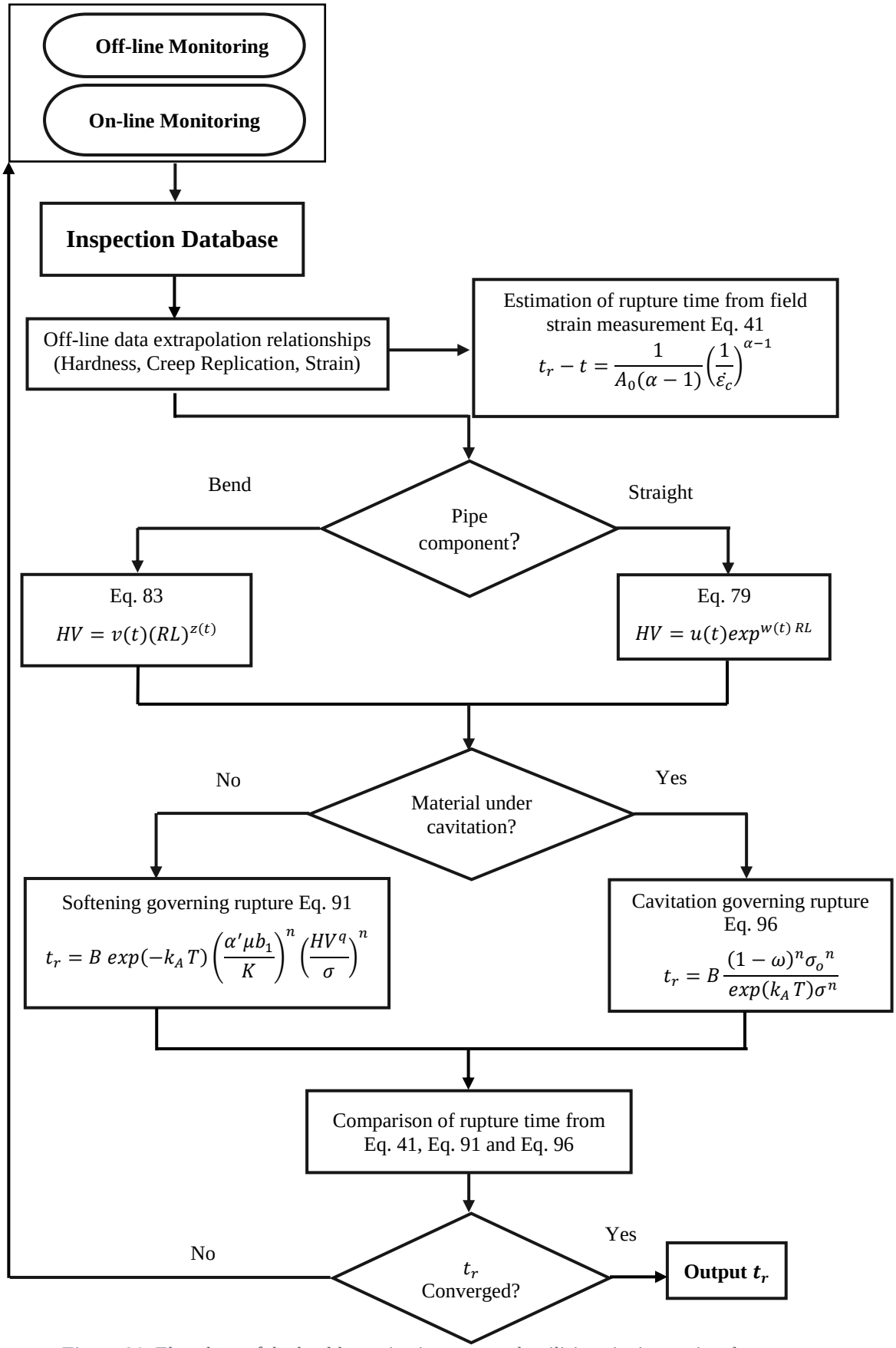

Figure 64: Flowchart of the health monitoring approach utilising site inspection data

5.3.4 Case demonstration

The implementation of the flowchart in Figure 64 is approached in the following case demonstration where the rupture time is estimated using parameters available in literature and field data extracted from sections 5.3.2.1 and 5.3.2.2.

The example is referenced to a straight pipe section, but the same approach is applicable for bends. The creep strain rate and consequently the rupture time will be calculated for the particle coarsening and the creep cavitation regions following Equations from (90) to (92) and (96). The input parameters that are used in the equations are given in Table 18.

Table 18: Constants of creep strain rate model

A	k_A [1/K]	T [K]	K [µm HV]	q	α'
4.2×10^{-35}	0.053	841.75	3.34028×10^{17}	8.2133	0.228
μ [MPa]	b_1 [µm]	n	M	σ_h [MPa]	B
63200	2.45×10^{-4}	4	0.013	40.8	8.59×10^{28}

The temperature T and hoop stress σ_h are typical operational power plant conditions and the value of the creep rate stress exponent n is typical for service conditions at low stress regime [277]. The constants A_2, k_A, α, μ and b_1 are taken from [270] as well as K, q that are extrapolated from the interparticle spacing-hardness relationship.

M is the Monkman-Grant constant taken from [60] and B is calculated from M and A . For the first region in which the precipitate coarsening is the principal degradation mechanism and the cavity number is negligible, the minimum creep strain rate is computed in units of s^{-1} with Equation (90) using hardness values obtained from Equation (82) with $RL = 0$ at chosen different service times. The estimated creep life is computed from Equation (91).

In the second region where the rupture time is influenced mainly by creep cavitation, the same procedure is followed considering $RL \neq 0$ with the number of cavities taken from field measurements. The strain rate is estimated using Equation (92) through ω

in Equation (94) for straight pipes and the remaining rupture time is given by Equation (96). The results of creep strain rate together with the estimated creep life are shown in Table 19 in units of hrs^{-1} and hrs, respectively.

Table 19: Estimated hardness, strain rate and rupture time

Service Hours [khrs]	**Cavity Density [cavities/mm^2]**	**HV**	ω	**Strain Rate [1/hrs]**	t_r **[hrs]**
0	0	168	0	6.39×10^{-11}	2.04×10^{8}
35	0	164	0	1.50×10^{-10}	8.66×10^{7}
70	0	159	0	3.61×10^{-10}	3.60×10^{7}
105	0	155	0	8.9×10^{-10}	1.46×10^{7}
140	0	151	0	2.25×10^{-9}	5.78×10^{6}
175	0	146	0	5.83×10^{-9}	2.23×10^{6}
210	0	141	0	1.56×10^{-8}	8.34×10^{5}
245	0	138	0	4.29×10^{-8}	3.03×10^{5}
	50	137	0.2	1.36×10^{-7}	9.59×10^{4}
	150	134	0.6	3.64×10^{-6}	3.58×10^{3}
	250	132	1	inf	0
280	0	133	0	1.22×10^{-7}	1.07×10^{5}
	50	131	0.2	5.96×10^{-7}	2.18×10^{4}
	150	125	0.6	3.82×10^{-5}	3.40×10^{2}
	250	120	1	inf	0
315	0	129	0	3.59×10^{-7}	3.62×10^{4}

	50	125	0.2	2.71×10^{-6}	4.79×10^{3}
	150	116	0.6	4.16×10^{-4}	3.13×10^{1}
	250	109	1	inf	0
350	0	125	0	1.10×10^{-6}	1.19×10^{4}
	50	119	0.2	1.28×10^{-5}	1.02×10^{3}
	150	108	0.6	4.69×10^{-3}	2.77
	250	98	1	inf	0

As expected, the remaining failure life predicted in absence of cavities in Table 19 is higher than the value calculated with the effect of creep cavitation. A graphic representation with lines of the hardness values collected in Table 19 is presented in Figure 65(a) as function of service time together with the measures of hardness taken from field inspection at a certain replica level shown with points. The reference critical replica level is set at 250 cavities/mm^2. The effect of changing the critical cavity level on the rupture time is represented in Figure 65(b) for three cavity levels from 250 to 500 cavities/mm^2.

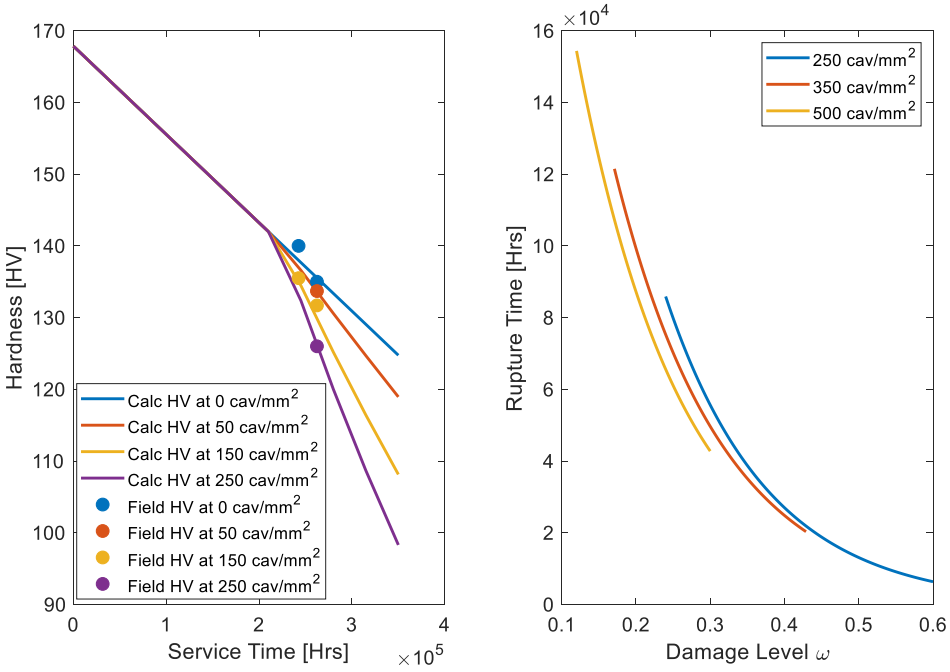

(a) *(b)*

Figure 65: (a) Estimated and field Hardness variation as function of service time, and (b) Rupture time variation as function of damage level for different critical cavity levels.

A scenario that can be envisaged for practical power plant inspections is shown below as the station approaches end of life. This illustrates the periodic outage data capture and re-assessment process that would be applied in practice to inform decisions based on observed cavity counts. Table 20 illustrates the proposed approach, with the critical cavity density level being reassessed and reset at the last inspection point.

Table 20: Application of the new approach during inspections

Service Hours at Inspection Point [hrs]	**HV**	**Cavity Density** $\left[\frac{cavities}{mm^2}\right]$	ω	**Strain Rate [1/hrs]**	t_r **[hrs]**	**Critical Cavity Density** $\left[\frac{cavities}{mm^2}\right]$
241,734	137	60	0.24	1.52×10^{-07}	87,106	250
253,734	134.2	80	0.32	4.67×10^{-07}	27,840	250
259,734	132.6	90	0.36	8.76×10^{-07}	14,850	250
265,734	130.5	110	0.44	2.51×10^{-06}	5,174	250
265,734	130.5	110	0.338	1.29×10^{-06}	11,530	350

The average creep strain rate calculated from diametral strain measurements across installed creep pips for a period until 241,734 hrs on the main steam pipework has been reported from site diametral surveys to be in the order of 3.173×10^{-8} hrs^{-1}, which gives a projected remaining life of 371 khrs. In this case the strain rates are estimated over different strain measurements samples taken at different operating periods allowing for the use of the Failure Forecast Method based on strain rate as a damage indicator [60]. The estimated remaining rupture time from Equation (91) in absence of cavities at 241,734 service hours is 333.4 khrs. The two values of remaining life calculated with the creep strain laws from Section 5.3.2.3 and the Failure Forecast Method are similar suggesting a good convergence of results in the absence of creep cavitation.

5.4 Discussion and concluding remarks

5.4.1 A holistic lifing methodology

A hardness and creep replica assessment relationship has been quantified, for the first time, for parent material straight and bend sections using data extracted from in-service inspections on CrMoV material. This provides the capability to predict the residual life of ageing parent materials in service using a combination of hardness, surface replica data and strain, as illustrated in Figure 64. In practice there is a need to

compare different residual life predictions based on assessments of field inspection data [60] against other computational predictions based on component reference stress and online plant temperature and pressure data [13].

The empirical solutions for the creep strain rate calculated from Equations (90) and (92) through the integration with online (stress and temperature) and offline (hardness and replication) data show a good predictive capability and agree well with the strain rate values calculated from field measurements in Section 5.3.4 . The creep rupture life is thus predicted suitably through its relationship with the creep strain rate. The master Equations (82) and (86) that describe the straight and bend pipes behaviour allow the estimation of the strain rate with the advantage of providing a better comprehension of the in-service evolution of the failure mechanism that characterizes the material under investigation. Hardness and creep replica data must be used in conjunction for a correct projection of the material microstructure evolution and for the estimation of the strain rate and remaining life.

The approach takes account of the initial effect of thermal softening (hardness reduction in region 1) and creep damage (accelerated hardness reduction in region 2) illustrated by the hardness and creep cavity behaviour. As material ages in service, the model can be further tuned by comparison between the estimated and measured value of hardness. Once the model is finely tuned, the field hardness measure will allow a more reliable estimation of creep cavities and consequently of creep strain rate. The examples presented in Section illustrate this concept.

5.4.2 Industrial significance

The approach developed in this chapter complements the real decision-making process on an operating station, which considers all relevant data before making significant run-repair-replace decisions. The capability to detect the acceleration in damage is particularly important for the plant operator, since this acceleration is invariably the key behaviour that focusses attention and prompts decisions.

Currently hardness and surface replica data are not routinely used in predictive residual life models. The baseline inspection data used to develop the models for parent CrMoV has been acquired by very experienced inspection teams on ageing

plant across multiple operating units, hence the quality is considered representative of good practice.

The assessment reveals definite trends in the population statistics for hardness data as plant ages, however the trends are less evident for the surface replica inspection data. It should be noted that the expected change in replica cavity count as the material ages has been affected by the sites' very conservative decision for wholesale pipework replacements on the inspected units. Other studies [214, 222] of ex-service CrMoV specimens extracted from the same pipework systems have confirmed that the decision to replace the pipework was very conservative.

5.4.3 Capabilities and further development

The models developed in this research illustrate the potential to better utilise existing inspection data for predictions of residual creep life. This innovation is even more powerful if it is complemented by, or integrated with, more sophisticated computational life assessment models that can efficiently account for the stress state in components and interpret the nuances associated with real plant operation [60].

The predictive capability and the accuracy of the empirical relationships proposed in this chapter will improve with access to more field data, spread over longer operational periods. The new predictive models developed in this study show the potential future direction; for example in combination with a neural network approach [265] to efficiently determine the stress state and integrated with online monitor data.

6 Microstructure evolution and deformation mechanisms of service-exposed P91 steel via interrupted uniaxial creep tests at 660 ºC

6.1 Introduction

In the previous chapters, lifing model techniques have been developed that integrate inspection-based data with operational data. In particular, in Chapter 5, a hardness and creep replica relationship has been developed for parent material straight and bend sections using data extracted from in-service inspections on CrMoV material. This relationship provides the capability to predict the residual life of ageing parent materials in service using a combination of hardness, surface replica assessment data and measured strain. The fundamental concept upon which this correlation was developed is that NDT techniques such as strain and hardness measurements and metallographic replica all provide an indication of the damage of a component. Moreover, since hardness is easier and more convenient to measure during inspections than surface replicas and strain, in this thesis it has been adopted as the principal measure to quantify and represent damage.

This chapter has the primary aim of validating the developed models by investigating the effects of the microstructural changes of a P91 steel under creep testing on hardness variation. This seeks to provide a physically-based explanation to underpin the proposed models and to develop confidence that hardness can be used to quantify material degradation in service and to estimate residual life.

As already mentioned in the previous chapters, creep damage is one of the main causes of failure and concern for materials exposed to high temperature and pressure in modern power plants. A prolonged creep exposure is responsible for the deterioration of material properties so that methods to estimate and predict the remaining life of components are urgently needed [22, 196, 278]. One of the main factors responsible for the reduction of creep strength is the nucleation, growth and coalescence of cavities

that is related to the microstructure evolution under high temperature service conditions and material composition, which causes a transition from a ductile to brittle fracture [279, 280]. This chapter aims to improve the understanding of the microstructural evolution of P91 steels in service since this will become increasingly important for the operator in order to safely manage power generation systems and to remain commercially viable. In addition, a deep and clear knowledge of the microstructural changes will allow the development of modified and more advanced versions of P91, which are crucial for the achievement of the new thermal efficiency target [281].

Under long-term creep conditions, creep failure for P91 steel occurs primarily in the heat-affected zones of welds well before the estimated rupture life for the base metal due to Type IV creep cracking that originates from cavity nucleation and growth [282, 283]. The base material also experiences a reduction of creep strength and failure before the predicted extrapolated life obtained from short-term creep life testing, due to void nucleation and inter-linkage [279]. To underpin the safe operation of components it is therefore of vital importance to understand the root causes of cavity formation in the microstructure and the impact of material composition on cavity nucleation. Common microstructural changes for P91 steel under service exposure that lead to cavity formation and final failure are recovery of the lath martensitic microstructure, precipitation and coarsening of Laves phase, coarsening and agglomeration of $M_{23}C_6$ and MX particles and formation of Z-phase [220, 284-287].

Currently P91 systems are managed in a similar way to other high temperature steels in that confirmation of condition is ascertained during periodic invasive statutory physical inspections where non-destructive inspections and field metallographical inspections and assessments are undertaken. The application of non-destructive techniques (NDTs) has proven the most reliable method to determine the in-service condition [9]. An exhaustive review of NDTs normally used in power generation industry and in oil and gas plants is given by Sposito et al. [206] and their use to assess creep damage is shown in Figure 66.

Hardness measurement, among all NDTs, is routinely used in combination with metallographic replication during outage overhauls to provide an indication of creep

softening over time and has been used predictively for the estimation of the remaining life in plant applications, often in conjunction with the Larson Miller parameter (LMP) [85, 196, 199, 209]. Hardness reduction is due to the primary material degradation processes listed above, mainly precipitation coarsening and change in the lath structure, thus allowing an estimation of the evolution of creep resistance and consequently of material life [288, 289].

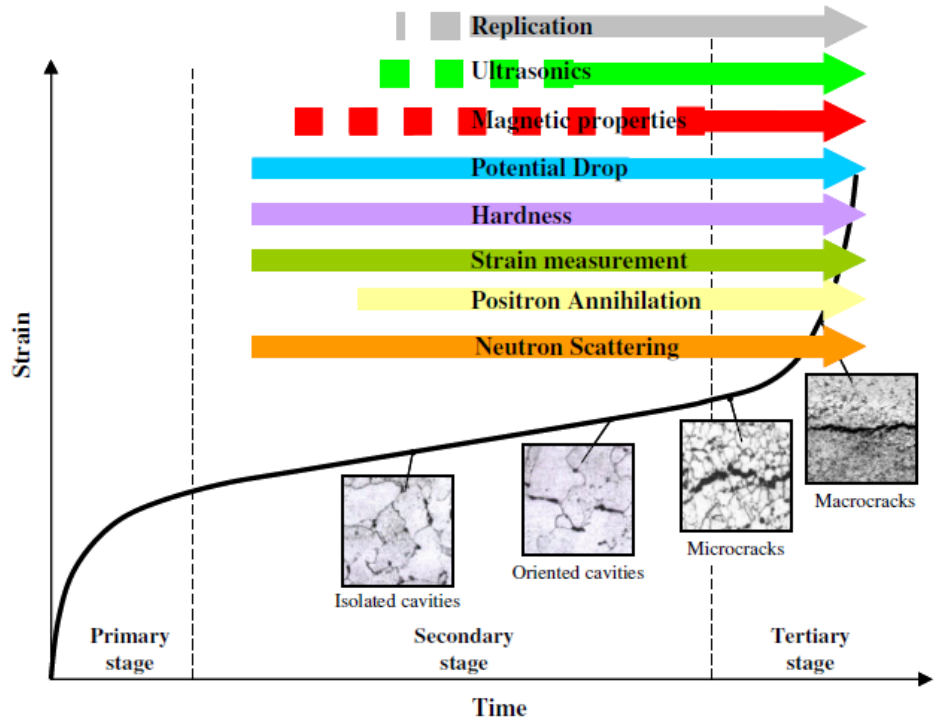

Figure 66: Typical creep curve showing a typical evolution of creep damage with a qualitative overview of NDT and their range of applicability [206]

The challenges associated with evaluating the remaining life of in-service P91 steels using common field inspection techniques are well known and these are summarized as: i) uncertainty in determining optimal and necessary locations for inspection, ii) defining the optimal time to perform inspections and to conduct preventive maintenance in order to ensure integrity of plant operations, iii) selection of the best combination of NDTs able to detect early stages of creep damage, iv) criticality of operations, skilled workforce and cost [9, 290]. As a result of this, in practice the long-term creep life on operating power plants has invariably shown to be below the design life extrapolated from short-term creep data, probably due to some differences in the metallurgical evolution [279, 291-293].

The challenge for field examination is how to detect meaningful changes in microstructure or physical properties from periodic inspections and with sufficient time to implement practical mitigations, which could be repairs, replacements or adjustments to operating conditions to maintain continued safe operation. An already mentioned in the previous chapters, the final aim is therefore the development of an optimal and integrated creep monitoring strategy that allows a reliable assessment of the remaining life of components operating under creep. The opportunity is to consider, and if possible develop, improved assessment models that reflect the in-service ageing characteristics and therefore provide an earlier and more reliable remnant life assessment.

Interrupted creep tests have been extensively performed both under short-term and long-term creep conditions at different temperatures and stresses to study the microstructural mechanisms responsible for material degradation [179, 207-210]. Short-term and long-term creep tests are in accord in the identification of primary processes that govern the microstructural evolution for 9-12% Cr steels, the key ones being the transformation of the original martensitic lath structure, reduction in dislocation density and coarsening of precipitates. Processes such as the precipitation of Z-phase and Laves phases are also observed under long-term creep exposure, but despite this, it has been argued that short-term creep tests are broadly sufficient in providing key information related to material degradation as a result of microstructural changes [207].

In this work, a series of interrupted creep tests at 660°C and 80 MPa have been performed on a service-aged P91 steel removed from a superheater pipe. After each test, the microstructure evolution is studied using TEM, SEM, EBSD, EDS and optical microscopy. TEM is used primarily for imaging of dislocation arrangement, nano-scale precipitates and sub-structure detection. SEM has been employed for fracture surface analysis, and for imaging of the distribution of large scale precipitates and of high angle boundaries (prior austenitic grains, packets and blocks). EBSD has been employed for analysis of crystallographic orientation and phase detection. EDS has been employed for chemical analysis of the identified phases and optical microscope for cavities count. Vickers hardness has been measured with a microhardness test machine.

In addition to the primary aim explained at the beginning of this introduction, another objective of this chapter is the investigation of the microstructural evolution and the degradation mechanisms responsible for the reduction in creep strength and hardness leading to the final fracture. The understanding of creep damage, strengthening and degradation mechanisms is of primary importance for power industry operators in order to assess the reliability of the components and their in-service life and to run the unit safely. Even if creep damage is often concentrated in HAZ for P91-based structures, a comprehensive study on the behaviour of the base material after service exposure is still lacking and therefore required [279, 294]. Finally, the potential of physics-based hardness models and how to use them in conjunction with other condition monitoring techniques for the purpose of life assessment will be discussed.

6.2 Methodology: material and experimental work

The P91 pipe material under investigation was removed from the HP Superheater Field Outlet tee manifold of a CCGT power station. The pipe operated under HP steam conditions that are 137 bar, 565°C and, at the time of removal, the unit had run for 41,477 hours with 1,037 starts. The hoop stresses in the main steam pipework are estimated to vary between 63MPa to 77MPa. The material is P91 EN10216-2, X10CrMoVNb9-1 with the compositional specification as detailed in Table 21.

Table 21: Compositional specification of P91 steel

Element	**C**	**Si**	**Mn**	**Ni**	**P**	**S**	**Cr**	**Mo**	**V**	**N**	**Nb**	**Al**	**Fe**
min (wt%)	0.08	0.2	0.3				8	0.85	0.18	0.03	0.06		To balance
max (wt%)	0.12	0.5	0.6	0.4	0.025	0.015	9.5	1.05	0.25	0.07	0.1	0.03	

Cr provides oxidation and corrosion resistance and allows the formation of $Cr_{23}C_6$. Mo is added to improve the creep strength under high temperature conditions via solid solution strengthening. V, Nb promote the formation of MX carbonitrides with the purpose to increase the creep resistance through precipitation strengthening. Si has been found to be useful for the improvement of oxidation resistance. The addition of

Ni gives a better thermal resistance and, similarly to Cr, corrosion/oxidation resistance, improving at the same time the creep strength. Mn helps to stabilize the austenite phase [295-297]. The understanding of the significance of the chemical composition is extremely important as it affects the final microstructure and the creep properties of the material. EPRI published a guideline for the specification of alloying elements in 9-12%Cr steels as some of the elements cause susceptibility to cavity formation and are related to a reduction in creep ductility [298].

6.2.1 Creep tests

Uniaxial cylindrical creep specimens were machined out from the received tee material with a gauge length of 50 mm and gauge diameter of 10 mm. The dimensions of the specimen are shown in Figure 67.

All creep tests were performed in air in a creep testing machine equipped with a resistance furnace at 660 °C under a stress of 80 MPa, with the loading direction along the longitudinal axis of the specimen. The value of the applied stress was chosen to reflect the service hoop stress in the main steam pipework while the test temperature is higher than the operating temperature to reduce the test time. Three thermocouples positioned equally along the gauge length allowed to obtain a homogeneous temperature while a high-temperature extensometer was used to measure the creep strain.

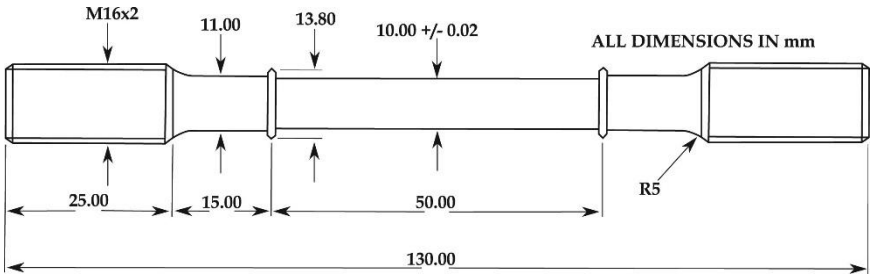

Figure 67: Uniaxial creep test specimen [175]

A total of four creep tests were conducted and the corresponding creep strains with times are recorded in Table 22. A continuous creep test until failure (t_r) was first conducted, followed by interrupted creep tests at selected time ratio $t/t_r = 0.43, t/t_r = 0.9, t/t_r = 0.98$. For the complete test, the failure occurs at 3,281 hours. The interrupted creep tests have been selected intentionally in the secondary and

tertiary creep stages to monitor and investigate the evolution of the main microstructural factors affecting the properties of the macrostructure. It is known that the microstructure changes rapidly in the tertiary stage, and so detailed microstructural characterisation was performed on each sample (see section 6.2.2).

Table 22: Creep strain and life fraction obtained from creep rupture and interrupted tests at 80MPa and 660°C

Test Conditions	Creep Tests	Creep strain [%]	Time [hours]	t/t_r
σ = 80 MPa T = 660°C	1	2	1,500	0.43
	2	4	2,950	0.9
	3	7	3,213	0.98
	4 (failure)	21.4	3,281	1

Creep strain versus time and creep strain rate versus life fraction are reported in Figure 68. The creep rate was calculated from raw creep data using the moving average function in Matlab over 60 neighbouring points.

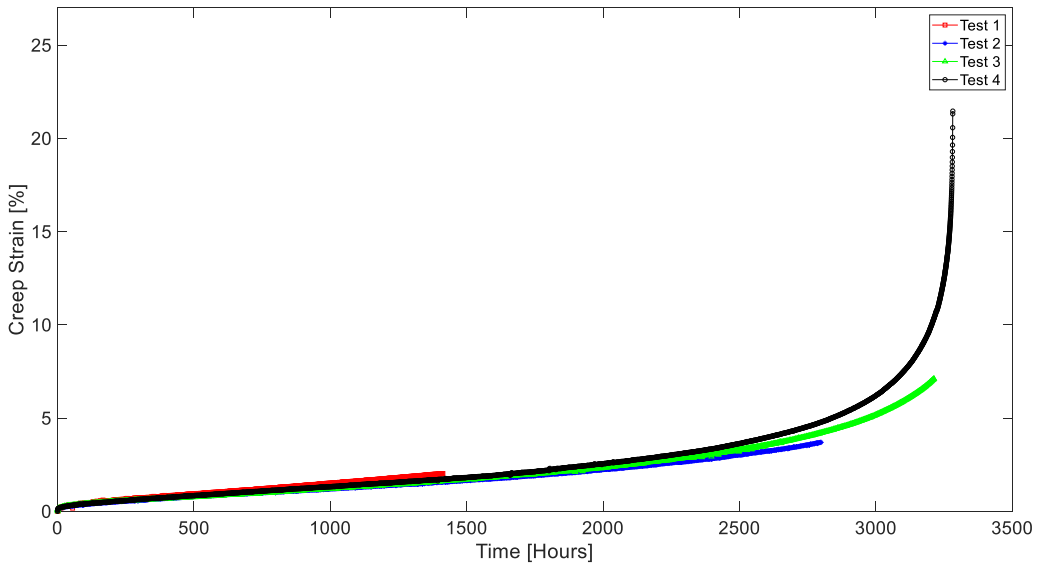

(a)

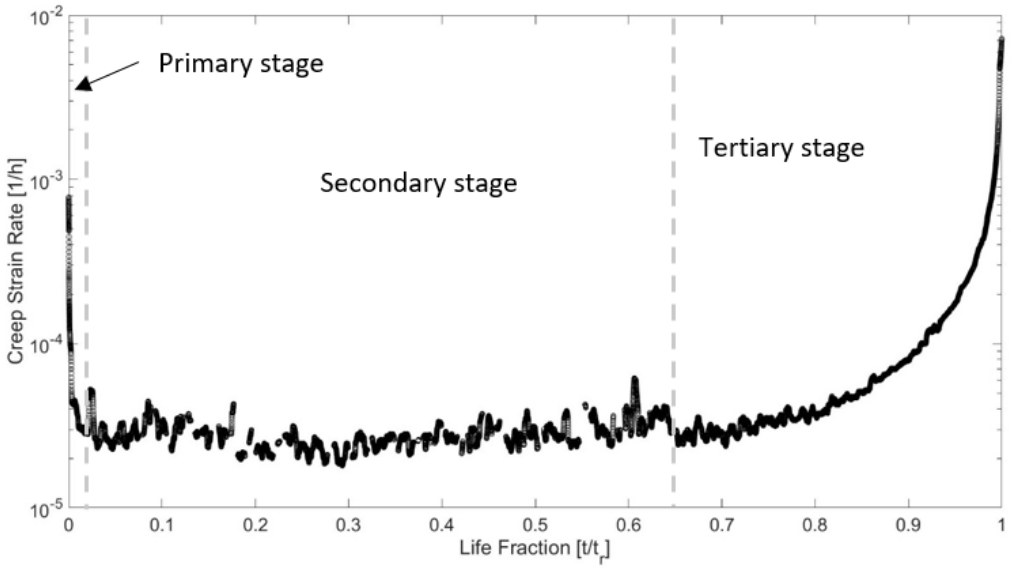

(b)

Figure 68: Interrupted creep tests at 80 MPa and 660°C, (a) Creep strain-time curves, and (b) creep strain rate-life fraction curves for Test 4 (test to failure)

6.2.2 Microstructural investigation techniques

After creep tests, the samples for microstructural investigation were obtained by cutting the specimen in the gauge region perpendicularly to the direction of loading application. Sections were taken close to the middle of the gauge section and specifically in regions where cracks had started to appear on the external surface in samples which had entered tertiary creep. After cutting and hot mounting in Bakelite resin, the sample cross-sections were ground with silicon carbide papers and polished with diamond paste, followed by colloidal silica. Etching with Villella's reagent was conducted only for samples used in SEM and optical microscopy. The microstructure was studied with a range of techniques.

Electron backscatter diffraction (EBSD) and energy dispersive x-ray spectroscopy (EDS) techniques were used to understand the changes in the crystallographic orientation of the sample and to characterise the variations within the crystal structure in terms of size and nature of phases. This was conducted with a JEOL JSM-7100F field emission gun scanning electron microscope (SEM) fitted with an Oxford Instruments AZtec EBSD and EDS system, using NordlysMax3 and X-Max 150 detectors. The following settings were used: SEM – accelerating voltage 15 kV, probe

current 2 to 3 nA, working distance 16 to 17 mm, sample tilt 70°; EBSD – binning 4x4, exposure time 47 to 55 ms, gain 3 to 5, averaging 2 to 4 frames, static and auto background subtraction, Hough resolution 64, detecting band centres, 8 bands, refined accuracy indexing mode, TruPhase identification with reference EDS spectra; EDS – energy range 20 keV, 2048 channels, process time 4. For EBSD indexing the phase definitions were: from AZtec's HKL Phases database – Iron bcc [105]; from the Inorganic Crystal Structure Database – $Cr_{23}C_6$ (ICSD-62667 [299]), Fe Mo Si (ICSD-53434 [300]), Nb N.58 (ICSD-40075 [301]). The cubic ferrite phase was used for indexing the tetragonal martensite matrix because the technique is insensitive to small changes in lattice parameter ratios.

The mapping was conducted at different scales: 400 μm square with a step size of 0.8 μm to reveal the texture and general microstructure, 100 μm square with a step size of 0.3 μm to assess grain boundary misorientation and reconstruct PAGs, and 20 μm square with a step size of 0.075 μm to show the details of the microstructure including precipitates.

The raw maps were processed using Oxford Instruments AZtec and AZtecCrystal software. In AZtec the Analyze Phases tool was used to generate typical spectra for each phase from the map data. The EBSD maps were processed with AZtecCrystal, using the Auto Clean-up routine to remove wild spikes and some zero solutions. Pole figures were generated for the matrix phase with a contouring half-width of 10° and equal area upper hemisphere projection. Texture component maps were generated for the matrix phase, yielding area fractions. Kernel average misorientation maps were generated for the matrix phase with a 3x3 kernel and a maximum angle of 20°. This angle was chosen because it included over 99.95% of pixels in the map with the widest misorientation distribution. The 'Parent Grain' analysis tool in Oxford Instruments AztecCrystal software was used for the reconstruction of PAGs from the child martensitic microstructure. A Kurdjumov-Sachs (K-S) parent-child orientation transformation has been selected since it is known to yield the best prediction of the crystallographic orientation between the austenite (parent) and the resulting martensite (child) phases [210, 302]. Following the K-S distribution, the grain boundaries created during the transformation that have a misorientation angle < 20° are defined as low-

angle boundaries (LABs) with high-angle boundaries (HABs) being defined as having a misorientation angle > 20° and showing a peak in the region 30-60°.

The as-service-exposed and fractured P91 samples were observed also using the FEI Quanta600 SEM using secondary electrons (SE) and backscattered electrons (BSE) in order to investigate the distribution of large precipitates along the grain boundaries, to study the topography of the ruptured surface and the typology of cavitation damage. The SEM had a tungsten filament electron source and was operated at an accelerating voltage of 20 kV. For SE imaging, spot sizes of 4.0 and 4.5 were used, and working distances from 13 to 19 mm. For BSE, spot size 6.0 and working distance 9 mm were used.

For transmission electron microscopy (TEM), thin lamellae were extracted from the bulk material of each sample using a FEI Quanta 200 3D focussed ion beam (FIB) SEM. The samples were thinned to under 200 nm, and then polished with a 5 kV ion beam to reduce beam damage using a Zeiss Crossbeam 550 FIB-SEM. Imaging, diffraction and EDS mapping were carried out on a JEOL JEM-2100Plus TEM at 200 kV, with Gatan OneView camera and Oxford Instruments EDS system. A double-tilt sample holder and 20 μm objective aperture were used to obtain two-beam {110} bright field (BF) images showing dislocations and other defects. These are marked with the diffraction vector **g** for the grain at the centre of the image. The thickness of the lamella at each location was calculated by the Kelly-Allen technique from the spacing of the fringes in the convergent beam electron diffraction (CBED) patterns which were collected using {221} and {200} Kikuchi bands using spot size 2 nm, alpha 3 and camera length 500 mm. The thickness measurements were used for the estimation of the dislocation density with the line intercept method. Scanning TEM (STEM) BF images were collected with a 50 μm condenser aperture, spot size 4 and camera length 800 mm, to observe the nanoscale precipitates which are not visible with the SEM. EDS maps were collected to identify the precipitate phases.

Optical microscopy (OM) was used to show the distribution of cavities and the images captured from OM were used in ImageJ software to analyse and count cavity density. The microscope used is Nikon Eclipse LV100ND with a Nikon DS-Ri1 camera attached that uses a Nikon LV-NCNT 2 motorised magnifier. The software used to

process the images is the Nikon NIS-Elements calibrated by laboratory technicians. The processing of images with NIS-Elements included adding a scale bar to have size information and adjusting the focus, brightness and contrast to achieve high-resolution imaging. The images captured with OM were then imported into ImageJ software where firstly the scale was set using the known distance from the scale bar of the OM in order to present measurement results in calibrated units. Then, the adjust threshold black and white function was used to have the features (cavities) displayed in black and the background in white, any white dots found in the middle of the cavities were filled with the fill holes step and finally the Analyze Particles tool was employed on the entire image to obtain information about the count, the area and the size of cavities.

Vickers microhardness testing was employed to measure the hardness of each P91 sample using a load of 1 kgf applied for 10 seconds. For every sample, the measurement was repeated 10 times at different locations to reduce the observational error. The microhardness tester used was a Buehler 1600 series set at 220 V AC. Hardness represents a practical method for investigating the softening mechanisms of the material as will be discussed later.

6.3 Results and discussion

6.3.1 Creep properties and mechanism

From the creep strain curves in Figure 68a and the associated creep strain rates in Figure 68b, it is noted that the primary creep stage is essentially negligible, while the secondary (steady-state) stage accounts for the largest portion of the specimen life (about 80%) before entering the tertiary stage with a rapid increase in creep rate and deformation until the final fracture. Since the temperature and the stress of the creep tests are kept constant, the variation in creep rate before the formation of necking is the result of changes in the internal structure of the material that occur due to creep strain and time at temperature.

Creep material properties can be deduced from the creep test curves. The value of the steady-state creep rate $\dot{\varepsilon}_{ss}$ and the value of the stress exponent n, obtained from the logarithmic form of the Norton's law (Equation 97) once the creep constant A is known, are reported in Table 23.

$$\dot{\varepsilon}_{ss} = A\,\sigma^{n} \tag{97}$$

The value of A is taken from [303] and the value of the shear modulus G is obtained from the relationship $G = E/2 * (1 + \upsilon)$ where the Young's modulus $E = 218$ GPa at room temperature, typical for P91 [304], and the Poisson's ratio $\upsilon = 0.3$ [305].

Table 23: Creep properties associated with the creep curve (stress in MPa and time in hour)

$\dot{\varepsilon}_{ss}$ [h^{-1}]	A	G [GPa]	σ/G	n
1.1×10^{-5}	2.004×10^{-20}	83.85	0.95×10^{-3}	7.7

The calculated parameters σ/G and n suggest that the main creep deformation mechanism operating is dislocation (power-law) creep [15]. Dislocation creep is a result of the climb of dislocations that overcome obstacles aided by thermally activated mechanisms involving the diffusion of vacancies or interstitials [278, 306, 307].

6.3.2 As-service-exposed P91 material

The SEM SE image in Figure 69a shows that the as-service-exposed material has the complex hierarchical structure typical for P91 composed of martensitic laths of the same crystallographic orientation contained inside blocks. The blocks are in turn contained inside packets. Different packets form the prior austenitic grain (PAG) from which the martensite originates after quenching. The average PAG size is 22 μm and the lath width in the as-service-exposed condition is 0.75 μm, values consistent with a typical P91 steel [210, 308, 309]. The martensitic matrix was indexed as ferrite (body-centred cubic (BCC)) in the EBSD maps due to the technique being insensitive to small changes in the c/a ratio. LABs surround laths and sub-grains with misorientation angles < 20° while blocks, packets and PAGs are enclosed in HABs [310, 311]. The average misorientation angles for PAGs are in the range of 30-50° for the as-service-exposed material (Figure 69b).

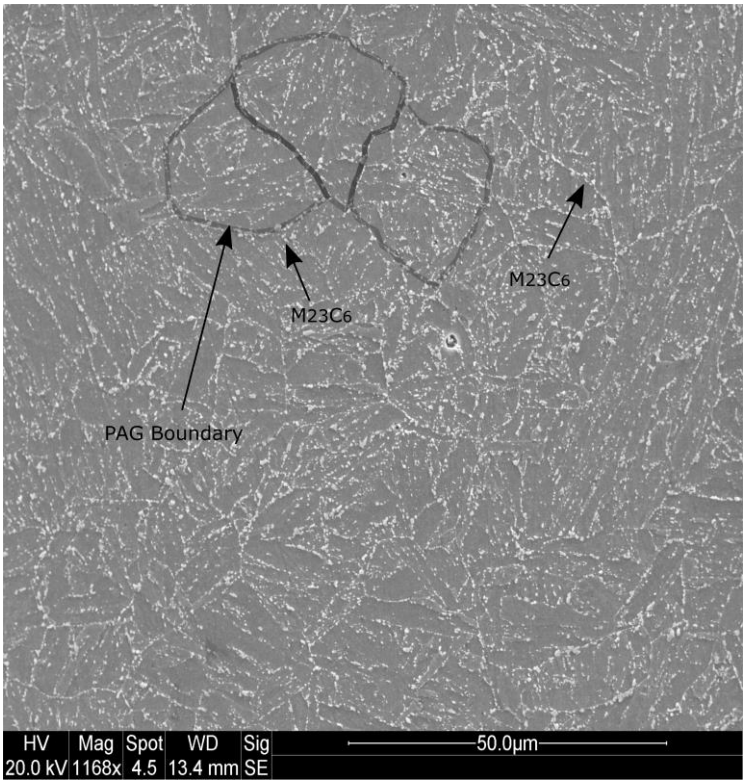
M23C6
M23C6
PAG Boundary
HV Mag Spot WD Sig
20.0 kV 1168x 4.5 13.4 mm SE
50.0µm

(a)

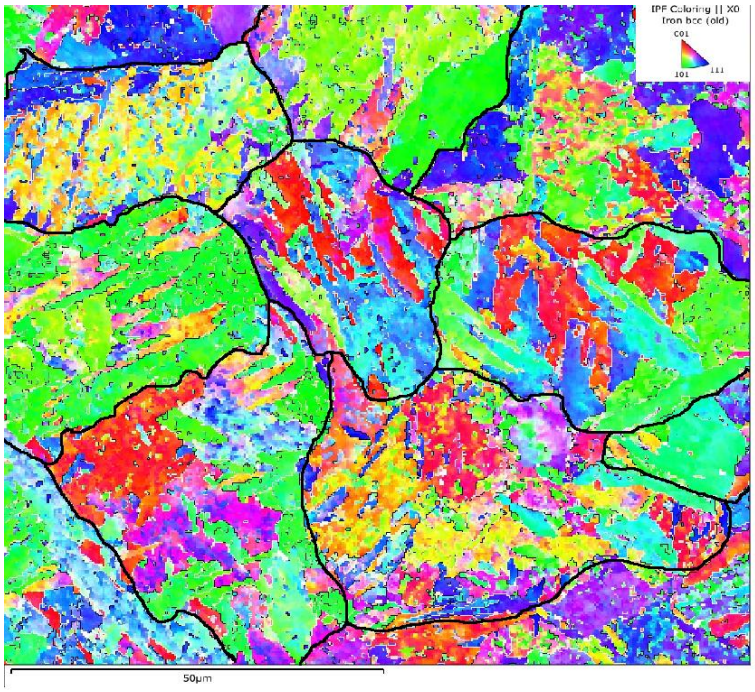
50µm

(b)

Figure 69: Micrographs of as-service-exposed P91 material (a) SEM SE showing PAGs studded with $M_{23}C_6$ particles at grain boundaries, and (b) EBSD orientation map providing an overview of the microstructure. The prior austenite grain boundaries are highlighted in black

The TEM analysis reveals stable sub-grain structures in the laths as shown by the dotted lines in Figure 70a. This suggests that the material under service conditions at high temperature is in a static recovery form in which the mobile dislocations inside the laths have moved along activated slip planes overcoming obstacles by thermal activation and by thermally assisted mechanisms such as vacancy diffusion [312]. As a consequence, the re-arrangement of mobile dislocations occurs and a well-developed sub-grain structure has developed in order to minimize the high elastic energy stored in the microstructure [313, 314]. The sub-grain boundaries are therefore formed by a wall of dislocations that hinder the movement of the other free dislocations contained inside the laths, significantly increasing the creep resistance [315]. The as-manufactured P91 steel after the typical heat treatments of normalizing and tempering shows a lath martensitic structure which contains a large number of dislocations but sub-grains are not expected to form [6, 316]. The formation of sub-grains within the laths occurs during the exposure to creep and add further strengthening to the material [175].

The static recovery condition can explain why the creep tests of the service-exposed material exhibit a negligible primary creep stage since recovery is a process that characterizes the secondary creep stage [15]. Dislocation density in the lath interior in the as-service-exposed state is high as visible in Figure 70b and dislocation tangles are observed. The initial dislocation density has been calculated as being 1.6×10^{14} m^{-2} using the line intercept method [315]. This value is approximately three times lower than that of as-received P91 material reported in [208] and in [317] and this is attributed to static recovery [208].

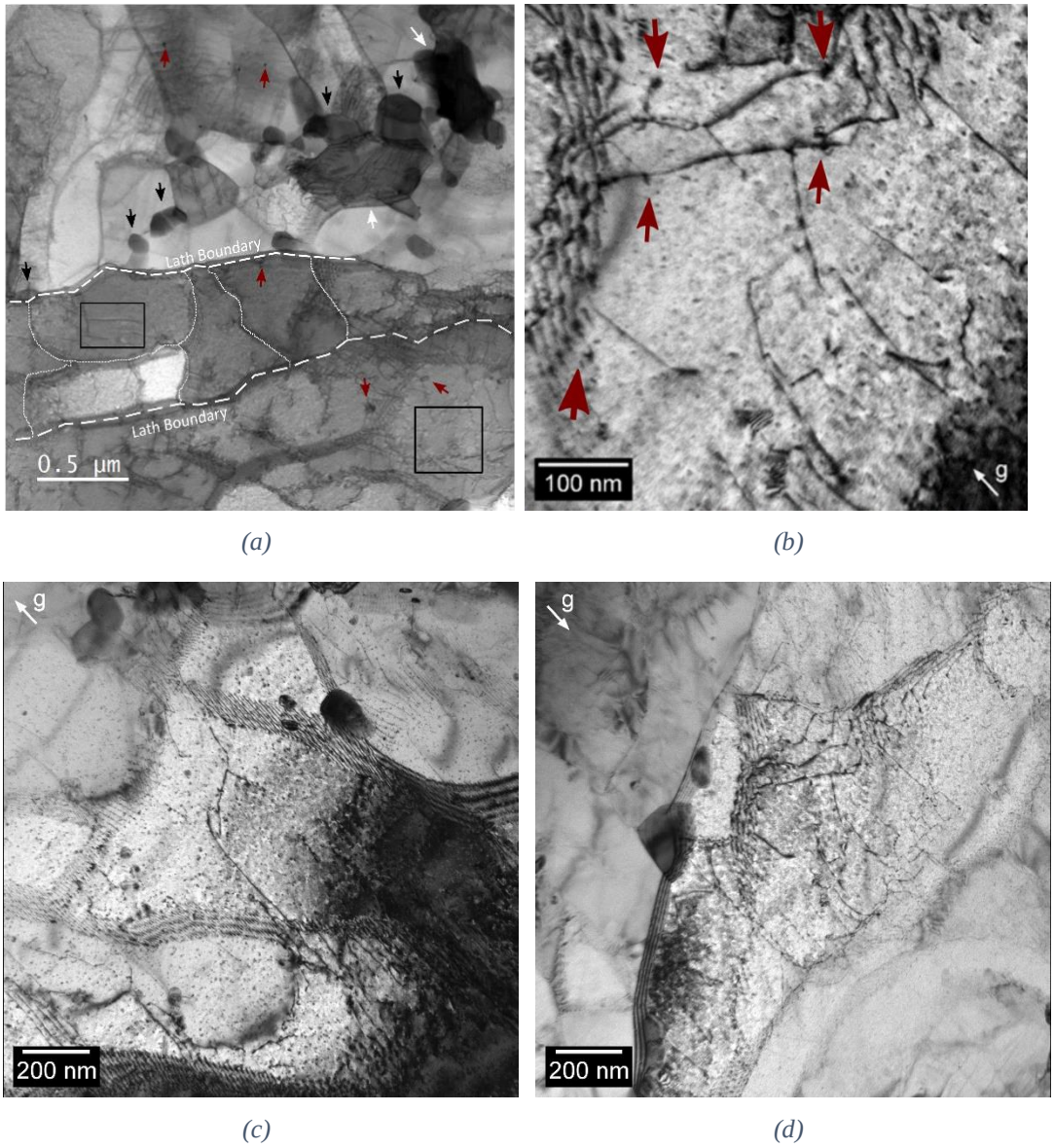

Figure 70: (a) STEM BF image of the as-service-exposed P91 material showing lath and sub-grain boundaries (dotted lines) and precipitates (red arrows for MX, black arrows for $M_{23}C_6$, white arrows for Laves phase). Square box to identify mobile dislocation inside the sub-grains, (b, c, d) Two-beam BF TEM images showing (b) line dislocations pinned by MX, (c) stabilization of sub-grains by MX and $M_{23}C_6$, and (d) $M_{23}C_6$ stabilizing effect on lath structure

In terms of precipitates, the as-service-exposed sample has been found to be characterized by a fine distribution of $M_{23}C_6$ carbides, where M is predominately rich in Cr with traces of Fe and Mo (Figure 70 and Figure 71), along with nano-scale Nb/V-rich MX carbonitrides that are best detected using TEM due to their small size (Figure 70a/b). $M_{23}C_6$ are located along LABs and HABs while MX are found to be distributed inside the laths in the sub-grain structure and in a lower measure along LABs. MX particles are pinning sites for the mobile dislocations as can be seen in Figure 70b,

strongly increasing the creep strength of P91 via precipitation strengthening [294, 318]. Also, $M_{23}C_6$ and MX that are spread along grain boundaries (GB) stabilize the microstructure, retarding the migration of the GBs under service conditions, and thus highly increasing the resistance to static recrystallization and grain growth (Figure 70c/d) [319].

MX carbonitrides and $M_{23}C_6$ carbides precipitate out in the initial martensitic microstructure from the supersaturated solid solution after quenching and tempering heat treatments. As reported from previous studies, $M_{23}C_6$ carbides nucleate copiously along grain boundaries (GB) favoured by the misorentiation between adjacent grains and the orientation of the GB [320, 321]. The $M_{23}C_6$ precipitates have a specific crystallographic orientation relationship indicating a coherent interface with at least one of the adjoining grains for which the boundary plane is close to the plane of the precipitate [322, 323]. MX carbonitrides precipitate mainly in the interior of the martensitic laths thanks to the coherency between their lattice and the surrounding ferritic matrix [318].

$(Fe,Si)_2Mo$-type Laves phase enriched in Fe, Mo and Si, with an average initial size of 300 nm is also identified mostly along PAG boundaries and partially on lath boundaries (Figure 70a, white arrow). $(Fe,Si)_2Mo$-type Laves phase is formed and results in depletion of Mo in the matrix causing a reduction of the material solid solution hardening during service conditions [293]. Other studies report that the precipitation of Laves phase is beneficial for the strengthening of the material at least in the early stage of creep deformation. Laves phase has a similar effect to $M_{23}C_6$, which increases the creep strength of the material by hindering grain boundary migration, thus retarding the growth of sub-grains [220, 285, 324]. The nucleation of Laves phase is accelerated by the presence of Si with Laves particles being found to form mostly in the proximity of $M_{23}C_6$ [325]. Two main mechanisms contribute to the nucleation of Laves phase. On one side, Si and Mo have a tendency to segregate to GBs and when the saturation of these elements is reached, Laves phase appears. On the other hand, $M_{23}C_6$ located along GBs act as preferential nucleation sites for Laves phase [220, 295, 325]. In virgin as-manufactured P91 steel, Laves phase is not observed, but it tends to precipitate after long-term creep with creep lives of around 1,500 hours at temperature higher than 600 °C [220, 316].

The compositional makeup of the different precipitates is reported in Figure 72. It is likely that the spectra for the precipitate phases include a contribution from the surrounding matrix, so quantification of the concentrations is not appropriate. However, the differences between these spectra and the matrix spectrum indicate which elements are present in the precipitates.

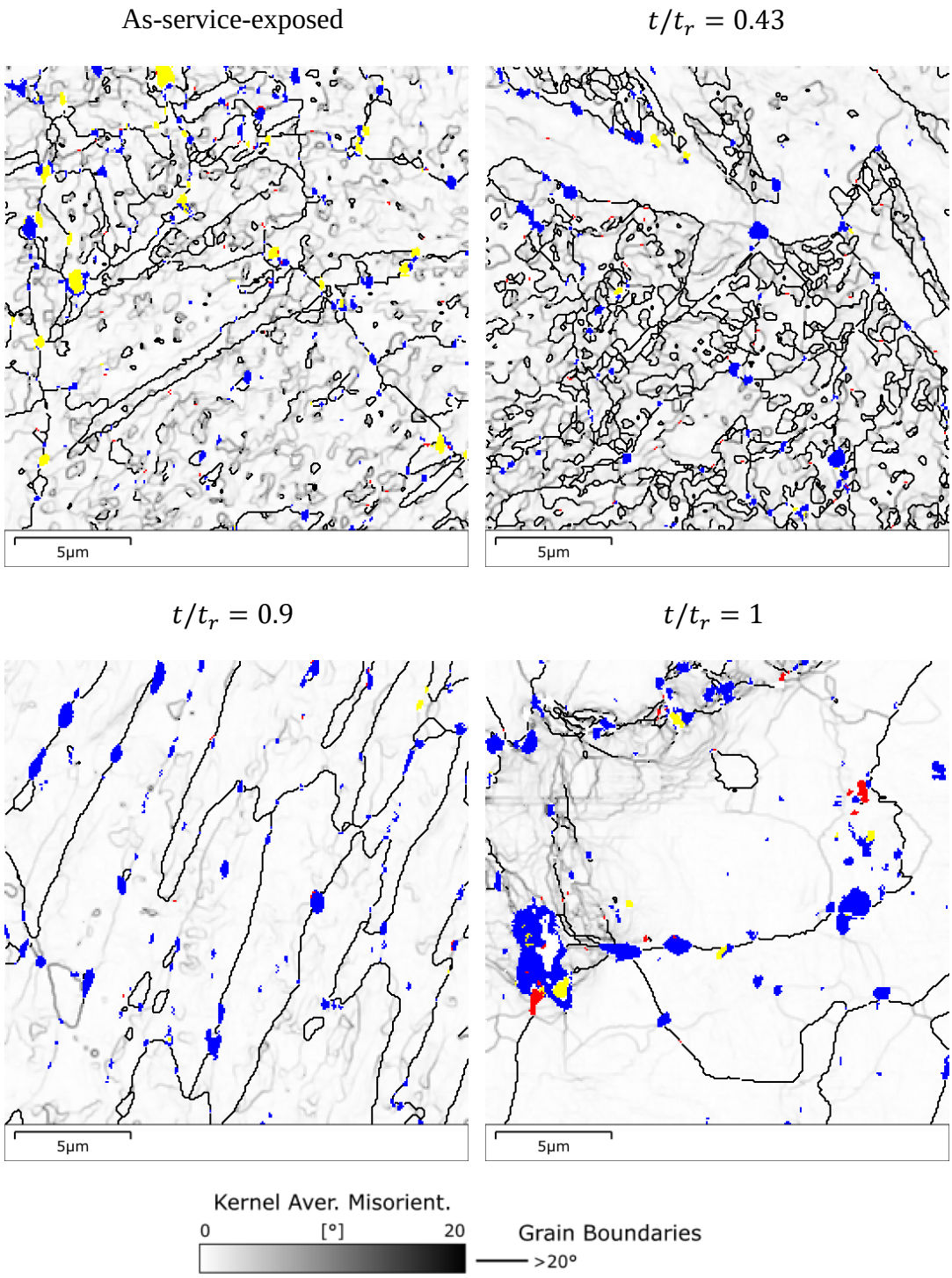

Figure 71: Layered EBSD images with kernel average misorientation colouring and grain boundary lines for the matrix, and phase colouring for secondary phases, showing the distribution and evolution of $M_{23}C_6$ (blue), MX (red) and Laves phase (yellow).

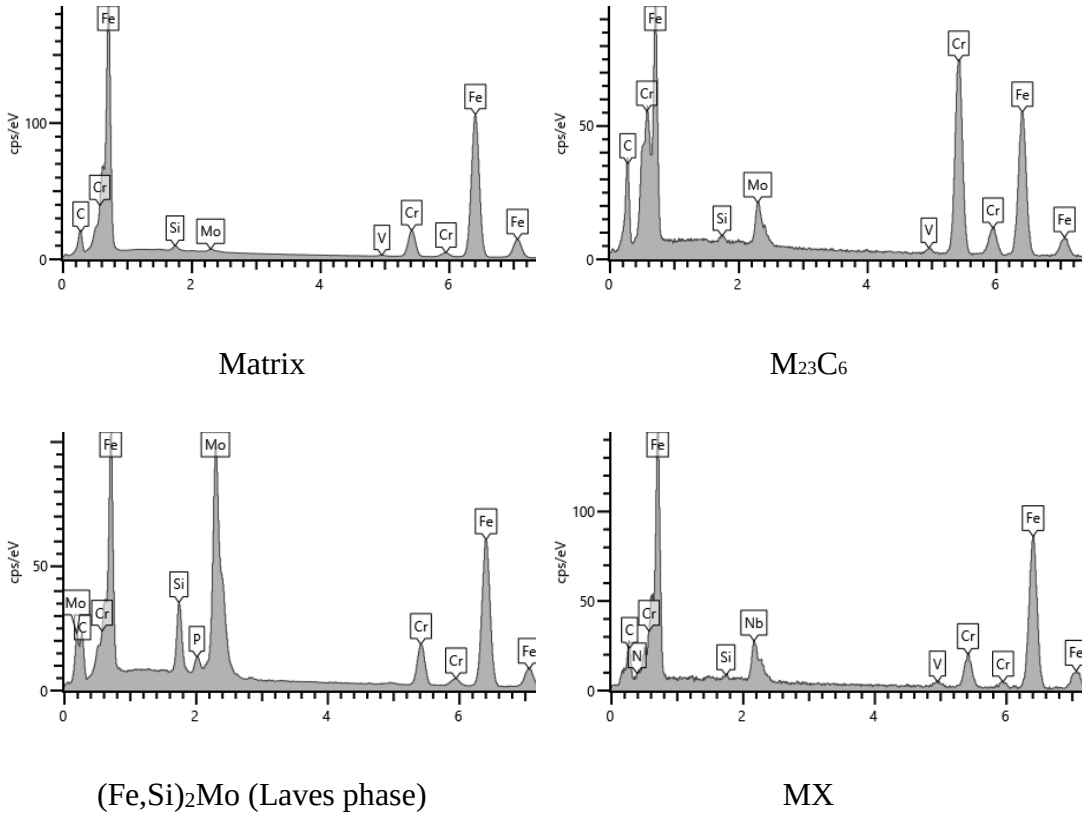

Figure 72: SEM-EDS analysis of the composition of the four main phases observed in the maps in Figure 71

Summarizing, the creep strength in P91 alloys is achieved by the following microstructural strengthening mechanisms, all of which are still operative in the as-service-exposed alloy:

- Lath and sub-block martensitic structure;
- Finely distributed MX and $M_{23}C_6$ boundary precipitates that block the grains from migrating by pinning them;
- $M_{23}C_6$ boundary precipitates impede knitting reactions between free dislocations and sub-grains dislocations;
- Finely distributed MX in the ferritic matrix that obstruct the movement of mobile dislocations;
- Substitutional solid-solution by Mo in the matrix that impedes dislocation climb and glide.

6.3.3 Microstructure evolution under post-service (laboratory) creep deformation

To study the relationship between the post-service (laboratory) creep deformation and the related microstructural evolution of P91, a series of EBSD maps have been collected and processed to show misorientation angle (MA) and inverse pole figure (IPF) colouring, with corresponding pole figures (PF). TEM images were also captured for the interrupted and test-to-failure laboratory creep tests. As noted previously, regions of the creep specimens investigated are perpendicular to the loading direction during the creep tests and chosen in the proximity of the highest strained area or where a crack was visible.

6.3.3.1 Disappearance of sub-grains, lath widening and formation of new grain structures

The results from EBSD mapping are shown in Figure 73 and Figure 74. The results for the failed specimen refer to the bulk material ~ 10 mm away from the fractured surface.

The IPF map for the as-service-exposed material has a high proportion of blue colouring (Figure 73a), indicating that the ⟨1 1 1⟩ direction of the matrix crystal structure is frequently orientated parallel to the Z-direction (the axis of loading) of the sample. The PF in Figure 73b reveals that this is a fibre texture with the ⟨1 1 1⟩ direction aligned to the Z-axis of the sample, which must be due to the original manufacture of the component. In Test 1 at $t/t_r = 0.43$ (secondary creep stage), there is a substantial strengthening of this texture, as shown by the increase in ⟨1 1 1⟩ pole density on the Z-axis in the PFs (from 5.2 times uniform density to 11.1 times). At the onset of the tertiary creep stage (Test 2 at $t/t_r = 0.9$) and continuing until failure (Test 4), the IPF-Z maps are less dominated by blue colouring, meaning that a change in the crystallographic orientation of the material has happened. The EBSD images in Figure 71 also highlight an evolution of the microstructure from typical lath martensite until $t/t_r = 0.9$ (Test 2) to the appearance of new more equiaxed grains at fracture (Test 4).

In the corresponding PFs there is a reduction of the concentric pattern associated with fibre texture, and at failure it has disappeared altogether, leaving what appears to be a random distribution of orientations.

The strength of the fibre texture is quantified in terms of map area fraction in Table 24. The fraction corresponding to the texture increases by a multiple of 1.8 from the as-service-exposed specimen to $t/t_r = 0.43$, then reduces to below the initial value at $t/t_r = 0.9$, and reaches a value close to random orientation by failure.

In terms of grain boundary misorientations, there is a decrease of misorientation between 2° and 20° during creep deformation as underlined by kernel average misorientation maps in Figure 74 where the blue colouring on the map increases. Although the individual boundaries are not well resolved at this scale, the maps in Figure 71 (at 0.075 µm step size) show that this range of misorientation is chiefly due to LABs. This suggests a strong reduction in the density of LABs from Test 1 ($t/t_r = 0.43$) to Test 2 ($t/t_r = 0.9$), and in Test 4 they are almost entirely absent. This means that at tertiary creep stage, the sub-grain structure has disappeared and is replaced by a new microstructure.

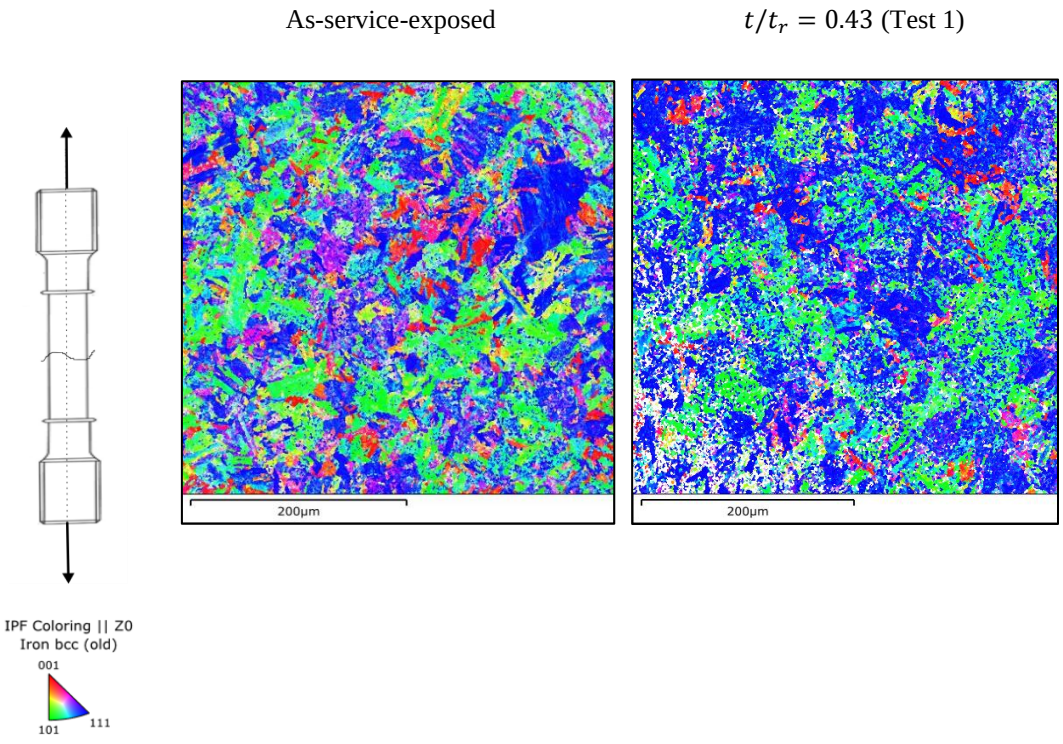

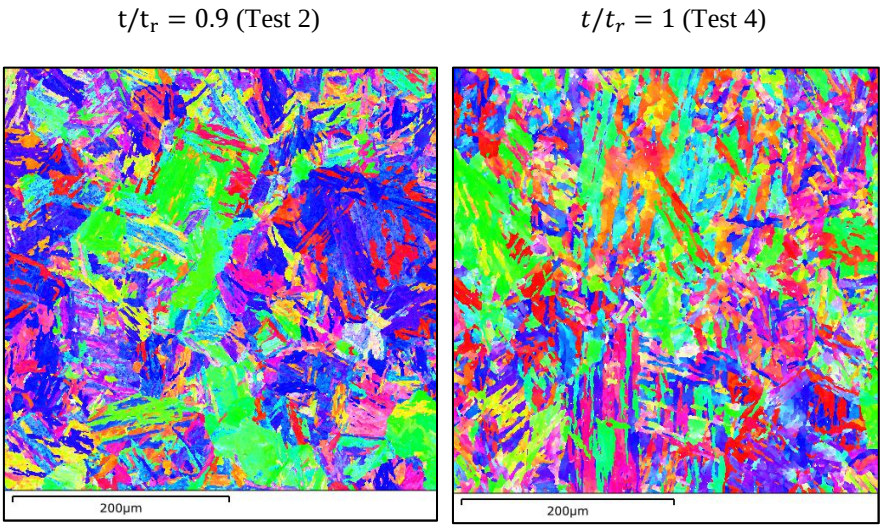
$t/t_r = 0.9$ (Test 2)
$t/t_r = 1$ (Test 4)
200μm
200μm

(a)

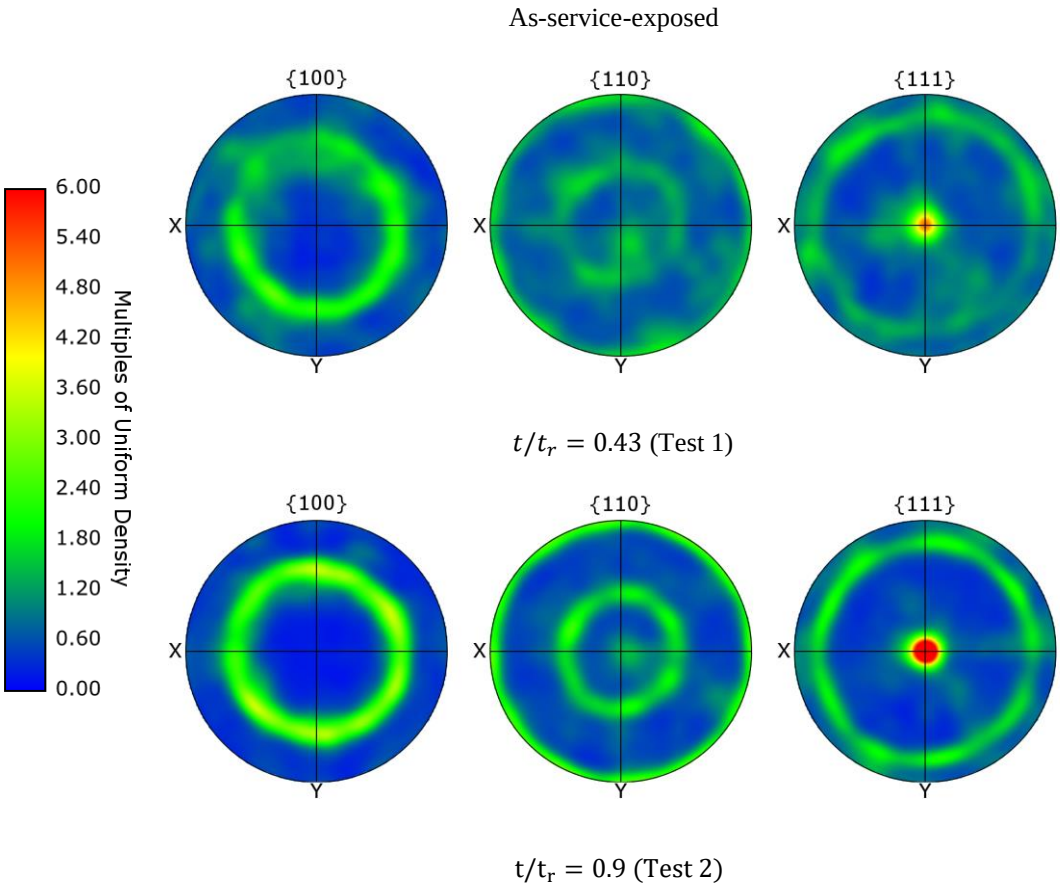
As-service-exposed
{100}
{110}
{111}
X
Y
6.00
5.40
4.80
4.20
3.60
3.00
2.40
1.80
1.20
0.60
0.00
Multiples of Uniform Density
$t/t_r = 0.43$ (Test 1)
$t/t_r = 0.9$ (Test 2)

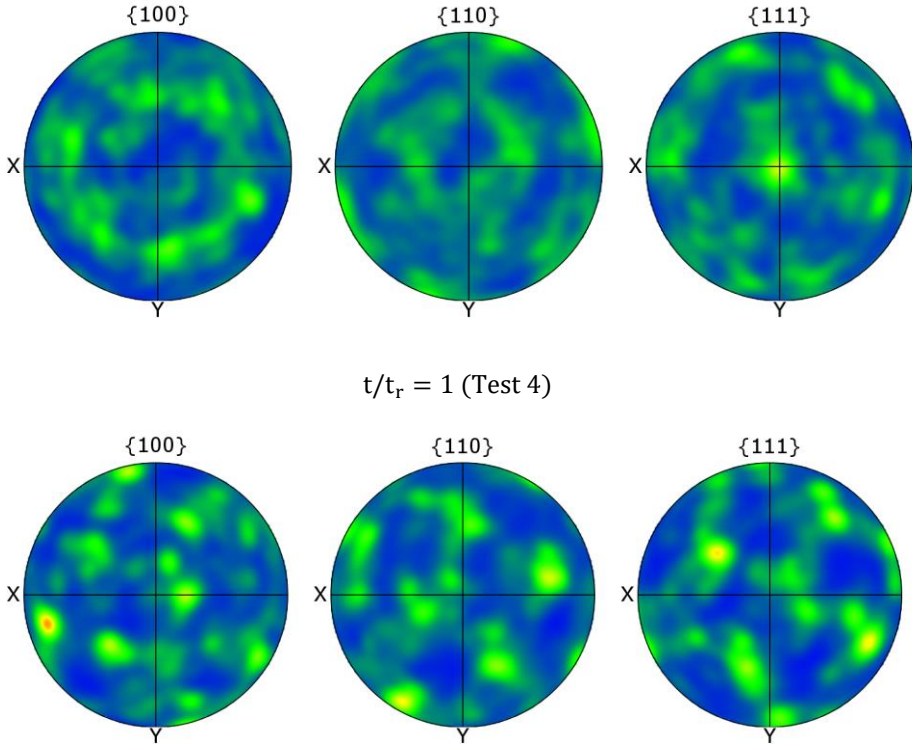

(b)

Figure 73: (a) IPF-Z maps and (b) Contoured PFs (upper hemisphere, equal area projection) for the matrix phase for the as-service-exposed P91 and for the same material after three subsequent creep test exposures as indicated.

Table 24: Area fractions of the maps in figure 7 that are within 10° of the fibre texture ⟨1 1 1⟩ ∥ Z

t/t_r	**Area fraction (%)**
As-service-exposed	23.3
0.43	41.8
0.9	17.3
1	5.3
Random orientation	6.1

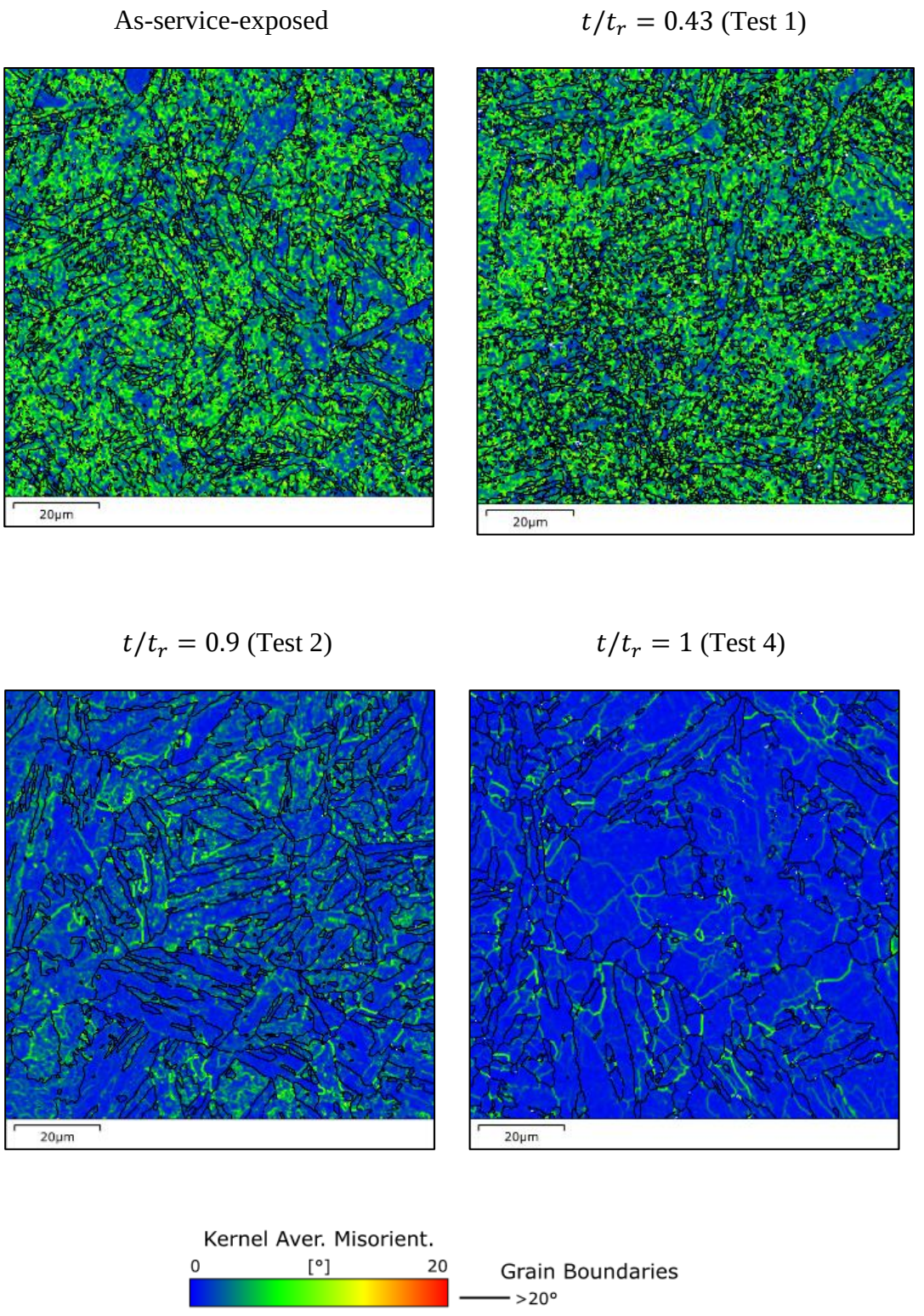

Figure 74: Kernel average misorientation maps for the as-service-exposed P91 and for the same material after three subsequent creep test exposures as indicated. See Figure 75 for more detailed misorientation maps.

To further investigate the evolution of sub-grains and laths and to confirm the outcomes from EBSD mapping, TEM analysis has been performed (Figure 76). The P91 steel following Test 1 creep ($t/t_r = 0.43$) still exhibits a sub-grain and lath structure not very different from the as-service-exposed state but where the lath width (Table 25) is slightly larger (Figure 76a). Following Test 2 ($t/t_r = 0.9$), rapid microstructural changes happen that cause the creep rate to increase after reaching its minimal value. After Test 2, the sub-grain structure is broken with MX carbonitrides losing their capability of pinning sub-grain boundaries. Sub-grains have almost disappeared while laths are still present but are wider compared to the material following Test 1. The lath width in the materials from Test 2 is on average 1.3μm (Figure 76b). Progressing to Test 3 ($t/t_r = 0.98$), a new microstructure composed of equiaxed grain structures is observed while the laths have now disappeared (Figure 76c). As the creep test progresses until creep failure (Test 4), the original martensitic structure is completely transformed into the newly microstructure with equiaxed grains (Figure 76d) [295]. This new microstructure is very similar to a typical hot-deformed structure suggesting that some form of dynamic recrystallization has taken place as the material approached failure after the occurrence of necking. The neck region is characterized by a local increase in creep rate due to a higher local stress that favour the transition to this type of microstructure [293, 319]. This is an interesting phenomenon already known for other high stacking fault energy materials such as martensitic stainless steel [326] but it is still not well understood for P91 steel, which will require further investigation [327]. Regardless, the equiaxed grain structure is not supposed to significantly influence the lifetime of the material since it is developed at the end of the tertiary creep stage just before failure when gross changes in microstructure have already taken place [293].

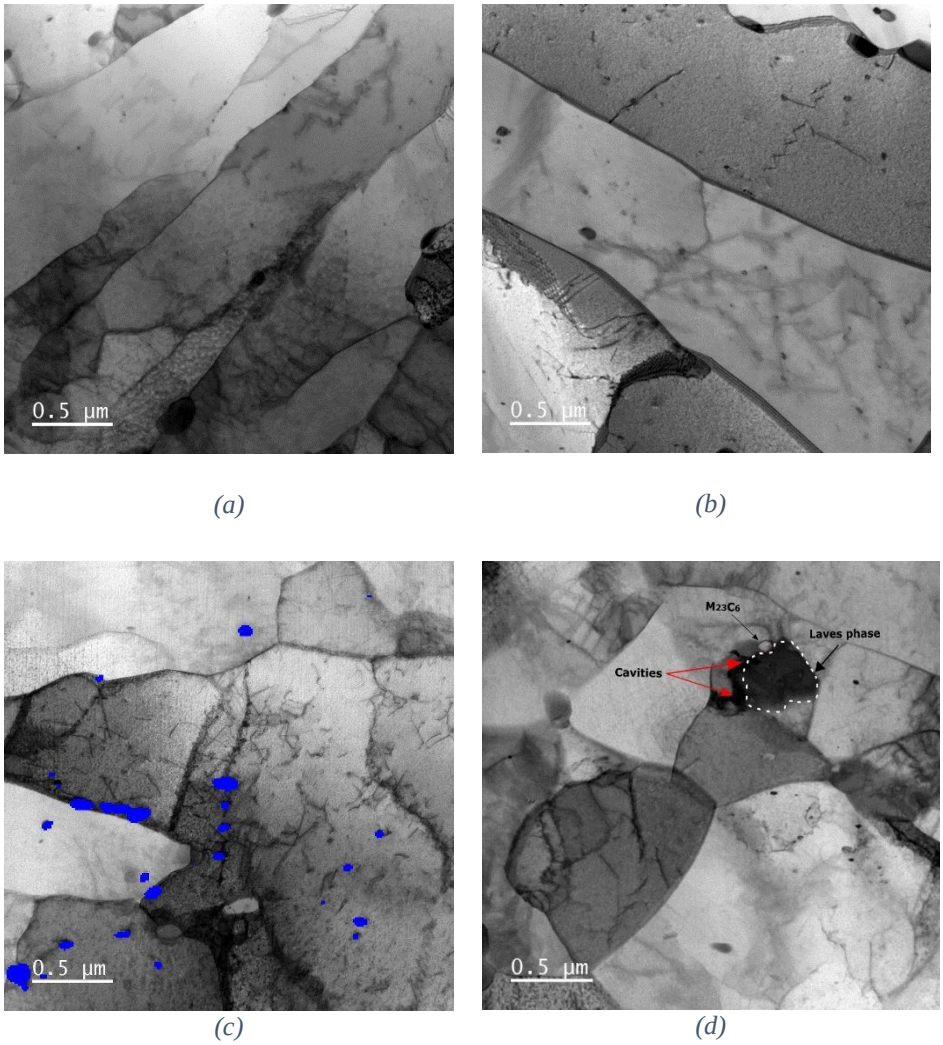

Figure 76: BF STEM micrographs (camera length 800 mm) showing the evolution of as-service-aged P91 microstructure following creep (a) Test 1 $t/t_r = 0.43$, (b) Test 2 $t/t_r = 0.9$ with visible MX inside the lath, (c) Test 3 $t/t_r = 0.98$ showing the formation of equiaxed grains (blue spots for V-rich MX), and (d) Test 4 $t/t_r = 1$ showing the complete transformation to an equiaxed grain structure

The presence in the matrix of these equiaxed sub-grains after creep is also revealed and confirmed by SEM-BSE investigations (Figure 77). This finding is consistent with results presented by Panait et al. [293]. Figure 77 shows also the distribution of Mo-rich Laves phase particles after creep being identified as the bright particles in BSE imaging.

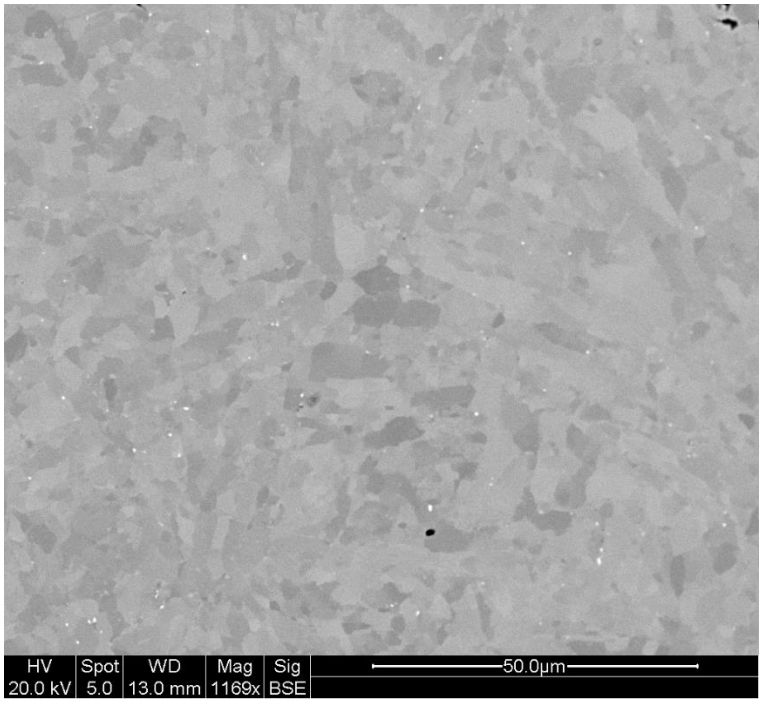

Figure 77: SEM-BSE of P91 sample at failure (Test 4) revealing equiaxed structures and Laves phase (white spots)

6.3.3.2 Dislocation density variation

The vanishing of LABs, the disappearance of sub-grains and the coarsening of the lath structure is explained by the annihilation theory introduced first by Eggeler and developed by Sauzay [308, 328]. Under creep conditions, mobile dislocations climb and glide along specific activated slip systems (according to the dislocation creep mechanism, see Paragraph 6.3.1) and interact with the boundary dislocations that form the sub-grain structure. When these two types of dislocations have an opposite sign, they annihilate each other. Also, mutual annihilation can occur in the case of two mobile dislocations that eliminate each other because of opposite sign [329, 330]. As a consequence, the dislocation density decreases accompanied by the disappearance of the sub-structure and the widening of lath structures [309]. This annihilation process is called dynamic recovery [317]. The variation of dislocation density is reported in Table 25.

Table 25: Density of mobile dislocation evolution, size of $M_{23}C_6$ precipitates, lath width and cavity density

	As-service-exposed	$\frac{t}{t_r} = 0.43$	$\frac{t}{t_r} = 0.9$	$\frac{t}{t_r} = 0.98$	$\frac{t}{t_r} = 1$
Dislocation density [x10^{13}m^{-2}]	16	6.5	5.8	4.9	2.6
$M_{23}C_6$ [nm]	120	140	154	198	250
Lath width [µm]	0.75	0.89	1.3		
Cavities [cavities/mm^2]	565	745	1300	2400	2800

The rapid decrease of mobile dislocations between the as-service-exposed state and following Test 1 (so during an early stage of creep deformation) is due to the dynamic recovery mechanism [179]. This high annihilation rate of mobile dislocations at the beginning of creep has also been stated in other experimental observations [293, 324].

Mobile dislocations are responsible for creep deformation. The relation between creep and dislocation density is governed by the Orowan equation reported below:

$$\dot{\varepsilon}_c = \rho\, b_1\, v \tag{98}$$

where $\dot{\varepsilon}_c$ is the creep strain rate, ρ is the density of mobile dislocations, b_1 is the Burgers vector, v is the average dislocation velocity. During dynamic recovery under creep, because of the decrease in dislocation density, the velocity of mobile dislocations increases and the final effect is an increase in creep rate [312, 317].

6.3.3.3 Evolution of precipitates

The analysis of the interrupted creep specimens shows an obvious size growth of $M_{23}C_6$ carbides. The average initial size of $M_{23}C_6$ in the as-service-exposed material is 120 nm whilst at fracture, this has increased to 250 nm, as reported in Table 25. The coarsening of $M_{23}C_6$ precipitates is followed by their coalescence as is shown in the EBSD images in Figure 71. Precipitate coarsening is driven by the increase in the lattice/particle surface interfacial energy that happens with creep at elevated

temperatures and long exposure times and follows the Ostwald ripening law [278, 331]. As a consequence of coarsening and coalescence, the stabilizing effect of $M_{23}C_6$ particles on LABs is lost, facilitating knitting reactions between free dislocations and dislocations at the boundaries of laths and sub-grains, which causes the substructure to disappear [294, 332, 333]. Thus, the dynamic recovery is affected by the distribution and size of $M_{23}C_6$ that give the major contribution to sub-grain stabilization. As well as dynamic recovery, the transformation to an equiaxed grain structure is also influenced by the distribution and size of precipitates in the microstructure. Coarse $M_{23}C_6$ particles are present along the equiaxed grains boundaries (Figure 78a) and it has been suggested that these particles conserve the same location as in their original martensitic lath and prior austenitic grain boundaries [327]. $M_{23}C_6$ precipitates represent a favourable position for the nucleation of the new grains due to dislocation pile-ups and tangles at the interface between precipitates and grain-boundaries that can trigger the formation of new grains (Figure 78b) [327, 334]. $M_{23}C_6$ coarsening and coalescence is one of the main creep degradation mechanisms leading to a rapid increase in the creep strain rate.

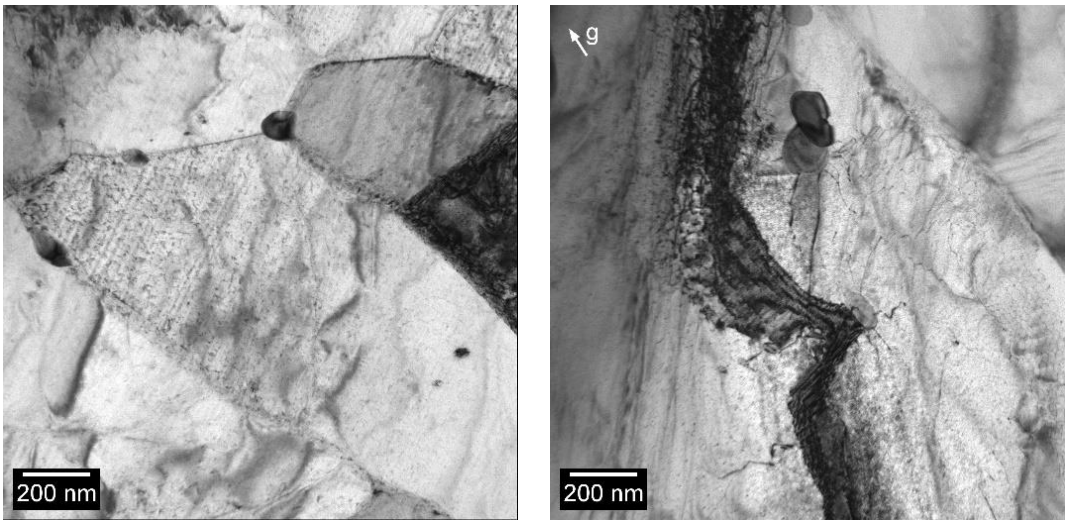

(a) *(b)*

Figure 78: BF TEM micrographs showing (a) $M_{23}C_6$ at equiaxed grains boundaries following Test 3, and (b) pile-ups and tangles of dislocation close to precipitates following Test 2

The volume fraction of MX appears to be stable during the interrupted creep tests. The stability of MX during creep helps to maintain the creep rate at minimum and contributes to keep the creep strength of the material by decreasing the microstructural

instability. The distribution and presence of MX at Test 3 and 4 close to failure is shown in Figure 76c/d [294]. In the literature, it is reported that Z-phase particles may form at the expense of MX carbonitrides [287, 333], but this behaviour has not been observed in the current work under the test conditions examined. The stability of MX until about 3,000 hours is also demonstrated in other studies regarding the creep behaviour of 9-12% Cr steels [22, 292]. Additionally, Nb/V-rich MX carbonitrides show good stability against particle coarsening during creep deformation maintaining an average size of 20 nm for NbX and 70 nm for VX [318, 319].

Laves phase particles are not observed to ripen and instead maintain an approximate size of 300 nm. Thus, under the tested creep conditions, Laves phase particles show a tendency to stability against coarsening. Laves particles, for their shape and size, are preferential sites for nucleation of cavities as can be seen in Figure 76d where a cavity is detected close to the Laves phase that grows in the proximity of a $M_{23}C_6$ particle.

6.3.3.4 Evolution of creep cavities

The combined effects of the processes listed above responsible for the microstructure evolution of P91 (i.e. coarsening of precipitates, Laves phase, dynamic recovery, disappearance of lath structures) cause the weakening of the material and trigger the formation of cavities [335].

The nucleation of voids happens primarily at the interface with second phase particles such as $M_{23}C_6$ and Laves phase along grain boundaries where dislocations pile ups generating areas of high stress concentration [34, 336, 337]. The subsequent growth and coalescence of voids under creep conditions is one of the main factor for the reduction of creep strength and for creep failure [280]. Different studies have reported that cavities can nucleate both early in creep life or late in creep life depending on the microstructure and composition of the material and on the test conditions used [279, 337]. For the material analysed in this paper, as reported in Table 25, pre-existing cavities are already present in the as-serviced-exposed state.

Cavities were counted using ImageJ software on microstructural images collected with an optical microscope. Cavity agglomeration and microcracks forming at the later stages of creep were not included in the cavity measurements.

Figure 79a shows the distribution of pre-existing cavities (black holes) in the as-serviced-exposed sample that occurs mainly along PAGs in the proximity of Laves phase and $M_{23}C_6$ carbides (blue colour particles enriched in Mo and green colour particles enriched in Cr respectively) and partially along lath boundaries. Figure 79b shows, using OM at larger scale, also the presence in the as-received material of pre-existing cavities that are quite large and circular while the white spots represent precipitates. These pre-existing large cavities are thought to be pores that form due to the presence of inclusions as S, Mn and Al in the composition but further investigation is needed. This finding is consistent with the study done by Yadav in [335] and by Siefert and Parker in [279] .

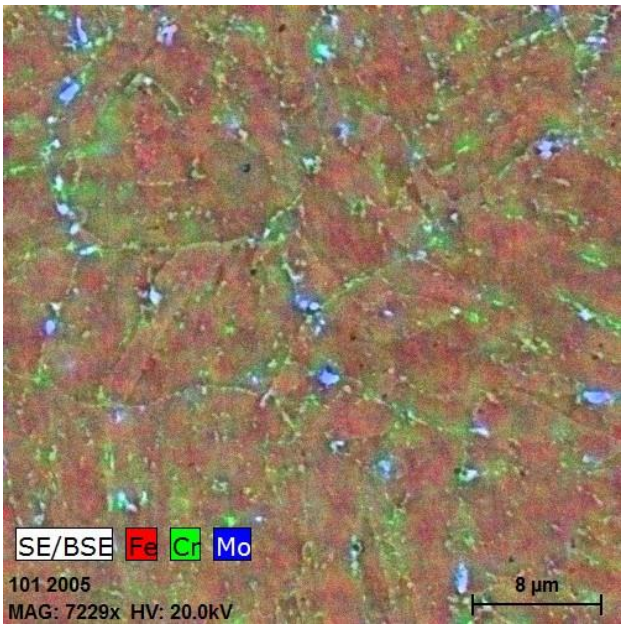

(a)

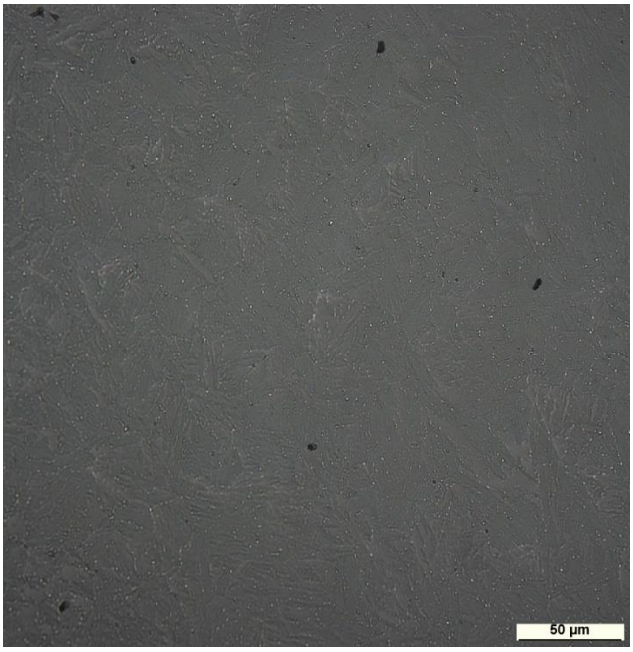

(b)

Figure 79: (a) EDS image showing cavity distribution in the as-service-exposed material (Cr in green indicates $M_{23}C_6$, Mo in blue Laves phase, black holes to represent cavities) (b) OM image revealing pre-existing cavities in the as-service-exposed material

The evolution of cavities for creep-loaded specimens is shown in Figure 80 for Test 2 at the onset of tertiary creep stage and for Test 4 at fracture using light optical microscope images. Figure 80a ($t/t_r = 0.9$) reveals some interesting features: growth of pre-existing large and circular cavities that have increased in diameter compared to the cavities in Figure 79b, and new smaller creep cavities visible around PAG boundaries forming chain-like patterns and start of coalescence. In Figure 80b, ($t/t_r = 1$), the cavities have agglomerated losing their regular and round shape, they are more elongated and micro cracks are formed.

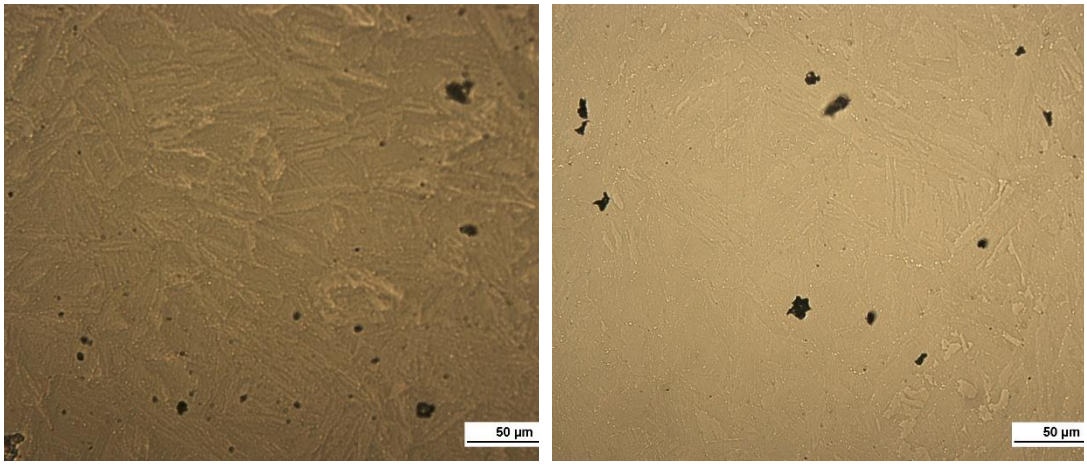

(a) *(b)*

Figure 80: OM images of (a) cavities at Test 2 ($t/t_r = 0.9$) and (b) cavities and micro cracks at fracture

Different modelling approaches have been evolved in the past years to describe the creep life through cavitation. A new life prediction model based on the original Hull-Rimmer creep cavity growth theory and applicable in stress controlled conditions, was developed by Jiang in [338] using the cavity radius as damage parameter. Even if this model claims to predict the lives in good agreement with experimental values, its application in the field is very limited since it relies on many variables that can be determined only through a deep metallographic investigation. A model able to predict the time to a given cavity area fraction was developed by Pohja [339]. This model is simpler to implement in industrial applications since it uses operational variables such as time, temperature and stress as predictive variables for the creep cavitation damage but it still needs validation for long-term damage evolution. EPRI developed a model where the prediction of creep life is related to the void fraction through a parameter function of tertiary creep strain. This is the simplest method for the assessment of life in power plant components but the parameters in the model change in accordance to steel composition and microstructure and uncertainty is added from the variability of methods used for characterization [279].

Without doubt, it is possible to state that the estimation of creep life through cavitation is a hard task and reliable procedures for cavity counting and characterization of cavity damage are required.

6.3.4 Fracture analysis

Fractography evaluation of the failed crept sample (Test 4) by SEM reveals a mixture of transgranular ductile dimple and intergranular fracture modes that is typical for short-term creep testing at high plastic deformation [175, 219, 278]. Dimples contain inclusions and second-phase particles identified by EDS as MnS and $M_{23}C_6$ respectively (Figure 81a and b). These are preferred sites for microvoid nucleation being locations of stress concentrations. Voids nucleate, grow and, after a certain threshold is exceeded, coalesce under the effect of plastic deformation. At the stress level of 80 MPa, just a few microcracks are formed since cracks give the strongest contribution to creep failure at higher stress [280]. Void coalescence is therefore the main reason for creep damage. Cavities have been found to form also around Laves phase (see Figure 71 at $t/t_r = 1$). Laves phase particles, with their broad and irregular dimensions and their brittleness, have been found to be areas of strain concentration that enhance the nucleation of voids and therefore the deterioration of creep strength [285] possibly triggering the transition from ductile to brittle fracture mode [295].

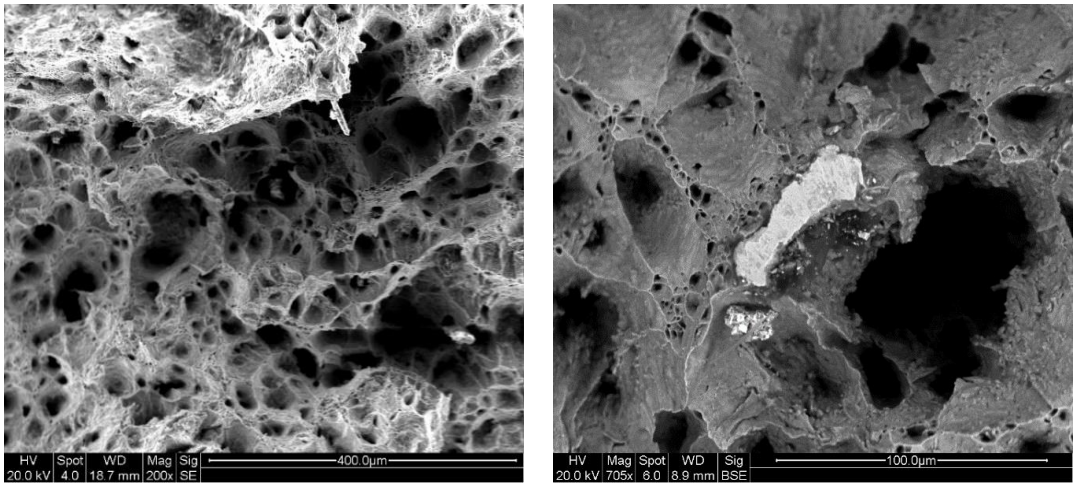

(a) *(b)*

Figure 81: SEM images of fracture surfaces following Test 4, (a) SE showing dimples with some containing inclusions, and (b) BSE showing detail of MnS inclusion (bright area)

6.3.5 Softening mechanism

Creep models that relate the creep response to the evolution of microstructural parameters have already been successfully developed. Xiao et al. [340] modelled the creep deformation of a G115 steel (a tempered martensitic steel) through a modified version of Orowan's equation where the softening effect caused by precipitation

coarsening and creep cavitation was incorporated via two damage parameters. Yadav et al. [324] developed a model for P91 steel based on a hybrid concept where a physical-based approach, used to describe the microstructural evolution, is coupled with the continuum damage mechanics (CDM) theory used to address damage evolution. These models exhibit a good agreement with the experimental creep data at various creep conditions but their application in the power generation industry is not widespread since they are based on the time-intensive detailed measurement of a variety of microstructural parameters such as, for example, dislocation densities, sub-grain size, number of precipitates per unit volume and precipitate mean radii.

Hardness instead is a measurable indicator of the microstructural softening that happens under creep exposure due to the internal material mechanisms listed in section 6.3.3, i.e. lath widening and substructure disappearance, particle coarsening and coalescence, recovery and formation of equiaxed grains [288]. Hardness has been used to develop models for the remaining life of high temperature components often in relation with the Larson-Miller parameter (LMP) [85]. Figure 82 shows the evolution of hardness (measured at room temperature) with life fraction.

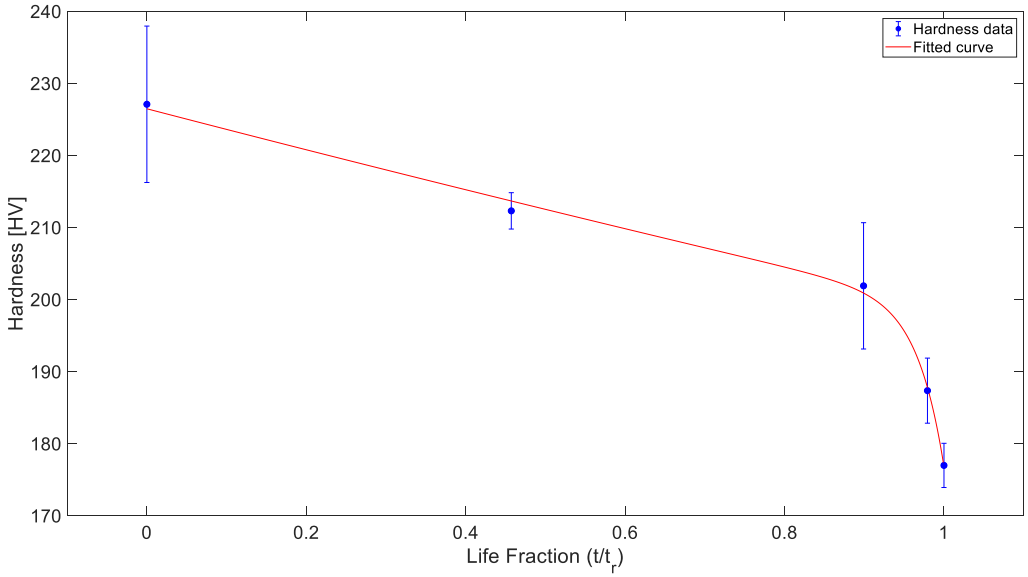

Figure 82: Hardness evolution of the service-exposed P91 as a function of creep life fraction

The mean value of hardness for the as-service-exposed P91 is 227 HV whilst following creep rupture, it has dropped to 177 HV. The best relation that represents the evolution

of hardness as function of life fraction is given by a two terms exponential equation given in Equation 99, for which goodness of fit can be seen in Figure 82.

$$HV = -2.07 \times 10^{-12} \exp\left(30\frac{t}{t_r}\right) + 226.5 \exp\left(-0.127\frac{t}{t_r}\right) \quad (99)$$

Following the work done by Masuyama [196, 341], a linear empirical equation between hardness ratio and life fraction can be extrapolated once the hardness ratio is calculated from the original hardness value for the as-service-exposed sample HV_0 (Equation 100).

$$\frac{HV}{HV_0} = -0.186\ \frac{t}{t_r} + 1.01 \quad (100)$$

Equation 100 is very similar to the one proposed by Masuyama [196, 341]. The advantage of Equation 99 is the ability to describe accurately the acceleration of hardness drop in the tertiary creep stage.

The hardness variation is faster from $t/\ t_r = 0.9$ at the onset of tertiary creep while until the secondary creep stage the hardness reduction is less rapid and it is characterised by a more linear behaviour. The significant change in the slope of hardness curve at $t/\ t_r = 0.9$ could be an indication of a change in the controlling mechanism for creep deformation. This would confirm the outcomes research in Chapter 5 [288].

Previous research reports a hardness evolution shape as above and attributes the main reason for hardness decline to the widening of the lath structure during long-term creep [196] and to particle coarsening during short-term creep [179, 207, 342]. On the other hand, the increase in lath size is closely related to changes in precipitation behaviour and to a change in the interaction between precipitates and dislocations. Dislocation rearrangement is known to be the dominant creep deformation mechanism for high-strength martensitic steel [340].

Hardness is known to be proportional to the square root of dislocation density through the relation between hardness and the flow stress, and therefore hardness is indirectly related as well to subgrain size and precipitates [196]. The effect on hardness from lath strengthening is estimated by the Hall-Petch relationship where the grain growth is accounted for by introducing an evolution equation for the grain diameter. The

relationship between hardness and precipitation strengthening is established by the Orowan's law that is coupled with the Ostwald ripening process equation to describe precipitation coarsening [57, 85].

The growth and disappearance of subgrains and lath structure, the decrease of dislocation density, the coarsening of precipitates during creep and the presence of Laves phase cause hardness to decline. Apart from these microstructural changes, also the increase in creep cavity density plays a key role in the fall of hardness (see paragraph 6.3.3.4).

What is challenging in creep strength enhanced ferritic steel (9-12% Cr) is the understanding of the importance and the influence of each microstructural process on the creep behaviour of the steel [227]. Microstructural degradation and creep cavitation normally occur at the same time but the dominance of each factor is different according the original microstructure, creep conditions and stress state [57].

Figure 83 shows the evolution of the main factors throughout the creep life with the values taken from Table 25.

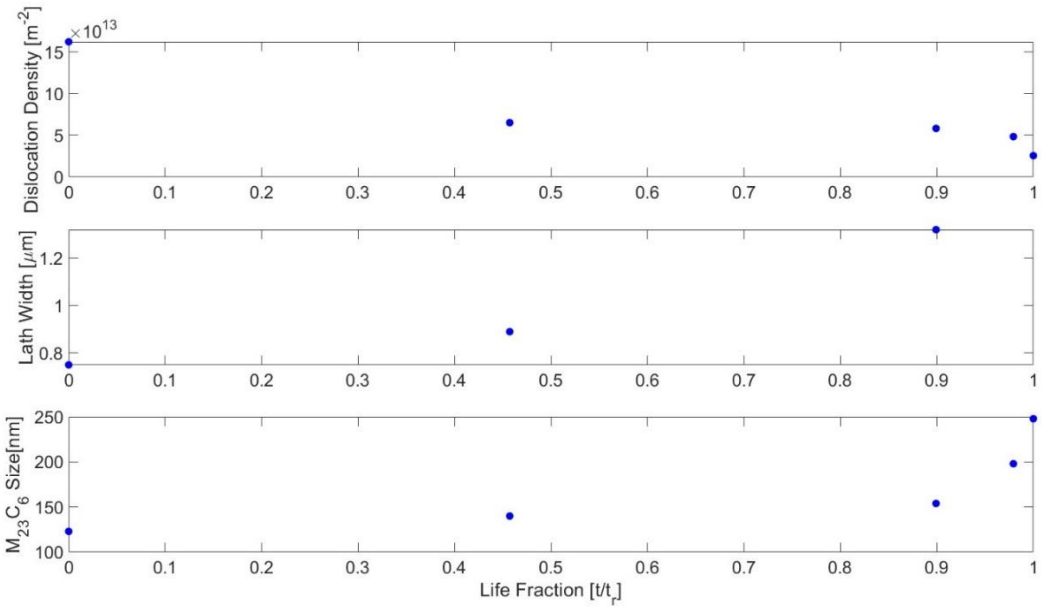

(a)

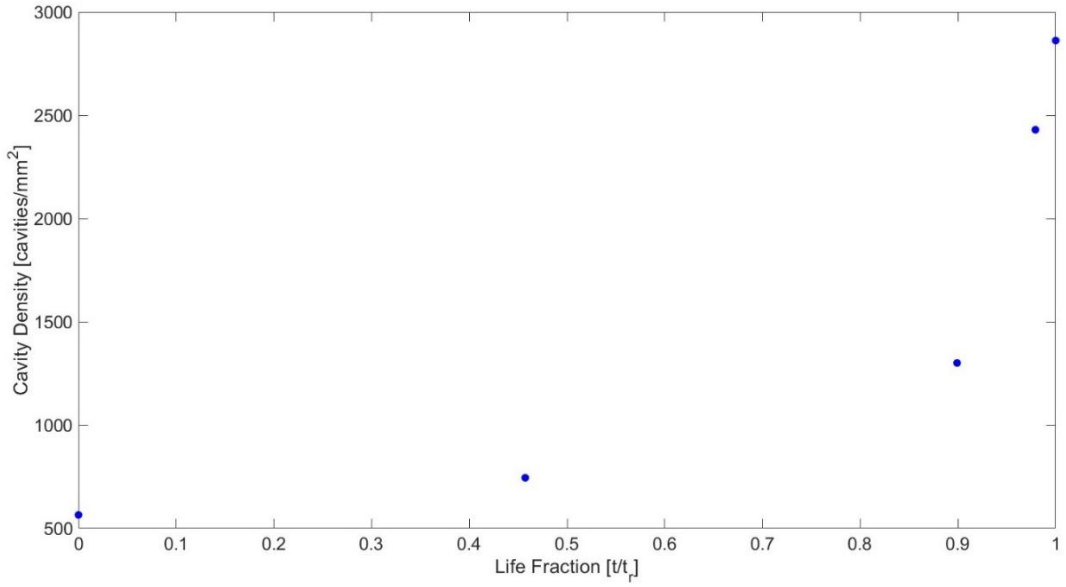

(b)

Figure 83 : Evolution of microstructural features in service-exposed P91 as a function of creep: (a) evolution of microstructural parameters, (b) evolution of cavity density

From Figure 83 it appears that microstructural changes are most influential during the secondary creep stage whilst cavity evolution is more significant in the tertiary creep stage where the cavitation rate is higher. At the onset of tertiary stage, the coarsening of $M_{23}C_6$ (associated with decrease in number of dislocations and increase in interparticle spacing) can trigger a faster nucleation and growth of cavities that finally lead to material failure. This would support the assertions made by the authors in the paper for CrMoV [288] but further data need to be collected from laboratory tests to assess the importance of individual microstructural factors and to develop more insightful predictive models for creep life. Also creep cavities results in the tertiary creep behaviour [340, 343].

Nonetheless, it is possible to state that all the aforementioned processes are responsible for creep damage and contribute to the decrease of hardness so that hardness measurement can be used as method to estimate the material microstructural creep degradation and to develop predictive lifing models [6, 288].

A hardness-based model for rupture life estimation has been proposed by the authors in Chapter 5 [288] for CrMoV steel. Since the physical basis of the model is similar to the findings in the present study, the validity of the model could be extended also to P91 steel and in general to all high-strength martensitic steels (because of their very

similar microstructure) using material-specific parameters. Finally, the validation of the model should be performed with measured and existing values from creep tests or inspection data.

6.4 Concluding remarks

The degradation of the microstructure for a P91 steel and its effect on the material mechanical properties has been investigated through interrupted creep tests and the results have been discussed in this paper. A good understanding of the microstructure evolution for 9-12% Cr steels is extremely important in order to evaluate their reliability during service under high temperature and stress conditions. The main factors affecting the increase in the creep rate and the reduction in hardness are summarised as follows: i) decrease of mobile free dislocations inside the lath structure by dynamic recovery processes, ii) disappearance of martensitic lath structure and final transformation into an equiaxed microstructure, iii) coarsening/coalescence of $M_{23}C_6$ precipitates and broad Laves phase both providing nucleation sites for cavities, iv) creep cavitation.

During the secondary creep stage, the lath and sub-grain structure and the fine distribution of precipitates counterbalance the start of the dynamic recovery process with the effect of keeping the creep rate stable and with a slight hardness reduction. From the tertiary creep stage the internal material changes listed above from i) to iii) are more rapid and together with the significant increase of cavity density, the creep rate accelerates until the final fracture and the hardness rapidly drops. Figure 84 provides a schematic summary of the internal mechanisms that influence the change in the creep strain curve.

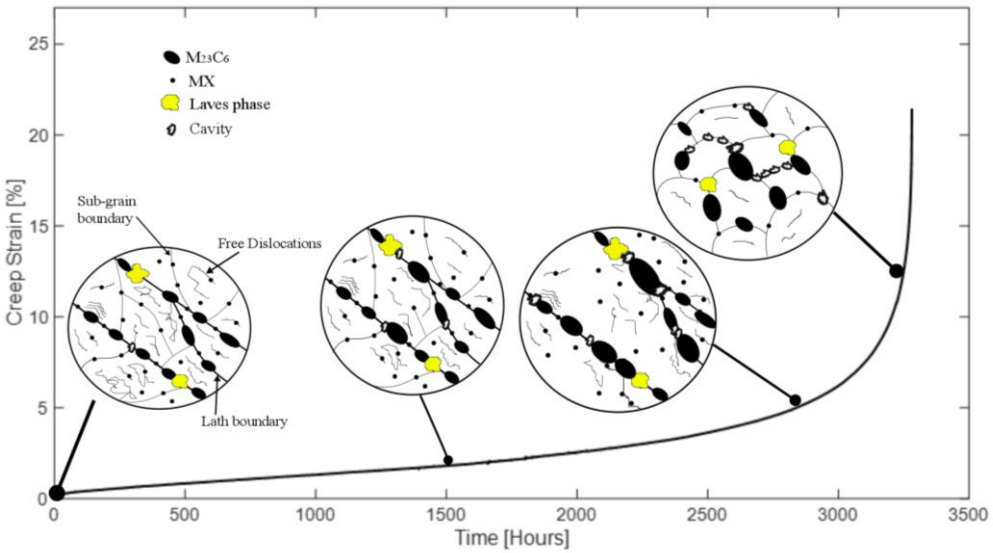

Figure 84: Schematic representation of microstructure changes during creep

Further to Figure 84, it is possible to develop an 'interactive diagram' shown in Figure 85 to illustrate the interactions between the various microstructural and mechanical variables, which collectively contribute to the degradation of the material (deformation mechanisms) and eventually lead to creep rupture.

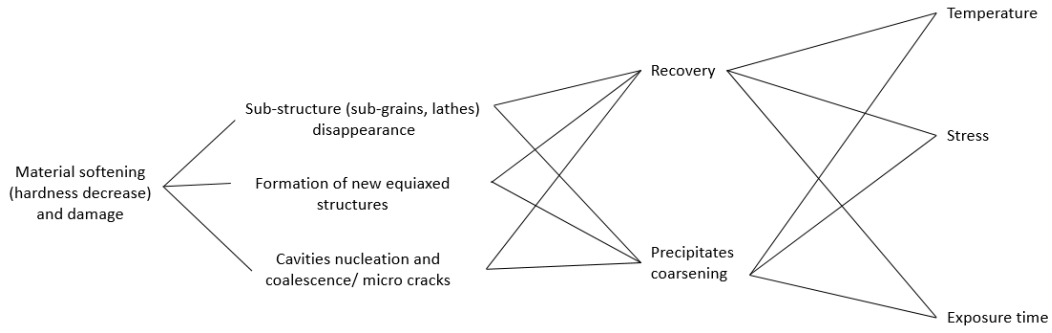

Figure 85: Interactive diagram illustrating the relationship between microstructural changes and final damage. Input: Temperature, stress and exposure time. Output: Material softening and final damage

The changes in the microstructure lead to a complex interaction between primary microstructural features such as dislocations, precipitates, lattice and cavities. The understanding of their relationship is facilitated through the microstructural characterization of the material by microscopy techniques as TEM and SEM and diffraction techniques as EBSD. Industrial practice uses periodic inspections, mainly non-destructive techniques (NDT) such as hardness measurement because of their ease

of implementation and cost effectiveness. Thus, a hardness-based model would complement current inspection practice and should be further developed for the prediction of creep life. Hardness can be successfully deployed as indicator for the estimation of creep damage since it has been seen from Section 6.3.5 that Vickers hardness changes can be related to the variation of dislocation, $M_{23}C_6$, lath structure and voids.

Hardness-based models would be welcomed for practical deployment to support decisions on operating plant. However, there are some important requirements to ensure reliable deployment of the model on operating plant.

1. The Station should adopt a consistent approach to the collection of inspection data over successive outages, and operational data, to provide the information required to optimise the model.
2. The authors have developed similar models for CrMoV steels in use on high temperature plant based on field inspection data resulting from very long exposure times to plant operating conditions [288]. This CrMoV model showed a transition in behaviour when cavitation was seen to dominate the later stages of useable life. Importantly this showed the benefits of implementing a systematic inspection schedule.
3. Hence, the use of a similar P91 model in the field could be calibrated and optimised to account for plant operating conditions, which can be achieved if point 1 above is adopted in conjunction with suitable laboratory tests.

The insights given in this chapter aimed to give an exhaustive explanation of the main microstructural factors involved in the structural stability of P91 during service and how these factors have an impact on the softening of the material. Further research is needed to focus on the improvement of life assessment techniques for long-term creep exposure. New models should investigate the impact of each microstructural parameter on the variation of hardness so that hardness-based life techniques incorporating service conditions can be used in conjunction with other monitoring strategies as non-destructive examination in order to assist in determining the safe operating life for the material under investigation.

7 Conclusions and future work

7.1 Conclusions

The research presented in this thesis was mainly focussed on developing the foundations for a new predictive and practical life assessment modelling methodology for high temperature power plant components. This methodology is based upon use of operational data (etc. temperature and pressure) more proactively in combination with periodic inspection data (etc. hardness and surface creep replicas), metallurgical data and currently available or modified creep/fatigue models in order to improve the estimates of residual life. The final aim is to provide rigorous life predictions that allow the plant operator to efficiently optimise plant operation and reduce through-life inspections costs.

The main conclusions are outlined as follows:

- It is necessary to use a range of lifing models of varying complexity, which reflect the material behaviour under service conditions. These models need to be continuously updated and nudged with operational and inspection data.

- It is important to establish the rate of change of inspection-derived data as a key factor for monitoring purposes when assessing the condition of the material and its residual life.

- The concept of life assessment transfer function (LATF) has been proposed and developed. The LATF filters, harmonises and arranges the continuous online data and periodic data obtained from an outage inspection into a suitable format for assessment in the material model.

An important aspect of the methodology that has been developed for the first time in this thesis is the formulation of holistic empirical creep lifing models designed specifically to be used iteratively with surface replica and hardness data available from outage inspections.

This study has shown that:

- Routinely collected inspection data can be better and more efficiently utilized in a database to provide operators with predictions of residual creep life.

- A hardness and creep replica assessment relationship can be quantified using data extracted from in-service inspections on CrMoV material. This provides the capability to predict the residual life of ageing parent materials in service using a combination of hardness, surface replica data and strain.

- The hardness change in the material is influenced both by creep cavitation and by thermal ageing effects that are the main factors responsible for material softening. Therefore, the effect of creep cavitation and of thermal ageing on strain rate and remaining life predictions needs to be described with different models.

A unified viscoplastic model linked with the R5 procedure was proposed and applied to an industrial gas turbine rotor made of FV566 steel with the aim of providing more accurate creep and fatigue life estimations and to simplify the current industrial lifing assessment procedure. The viscoplastic model was incorporated into ABAQUS FEA software using an in-house subroutine to simulate the behaviour of FV566 steel in a realistic industrial gas turbine rotor and was applied to a 2D FE model of the gas turbine rotor during its typical loading cycle to predict its stress and strain behaviour. The main results of this novel integrated life assessment procedure can be summarised as follows:

- Important parameters required for the R5 life assessment procedure such as the stress relaxation per cycle and the elastic-follow up factor can be obtained directly from the FE simulation, avoiding several complicated steps of the R5 procedure.

- Regions of interest can be identified through FE analysis as locations where stresses and strains are maximum. These locations are considered the most damage-prone positions, which are most likely to experience crack initiation. Therefore, damage and life assessment need to be conducted in these regions.

- The accuracy of any stress analysis is always dependent on the ability of the material model and the associated material properties used to reproduce the cyclic responses of the material.

A microstructural analysis was finally performed to investigate the physical behaviour of an ex-service P91 steel under interrupted creep testing by the examination of microstructural features. The microstructure evolution was investigated using SEM, EBSD, TEM and optical microscopy techniques. The main results of the material characterisation can be summarised as follows:

- The hardness decline is attributed to the growth and disappearance of subgrains and the lath structure, a decrease of dislocation density, the coarsening of precipitates, the presence of Laves phase and an increase in creep cavity density. However, it is challenging to understand the influence and weight of each microstructural change on the creep behaviour of the steel.

- Despite this complexity, hardness measurement can be used as method to estimate the material creep degradation and to develop predictive lifing models.

- Hardness-based models are useful for practical deployment to support decisions on operating plant with the requirement to adopt a consistent approach to the collection of inspection data over successive outages, and operational data, to provide the information required to optimise the model.

Summarizing, a more rigorous approach for condition monitoring and assessment has been developed in this research compared to the current industrial practice where run-repair decisions are based on site inspection data along with a review of operational conditions. For the first time in this thesis, a correlation between off-load tests (creep cavitation and hardness) was established by a better exploitation of the extensive plant data acquired during outages. This correlation is used in the improved approach to provide a more rigorous future-life prediction that allows the plant operator to efficiently optimise plant operation and reduce through-life inspection costs. In this

thesis, it has been described how these newly developed empirical lifing models based on off-load data can be coupled and integrated with computational models based on on-load data from the operating plant to improve the predictive life assessment framework. Most importantly, the rupture life calculated with this new approach shows a good predictive capability and the strain rate shows a good agreement with the values calculated from field measurements. The industrial significance is that the approach developed in this thesis complements the real decision-making process on an operating station, and facilitates the consideration all relevant data before making significant run-repair-replace decisions.

7.2 Future work

At the end of each research chapter, comments have been made as to how the research in that particular area may develop in the future. Some potential improvements and extensions to the current work can be implemented in future as follows:

- The predictive capability and the accuracy of the lifing methodology proposed will improve with access to more field data, spread over longer operational periods. The field data will be added to the newly developed database and the information in the dataset will be used to refine the lifing approach proposed.

- Since the thesis has shown the potential benefits of more integrated models, there is the possibility to develop a neural network/machine learning approach in combination with the proposed models to efficiently determine the stress state in a component and integrated with online monitor data. In addition, the implementation of a neural network will allow an easier recognition and determination of possible trends between inspection-based data.

- The future of large generation plants will be without any doubt more nuclear stations. Current designs and the Gen IV designs (without forgetting the potential for fusion plants) that are being developed are high temperature applications which will all benefit from more integrated life prediction models, which in essence should help the operator to plan and execute their inspections more efficiently as well as assisting the designer.

- Small specimen creep testing will be very useful within a life assessment framework to obtain creep data to be compared with industrial data currently acquired for assessing the condition of materials. There is a need to develop validated codes of practice and standards for small specimen test methods.

- The current Chaboche viscoplastic model does not contain a damage variable that allows a direct determination of material life, and it would be useful if future developments could work towards incorporation of a damage evolution equation. The validation of the new model will go through experimental testing that allows the calculation of a test damage to be compared with the modelled damage.

8 References

[1] N. Mukhopadhyay, B. Dutta, and H. Kushwaha, “On-line fatigue–creep monitoring system for high-temperature components of power plants,” *International Journal of Fatigue,* vol. 23, no. 6, pp. 549-560, 2001.

[2] A. Shibli, "Boiler steels, damage mechanisms, inspection and life assessment," *Power Plant Life Management and Performance Improvement*, J. E. Oakey, ed., pp. 272-303, Chapter 7: Woodhead Publishing, 2011.

[3] Y. Rae, “Characterisation and computational modelling of high temperature cyclic viscoplastic behaviour of turbine steel,” University of Nottingham, 2020, PhD Thesis.

[4] D. Rojas, J. Garcia, O. Prat, G. Sauthoff, and A. Kaysser-Pyzalla, “9% Cr heat resistant steels: Alloy design, microstructure evolution and creep response at 650 C,” *Materials Science and Engineering: A,* vol. 528, no. 15, pp. 5164-5176, 2011.

[5] F. Abe, "Grade 91 heat-resistant martensitic steel," *Coal Power Plant Materials and Life Assessment*, pp. 3-51, Chapter 1: Woodhead Publishing, 2014.

[6] F. Abe, T. U. Kern, and R. Viswanathan, *Creep-Resistant Steels*: Elsevier Science, 2008.

[7] A. Fabricius, and P. Jackson, “Premature Grade 91 failures — worldwide plant operational experiences,” *Engineering Failure Analysis,* vol. 66, pp. 398-406, 2016.

[8] I. Paterson, and J. Wilson, “Use of damage monitoring systems for component life optimisation in power plant,” *International Journal of Pressure Vessels and Piping,* vol. 79, no. 8-10, pp. 541-547, 2002.

[9] C. Maharaj, J. Dear, and A. Morris, “A review of methods to estimate creep damage in low-alloy steel power station steam pipes,” *Strain,* vol. 45, no. 4, pp. 316-331, 2009.

[10] *Safe Management of Grade 91 Pressure Parts in Conventional UK Power Stations*, vol. GENSIP/GPG/PS/007, Coal Generators Safety and Integrity Programme – GENSIP, 2016.

[11] *CMV Pipework Management in Conventional UK Power Stations*, vol. GENSIP/GPG/PS001, Coal Generators Safety and Integrity Programme - GENSIP, 2011.

[12] S. J. Brett, and E. M. Hawkes, *Technical Report - Creep Damage Mapping Of CrMoV Straight Pipes*, vol. GENSIP/TR/PS036, 2016.

[13] A. Morris, B. Cacciapuoti, and W. Sun, “The role of small specimen creep testing within a life assessment framework for high temperature power plant,” *International Materials Reviews,* vol. 63, no. 2, pp. 102-137, 2018/02/17, 2018.

[14] M. E. Kassner, *Fundamentals of creep in metals and alloys*: Butterworth-Heinemann, 2015.

[15] G. E. Dieter, and D. Bacon, *Mechanical metallurgy*: McGraw-Hill, 1976.

[16] R. Car, P. J. Kelly, A. Oshiyama, and S. T. Pantelides, "Microscopic theory of atomic diffusion mechanisms in silicon," *Physica B+C,* vol. 127, no. 1-3, pp. 401-407, 1984.

[17] H. Schmidt, M. Gupta, T. Gutberlet, J. Stahn, and M. Bruns, "How to measure atomic diffusion processes in the sub-nanometer range," *Acta Materialia,* vol. 56, no. 3, pp. 464-470, 2008.

[18] M. A. Meyers, and K. K. Chawla, *Mechanical behavior of materials*: Cambridge University Press, 2008.

[19] J. P. Rouse, "Computational Component Analysis Techniques for High Temperature Power Plant Applications," University of Nottingham, 2014, PhD Thesis.

[20] R. W. Evans, and B. Wilshire, *Introduction to creep*: The Institute of Materials 1993.

[21] K. Naumenko, and Y. Kostenko, "Structural analysis of a power plant component using a stress-range-dependent creep-damage constitutive model," *Materials Science and Engineering: A,* vol. 510-511, pp. 169-174, 2009.

[22] V. Sklenička, K. Kuchařová, M. Svoboda, L. Kloc, J. Buršık, and A. Kroupa, "Long-term creep behavior of 9–12% Cr power plant steels," *Materials Characterization,* vol. 51, no. 1, pp. 35-48, 2003.

[23] T. Shrestha, M. Basirat, I. Charit, G. P. Potirniche, K. K. Rink, and U. Sahaym, "Creep deformation mechanisms in modified 9Cr–1Mo steel," *Journal of Nuclear Materials,* vol. 423, no. 1, pp. 110-119, 2012.

[24] M. H. Sabour, "Creep," *Encyclopedia of Tribology*, pp. 618-627: Springer US, 2013.

[25] B. P. Kashyap, and K. Singh, "Towards Interrelating the Nature of High Temperature Stress–Strain Curves and Creep Curves with Concomitant Microstructure Evolution," *Transactions of the Indian National Academy of Engineering,* vol. 7, no. 2, pp. 601-613, 2022.

[26] A. Chatterjee, "Effect of Microstructure and Crystallographic Texture on Mechanical Properties of Modified 9Cr-1Mo Steel," Engineering Indian Institute of Technology, 2018, PhD Thesis.

[27] H. Kraus, and H. Saunders, "Creep analysis," *Transaction of the ASME,* vol. 104, Issue 3, pp. 530-780, 1982.

[28] R. K. Penny, and D. L. Marriott, *Design for creep*: Springer Science & Business Media, 1995.

[29] J. T. Boyle, and J. Spence, *Stress analysis for creep*: Elsevier, 2013.

[30] J. Betten, *Creep mechanics*: Springer Science & Business Media, 2008.

[31] X. Duan, H. Yuan, W. Tang, J. He, and X. Guan, “A phenomenological primary–secondary–tertiary creep model for polymer-bonded composite materials,” *Polymers,* vol. 13, no. 14, pp. 1-19, 2021.

[32] B. Chen, P. E. J. Flewitt, A. C. F. Cocks, and D. J. Smith, “A review of the changes of internal state related to high temperature creep of polycrystalline metals and alloys,” *International Materials Reviews,* vol. 60, no. 1, pp. 1-29, 2015.

[33] J. L. Chaboche, “Continuum Damage Mechanics: Part I—General Concepts,” *Journal of Applied Mechanics,* vol. 55, no. 1, pp. 59-64, 1988.

[34] M. Kassner, and T. Hayes, “Creep cavitation in metals,” *International Journal of Plasticity,* vol. 19, no. 10, pp. 1715-1748, 2003.

[35] S. Brett, L. Buchanan, S. Concari, G. Cosso, S. Fenton, A. Fleming, R. Hales, V. Kanta, I. Marcelles, and I. G. Merckling, “Residual life assessment and microstructure,” *ECCC, Italy, ECCC Recommendation AC/MC/93*, 2005.

[36] L. M. Kachanov, E. Bishop, and A. J. Kennedy, *The theory of creep*, Boston Spa: National Lending Library for Science and Technology, 1967.

[37] Y. N. Rabotnov, F. A. Leckie, and W. Prager, “Creep Problems in Structural Members,” *Journal of Applied Mechanics,* vol. 37, no. 1, pp. 249-249, 1970.

[38] A. Zakaria, P. Karen, and A. Cris, "Creep Lifing Models and Techniques," *Creep*, pp. 115-149, Chapter 7: IntechOpen, 2018.

[39] I. J. Perrin, and D. R. Hayhurst, “Creep constitutive equations for a 0.5Cr–0.5Mo–0.25V ferritic steel in the temperature range 600–675°C,” *The Journal of Strain Analysis for Engineering Design*, vol. 31, no. 4, pp. 299-314, 1996.

[40] B. J. Cane, and P. F. Aplin, “Creep life assessment methods,” *The Journal of Strain Analysis for Engineering Design,* vol. 29, no. 3, pp. 225-232, 1994.

[41] B. J. Cane, and J. A. Williams, “Remaining life prediction of high temperature materials,” *International Materials Reviews,* vol. 32, no. 1, pp. 241-264, 1987.

[42] F. A. Leckie, and D. R. Hayhurst, “Constitutive equations for creep rupture,” *Acta Metallurgica,* vol. 25, no. 9, pp. 1059-1070, 1977.

[43] B. Dyson, “Use of CDM in Materials Modeling and Component Creep Life Prediction,” *Journal of Pressure Vessel Technology,* vol. 122, no. 3, pp. 281-296, 2000.

[44] J. P. Rouse, W. Sun, T. H. Hyde, and A. Morris, “Comparative assessment of several creep damage models for use in life prediction,” *International Journal of Pressure Vessels and Piping,* vol. 108-109, pp. 81-87, 2013.

[45] F. R. Larson, and J. Miller, “A time-temperature relationship for rupture and creep stresses,” *Transactions of the American Society of Mechanical Engineers,* vol. 74, no. 5, pp. 765-771, 1952.

[46] S. S. Manson, and A. M. Haferd, *A linear time-temperature relation for extrapolation of creep and stress-rupture data*, Lewis Flight Propulsion Laboratory, NACA, 1953.

[47] R. L. Orr, O. D. Sherby, and J. E. Dorn, *Correlations of rupture data for metals at elevated temperatures*, Institute of Engineering Research, University of California, Berkeley, 1953.

[48] F. C. Monkman, "An empirical relationship between rupture life and minimum creep rate in creep-rupture tests," *Proc of the ASTM,* vol. 56, pp. 593-620, 1956.

[49] R. W. Evans, and B. Wilshire, *Creep of metals and alloys*: The Institute of Materials, 1985.

[50] B. Wilshire, and A. J. Battenbough, "Creep and creep fracture of polycrystalline copper," *Materials Science and Engineering: A,* vol. 443, no. 1, pp. 156-166, 2007.

[51] M. Prager, "Development of the MPC Omega Method for Life Assessment in the Creep Range," *Journal of Pressure Vessel Technology,* vol. 117, no. 2, pp. 95-103, 1995.

[52] Y. Liu, and S. Murakami, "Damage Localization of Conventional Creep Damage Models and Proposition of a New Model for Creep Damage Analysis," *JSME International Journal Series A,* vol. 41, no. 1, pp. 57-65, 1998.

[53] F. Leckie, and D. Hayhurst, "Creep rupture of structures," *Proceedings of the Royal Society of London. A. Mathematical and Physical Sciences,* vol. 340, no. 1622, pp. 323-347, 1974.

[54] U. F. Kocks, "Laws for Work-Hardening and Low-Temperature Creep," *Journal of Engineering Materials and Technology,* vol. 98, no. 1, pp. 76-85, 1976.

[55] F. Barlat, M. V. Glazov, J. C. Brem, and D. J. Lege, "A simple model for dislocation behavior, strain and strain rate hardening evolution in deforming aluminum alloys," *International Journal of Plasticity,* vol. 18, no. 7, pp. 919-939, 2002.

[56] F. V. Ellis, "Life assessment using metallographic and mechanical methods," *Materials Characterization,* vol. 32, no. 2, pp. 79-87, 1994.

[57] B. Cane, P. Aplin, and J. Brear, "A mechanistic approach to remanent creep life assessment of low alloy ferritic components based on hardness measurements," *Journal of Pressure Vessel Technology,* vol. 107, no. 3, pp. 295-300, 1985.

[58] Y. Estrin, and H. Mecking, "A unified phenomenological description of work hardening and creep based on one-parameter models," *Acta Metallurgica,* vol. 32, no. 1, pp. 57-70, 1984.

[59] Y. Estrin, "Dislocation theory based constitutive modelling: foundations and applications," *Journal of Materials Processing Technology,* vol. 80-81, pp. 33-39, 1998.

[60] R. Bonetti, A. Morris, P. Shipway, and W. Sun, "Requirements for developing high temperature creep life models for ageing pipework systems using power plant condition monitoring and inspection data," *International Journal of Pressure Vessels and Piping,* vol. 188 no. 104233, pp. 1-16, 2020.

[61] O. D. Sherby, R. L. Orr, and J. E. Dorn, “Creep correlations of metals at elevated temperatures,” *JOM,* vol. 6, no. 1, pp. 71-80, 1954.

[62] Z. Abdallah, V. Gray, M. Whittaker, and K. Perkins, “A Critical Analysis of the Conventionally Employed Creep Lifing Methods,” *Materials,* vol. 7, no. 5, pp. 3371-3398, 2014.

[63] S. S. Manson, “Design Considerations for Long Life at Elevated Temperatures,” *Proceedings of the Institution of Mechanical Engineers,* vol. 178, no. 1, pp. 1045-1071, 1963.

[64] D. C. Dunand, B. Q. Han, and A. M. Jansen, “Monkman-Grant analysis of creep fracture in dispersion-strengthened and particulate-reinforced aluminum,” *Metallurgical and Materials Transactions A,* vol. 30, no. 3, pp. 829-838, 1999.

[65] Z. Abdallah, K. Perkins, and S. Williams, “Advances in the Wilshire extrapolation technique—Full creep curve representation for the aerospace alloy Titanium 834,” *Materials Science and Engineering: A,* vol. 550, pp. 176-182, 2012.

[66] F. Abe, “Creep Behavior, Deformation Mechanisms, and Creep Life of Mod.9Cr-1Mo Steel,” *Metallurgical and Materials Transactions A,* vol. 46, no. 12, pp. 5610-5625, 2015.

[67] D. Lonsdale, and P. Flewitt, “Relationship between minimum creep rate and time to fracture for 2% Cr-1% Mo steel,” *Metal Science,* vol. 12, no. 5, pp. 264-265, 1978.

[68] B. Wilshire, and D. R. J. Owen, *Recent advances in creep and fracture of engineering materials and structures*: Swansea : Pineridge Press, 1982.

[69] J. D. Parker, “Prediction of Creep Deformation and Failure for 1/2 Cr-1/2 Mo-1/4 V and 2-1/4 Cr-1 Mo Steels,” *Journal of Pressure Vessel Technology,* vol. 107, no. 3, pp. 279-284, 1985.

[70] M. Evans, “Predicting times to low strain for a 1CrMoV rotor steel using a 6-θ projection technique,” *Journal of Materials Science,* vol. 35, no. 12, pp. 2937-2948, 2000.

[71] B. Wilshire, and P. J. Scharning, “Extrapolation of creep life data for 1Cr–0.5Mo steel,” *International Journal of Pressure Vessels and Piping,* vol. 85, no. 10, pp. 739-743, 2008.

[72] B. Wilshire, and P. J. Scharning, “Long-term creep life prediction for a high chromium steel,” *Scripta Materialia,* vol. 56, no. 8, pp. 701-704, 2007.

[73] "API 579-1/ASME FFS-1, Fitness-For-Service," American Petroleum Institute (API) and ASME, 2016.

[74] M. Prager, “The Omega Method–An Engineering Approach to Life Assessment,” *Journal of Pressure Vessel Technology,* vol. 122, no. 3, pp. 273-280, 2000.

[75] T. L. Anderson, and D. A. Osage, “API 579: a comprehensive fitness-for-service guide,” *International Journal of Pressure Vessels and Piping,* vol. 77, no. 14, pp. 953-963, 2000.

[76] J. Lemaitre, “How to use damage mechanics,” *Nuclear Engineering and Design,* vol. 80, no. 2, pp. 233-245, 1984.

[77] A. Morris, B. Cacciapuoti, and W. Sun, “The role of hardness on condition monitoring and lifing for high temperature power plant structural risk management,” *Measurement,* vol. 131, pp. 501-512, 2019/01/01/, 2019.

[78] T. H. Hyde, A. A. Becker, W. Sun, and J. A. Williams, “Finite-element creep damage analyses of P91 pipes,” *International Journal of Pressure Vessels and Piping,* vol. 83, no. 11, pp. 853-863, 2006.

[79] C. J. Hyde, W. Sun, T. H. Hyde, M. Saber, and A. A. Becker, "Application of the Liu and Murakami damage model for creep crack growth predictions in power plant steels," *Computational and Numerical Simulations*, pp. 175-189, Chapter 9: IntechOpen, 2014.

[80] V. B. Pandey, I. V. Singh, and B. K. Mishra, “A stress triaxiality based modified Liu–Murakami creep damage model for creep crack growth life prediction in different specimens,” *International Journal of Fracture,* vol. 221, no. 1, pp. 101-121, 2020.

[81] C. J. Hyde, T. H. Hyde, W. Sun, and A. A. Becker, “Damage mechanics based predictions of creep crack growth in 316 stainless steel,” *Engineering Fracture Mechanics,* vol. 77, no. 12, pp. 2385-2402, 2010.

[82] S. J. Kang, H. Lee, J. B. Choi, and M. K. Kim, “Modified Dyson Continuum Damage Model for Austenitic Steel Alloy,” *Journal of Pressure Vessel Technology,* vol. 140(4), no. 4, pp. 1-6, 2018.

[83] A. M. Othman, B. F. Dyson, D. R. Hayhurst, and J. Lin, “Continuum damage mechanics modelling of circumferentially notched tension bars undergoing tertiary creep with physically-based constitutive equations,” *Acta Metallurgica et Materialia,* vol. 42, no. 3, pp. 597-611, 1994.

[84] M. Ashby, and B. Dyson, “Creep damage mechanics and micromechanisms,” *Fracture 84*, pp. 3-30, 1984.

[85] S. Mukhopadhyay, H. Roy, and A. Roy, “Development of hardness-based model for remaining life assessment of thermally loaded components,” *International Journal of Pressure Vessels and Piping,* vol. 86, no. 4, pp. 246-251, 2009.

[86] H. Mecking, B. Nicklas, N. Zarubova, and U. Kocks, “A “universal” temperature scale for plastic flow,” *Acta Metallurgica,* vol. 34, no. 3, pp. 527-535, 1986.

[87] F. Ellyin, and Z. Xia, “A general fatigue theory and its application to out-of-phase cyclic loading,” *Journal of Engineering Materials and Technology,* vol. 115, no. 4, pp. 411-416, 1993.

[88] D.-G. Shang, and W.-X. Yao, “A nonlinear damage cumulative model for uniaxial fatigue,” *International Journal of Fatigue,* vol. 21, no. 2, pp. 187-194, 1999.

[89] M. Kumbhalkar, D. Bhope, and A. Vanalkar, “Finite Element Analysis of Rail Vehicle Suspension Spring for Its Fatigue Life Improvement,” in Advanced

Manufacturing and Materials Science, Lecture Notes on Multidisciplinary Industrial Engineering, Springer Nature, 2018, pp. 39-53.

[90] A. F. Madayag, *Metal Fatigue - Theory and Design*: Wiley, 1969.

[91] Q. Bai, and Y. Bai, "Fatigue and Fracture," *Subsea Pipeline Design, Analysis, and Installation*, pp. 283-318, Chapter 12: Gulf Professional Publishing, 2014.

[92] S. Suresh, *Fatigue of materials*: Cambridge University Press, 1998.

[93] M. Rahman, A. Ariffin, S. Abdullah, M. Noor, R. Bakar, and M. Maleque, "Finite element based fatigue life prediction of cylinder head for two-stroke linear engine using stress-life approach," *Journal of Applied Sciences,* vol. 8, no. 19, pp. 3316-3327, 2008.

[94] G. Cheng, and A. Plumtree, "A fatigue damage accumulation model based on continuum damage mechanics and ductility exhaustion," *International Journal of Fatigue,* vol. 20, no. 7, pp. 495-501, 1998.

[95] R. I. Stephens, A. Fatemi, R. R. Stephens, and H. O. Fuchs, *Metal fatigue in engineering*: John Wiley & Sons, 2000.

[96] J. Yoo, and I. Al-Qadi, "A strain-controlled hot-mix asphalt fatigue model considering low and high cycles," *International Journal of Pavement Engineering,* vol. 11, pp. 565-574, 2010.

[97] S. L. Zhang, and F. Z. Xuan, "Interaction of cyclic softening and stress relaxation of 9–12% Cr steel under strain-controlled fatigue-creep condition: Experimental and modeling," *International Journal of Plasticity,* vol. 98, pp. 45-64, 2017.

[98] S. T. Kyaw, J. P. Rouse, J. Lu, and W. Sun, "Determination of material parameters for a unified viscoplasticity-damage model for a P91 power plant steel," *International Journal of Mechanical Sciences,* vol. 115, pp. 168-179, 2016.

[99] R. Mishnev, N. Dudova, and R. Kaibyshev, "Low Cycle Fatigue Behavior of a 10% Cr Martensitic Steel at 600°C," *ISIJ International,* vol. 55, 2015.

[100] J. Chaboche, and P. A. Lesne, "A non-linear continuous fatigue damage model," *Fatigue & fracture of engineering materials & structures,* vol. 11, no. 1, pp. 1-17, 1988.

[101] J. Lemaitre, and J. Dufailly, "Damage measurements," *Engineering Fracture Mechanics,* vol. 28, no. 5-6, pp. 643-661, 1987.

[102] J. L. Chaboche, "Continuous damage mechanics—a tool to describe phenomena before crack initiation," *Nuclear Engineering and Design,* vol. 64, no. 2, pp. 233-247, 1981.

[103] J. L. Chaboche, "Continuum damage mechanics: Part II—Damage growth, crack initiation, and crack growth," *Journal of Applied Mechanics,* vol. 55, no. 1, pp. 65-72, 1988.

[104] J. Lemaitre, and A. Plumtree, "Application of damage concepts to predict creep-fatigue failures," *Journal of Engineering Materials and Technology,* vol. 101, no. 3, pp. 284-292, 1979.

[105] Z. Fan, X. Chen, L. Chen, and J. Jiang, "A CDM-based study of fatigue–creep interaction behavior," *International Journal of Pressure Vessels and Piping,* vol. 86, no. 9, pp. 628-632, 2009.

[106] T. P. Farragher, S. Scully, N. P. O'Dowd, and S. B. Leen, "Development of life assessment procedures for power plant headers operated under flexible loading scenarios," *International Journal of Fatigue,* vol. 49, pp. 50-61, 2013.

[107] N. K. Mukhopadhyay, B. K. Dutta, and H. S. Kushwaha, "On-line fatigue–creep monitoring system for high-temperature components of power plants," *International Journal of Fatigue,* vol. 23, no. 6, pp. 549-560, 2001.

[108] J. Sun, and H. Yuan, "Life assessment of multiaxial thermomechanical fatigue of a nickel-based superalloy Inconel 718," *International Journal of Fatigue,* vol. 120, pp. 228-240, 2019.

[109] S.-L. Zhang, and F.-Z. Xuan, "Interaction of cyclic softening and stress relaxation of 9–12% Cr steel under strain-controlled fatigue-creep condition: Experimental and modeling," *International Journal of Plasticity,* vol. 98, pp. 45-64, 2017.

[110] R. Skelton, and D. Gandy, "Creep–fatigue damage accumulation and interaction diagram based on metallographic interpretation of mechanisms," *Materials at High Temperatures,* vol. 25, no. 1, pp. 27-54, 2008.

[111] J. Parker, "Creep fatigue interactions in power plant components," *Materials at High Temperatures,* vol. 31, no. 4, pp. 370-377, 2014.

[112] V. Kalyanasundaram, "Creep, fatigue and creep-fatigue interactions in modified 9% Chromium-1% Molybdenum (P91) steels," University of Arkansas, 2013, PhD Thesis.

[113] B. Fournier, M. Sauzay, C. Caës, M. Noblecourt, M. Mottot, L. Allais, I. Tournie, and A. Pineau, "Creep-fatigue interactions in a 9 pct Cr-1 pct Mo martensitic steel: Part I. Mechanical test results," *Metallurgical and Materials Transactions A,* vol. 40, pp. 321-329, 2009.

[114] P. Zhao, and F. Z. Xuan, "Ratchetting behavior of advanced 9–12% chromium ferrite steel under creep-fatigue loadings," *Mechanics of Materials,* vol. 43, no. 6, pp. 299-312, 2011.

[115] M. Yaguchi, and Y. Takahashi, "Ratchetting of viscoplastic material with cyclic softening, part 1: experiments on modified 9Cr–1Mo steel," *International Journal of Plasticity,* vol. 21, no. 1, pp. 43-65, 2005.

[116] S. K. Paul, "A critical review of experimental aspects in ratcheting fatigue: microstructure to specimen to component," *Journal of Materials Research and Technology,* vol. 8, no. 5, pp. 4894-4914, 2019.

[117] B. Fournier, M. Sauzay, C. Caës, M. Mottot, M. Noblecourt, and A. Pineau, "Analysis of the hysteresis loops of a martensitic steel: Part II: study of the influence of creep and stress relaxation holding times on cyclic behaviour," *Materials Science and Engineering: A,* vol. 437, no. 2, pp. 197-211, 2006.

[118] B. Fournier, M. Sauzay, F. Barcelo, E. Rauch, A. Renault, T. Cozzika, L. Dupuy, and A. Pineau, "Creep-Fatigue Interactions in a 9 Pct Cr-1 Pct Mo

Martensitic Steel: Part II. Microstructural Evolutions," *Metallurgical and Materials Transactions A,* vol. 40, no. 2, pp. 330-341, 2009.

[119] B. Fournier, F. Dalle, M. Sauzay, J. Longour, M. Salvi, C. Caës, I. Tournié, P. F. Giroux, and S. H. Kim, "Comparison of various 9–12%Cr steels under fatigue and creep-fatigue loadings at high temperature," *Materials Science and Engineering: A,* vol. 528, no. 22, pp. 6934-6945, 2011.

[120] B. Fournier, M. Sauzay, C. Caës, M. Noblecourt, M. Mottot, A. Bougault, V. Rabeau, and A. Pineau, "Creep–fatigue–oxidation interactions in a 9Cr–1Mo martensitic steel. Part I: Effect of tensile holding period on fatigue lifetime," *International Journal of Fatigue,* vol. 30, no. 4, pp. 649-662, 2008.

[121] D. Hu, Q. Ma, L. Shang, Y. Gao, and R. Wang, "Creep-fatigue behavior of turbine disc of superalloy GH720Li at 650 C and probabilistic creep-fatigue modeling," *Materials Science and Engineering: A,* vol. 670, pp. 17-25, 2016.

[122] N. Ohno, and Y. Kachi, "A Constitutive Model of Cyclic Plasticity for Nonlinear Hardening Materials," *Journal of Applied Mechanics,* vol. 53, no. 2, pp. 395-403, 1986.

[123] E. Contesti, and G. Cailletaud, "Description of creep-plasticity interaction with non-unified constitutive equations: application to an austenitic stainless steel," *Nuclear Engineering and Design,* vol. 116, no. 3, pp. 265-280, 1989.

[124] G. Cailletaud, and K. Saï, "Study of plastic/viscoplastic models with various inelastic mechanisms," *International Journal of Plasticity,* vol. 11, no. 8, pp. 991-1005, 1995.

[125] V. Velay, G. Bernhart, and L. Penazzi, "Cyclic behavior modeling of a tempered martensitic hot work tool steel," *International Journal of Plasticity,* vol. 22, no. 3, pp. 459-496, 2006.

[126] A. Benaarbia, Y. Rae, and W. Sun, "Unified viscoplasticity modelling and its application to fatigue-creep behaviour of gas turbine rotor," *International Journal of Mechanical Sciences,* vol. 136, pp. 36-49, 2018.

[127] S. R. Bodner, and Y. Partom, "Constitutive Equations for Elastic-Viscoplastic Strain-Hardening Materials," *Journal of Applied Mechanics,* vol. 42, no. 2, pp. 385-389, 1975.

[128] A. Miller, "An Inelastic Constitutive Model for Monotonic, Cyclic, and Creep Deformation: Part I—Equations Development and Analytical Procedures," *Journal of Engineering Materials and Technology,* vol. 98, no. 2, pp. 97-105, 1976.

[129] D. N. Robinson, "A unified creep-plasticity model for structural metals at high temperature," *Oak Ridge National Library,* no. Report ORNL-TM-5969, 1978.

[130] K. P. Walker, "Research and Development Program for Non-linear Structural Modeling with Advanced Time-temperature Dependent Constitutive Relationships," *Report PWA-5700e5750, NASA CR-165533,* 1981.

[131] E. Krempl, J. J. McMahon, and D. Yao, "Viscoplasticity based on overstress with a differential growth law for the equilibrium stress," *Mechanics of Materials,* vol. 5, no. 1, pp. 35-48, 1986.

[132] O. Watanabe, and S. N. Atluri, "Constitutive modeling of cyclic plasticity and creep, using an internal time concept," *International Journal of Plasticity,* vol. 2, no. 2, pp. 107-134, 1986.

[133] P. Delobelle, "Sur les lois de comportement viscoplastique à variables internes - Exemples de deux alliages industriels : inoxydable austénitique 17-12 SPH et superalliage INCO718," *Revue de Physique Appliquee,* vol. 23, no. 1, pp. 1-61, 1988.

[134] R. A. Barrett, P. E. O'Donoghue, and S. B. Leen, "An improved unified viscoplastic constitutive model for strain-rate sensitivity in high temperature fatigue," *International Journal of Fatigue,* vol. 48, pp. 192-204, 2013.

[135] J. L. Chaboche, "Viscoplastic constitutive equations for the description of cyclic and anisotropic behaviour of metals," *Bull. Acad. Polonaise Sci.,* vol. 25, no. 1, pp. 33–42, 1977.

[136] J. L. Chaboche, and G. Rousselier, "On the Plastic and Viscoplastic Constitutive Equations—Part I: Rules Developed With Internal Variable Concept," *Journal of Pressure Vessel Technology,* vol. 105, no. 2, pp. 153-158, 1983.

[137] J. L. Chaboche, "Constitutive equations for cyclic plasticity and cyclic viscoplasticity," *International Journal of Plasticity,* vol. 5, no. 3, pp. 247-302, 1989.

[138] J. L. Chaboche, and D. Nouailhas, "A Unified Constitutive Model for Cyclic Viscoplasticity and Its Applications to Various Stainless Steels," *Journal of Engineering Materials and Technology,* vol. 111, no. 4, pp. 424-430, 1989.

[139] J. L. Chaboche, "Time-independent constitutive theories for cyclic plasticity," *International Journal of Plasticity,* vol. 2, no. 2, pp. 149-188, 1986.

[140] J. L. Chaboche, "A review of some plasticity and viscoplasticity constitutive theories," *International Journal of Plasticity,* vol. 24, no. 10, pp. 1642-1693, 2008.

[141] J. Lu, "Material characterisation and finite element modelling of the cyclic plasticity behaviour of steels," University of Nottingham, 2016, PhD Thesis.

[142] A. Bertarelli, "Beam-Induced Damage Mechanisms and their Calculation," in Proceedings of the 2014 Joint International Accelerator School: Beam Loss and Accelerator Protection, 2016.

[143] A. A. Saad, "Cyclic plasticity and creep of power plant materials," University of Nottingham, 2012, PhD Thesis.

[144] W. Prager, "Recent Developments in the Mathematical Theory of Plasticity," *Journal of Applied Physics,* vol. 20, no. 3, pp. 235-241, 1949.

[145] C. O. Frederick, and P. J. Armstrong, "A mathematical representation of the multiaxial Bauschinger effect," *Materials at High Temperatures,* vol. 24, no. 1, pp. 1-26, 2007.

[146] J. L. Chaboche, "On some modifications of kinematic hardening to improve the description of ratchetting effects," *International Journal of Plasticity,* vol. 7, no. 7, pp. 661-678, 1991/01/01/, 1991.

[147] N. Ohno, and J. D. Wang, “Kinematic hardening rules with critical state of dynamic recovery, part I: formulation and basic features for ratchetting behavior,” *International Journal of Plasticity,* vol. 9, no. 3, pp. 375-390, 1993.

[148] J. L. Chaboche, “Sur l’utilisation des variables d’état interne pour la description de la viscoplasticité cyclique avec endommagement. In Problèmes Non Linéaires de Mécanique,” in Symposium Franco-Polonais de Rhéologie et Mécanique, Cracovie, 1977, pp. 137–159.

[149] M. Yaguchi, M. Yamamoto, and T. Ogata, “A viscoplastic constitutive model for nickel-base superalloy, part 1: kinematic hardening rule of anisotropic dynamic recovery,” *International Journal of Plasticity,* vol. 18, no. 8, pp. 1083-1109, 2002.

[150] S. Guo, F. Xuan, Z. Wang, and G. Kang, “Constitutive modelling concerning the effects of particulate shapes for the cyclic deformation of SiCP/6061Al composites at high temperature,” *Materials at High Temperatures,* vol. 32, no. 5, pp. 447-454, 2015.

[151] J. L. Chaboche, K. Dang Van, and G. Cordier, *Modelization of the strain memory effect on the cyclic hardening of 316 stainless steel*, vol. 11-3, SMIRT-51979, Division L Berlin, 1979.

[152] N. Ohno, “A Constitutive Model of Cyclic Plasticity With a Nonhardening Strain Region,” *Journal of Applied Mechanics,* vol. 49, no. 4, pp. 721-727, 1982.

[153] J. Lemaitre, and J. L. Chaboche, *Mechanics of solid materials*: Cambridge University Press, 1994.

[154] G. Bernhart, G. Moulinier, O. Brucelle, and D. Delagnes, “High temperature low cycle fatigue behaviour of a martensitic forging tool steel,” *International Journal of Fatigue,* vol. 21, no. 2, pp. 179-186, 1999.

[155] A. A. Saad, T. H. Hyde, W. Sun, C. J. Hyde, and D. W. J. Tanner, “Characterization of viscoplasticity behaviour of P91 and P92 power plant steels,” *International Journal of Pressure Vessels and Piping,* vol. 111-112, pp. 246-252, 2013.

[156] D. L. Wu, F. Z. Xuan, S. J. Guo, and P. Zhao, “Uniaxial mean stress relaxation of 9–12% Cr steel at high temperature: Experiments and viscoplastic constitutive modeling,” *International Journal of Plasticity,* vol. 77, pp. 156-173, 2016.

[157] Y. Takahashi, “Study on creep-fatigue evaluation procedures for high-chromium steels—Part I: Test results and life prediction based on measured stress relaxation,” *International Journal of Pressure Vessels and Piping,* vol. 85, no. 6, pp. 406-422, 2008.

[158] D. W. Dean, P. J. Budden, and R. A. Ainsworth, “R5 procedures for assessing the high temperature response of structures: current status and future developments,” in Pressure Vessels and Piping (PVP) Conference, 2007, pp. 403-412.

[159] S. Paddea, F. Masuyama, and A. Shibli, "T23 and T24–new generation low alloyed steels," *Coal Power Plant Materials and Life Assessment*, pp. 87-106, Chapter 3, 2014.

[160] W. F. Lima, G. Rigueira, H. C. Furtado, M. B. Lisboa, and L. H. d. Almeida, “Microstructure evolution and creep properties of 2.25 Cr-1Mo ferrite-pearlite and ferrite-bainite steels after exposure to elevated temperatures,” *Materials Research,* vol. 20, pp. 418-422, 2017.

[161] D. Robertson, "Traditional low alloy steels in power plant design," *Coal Power Plant Materials and Life Assessment*, pp. 107-126, Chapter 4, 2014.

[162] S. Kim, G. Kim, S. W. Song, and J. H. Kim, “Effects of Cr and Mo contents on the flow-accelerated corrosion behavior of low alloy steels in the secondary side of pressurized water reactors,” *Journal of Nuclear Materials,* vol. 585, no. 154652, pp. 1-17, 2023.

[163] Y. Nishizaka, Y. Hara, A. Hori, H. Tsukahara, K. Miyano, T. Wada, and T. Cox, “Changes in microstructure and mechanical properties of Cr-Mo reactor vessel steels during long-term service,” *Journal of Pressure Vessel Technology,* vol. 107, no. 3, pp. 285-294, 1985.

[164] R. Raj, “Nucleation of cavities at second phase particles in grain boundaries,” *Acta Metallurgica,* vol. 26, no. 6, pp. 995-1006, 1978.

[165] J. Dobrzański, A. Hernas, and G. Moskal, "Microstructural degradation in boiler steels: materials developments, properties and assessment," *Power Plant Life Management and Performance Improvement*, pp. 222-271, Chapter 6: Woodhead Publishing, 2011.

[166] F. Chen, W. Zhang, K. Zhang, Q. Yang, X. Wang, and C. Zhou, “Low cycle fatigue and creep-fatigue interaction behavior of 2.25 CrMoV steel at high temperature,” *Journal of Materials Research and Technology,* vol. 28, pp. 3155-3165, 2024.

[167] J. Zhang, D. Yu, Z. Zhao, Z. Zhang, G. Chen, and X. Chen, “Low cycle fatigue of 2.25 Cr1Mo steel with tensile and compressed hold loading at elevated temperature,” *Materials Science and Engineering: A,* vol. 667, pp. 251-260, 2016.

[168] A. Benaarbia, J. P. Rouse, and W. Sun, “A thermodynamically-based viscoelastic-viscoplastic model for the high temperature cyclic behaviour of 9–12% Cr steels,” *International Journal of Plasticity,* vol. 107, pp. 100-121, 2018.

[169] M. K. Booker, V. Sikka, and B. L. Booker, *Comparison of the mechanical strength properties of several high-chromium ferritic steels*, Oak Ridge National Lab.(ORNL), Oak Ridge, TN (United States), 1981.

[170] R. A. Barrett, C. J. Hyde, P. E. O'Donoghue, and S. B. Leen, “Thermomechanical fatigue in 9-12Cr steels: Life prediction models and the effect of tensile dwell periods,” *International Journal of Fatigue,* vol. 126, pp. 335-345, 2019/09/01/, 2019.

[171] W. Yan, W. Wang, Y. Y. Shan, and K. Yang, “Microstructural stability of 9–12% Cr ferrite/martensite heat-resistant steels,” *Frontiers of Materials Science,* vol. 7, pp. 1-27, 2013.

[172] F. Sun, E. D. Meade, and P. Noel, “Microscale modelling of the deformation of a martensitic steel using the Voronoi tessellation method,” *Journal of the Mechanics and Physics of Solids,* vol. 113, pp. 35-55, 2018.

[173] Y. Rae, X. Guo, A. Benaarbia, N. Neate, and W. Sun, “On the microstructural evolution in 12% Cr turbine steel during low cycle fatigue at elevated temperature,” *Materials Science and Engineering: A,* vol. 773, no. 138864, pp. 1-12, 2020.

[174] B. J. Golden, D. F. Li, Y. Guo, P. Tiernan, S. B. Leen, and N. P. O'Dowd, “Microscale deformation of a tempered martensite ferritic steel: Modelling and experimental study of grain and sub-grain interactions,” *Journal of the Mechanics and Physics of Solids,* vol. 86, pp. 42-52, 2016.

[175] A. Benaarbia, X. Xu, W. Sun, A. A. Becker, and M. A. E. Jepson, “Investigation of short-term creep deformation mechanisms in MarBN steel at elevated temperatures,” *Materials Science and Engineering: A,* vol. 734, pp. 491-505, 2018/09/12/, 2018.

[176] F. Sun, E. D. Meade, and N. P. O′Dowd, “Microscale modelling of the deformation of a martensitic steel using the Voronoi tessellation method,” *Journal of the Mechanics and Physics of Solids,* vol. 113, pp. 35-55, 2018.

[177] B. Fournier, M. Sauzay, and A. Pineau, “Micromechanical model of the high temperature cyclic behavior of 9–12% Cr martensitic steels,” *International Journal of Plasticity,* vol. 27, no. 11, pp. 1803-1816, 2011.

[178] B. Sonderegger, S. Mitsche, and H. Cerjak, “Microstructural analysis on a creep resistant martensitic 9–12% Cr steel using the EBSD method,” *Materials Science and Engineering: A,* vol. 481, pp. 466-470, 2008.

[179] L. Zhu, X. Liu, P. Fan, and J. Liu, “A Study of Microstructure Evolution During Creep of 9Cr-1Mo Steel Using Ultrasonic and Hardness Measurements,” *Journal of Materials Engineering and Performance,* vol. 28, pp. 2348-2355, 2019.

[180] P. Zhao, F. Z. Xuan, and C. Wang, “A physically-based model of cyclic responses for martensitic steels with the hierarchical lath structure under different loading modes,” *Journal of the Mechanics and Physics of Solids,* vol. 124, pp. 555-576, 2019.

[181] M. Sauzay, B. Fournier, M. Mottot, A. Pineau, and I. Monnet, “Cyclic softening of martensitic steels at high temperature—Experiments and physically based modelling,” *Materials Science and Engineering: A,* vol. 483, pp. 410-414, 2008.

[182] B. Fournier, M. Sauzay, F. Barcelo, E. Rauch, A. Renault, T. Cozzika, L. Dupuy, and A. Pineau, “Creep-fatigue interactions in a 9 Pct Cr-1 Pct Mo martensitic steel: part II. Microstructural evolutions,” *Metallurgical and Materials Transactions A,* vol. 40, pp. 330-341, 2009.

[183] D. L. Wu, P. Zhao, Q. Q. Wang, and F. Z. Xuan, “Cyclic behavior of 9–12% Cr steel under different control modes in low cycle regime: A comparative study,” *International Journal of Fatigue,* vol. 70, pp. 114-122, 2015.

[184] M. Kimura, K. Yamaguchi, M. Hayakawa, K. Kobayashi, and K. Kanazawa, “Microstructures of creep-fatigued 9–12% Cr ferritic heat-resisting steels,” *International Journal of Fatigue,* vol. 28, pp. 300-308, 2006.

[185] L. Taleb, “About the cyclic accumulation of the inelastic strain observed in metals subjected to cyclic stress control,” *International Journal of Plasticity,* vol. 43, pp. 1-19, 2013.

[186] S. S. Manohar, A. Sahoo, A. Subramaniam, and S. K. Panda, “Condition monitoring of power electronic converters in power plants—A review,” in 20th International Conference on Electrical Machines and Systems (ICEMS), 2017, pp. 1-5.

[187] P. Baraldi, F. Di Maio, L. Pappaglione, E. Zio, and R. Seraoui, “Condition monitoring of electrical power plant components during operational transients,” in Proceedings of the Institution of Mechanical Engineers, Part O: Journal of Risk and Reliability, 2012, pp. 568-583.

[188] A. Catchpole, *Metallurgical assessment of sections taken from Unit 1 convection reheater outlet header, removed during the 2015 statutory outage*, Uniper Technologies, UTG/16/ASI/WE/569/R, June 2016.

[189] C. Taylor, and E. N. Burton, *West Burton Unit 4: Integrity status of header systems - 2011 outage*, E.ON New Build & Technology, ENT/13/TSP/IA/601/R, September 2013.

[190] A. Catchpole, and G. Degnan, *West Burton power station: Unit 3 - Metallurgical assessments carried out on high temperature pipework and welds during the 2012 statutory outage and 2014 interim outage*, Uniper Technologies, ENT/13/TSP/WE/359/R, February 2016.

[191] BSI, "BS7910: Guide on methods for assessing the acceptability of flaws in metallic structures," British Standard Institution, 1999.

[192] J. A. Williams, and M. C. Coleman, *Application of current strain based remanent life models to real components* CEGB (Central Electricity Generating Board), TPRD/M/1277/N82, 1982.

[193] J. A. Clowes, D. R. Barraclough, R. J. Browne, B. Cane, J. K. Hepworth, J. L. Phillips, and B. Plastow, *Creep Life Assessment of Boiler Pressure Parts Using Strain Data*, CEGB (Central Electricity Generating Board), NWR/SSD/85/0031/R, 1985.

[194] J. Corcoran, and C. Davies, “Monitoring power-law creep using the Failure Forecast Method,” *International Journal of Mechanical Sciences,* vol. 140, pp. 179-188, 2018.

[195] B. Cardoso, C. F. T. Matt, H. Furtado, and L. De Almeida, “Creep damage evaluation in high-pressure rotor based on hardness measurement,” *Journal of Materials Engineering and Performance,* vol. 24, pp. 2784-2791, 2015.

[196] F. Masuyama, “Hardness model for creep-life assessment of high-strength martensitic steels,” *Materials Science and Engineering: A,* vol. 510, pp. 154-157, 2009.

[197] F. Masuyama, “Creep degradation in welds of Mod. 9Cr-1Mo steel,” *International Journal of Pressure Vessels and Piping,* vol. 83, no. 11-12, pp. 819-825, 2006.

[198] N. Saito, K. Ishiyama, T. Yamaguchi, and F. Masuyama, "Effect of Creep Degradation on Hardness Changes of Ni-based Alloys for A-USC Power Boiler," *ISIJ International,* vol. 59, no. 9, pp. 1695-1704, 2019.

[199] D. J. Allen, and S. T. Fenton, "A hardness-based creep rupture model for new and service aged P91 steel," *BALTICA VII, Life Management and Maintenance for Power Plants Vol. 1,* 2007.

[200] D. J. Allen, "GENSIP Grade 91 Good Practice Guide, Report R17 (GENSIP/R/PS027): A Hardness -Normalised Model Of Creep Rupture For P91 Steel," GENSIP2013.

[201] M. S. Shammas, *Remanent Life Assessment of Ferritic Weld Heat Affected Zones by a Metallographic Measurement of Cavitation Damage: The'A'Parameter*: Central Electricity Generating Board (CEGB) Technology Planning and Research, 1987.

[202] R. Viswanathan, *Damage mechanisms and life assessment of high temperature components*: ASM International, 1989.

[203] H. Riedel, "Life prediction methods for constrained grain boundary cavitation," *International Journal of Pressure Vessels and Piping,* vol. 39, no. 1-2, pp. 119-134, 1989.

[204] J. W. Wilson, D. J. Allen, A. J. Peyton, A. Shibli, and C. Davis, "Detection of creep degradation during pressure vessel testing using electromagnetic sensor technology," *Materials at High Temperatures,* vol. 34, no. 5-6, pp. 448-457, 2017.

[205] J. Corcoran, P. Hooper, C. Davies, P. B. Nagy, and P. Cawley, "Creep strain measurement using a potential drop technique," *International Journal of Mechanical Sciences,* vol. 110, pp. 190-200, 2016.

[206] G. Sposito, C. Ward, P. Cawley, P. Nagy, and C. Scruby, "A review of non-destructive techniques for the detection of creep damage in power plant steels," *NDT & E International,* vol. 43, no. 7, pp. 555-567, 2010.

[207] A. Aghajani, C. Somsen, and G. Eggeler, "On the effect of long-term creep on the microstructure of a 12% chromium tempered martensite ferritic steel," *Acta Materialia,* vol. 57, no. 17, pp. 5093-5106, 2009.

[208] C. Panait, A. Zielińska-Lipiec, T. Kozieł, A. Czyrska-Filemonowicz, A.-F. Gourgues-Lorenzon, and W. Bendick, "Evolution of dislocation density, size of subgrains and MX-type precipitates in a P91 steel during creep and during thermal ageing at 600 °C for more than 100,000 h," *Materials Science and Engineering A,* vol. 527, 2010.

[209] L. Zhu, X. Liu, P. Fan, Y. Yang, K. Zhang, K. Wang, and L. Wang, "Evaluation of microstructure degradation during creep of P91 steel using electrochemical detection technique," *Materials Today Communications,* vol. 34, pp. 105039, 2023.

[210] K. Zhang, X. Liu, and L. Zhu, "Characterisation of microstructure evolution during creep of P91 steel using the electron backscatter diffraction technique," *Materials at High Temperatures,* vol. 38, no. 3, pp. 158-165, 2021/05/04, 2021.

[211] *Coal Generation Great Britain. The pathway to a low-carbon future: consultation document* Department for Business, Energy & Industrial Strategy November 2016.

[212] *Powering up Britain* Department for Energy Security and Net Zero, March 2023.

[213] TWI Ltd, ABB Engineering Services, SCS (INTL) Ltd, and A. C. Engineering, *RR509-Plant ageing: Management of equipment containing hazardous fluids or pressure*, Health and Safety Executive (HSE), 2006.

[214] B. Cacciapuoti, A. Morris, W. Sun, D. G. McCartney, and J. Hulance, "Correlation and capability of using site inspection data and small specimen creep testing for a service-exposed CrMoV pipe section," *Materials at High Temperatures,* vol. 36, no. 2, pp. 173-186, 2019.

[215] M. J. Cohn, "Main Steam Piping Creep Life Consumption in Circumferential Welds," in Pressure Vessels and Piping Conference, 2011, pp. 527-539.

[216] J. Rouse, M. Leom, W. Sun, T. Hyde, and A. Morris, "Steady-state creep peak rupture stresses in 90 power plant pipe bends with manufacture induced cross-section dimension variations," *International Journal of Pressure Vessels and Piping,* vol. 105, pp. 1-11, 2013.

[217] *Pressure Systems Safety Regulations 2000*, Health and Safety Executive (HSE), 2000.

[218] S. Tosney, *Safe Management of Grade 91 Pressure Parts in Conventional UK Power Stations* vol. GENSIP/GPG/PS/007, 2016.

[219] G. Eggeler, J. Earthman, N. Nilsvang, and B. Ilschner, "Microstructural study of creep rupture in a 12% chromium ferritic steel," *Acta Metallurgica,* vol. 37, no. 1, pp. 49-60, 1989.

[220] H. Zhao, Z. Wang, X. Han, and M. Wang, "Effect of Long-Term Aging on the Microstructural Evolution in a P91 Steel," *Materials,* vol. 15, no. 8, pp. 2847, 2022.

[221] A. Di Gianfrancesco, S. T. Vipraio, and D. Venditti, "Long term microstructural evolution of 9-12% Cr steel grades for steam power generation plants," *Procedia Engineering,* vol. 55, pp. 27-35, 2013.

[222] M. Ejaz, "Creep life prediction of new and service exposed 0.5 Cr-0.5 Mo-0.25 V steel pipework," Imperial College London, 2019, PhD Thesis.

[223] G. Degnan, and S. Fenton, *West Burton Unit 3 - Metallurgical assessments carried out on high temperature pipework and welds during 2008/2010 statutory outage,* E.ON New Build & Technology, ENT/11/TSP/IA/1769/R, February 2012

[224] J. Parker, and J. Siefert, *An Informed Perspective on the Use of Hardness Testing in an Integrated Approach to the Life Management of Grade 91 Steel Componentsnter title,* Electric Power Research Institute (EPRI), 2016.

[225] J. Corcoran, "Rate-based structural health monitoring using permanently installed sensors," *Proceedings of the Royal Society A: Mathematical, Physical and Engineering Sciences,* vol. 473, no. 2205, pp. 20170270, 2017.

[226] F. Abe, “Creep behavior, deformation mechanisms, and creep life of Mod. 9Cr-1Mo steel,” *Metallurgical and Materials Transactions A,* vol. 46, pp. 5610-5625, 2015.

[227] J. Parker, “Creep cavitation in CSEF steels,” *EPRI Advanced Materials Conference,* 2013.

[228] M. Whittaker, and W. Harrison, “Evolution of Wilshire equations for creep life prediction,” *Materials at High Temperatures,* vol. 31, no. 3, pp. 233-238, 2014.

[229] Z. Abdallah, K. Perkins, and C. Arnold, "Creep lifing models and techniques," *Creep,* pp. 115-149, Chapter 7: IntechOpen, 2018.

[230] J. Rouse, C. Hyde, and A. Morris, “A neural network approach for determining spatial and geometry dependent Green's functions for thermal stress approximation in power plant header components,” *International Journal of Pressure Vessels and Piping,* vol. 168, pp. 269-288, 2018.

[231] M. Cooper, *CMV Pipework Management in Conventional UK Power Stations, Coal Generators Safety and Integrity Programme Good Practice Guide* vol. GENSIP/GPG/PS001, 2011.

[232] M. Evans, “The importance of creep strain in linking together the Wilshire equations for minimum creep rates and times to various strains (including the rupture strain): An illustration using 1CrMoV rotor steel,” *Journal of Materials Science,* vol. 49, pp. 329-339, 2014.

[233] B. Wilshire, and P. Scharning, “Prediction of long term creep data for forged 1Cr–1Mo–0· 25V steel,” *Materials Science and Technology,* vol. 24, no. 1, pp. 1-9, 2008.

[234] D. B. J. Clowes, R. Browne, B. Cane, J. Hepworth, J. Phillips, B. Plastow, *Creep Life Assessment of Boiler Pressure Parts using Strain Data,* vol. CEGB Report NWR/SSD/85/0031/R, 1985.

[235] C. Taylor, *West Burton Unit 1: Diametral measurements on main steam and hot reheat pipework - 2009 outage,* E.ON New Build & Technology, ENT/11/TSP/IA/1395/R, 2011.

[236] C. Shen, *Modeling creep-fatigue-environment interactions in steam turbine rotor materials for advanced ultra-supercritical coal power plants,* General Electric Global Research, Niskayuna, NY (United States), 2014.

[237] R. E. Dundas, “The use of performance-monitoring to prevent compressor and turbine blade failures,” *ASME, Turbo Expo: Power for Land, Sea, and Air* vol. 79580, no. 82-GT-66, V003T07A003, 1982.

[238] M. Chrzanowski, “Use of the damage concept in describing creep-fatigue interaction under prescribed stress,” *International Journal of Mechanical Sciences,* vol. 18, no. 2, pp. 69-73, 1976.

[239] Y. N. Fan, H. J. Shi, and K. Tokuda, “A generalized hysteresis energy method for fatigue and creep-fatigue life prediction of 316L (N),” *Materials Science and Engineering: A,* vol. 625, pp. 205-212, 2015.

[240] S. Manson, “Interfaces between fatigue, creep, and fracture,” *International Journal of Fracture Mechanics,* vol. 2, pp. 327-327, 1966.

[241] R. Hill, “A Variational Principle of Maximum Plastic Work in Classical Plasticity,” *The Quarterly Journal of Mechanics and Applied Mathematics,* vol. 1, no. 1, pp. 18-28, 1948.

[242] W. Prager, “The theory of plasticity: a survey of recent achievements,” *Proceedings of the Institution of Mechanical Engineers,* vol. 169, no. 1, pp. 41-57, 1955.

[243] R. Neu, and H. Sehitoglu, “Thermomechanical fatigue, oxidation, and creep: Part I. Damage mechanisms,” *Metallurgical Transactions A,* vol. 20, pp. 1755-1767, 1989.

[244] R. Neu, and H. Sehitoglu, “Thermomechanical fatigue, oxidation, and creep: Part II. Life prediction,” *Metallurgical Transactions A,* vol. 20, pp. 1769-1783, 1989.

[245] R. Skelton, and M. Loveday, “A re-interpretation of the BCR/VAMAS low cycle fatigue intercomparison programme using an energy criterion,” *Materials at High Temperatures,* vol. 14, no. 1, pp. 53-68, 1997.

[246] G. Marahleh, A. R. I. Kheder, and H. F. Hamad, “Creep-life prediction of service-exposed turbine blades,” *Materials Science,* vol. 42, no. 4, pp. 476-481, 2006.

[247] A. Nayebi, H. Ranjbar, and H. Rokhgireh, “Analysis of unified continuum damage mechanics model of gas turbine rotor steel: Life assessment,” *Proceedings of the Institution of Mechanical Engineers, Part L: Journal of Materials: Design and Applications,* vol. 227, no. 3, pp. 216-225, 2013.

[248] ASME, "Boiler and Pressure Vessel Code (BPVC)," 2010.

[249] "RCC-MR: Design and Construction Rules for Mechanical Components of Nuclear Installations," *Association française pour les règles de conception, de construction et surveillance en exploitation des matériels des chaudières électro-nucléaires,* Afcen, 2007.

[250] Y. Takahashi, “Study on Creep-Fatigue Life Prediction Methods Based on Long-Term Creep-Fatigue Tests for Austenitic Stainless Steel,” in IUTAM Symposium on Creep in Structures: Proceedings of the IUTAM Symposium 2001, pp. 311-320.

[251] R. Ainsworth, P. Budden, and R. Hales, “Assessment of the high-temperature response of structures: developments in the R5 procedure,” in Mechanical Engineering Publications, United Kingdom, 1996.

[252] C. J. Smithells, *Metals Reference Book*: Elsevier Butterworth Heinemann and ASM International, 2013.

[253] Y. Rae, A. Benaarbia, J. Hughes, and W. Sun, “Experimental characterisation and computational modelling of cyclic viscoplastic behaviour of turbine steel,” *International Journal of Fatigue,* vol. 124, pp. 581-594, 2019.

[254] S. T. Kyaw, J. P. Rouse, J. Lu, and W. Sun, “Determination of material parameters for a unified viscoplasticity-damage model for a P91 power plant steel,” *International Journal of Mechanical Sciences,* vol. 115-116, pp. 168-179, 2016.

[255] J. Lu, W. Sun, A. Becker, and A. A. Saad, “Simulation of the fatigue behaviour of a power plant steel with a damage variable,” *International Journal of Mechanical Sciences,* vol. 100, pp. 145-157, 2015.

[256] W. Sun, D. W. J. Tanner, T. H. Hyde, and A. A. Saad, “Thermal-mechanical fatigue behaviour of 9–12%Cr power plant steels and pipes,” in International Conference on Sustainable Power Generation and Supply (SUPERGEN 2012), 2012, pp. 1-8.

[257] V. P. Swaminathan, G. J. Dean, and J. R. Scheibel, “Integrated Approach to Gas Turbine Rotor Condition Assessment and Life Management,” in ASME Turbo Expo 2012: Turbine Technical Conference and Exposition, 2012, pp. 621-631.

[258] X. Guan, and J. He, “Life time extension of turbine rotating components under risk constraints: A state-of-the-art review and case study,” *International Journal of Fatigue,* vol. 129, no. 104799, pp. 1-8, 2019.

[259] D. Barraclough, C. Hamm, and B. Plastow, *Creep Rupture Equations of Steels for Use in Life Assessment Calculations Based on ISO (1978) Data*, 1984.

[260] S. Holdsworth, “The European Creep Collaborative Committee (ECCC) approach to creep data assessment,” *Journal of Pressure Vessel Technology,* vol. 130, no. 2, pp. 1-6, 2008.

[261] BSI, "Elevated Temperature Properties for Steels for Pressure Purposes, PD 6525:Part 1," *British Standard Institution,* 1990.

[262] B. Neubauer, “Remaining-life estimation for high-temperature materials under creep load by replicas,” *Nuclear Technology,* vol. 66, no. 2, pp. 308-312, 1984.

[263] S. W. Palocsay, I. S. Markham, and S. E. Markham, “Utilizing and teaching data tools in Excel for exploratory analysis,” *Journal of Business Research,* vol. 63, no. 2, pp. 191-206, 2010.

[264] J. P. Sewell, “Getting the most from your software: using Excel as the poor man's database,” *CIN: Computers, Informatics, Nursing,* vol. 24, no. 1, pp. 13-17, 2006.

[265] J. Rouse, W. Sun, T. Hyde, A. Morris, and W. Montgomery, “A Method to Approximate the Steady-State Creep Response of Three-Dimensional Pipe Bend Finite Element Models Under Internal Pressure Loading Using Two-Dimensional Axisymmetric Models,” *Journal of Pressure Vessel Technology,* vol. 136, 2013.

[266] T. H. Hyde, A. A. Becker, W. Sun, and J. A. Williams, “Influence of geometry change on creep failure life of 90° pressurised pipe bends with no initial ovality,” *International Journal of Pressure Vessels and Piping,* vol. 82, no. 7, pp. 509-516, 2005.

[267] BSI, "BS EN 10222-2: Steel forgings for pressure purposes - Part 2: Ferritic and martensitic steels with specified elevated temperature properties," British Standard Institution, 2000.

[268] E. Pavlina, and C. Van Tyne, “Correlation of yield strength and tensile strength with hardness for steels,” *Journal of Materials Engineering and Performance,* vol. 17, no. 6, pp. 888-893, 2008.

[269] J. Rouse, M. Leom, W. Sun, T. Hyde, and A. Morris, “Steady-state creep peak rupture stresses in 90° power plant pipe bends with manufacture induced cross-section dimension variations,” *International Journal of Pressure Vessels and Piping,* vol. 105, pp. 1-11, 2013.

[270] B. J. Cane, P. F. Aplin, and J. M. Brear, “A Mechanistic Approach to Remanent Creep Life Assessment of Low Alloy Ferritic Components Based on Hardness Measurements,” *Journal of Pressure Vessel Technology,* vol. 107, no. 3, pp. 295-300, 1985.

[271] S. Brett, L. Buchanan, S. Concari, G. Cosso, S. Fenton, A. Fleming, R. Hales, V. Kanta, I. Marcelles, and I. G. Merckling, *Residual life assessment and microstructure*, vol. 6, ECCC Recommendation, AC/MC/93, 2005.

[272] U. F. Kocks, “A statistical theory of flow stress and work-hardening,” *The Philosophical Magazine: A Journal of Theoretical Experimental and Applied Physics,* vol. 13, no. 123, pp. 541-566, 1966.

[273] L. Kachnov, “Time of the rupture process under creep conditions,” *Izvestiia Akademii Nauk SSSR, Otdelenie Teckhnicheskikh Nauk,* vol. 8, pp. 26-31, 1958.

[274] Y. N. Rabotnov, “Creep problems in structural members,” *Journal of Applied Mechanics,* vol. 37, no. 1, pp. 249, 1969.

[275] J. Lemaitre, “A continuous damage mechanics model for ductile fracture,” *Journal of Engineering Materials and Technology*, no. 107(1), pp. 83-89, 1985.

[276] B. J. Cane, “Remaining creep life estimation by strain assessment on plant,” *International Journal of Pressure Vessels and Piping,* vol. 10, no. 1, pp. 11-30, 1982.

[277] K. R. Williams, and B. Wilshire, “Effects of microstructural instability on the creep and fracture behaviour of ferritic steels,” *Materials Science and Engineering,* vol. 28, no. 2, pp. 289-296, 1977.

[278] V. Sklenička, K. Kuchařová, P. Král, M. Kvapilová, M. Svobodová, and J. Čmakal, “The effect of hot bending and thermal ageing on creep and microstructure evolution in thick-walled P92 steel pipe,” *Materials Science and Engineering: A,* vol. 644, pp. 297-309, 2015.

[279] J. A. Siefert, and J. D. Parker, “Evaluation of the creep cavitation behavior in Grade 91 steels,” *International Journal of Pressure Vessels and Piping,* vol. 138, pp. 31-44, 2016.

[280] K. Han, H. Ding, X. Fan, W. Li, Y. Lv, and Y. Feng, “Study of the creep cavitation behavior of P91 steel under different stress states and its effect on high-temperature creep properties,” *Journal of Materials Research and Technology,* vol. 20, pp. 47-59, 2022.

[281] D. Samantaray, C. Phaniraj, S. Mandal, and A. Bhaduri, “Strain dependent rate equation to predict elevated temperature flow behavior of modified 9Cr-1Mo (P91) steel,” *Materials Science and Engineering: A,* vol. 528, no. 3, pp. 1071-1077, 2011.

[282] H. Hongo, M. Tabuchi, and T. Watanabe, “Type IV Creep Damage Behavior in Gr.91 Steel Welded Joints,” *Metallurgical and Materials Transactions A,* vol. 43, no. 4, pp. 1163-1173, 2012.

[283] Y. Wang, W. Zhang, Y. Wang, and Z. Feng, “Characteristics of premature creep failure in over-tempered base metal of grade 91 steel weldment,” *International Journal of Pressure Vessels and Piping,* vol. 192, pp. 104396, 2021.

[284] D. T. Erten, T. T. Nguyen, T. M. Jeong, and K. B. Yoon, “Creep deformation and rupture behaviour of service exposed P91 weld and base steel measured by miniature tensile creep testing,” *Materials at High Temperatures,* vol. 34, no. 5-6, pp. 425-433, 2017.

[285] Y. Xu, Y. Nie, M. Wang, W. Li, and X. Jin, “The effect of microstructure evolution on the mechanical properties of martensite ferritic steel during long-term aging,” *Acta Materialia,* vol. 131, pp. 110-122, 2017.

[286] M. Mitsuhara, S. Yamasaki, M. Miake, H. Nakashima, M. Nishida, J. Kusumoto, and A. Kanaya, “Creep strengthening by lath boundaries in 9Cr ferritic heat-resistant steel,” *Philosophical Magazine Letters,* vol. 96, no. 2, pp. 76-83, 2016.

[287] H. K. Danielsen, and J. Hald, “Behaviour of Z phase in 9–12% Cr steels,” *Energy Materials,* vol. 1, no. 1, pp. 49-57, 2006.

[288] R. Bonetti, A. Morris, P. H. Shipway, and W. Sun, “Empirical relationships between hardness, replica and strain and their roles in health monitoring based life assessment for aged power plant materials,” *International Journal of Pressure Vessels and Piping,* vol. 199, pp. 104735, 2022.

[289] K. Guguloth, and N. Roy, “Creep deformation behavior of 9Cr1MoVNb (ASME Grade 91) steel,” *Materials Science and Engineering: A,* vol. 680, pp. 388-404, 2017.

[290] R. Pohja, S. Tuurna, T. J. Hakala, P. Auerkari, U. McNiven, L. Laaksonen, and R. Nikkarila, “Life assessment and maintenance of welded piping operating at high temperatures,” in Baltica IV-Energiantuotannon kunnossapitokokemukset, 2019.

[291] J. Parker, and J. Henry, “The Performance of Creep-Strengthened Ferritic Steels in Power Generating Plant,” in ASME 2007 Pressure Vessels and Piping Conference, 2007, pp. 607-616.

[292] H. Ghassemi Armaki, R. Chen, K. Maruyama, and M. Igarashi, “Creep Behavior and Degradation of Subgrain Structures Pinned by Nanoscale Precipitates in Strength-Enhanced 5 to 12 Pct Cr Ferritic Steels,” *Metallurgical and Materials Transactions A,* vol. 42, pp. 3084-3094, 2011.

[293] C. G. Panait, W. Bendick, A. Fuchsmann, A. F. Gourgues-Lorenzon, and J. Besson, “Study of the microstructure of the Grade 91 steel after more than 100,000 h of creep exposure at 600 °C,” *International Journal of Pressure Vessels and Piping,* vol. 87, no. 6, pp. 326-335, 2010.

[294] E. Cerri, E. Evangelista, S. Spigarelli, and P. Bianchi, “Evolution of microstructure in a modified 9Cr–1Mo steel during short term creep,” *Materials Science and Engineering: A,* vol. 245, no. 2, pp. 285-292, 1998.

[295] W. Yan, W. Wang, Y. Y. Shan, and K. Yang, “Microstructural stability of 9–12%Cr ferrite/martensite heat-resistant steels,” *Frontiers of Materials Science,* vol. 7, no. 1, pp. 1-27, 2013.

[296] S. N. Lekakh, M. Buchely, M. Li, and L. Godlewski, “Effect of Cr and Ni concentrations on resilience of cast Nb-alloyed heat resistant austenitic steels at extreme high temperatures,” *Materials Science and Engineering: A,* vol. 873, pp. 145027, 2023.

[297] T. Liu, Y. Cui, K. Zheng, F. Yin, and Z. Luo, “Synergistic effect of grain size and second-phase particle on the oxidation behaviour of a high-manganese austenitic heat-resistant steel,” *Corrosion Science,* vol. 215, pp. 111054, 2023.

[298] J. Parker, and J. Siefert, “Metallurgical and stress state factors which affect the creep and fracture behavior of 9% Cr steels,” *Advances in Materials Science and Engineering,* vol. 2018, pp. 1-15, 2018.

[299] H. Yakel, “Atom distributions in tau-carbide phases: Fe and Cr distributions in (Cr23− xFex) C6 with x= 0, 0· 74, 1· 70, 4· 13 and 7· 36,” *Acta Crystallographica Section B: Structural Science,* vol. 43, no. 3, pp. 230-238, 1987.

[300] E. Gladyshevskii, and Y. B. Kuz'ma, “Crystal structure of ternary phases in the systems Mo (W)-Fe (Co, Ni)-Si,” *Journal of Structural Chemistry,* vol. 1, no. 1, pp. 57-62, 1960.

[301] S. J. Kim, H. Franzen, and W. Lengauer, “Non-stoichiometry and twinning in NbN1− x: a study of synthesis and structure in a defect NaCl-type solid,” *Journal of the Less Common Metals,* vol. 160, no. 1, pp. 193-196, 1990.

[302] B. Sonderegger, S. Mitsche, and H. Cerjak, “Microstructural analysis on a creep resistant martensitic 9–12% Cr steel using the EBSD method,” *Materials Science and Engineering: A,* vol. 481-482, pp. 466-470, 2008.

[303] T. H. Hyde, W. Sun, A. A. Becker, and J. A. Williams, “Creep properties and failure assessment of new and fully repaired P91 pipe welds at 923 K,” *Proceedings of the Institution of Mechanical Engineers, Part L: Journal of Materials: Design and Applications,* vol. 218, no. 3, pp. 211-222, 2004.

[304] S. G. GMBH. "1.4903 (X10CRMOVNB9-1) Quenched and Tempered "; https://www.stahlportal.com/en/stock/14903-x10crmovnb9-1-quenched-and-tempered/.

[305] J. Zhang, J. Li, J. Zan, Z. Guo, and K. Liu, “A Creep Constitutive Model, Based on Deformation Mechanisms and Its Application to Creep Crack Growth,” *Metals,* vol. 12, pp. 2179, 2022.

[306] S. D. Yadav, S. Kalácska, M. Dománková, D. C. Yubero, R. Resel, I. Groma, C. Beal, B. Sonderegger, C. Sommitsch, and C. Poletti, “Evolution of the substructure of a novel 12% Cr steel under creep conditions,” *Materials Characterization,* vol. 115, pp. 23-31, 2016.

[307] G. Po, Y. Huang, Y. Li, K. Baker, B. R. Flores, T. Black, J. Hollenbeck, and N. Ghoniem, “A model of thermal creep and annealing in finite domains based on coupled dislocation climb and vacancy diffusion,” *Journal of the Mechanics and Physics of Solids,* vol. 169, pp. 105066, 2022.

[308] B. Fournier, M. Sauzay, and A. Pineau, “Micromechanical model of the high temperature cyclic behavior of 9–12%Cr martensitic steels,” *International Journal of Plasticity,* vol. 27, no. 11, pp. 1803-1816, 2011.

[309] K. Sawada, K. Maruyama, Y. Hasegawa, and T. Muraki, “Creep Life Assessment of High Chromium Ferritic Steels by Recovery of Martensitic Lath Structure,” *Key Engineering Materials,* vol. 171-174, pp. 109-114, 1999.

[310] L. Ryde, “Application of EBSD to analysis of microstructures in commercial steels,” *Materials Science and Technology,* vol. 22, pp. 1297-1306, 2006.

[311] S. Collomb, P. Gressel, J. Ghanbaja, A. Jacques, and A. Redjaïmia, “Characterization of welded joint in martensitic steel Grade 91 after interrupted creep test at 600 °C,” *Materials Science and Engineering: A,* vol. 855, pp. 143851, 2022.

[312] J. Zhao, J. Gong, A. Saboo, D. C. Dunand, and G. B. Olson, “Dislocation-based modeling of long-term creep behaviors of Grade 91 steels,” *Acta Materialia,* vol. 149, pp. 19-28, 2018.

[313] N. M. Ghoniem, J. Matthews, and R. J. Amodeo, “A dislocation model for creep in engineering materials,” *Res Mechanica,* vol. 29, no. 3, pp. 197-219, 1990.

[314] C. Schäfer, V. Mohles, and G. Gottstein, “Modeling of non-isothermal annealing: Interaction of recrystallization, recovery, and precipitation,” *Acta Materialia,* vol. 59, no. 17, pp. 6574-6587, 2011.

[315] D. M. Norfleet, D. M. Dimiduk, S. J. Polasik, M. Uchic, and M. J. Mills, “Dislocation Structures and Their Relationship to Strength in Deformed Nickel Microcrystals,” *Acta Materialia,* vol. 56, no. 13, pp. 2988-3001, 2008.

[316] C. Pandey, M. Mahapatra, P. Kumar, R. Vidyrathy, and A. Srivastava, “Microstructure-based assessment of creep rupture behaviour of cast-forged P91 steel,” *Materials Science and Engineering: A,* vol. 695, pp. 291-301, 2017.

[317] J. Pešička, R. Kužel, A. Dronhofer, and G. Eggeler, “The evolution of dislocation density during heat treatment and creep of tempered martensite ferritic steels,” *Acta Materialia,* vol. 51, no. 16, pp. 4847-4862, 2003.

[318] K. Sawada, K. Kubo, and F. Abe, “Creep behavior and stability of MX precipitates at high temperature in 9Cr–0.5Mo–1.8W–VNb steel,” *Materials Science and Engineering: A,* vol. 319-321, pp. 784-787, 2001.

[319] V. Dudko, A. Belyakov, D. Molodov, and R. Kaibyshev, “Microstructure Evolution and Pinning of Boundaries by Precipitates in a 9 pct Cr Heat Resistant Steel During Creep,” *Metallurgical and Materials Transactions A,* vol. 44, no. 1, pp. 162-172, 2013.

[320] B. Tang, L. Jiang, R. Hu, and Q. Li, “Correlation between grain boundary misorientation and M23C6 precipitation behaviors in a wrought Ni-based superalloy,” *Materials Characterization,* vol. 78, pp. 144-150, 2013.

[321] H. U. Hong, B. S. Rho, and S. W. Nam, “Correlation of the M23C6 precipitation morphology with grain boundary characteristics in austenitic stainless steel,” *Materials Science and Engineering: A,* vol. 318, no. 1, pp. 285-292, 2001.

[322] J. K. Park, and A. J. Ardell, “Precipitation at grain boundaries in the commercial alloy Al 7075,” *Acta Metallurgica,* vol. 34, no. 12, pp. 2399-2409, 1986.

[323] L. Priester, "Precipitation at Grain Boundaries," *Grain Boundaries: From Theory to Engineering,* pp. 217-240, Chapter 7, Dordrecht: Springer, 2012.

[324] S. Yadav, T. Scherer, G. P. Reddy, K. Laha, G. Sasikala, S. Albert, and C. Poletti, “Creep modelling of P91 steel employing a microstructural based hybrid concept,” *Engineering Fracture Mechanics,* vol. 200, pp. 104-114, 2018.

[325] M. Isik, A. Kostka, and G. Eggeler, “On the nucleation of Laves phase particles during high-temperature exposure and creep of tempered martensite ferritic steels,” *Acta Materialia,* vol. 81, pp. 230-240, 2014.

[326] H. A. Derazkola, E. García Gil, A. Murillo-Marrodán, and D. Méresse, “Review on dynamic recrystallization of martensitic stainless steels during hot deformation: Part I—Experimental Study,” *Metals,* vol. 11, no. 4, pp. 3-25, 2021.

[327] Q. Gao, X. Di, Y. Liu, and Z. Yan, “Recovery and recrystallization in modified 9Cr-1Mo steel weldments after post-weld heat treatment,” *International Journal of Pressure Vessels and Piping,* vol. 93, pp. 69-74, 2012.

[328] M. Sauzay, “Modelling of the evolution of micro-grain misorientations during creep of tempered martensite ferritic steels,” *Materials Science and Engineering: A,* vol. 510-511, pp. 74-80, 2009.

[329] R. A. Barrett, P. E. O'Donoghue, and S. B. Leen, “A physically-based constitutive model for high temperature microstructural degradation under cyclic deformation,” *International Journal of Fatigue,* vol. 100, pp. 388-406, 2017.

[330] P. F. Giroux, F. Dalle, M. Sauzay, J. Malaplate, B. Fournier, and A. F. Gourgues-Lorenzon, “Mechanical and microstructural stability of P92 steel under uniaxial tension at high temperature,” *Materials Science and Engineering: A,* vol. 527, no. 16-17, pp. 3984-3993, 2010.

[331] J. Hald, “Microstructure and long-term creep properties of 9–12% Cr steels,” *International Journal of Pressure Vessels and Piping,* vol. 85, no. 1, pp. 30-37, 2008.

[332] G. Eggeler, “The effect of long-term creep on particle coarsening in tempered martensite ferritic steels,” *Acta Metallurgica,* vol. 37, no. 12, pp. 3225-3234, 1989.

[333] R. Kaibyshev, R. Mishnev, A. Fedoseeva, and N. Dudova, “The Role of Microstructure in Creep Strength of 9-12%Cr Steels,” *Materials Science Forum,* vol. 879, pp. 36-41, 2017.

[334] S. Dasari, A. Sarkar, A. Sharma, B. Gwalani, D. Choudhuri, V. Soni, S. Manda, I. Samajdar, and R. Banerjee, “Recovery of cold-worked Al0. 3CoCrFeNi complex concentrated alloy through twinning assisted B2 precipitation,” *Acta Materialia,* vol. 202, pp. 448-462, 2021.

[335] S. D. Yadav, B. Sonderegger, B. Sartory, C. Sommitsch, and C. Poletti, "Characterisation and quantification of cavities in 9Cr martensitic steel for power plants," *Materials Science and Technology,* vol. 31, no. 5, pp. 554-564, 2015.

[336] M. Yoo, and H. Trinkaus, "Crack and cavity nucleation at interfaces during creep," *Metallurgical Transactions A,* vol. 14, pp. 547-561, 1983.

[337] S. D. Yadav, U. Jäntsch, T. Scherer, M. R. Ahmadi, J. Rosc, and C. Poletti, "Investigation of creep cavities in a novel 12Cr0.36Ta steel employing three-dimensional electron backscatter diffraction technique," *Materials Letters,* vol. 207, pp. 76-79, 2017.

[338] H. Jiang, X. Chen, Z. Fan, J. Dong, and S. Lu, "A new empirical life prediction method for stress controlled fatigue–creep interaction," *Materials Letters,* vol. 62, no. 24, pp. 3951-3953, 2008.

[339] R. Pohja, P. Auerkari, and P. Vilaça, "Modelling for creep cavitation damage and life of three metallic materials," *Materials at High Temperatures,* vol. 39, no. 1, pp. 86-96, 2022.

[340] B. Xiao, S. D. Yadav, L. Zhao, Z. Tang, Y. Han, X. Yang, J.-J. Kai, T. Yang, and L. Xu, "Deep insights on the creep behavior and mechanism of a novel G115 steel: Micromechanical modeling and experimental validation," *International Journal of Plasticity,* vol. 147, no. 103124, pp. 1-15, 2021.

[341] F. Masuyama, "Advances in Creep Damage/Life Assessment Technology for Creep Strength Enhanced Ferritic Steels," *Procedia Engineering,* vol. 55, pp. 591-598, 2013.

[342] K. Sawada, K. Maruyama, Y. Hasegawa, and T. Muraki, "Creep life assessment of high chromium ferritic steels by recovery of martensitic lath structure," *Key Engineering Materials,* vol. 171, pp. 109-114, 1999.

[343] B. Xiao, L. Xu, Z. Tang, L. Zhao, H. Jing, Y. Han, and H. Li, "A physical-based yield strength model for the microstructural degradation of G115 steel during long-term creep," *Materials Science and Engineering: A,* vol. 747, pp. 161-176, 2019.